



# *University of* **HUDDERSFIELD**

## **University of Huddersfield Repository**

Hanif, Imran

Ion Irradiation Modification of Silicon Nanowires

### **Original Citation**

Hanif, Imran (2017) Ion Irradiation Modification of Silicon Nanowires. Doctoral thesis, University of Huddersfield.

This version is available at <http://eprints.hud.ac.uk/id/eprint/32630/>

The University Repository is a digital collection of the research output of the University, available on Open Access. Copyright and Moral Rights for the items on this site are retained by the individual author and/or other copyright owners. Users may access full items free of charge; copies of full text items generally can be reproduced, displayed or performed and given to third parties in any format or medium for personal research or study, educational or not-for-profit purposes without prior permission or charge, provided:

- The authors, title and full bibliographic details is credited in any copy;
- A hyperlink and/or URL is included for the original metadata page; and
- The content is not changed in any way.

For more information, including our policy and submission procedure, please contact the Repository Team at: [E.mailbox@hud.ac.uk](mailto:E.mailbox@hud.ac.uk).

<http://eprints.hud.ac.uk/>

# **ION IRRADIATION MODIFICATION OF SILICON NANOWIRES**

**IMRAN HANIF**

A thesis submitted to the University of Huddersfield in partial fulfilment  
of the requirements for the degree of Doctor of Philosophy

April 2017

## **Copyright Statement**

- i. The author of this thesis (including any appendices and/or schedules to this thesis) owns any copyright in it (the “Copyright”) and s/he has given The University of Huddersfield the right to use such copyright for any administrative, promotional, educational and/or teaching purposes.
- ii. Copies of this thesis, either in full or in extracts, may be made only in accordance with the regulations of the University Library. Details of these regulations may be obtained from the Librarian. This page must form part of any such copies made.
- iii. The ownership of any patents, designs, trademarks and any and all other intellectual property rights except for the Copyright (the “Intellectual Property Rights”) and any reproductions of copyright works, for example graphs and tables (“Reproductions”), which may be described in this thesis, may not be owned by the author and may be owned by third parties. Such Intellectual Property Rights and Reproductions cannot and must not be made available for use without the prior written permission of the owner(s) of the relevant Intellectual Property Rights and/or Reproductions.

# Contents

<b>Acknowledgements.....</b>	<b>i</b>
<b>Declaration.....</b>	<b>ii</b>
<b>Abstract.....</b>	<b>iii</b>
<b>List of Figures.....</b>	<b>iv</b>
<b>1 Introduction .....</b>	<b>1</b>
1.1 Background.....	1
1.2 Thesis Overview .....	6
<b>2 Literature Review .....</b>	<b>9</b>
2.1 Introduction.....	9
2.2 Crystallography.....	10
2.2.1 Lattice Points.....	10
2.2.2 Lattice Vectors .....	10
2.2.3 Crystal Basis .....	11
2.2.4 Primitive Unit Cell .....	11
2.2.5 Conventional Unit Cell .....	12
2.3 Crystal System .....	12
2.3.1 Bravais Lattice .....	13
2.3.2 Reciprocal Space.....	13
2.3.3 Coordination Number.....	13
2.4 Face Centred Cubic System.....	14
2.5 Miller Indices.....	14
2.5.1 Families of Directions and Planes.....	15



2.6	Distance between Planes (d–Spacing) .....	16
2.7	Structural Properties of Si.....	17
2.8	Atomic Collisions in Solids .....	19
2.9	Taxonomy of Defects by Dimensionality .....	19
2.9.1	Point Defects .....	20
2.9.2	Frenkel Defect and IV Pair .....	22
2.10	Defects in Silicon.....	22
2.11	Ion-beam-Induced Amorphisation.....	25
2.11.1	Introduction .....	25
2.11.2	Homogenous Amorphisation .....	25
2.11.3	Heterogeneous Amorphisation.....	26
2.11.4	Nucleation Limited Model of Amorphisation.....	28
2.12	Amorphisation of Silicon.....	29
2.12.1	Defect-based Models.....	29
2.13	Recrystallisation.....	32
2.13.1	Annealing .....	32
2.13.2	Solid Phase Epitaxial Growth .....	32
2.13.3	Random Nucleation Growth .....	33
2.13.4	Regrowth Rate and Orientation Dependence .....	34
2.13.5	Solid Phase Epitaxial Growth Models .....	34
2.14	Bending of Semiconductor Nanowires under Ion Irradiation.....	36
2.15	Van Der Waals Forces .....	40
2.15.1	Introduction to Van der Waals Forces .....	40
2.15.2	Microscopic and Macroscopic Models .....	40

2.16	Force Measurement Techniques .....	44
2.17	Mechanical Properties of Nanowires .....	48
2.17.1	Young's Modulus Dependence on Nanowire Diameter .....	51
2.17.2	Temperature Effects .....	54
2.17.3	Temperature Effects .....	56
2.18	Thermal Conductivity of Silicon Nanowires .....	57
2.18.1	Thermal Conductivity of Silicon Dioxide.....	61
2.19	Summary.....	64
<b>3</b>	<b>Experimental Methods .....</b>	<b>66</b>
3.1	Introduction.....	66
3.2	Sample Preparation .....	66
3.3	Transmission Electron Microscopy .....	67
3.4	Physics of Electrons Moving in an Magnetic Field.....	67
3.4.1	Deflection of Electron Beam.....	71
3.5	Introduction to Elastic Scattering .....	72
3.5.1	Interaction Cross-Section .....	72
3.5.2	Differential Cross-Section.....	73
3.5.3	Total Probability of Scattering .....	74
3.5.4	Mean Free Path .....	75
3.6	Atomic Scattering Factor .....	75
3.6.1	The Structure Factor.....	76
3.7	Coherent Elastic-Scattering and Bragg's Law .....	77
3.7.1	Deviation Parameter ( $S_g$ ).....	79
3.7.2	Incoherent Elastic-Scattering .....	79

3.7.3	Kikuchi Lines .....	80
3.7.4	Ewald Sphere .....	80
3.8	Electron Sources .....	81
3.8.1	Wehnelt Cap.....	82
3.9	Electromagnetic Lens in TEM.....	83
3.9.1	Condenser lens .....	84
3.9.2	Objective Lens .....	86
3.9.3	Intermediate Lens.....	86
3.9.4	Projector Lens .....	87
3.10	Deflectors.....	87
3.10.1	Pivot Points .....	89
3.10.2	Voltage and Current Centring.....	89
3.11	Astigmatism.....	89
3.12	Stigmators .....	90
3.13	Apertures.....	91
3.13.1	Condenser Aperture .....	91
3.13.2	Objective Aperture .....	92
3.13.3	Selected Area Aperture .....	92
3.14	Detection Devices .....	92
3.15	Aberrations.....	93
3.15.1	Airy Disk.....	93
3.15.2	Spherical Aberration .....	94
3.15.3	Chromatic Aberration.....	94
3.16	Imaging Techniques.....	95

3.16.1	Bright Field Imaging .....	95
3.16.2	Dark Field Imaging .....	95
3.16.3	Two-Beam Conditions .....	96
3.17	The MIAMI Facility .....	97
3.17.1	Introduction .....	97
3.17.2	Overall Design of the MIAMI Facility .....	97
3.17.3	Ion Source .....	98
3.17.4	Beam Transport.....	98
3.17.5	Beam Profile Monitors .....	101
3.17.6	Current Metering Rod .....	103
3.18	Atomic Force Microscope .....	103
3.19	Working Principle of AFM.....	104
3.19.1	Modes of Operation.....	105
3.20	Artefacts in AFM images.....	106
3.20.1	Probing Tip Artefacts .....	106
3.20.2	Scanner Artefacts .....	107
3.20.3	Features along the Scan Direction .....	109
3.20.4	External and Internal Noise.....	110
3.21	Experimental Method for Irradiation of Nanowires .....	110
3.21.1	Tilt Image Series of Nanowires .....	111
3.21.2	Determination of Angle of Inclination of Nanowires .....	112
3.22	Summary .....	115
<b>4</b>	<b>Ion Irradiation Calculations .....</b>	<b>117</b>
4.1	Introduction.....	117

4.2	Ion-Solid Interactions .....	117
4.2.1	Collision Cascades .....	119
4.2.2	Displacement Spike.....	120
4.2.3	Thermal Spike .....	120
4.2.4	Stopping Power .....	121
4.2.5	Elastic Energy Loss (Nuclear Stopping) .....	121
4.2.6	Inelastic Energy Loss (Electronic Stopping) .....	121
4.2.7	Total Stopping Power.....	122
4.2.8	Range of Ions .....	123
4.2.9	Channelling .....	124
4.3	Binary Collision Approximation .....	125
4.3.1	The SRIM Monte Carlo Computer Code.....	127
4.3.2	Types of Damage Calculation.....	128
4.4	SRIM Outputs .....	129
4.5	Modelling Radiation Damage in Nanowires Using SRIM .....	130
4.5.1	Threshold Displacement Energy of Silicon .....	130
4.5.2	Multislice SRIM Method .....	130
4.6	Selection of Ion Irradiation Conditions .....	133
4.7	Summary .....	135
<b>5</b>	<b>Bending of Silicon Nanowires.....</b>	<b>137</b>
5.1	Introduction.....	137
5.2	Ion Irradiation Conditions.....	138
5.3	Procedure for Nanowire Bending Experiments.....	142
5.4	Ion Irradiation Experimental Results.....	143

5.4.1	Bending of Silicon Nanowires .....	143
5.4.2	Fully Amorphous Silicon Nanowires.....	148
5.5	Recrystallisation of Silicon Nanowires.....	150
5.6	Summary .....	153
<b>6</b>	<b>Comparative Experiments to Borschel.....</b>	<b>154</b>
6.1	Introduction.....	154
6.2	Establishing Nanowire Orientation to Irradiate 35° off Normal .....	155
6.2.1	Ion Range Matching.....	157
6.2.2	Peak Damage Depth Matching.....	160
6.2.3	DPA Matching .....	164
6.3	Summary .....	165
<b>7</b>	<b>Industrial Semiconductor Processing Conditions .....</b>	<b>166</b>
7.1	Introduction.....	166
7.2	Structural Defects and Plastic Deformation.....	167
7.3	Xenon Bubbles in Silicon Nanowires .....	172
7.4	Measurement of Damage Depth .....	173
7.5	Summary .....	178
<b>8</b>	<b>Finite Element Modelling of Si Nanowires.....</b>	<b>179</b>
8.1	Introduction.....	179
8.2	Setting up of the Problem for Modelling .....	179
8.3	Surface Morphology of Silicon Nanowires .....	182
8.3.1	AFM Sample Preparation and Si NW Selection.....	182
8.3.2	Roughness Measurements.....	183
8.3.3	Roughness Analysis .....	183

8.4	Summary .....	187
<b>9</b>	<b>Discussion .....</b>	<b>189</b>
9.1	Introduction.....	189
9.2	Semiconductor Nanowire Bending Mechanisms.....	194
9.2.1	Volume Change due to Damage Accumulation.....	194
9.2.2	Amorphisation Facilitated Mechanisms.....	196
9.2.3	Spatial Distributions of Vacancy and Interstitials.....	197
9.2.4	Viscoelastic Thermal Spike Models .....	198
9.3	Damage and Its Distance from NW Surface.....	199
9.4	Recrystallisation of Si NWs.....	201
9.5	Summary and Conclusion.....	201
<b>10</b>	<b>Summary and Conclusion.....</b>	<b>203</b>
10.1	Future Work.....	204
	<b>References .....</b>	<b>205</b>
	<b>Appendix A .....</b>	<b>242</b>
	<b>Appendix B .....</b>	<b>250</b>

## Acknowledgements

*All praise is due to the Almighty **ALLAH** who is the most Gracious and the most Merciful.*

I am humbled and thankful to the Almighty **ALLAH** who has granted me the opportunities and strength to complete the course of my studies.

I would like to express my gratitude to my supervisors Professor Stephen Donnelly and Dr Jonathan Hinks for supporting me throughout my work in the Microscope and Ion Accelerator for Materials Investigation (MIAMI) facility at the University of Huddersfield. I would specially like to thank and mention Dr Jonathan Hinks excellent supervision and personality who has always been a beacon of knowledge and inspiration to me. I have benefited a lot from his in depth scientific knowledge of transmission electron microscopy, ion-beam-induced radiation damage in materials, strong attention to details, time management and discipline.

I am thankful to my family members in Pakistan for their support and appreciations. I would especially like to mention my Dad and Ammi G (mother) for everything they have done for me, their love, affection and prayers without whom I could never achieve this milestone. I dedicate this thesis to my Dad and Ammi G.

I am indebted to my Brother Imtiaz Ali for his countless favours, kindness, well wishes, and support to smoothly carrying out the PhD studies. I would especially like to mention and say a special thanks to my wife Humaira Imran for her forbearance, understanding, support, prayers and love.

Finally, I would like to thank all my colleagues in the MIAMI facility for their support and discussions which help me improving my scientific understanding of materials. I have spent truly a wonderful time in the laboratory.



## Declaration

The research work reported in this thesis is the work of the author with the following exemption. The development of the computer code to incorporate the *Stopping and Range of Ions in Matter* (SRIM) program into MatLab was carried out in collaboration with Jonathan Hinks, Graeme Greaves and Matheus Tunes in the Electron Microscopy and Materials Analysis (EMMA) research group at the University of Huddersfield.

## Abstract

Ion irradiation modification of silicon nanowires has been explored *in-situ* using the Microscope and Ion Accelerator for Materials Investigations (MIAMI) facility at the University of Huddersfield. Ion irradiation experiments were designed using the Stopping and Range of Ions in Matter (SRIM) Monte Carlo computer code. A multislice SRIM method was developed to estimate the damage and ion implantation in a nanowires geometry and a code was developed to incorporate SRIM into MatLab.

*In-situ* Transmission Electron Microscopy (TEM) has been used to explore the ion-beam-induced bending of silicon nanowires under different irradiation conditions and the underlying mechanisms which drive nanowire bending have been identified. Furthermore, a tipping point for direction reversal of bending under different irradiation conditions has been identified. Recrystallisation of silicon nanowires was also investigated using thermal annealing.

The effects of 7 keV  $\text{Xe}^+$  ions on silicon nanowires have been investigated under industrial processing conditions. Structural and morphological changes of silicon nanowires have been observed. These include nanowire bending, amorphisation, bubble formation and sputtering. The depth of damage has also been measured experimentally and was compared with the predictive damage using SRIM.

In order to calculate the temperature along a nanowire during an *in-situ* TEM heating experiment, the relevant parameters have been found from the literature which will be used to set up a finite element model. Atomic Force Microscopy (AFM) was used to measure the surface roughness of silicon nanowires and molybdenum grids. Other parameters of interest include the Hamaker's constant for the Van der Waals forces as well as the Young's modulus, thermal conductivity and specific heat capacity of silicon nanowires and the ultra-thin oxide layer on their surface.

## List of Figures

<b>Figure 1.1:</b> The first transistor invented and assembled in 1947 at Bell Labs, USA. Reproduced from [3].	2
<b>Figure 1.2:</b> The graph is showing the progress of semiconductor technology and the adherence to Moore's Law. Reproduced from [8].	2
<b>Figure 1.3:</b> Schematic showing a four terminal field effect transistor illustrating the source, drain, gate and substrate. Reproduced from [13].	3
<b>Figure 2.1:</b> Translation vectors <b>a</b> , <b>b</b> and <b>c</b> with the angles $\alpha$ , $\beta$ and $\gamma$ between them.	11
<b>Figure 2.2:</b> The seven crystal systems. reproduced from [86].	12
<b>Figure 2.3:</b> A representation of a conventional unit cell of FCC with lattice constant, <b>a</b> , made with Balls and Sticks software [88].	14
<b>Figure 2.4:</b> Vector diagram to illustrate the derivation of $d_{hkl}$ .	16
<b>Figure 2.5:</b> (a) Schematic view of a Si conventional unit cell containing 14 atoms as FCC structure (b) along [001] created using Balls and Sticks software[88].	18
<b>Figure 2.6:</b> (a) Perfect crystalline structure of c-Si {110} with six-member rings in which each central atom bonding with four atoms at the vertices of a tetrahedron; and (b) a-Si with 5 and 7 member rings and long range order is lost. Reproduced from [96].	19
<b>Figure 2.7:</b> Schematic illustration of point defects in a crystal.	21
<b>Figure 2.8:</b> Crystalline structure of a di-vacancy in silicon. Reproduced from [105].	22
<b>Figure 2.9:</b> Vacancy type defect annealing in Si is shown with dotted lines during 15 min isochronal annealing. Reproduced from [100].	23

<b>Figure 2.10:</b> Cylindrical model of radius, $R_o$ , for the volume surrounding the path of an ion track. $\delta R$ is the sheath for out-diffusion of defects and $R_o - \delta R$ is the stable amorphous core. Reproduced from [138].	27
<b>Figure 2.11:</b> Schematic representations of: (a) the c-Si structure showing the six-membered rings with a $\langle 100 \rangle$ split di-interstitial shown by the dotted bonds and atoms labelled A, B and C; (b) the local atomic rearrangement after the introduction of a D-D pair with atoms 3, 4, 5, A and B forming a five-member ring and atoms 3, B and C are part of a 7 member ring. Reproduced from [152].	30
<b>Figure 2.12:</b> Atomic structure of the IV pair: dotted lines indicate the atoms and bonds in a perfect Si crystal; arrows at atoms A and A' show the direction of displacement of the atoms from their sites in the perfect lattice; the bonding between atoms A and A' is switched between B and B'. Reproduced from [93].	31
<b>Figure 2.13:</b> Schematic representation of SPEG recrystallisation of a Si NW. Crystal-amorphous interface region shown as thick black line moving from left to right during thermal annealing.	33
<b>Figure 2.14:</b> Graph illustrating the regrowth rate of amorphous silicon is orientation dependant. It can be seen that regrowth is fastest for the $\langle 100 \rangle$ direction whilst it is slowest for the $\langle 111 \rangle$ . Reproduced from [46].	34
<b>Figure 2.15:</b> Schematic of semiconductor NWs bending under ion irradiation: a) downward bending; (b) upward bending. Arrows show the ion beam direction. Reproduced from [55].	37
<b>Figure 2.16:</b> Schematic of two flat planes interacting at a distance, D.	41
<b>Figure 2.17:</b> Schematic of a sphere and a plane interacting at a distance, D.	43
<b>Figure 2.18:</b> Schematic of a cylinder and a plane interacting at a distance, D.	43
<b>Figure 2.19:</b> Force-displacement curve for interactions between a tungsten tip and a graphite sample obtained by AFM. The cantilever is under extremely-light load which is completely due to surface forces. Reproduced from [212].	45
<b>Figure 2.20:</b> Graph showing a comparison between the Van der Waals and capillary forces as a function of distance, D. Reproduced from [216].	47

<b>Figure 2.21:</b> Force-displacement curve for surface forces as a function of tip radius. The parameters used to plot Fig. 2.20 are the: $A = 3.0 \times 10^{-19}$ J and $R = 20$ nm. Reproduced from [216].	47
<b>Figure 2.22:</b> Graph showing the force-displacement curve plotted using Equation 2.14. The adhesion force ( $F_a = -4.36$ nN, solid black line) and Van der Waals forces (open red circles) involved in the picking-up process of Ni clusters on HOPG. Reproduced from [204].	48
<b>Figure 2.23:</b> Young's modulus dependence on the diameter of NWs obtained using atomic force microscopy: (a) increasing with decreasing diameter for clamped Pb NWs; and (b) decreasing with decreasing diameter for cantilevered GaN NWs. The curves are the best fit for the experimental data. Reproduced from [59].	50
<b>Figure 2.24:</b> Young's modulus of strained Cu NWs calculated using MD simulations. Reproduced from [218].	51
<b>Figure 2.25:</b> Circular cross-sections of [110]-oriented Si NWs of different diameters used for MD simulations. Surface atoms have higher energy than inner atoms after relaxation. Reproduced from [229].	52
<b>Figure 2.26:</b> Results of MD simulations for Young's modulus of [111] and [110]-oriented Si NWs as a function of diameter and compared with bulk Si. The Young's modulus for both orientations decreases as a function of diameter. Reproduced from [229].	52
<b>Figure 2.27:</b> MD simulation results of the Young's modulus for [100]-, [110]- and [111]-oriented Cu NWs with values for the bulk indicated by horizontal line. For larger diameter NWs, the surface compressive strain is smaller and therefore the value of the Young's modulus is closer to the bulk. Reproduced from [221].	53
<b>Figure 2.28:</b> Diameter dependence of Young's modulus for Cu NWs obtained using the MD simulations. Reproduced from [218].	54
<b>Figure 2.29:</b> Graphs showing results of MD simulations: a) stress-strain curve for 5 nm Si NWs at different temperatures illustrating the decrease in stress as temperature increases; and b) tensile stress-strain curves for Si NWs of different diameters at room temperature. Reproduced from [229].	55

<b>Figure 2.30:</b> Variation in the Young's modulus of Cu NWs against temperature obtained using MD simulations. Reproduced from [218].	55
<b>Figure 2.31:</b> Graphs showing results of MD simulations: a) stress-strain curve for 5 nm Si NWs at different temperatures illustrating the decrease in stress as temperature increases; and b) tensile stress-strain curves for Si NWs of different diameters at room temperature. Reproduced from [229].	56
<b>Figure 2.32:</b> Variation in the Young's modulus of Cu NWs against temperature obtained using MD simulations. Reproduced from [218].	57
<b>Figure 2.33:</b> Sandwich-structured composites (SSCs) of SiNWs/Si/SiNWs grown on both sides of a Si wafer by etching. Conduction of heat introduced by the laser pulse was detected on the opposite side of the SSC as shown. Reproduced from [234].	60
<b>Figure 2.34:</b> Thermal conductivity dependence of SiO <sub>2</sub> films on different preparation techniques. Reproduced from [248].	61
<b>Figure 2.35:</b> Dependence of effective thermal conductivity on thickness of SiO <sub>2</sub> films obtained from FE modelling. Reproduced from [233].	63
<b>Figure 2.36:</b> Thermal conductivities of SiO <sub>2</sub> films as a function of film thickness, $d$ , measured using the $3\omega$ method. The solid line indicates the bulk value. Reproduced from [248].	64
<b>Figure 3.1:</b> A vector diagram of a left-hand rule to determine the direction of the Lorentz force, $\mathbf{F}$ , in a magnetic field, $\mathbf{B}$ , acting on a charged particle moving with velocity, $\mathbf{v}$ .	68
<b>Figure 3.2:</b> Schematics showing: (a) a breakdown of the velocity vector, $\mathbf{v}$ , into its components, $v_x$ , and $v_y$ with the direction of the magnetic field, $\mathbf{B}$ , parallel to $v_x$ ; (b) an electron with $\mathbf{v}_y$ entering in $\mathbf{B}$ (into paper) following a circular motion. The direction of the force acting on the electron has been found from left hand rule.	69
<b>Figure 3.3:</b> Schematic of the trajectory of an electron with velocity, $\mathbf{v}$ , entering a homogenous magnetic field, $\mathbf{B}$ , at an angle, $\theta$ . The parallel and perpendicular components of $\mathbf{v}$ relative to $\mathbf{B}$ are shown. In a TEM, electrons follow a helical path of radius, $r$ , through magnetic field, $\mathbf{B}$ , entering through point P and exiting at P'. The z-axis indicates the optical axis of the TEM. Redrawn and adapted from [260].	70

<b>Figure 3.4:</b> Schematic of a plane wave, $\mathbf{K}_0$ , interacting with an atom (blue circle) and scattered as a spherically wave (dashed red circle). Redrawn and adapted from [260].	73
<b>Figure 3.5:</b> A vector diagram illustrating an incident wave vector, $\mathbf{K}_0$ , diffracted wavevector, $\mathbf{K}_d$ , and the resulting wavevector, $\mathbf{K}$ , in going from $\mathbf{K}_0$ to $\mathbf{K}_d$ .	77
<b>Figure 3.6:</b> A schematic of plane wave scattered at an angle, $2\theta$ , by atomic planes separated by a distance, $d$ .	78
<b>Figure 3.7:</b> Vector diagram for diffraction deviating from the perfect Bragg angle, $\theta_B$ , by $\Delta\theta$ showing the deviation parameter, $s_g$ .	79
<b>Figure 3.8:</b> Incoherently elastically scattered electrons diffracting at the Bragg condition forming a pair of Kossel cones. Adapted from [260].	80
<b>Figure 3.9:</b> Construction of Ewald sphere with incident beam, $\mathbf{K}_0$ , and Bragg diffracted beam, $\mathbf{K}_d$ , forming an angle of $2\theta_B$ .	81
<b>Figure 3.10:</b> Schematic of the filament, Wehnelt cap and anode for a tungsten thermionic electron source (redrawn from [260]).	82
<b>Figure 3.11:</b> Schematic cross-section of an electromagnetic lens used in a TEM. Redrawn from [260].	83
<b>Figure 3.12:</b> Schematic ray diagrams for a TEM operating in (a) diffraction mode and (b) imaging mode. Redrawn from [260].	84
<b>Figure 3.13:</b> Schematic ray diagram for a single condenser lens showing the collection semi-angle, $\beta$ , and convergence semi-angle, $\alpha$ . Redrawn from [260].	85
<b>Figure 3.14:</b> Schematic ray diagram of a double-lens condenser system: (a) weak condenser lens forms a broader probe on the specimen, (b) strong condenser lens makes a sharper probe on the specimen. Redrawn from [260].	86
<b>Figure 3.15:</b> Schematic top-down view of a deflector illustrating the direction of the magnetic field, $\mathbf{B}$ (green) and magnetic force, $\mathbf{F}$ (red) while the direction of the electron beam is into the paper. The windings of the coil are shown in blue. Redrawn from [260].	87

<b>Figure 3.16:</b> Schematics demonstrating the use of condenser deflectors to (a) shift and (b) tilt the electron beam onto the specimen. Black dashed line shows the incident electron beam along the optical axis. ....	88
<b>Figure 3.17:</b> Schematic of a stigmator used in TEM. The windings of the coils are illustrated with blue lines while the direction of the magnetic fields is indicated with green solid arrows. Astigmatism in the electron beam is illustrated by the red dashed ellipsoids and the green circle indicates the ideal beam shape once astigmatism is corrected. Reproduced from [263]. ....	91
<b>Figure 3.18:</b> The intensity profile of images of two point sources: a) when the points are resolvable and airy disks are not overlapping; b) the two point sources are close and the airy disks are overlapping but are at the limit of resolvability; and c) airy disks are overlapping as points are too close and hence cannot be resolved. Reproduced and adapted from [4]. ....	93
<b>Figure 3.19:</b> A schematic ray diagram of BF imaging in a TEM. ....	96
<b>Figure 3.20:</b> A schematic ray diagram of DF imaging in a TEM. ....	96
<b>Figure 3.21:</b> MIAMI facility layout and transport system for ion beam. Reproduced from [264]. ....	98
<b>Figure 3.22:</b> The Colutron G-2 ion source installed in the MIAMI facility. Reproduced from [264]. ....	99
<b>Figure 3.23:</b> The bending magnet used in the MIAMI facility to deflect the ions through 37° (reproduced from [264]). ....	99
<b>Figure 3.24:</b> The nine-stage acceleration tube to accelerate the ion beam to higher energies if required. The white rings are ceramic used for the purpose of insulation between the acceleration stages (reproduced from [264]). ....	100
<b>Figure 3.25:</b> Einzel lens (right) with deflectors (left) used in the MIAMI facility. Reproduced from [264]. ....	101
<b>Figure 3.26:</b> Final deflection system used in the MIAMI facility to provide an electrostatic field to the ion beam entering the TEM (reproduced from [264]). ....	102



<b>Figure 3.27:</b> Skimming diaphragm between two apertures ensuring that the ion beam enters the final deflection system of the MIAMI on zero- potential line. Reproduced from [264].	102
<b>Figure 3.28:</b> The current metering rod to align and measure the ion beam current in a TEM (adapted from [264]).	103
<b>Figure 3.29:</b> A schematic of AFM operation. Interaction between the tip and the sample is measured by monitoring the deflection of the free end of the cantilever by a laser beam shown in red. The laser beam reflects off the cantilever onto a position sensitive photodiode. Reproduced from [267].	104
<b>Figure 3.30:</b> Schematic of how an artefact can be introduced by a large diameter tip: (a) overestimating and (b) underestimating the lateral dimensions. Arrow shows the scanning direction and trace. Redrawn from [8].	107
<b>Figure 3.31:</b> Schematic showing the traces of two tips with different sidewall angles. The side walls cause broadening of the lateral dimensions in the image. Redrawn from [284].	107
<b>Figure 3.32:</b> Schematic of edge overshoot caused by a fast scan speed. Arrow shows the scanning direction and trace. Redrawn from [283].	108
<b>Figure 3.33:</b> A topographic image of LiF crystal surface showing distortions due to thermal drift (left) with bowing apparent in the bottom of the image. The image without thermal drift (right). Reproduced from [283].	109
<b>Figure 3.34:</b> Distortion of features in an AFM image caused by creep. Reproduced from [284].	109
<b>Figure 3.35:</b> (a) A schematic representation of an electron beam and ion beam in the MIAMI facility and (b) a bright-field image of the NW at zero-tilt plus 45°-rotation such that the ion beam is at normal incidence.	111
<b>Figure 3.36:</b> Schematics demonstrating the tilt image series performed before and after the irradiation experiments to determine the bending direction of the Si NWs. A representation of the NW as seen by the electron beam in the TEM along the z-axis is shown in (a) to (c). The representation of the Si NW as seen from the x-axis of the TEM is illustrated in (d) to (f).	112

<b>Figure 3.37:</b> Overlaid images of a Si NW at zero-tilt and plus-45°-tilt where a and b are the projected length at these two tilts, respectively.....	113
<b>Figure 3.38:</b> Trigonometry of NW undergoing 45° x-tilt viewed in yz-plane of the TEM. ....	114
<b>Figure 3.39:</b> Trigonometry of the NW as seen in xz-plane of the TEM. ....	115
<b>Figure 4.1:</b> A schematic showing the probability of an atomic displacement occurring when the energy transferred to the target atom is between the minimum, $E_{d-min}$ , and maximum, $E_{d-max}$ , displacement energies. Redrawn from [263]. ....	118
<b>Figure 4.2:</b> A schematic showing a single atomic collision leading to the formation of a cascade: an incident ion with $E_0 > E_d$ displaces a target atom from its lattice site becoming a PKA, $a'$ ; a PKA with $E - E_d > E_d$ produces a secondary knock-on atom, $a''$ ; and in turn $a''$ produces a tertiary knock-on atom, $a'''$ , and so on. This process continues in the material until atom lose energy and come to rest or exit the target. ....	119
<b>Figure 4.3:</b> Schematic illustration of a displacement spike (reproduced from [296]). ....	120
<b>Figure 4.4:</b> A schematic of the energy loss due to electronic stopping of an ion moving with velocity, $v_{ion}$ , through a target. ....	122
<b>Figure 4.5:</b> Comparison between the electric and nuclear stopping powers: nuclear stopping power curve dominates at lower energies (typically between 10–100 keV) while electronic stopping is dominant at higher energies (typically MeV energies). Reproduced from [299]. ....	123
<b>Figure 4.6:</b> Schematic of an ion begin scattered during a series of collisions with the target atoms illustrating how the actual range of the ion and the path length (distance from A–B) can differ. In other words, the projected range, $R_p$ , is different from the path length, $R$ . ....	124
<b>Figure 4.7:</b> A schematic showing an ion being channelled in Si. The channelled ion may experience glancing collisions and will lose energy due to the electronic drag force but the probability of nuclear collisions is reduced. ....	125

<b>Figure 4.8:</b> A collision between two atoms of mass $M_1$ , and $M_2$ , drawn schematically in a centre-of-mass system: a “scattering triangle” is used to calculate the scattering angle, $\theta$ . The triangle is composed of are the distance of closest approach, $r_0$ , between the atoms, the radii of projectiles, $\rho_1$ and $\rho_2$ , and the correction terms, $\delta_1$ and $\delta_2$ , for different atomic potentials. ....	127
<b>Figure 4.9:</b> Diagram showing: (a) division of NW geometry into multiple slices to allow application of SRIM calculations; and (b) calculation of chord length, $x$ , at distance, $a$ , from centre, $C$ , of a NW of radius, $r$ , used to determine target thickness for the input parameters for the corresponding SRIM calculation.....	131
<b>Figure 4.10:</b> Plots of vacancies (a, c) and interstitials (b, d) created by 6 keV $\text{Ne}^+$ ions incident upon a 50 nm Si NW obtained using the multislice SRIM method. The results of the first implementation of this approach are shown in (a) and (b) with the results of the improved MatLab code is shown in (c) and (d). ....	133
<b>Figure 4.11:</b> Atomic percentages of ion implantation at amorphisation against ion energy in different thickness of Si calculated using SRIM.....	135
<b>Figure 5.1:</b> Distribution of the (a) atomic displacements and (b) ion implantation caused by 6 keV $\text{Ne}^+$ ions in 50 nm thick Si obtained using SRIM [289]......	139
<b>Figure 5.2:</b> Vacancy and interstitial distributions in 50 nm thick Si irradiated with 6 keV $\text{Ne}^+$ obtained using SRIM [289]......	139
<b>Figure 5.3:</b> Two-dimensional representations of (a) displacement distribution and (b) ion implantation in a 50 nm diameter Si NW irradiated with 6 keV $\text{Ne}^+$ ions. ....	140
<b>Figure 5.4:</b> Two-dimensional representation of (a) vacancies and (b) interstitials created by 6 keV $\text{Ne}^+$ ions in a 50 nm diameter Si NW.....	140
<b>Figure 5.5:</b> Distribution of displacement caused by 60 keV $\text{Ne}^+$ ions in 50 nm diameter Si NW calculated using the multislice SRIM method. ....	141
<b>Figure 5.6:</b> Ion implantation profile of 60 keV $\text{Ne}^+$ ions in 50 nm diameter Si NW calculated using the multislice SRIM method. ....	142
<b>Figure 5.7:</b> Illustration of the tilt and rotate procedure with the electron beam (shown in green) and the ion beam (shown in yellow): a) the selected NW is rotated	

to align with the x-axis of the TEM; b) the NW is then tilted to  $-30^\circ$  to capture the SAED corresponding to the crystallographic direction in which the irradiation will subsequently be performed (represented by a solid black line); c) the NW is next tilted back to the zero position; and d) is rotated to plus- $45^\circ$  such that the ion beam is normal to the axis of the NW. .... 143

**Figure 5.8:** A SAED pattern captured during the tilt-rotation procedure illustrated in **Figure 5.7** showing the crystallographic direction presented to the ion beam. .... 144

**Figure 5.9:** Micrographs showing the tilt image series of an Si NW before (a to c) and after (d to f) ion irradiation. The series was captured by tilting the NW at plus- $45^\circ$  (c and f) and minus- $45^\circ$  (a and d) about the x-axis of the TEM. The NW was irradiated with 6 keV  $\text{Ne}^+$  ions to an end fluence of  $5.2 \times 10^{16}$  ions. $\text{cm}^{-2}$ . The scale bar in f) applies to all images. .... 145

**Figure 5.10:** A BF-TEM image of the bent Si NW irradiated with 6 keV  $\text{Ne}^+$  ions to a fluence of  $1.1 \times 10^{16}$  ions. $\text{cm}^{-2}$ . The inset shows the SAED pattern with intense bright spots clearly demonstrating the residual crystallinity. .... 146

**Figure 5.11:** Micrographs showing a Si NW undergoing bending when irradiated with 6 keV  $\text{Ne}^+$  ions: (a) virgin NW with inset showing tip of NW; (b) the NW bends towards the ion beam during irradiation to a fluence of  $3.5 \times 10^{16}$  ions. $\text{cm}^{-2}$ ; (c) the sample was flipped to allow irradiation from the opposite side; (d) a bent NW demonstrates straightening when subsequently irradiated from the opposite side to a fluence of  $1.3 \times 10^{16}$  ions. $\text{cm}^{-2}$ ; and (e-f) continued to bend back towards the ion beam. The fluences for (e) and (f) are  $1.6 \times 10^{16}$  and  $2.4 \times 10^{16}$  ions. $\text{cm}^{-2}$ , respectively. The scale bar in (f) applies to all images. .... 147

**Figure 5.12:** BF-TEM images showing a Si NW at zero-tilt plus- $45^\circ$ -rotation: (a) virgin NW with corresponding SAED pattern shown in (b); (c) irradiated with 6 keV  $\text{Ne}^+$  ions to a fluence of  $5.2 \times 10^{16}$  ions. $\text{cm}^{-2}$  shows bending of the NW with corresponding SAED pattern shown in (d) demonstrating the residual crystallinity; (e) fully amorphous NW irradiated with 60 keV  $\text{Ne}^+$  ions to a fluence of  $6.1 \times 10^{15}$  ions. $\text{cm}^{-2}$ ; and (f) the absence of any detectable crystallinity is confirmed in the corresponding SAED pattern. The scale bar is the same for all images. .... 149

<b>Figure 5.13:</b> Graph showing the temperature ramp versus time used to monitor the recrystallisation of amorphous Si NWs. The temperature increment was reduced above 400°C and then again above 600°C to allow the recrystallisation of the NWs to be monitored more closely. ....	151
<b>Figure 5.14:</b> Micrographs showing: (a) amorphous Si NW after 60 keV Ne <sup>+</sup> ion irradiation to a fluence of $6.1 \times 10^{15}$ ions.cm <sup>-2</sup> ; and (b) recrystallisation of the Si NW achieved through thermal annealing to 720°C. The insets show the corresponding SAED patterns with amorphous rings transitioning into a pattern featuring bright spots indicative of a significant single crystalline region in combination with rings characteristic of polycrystalline material. This suggests that the recrystallisation occurred via a mixture of SPEG and RNG. ....	152
<b>Figure 6.1:</b> Schematic showing a Si NW which has been rotated 135° from the x-axis and x-tilted by -7° to give an angle with the NW of 35° off normal in the geometry of the MIAMI facility. The ion and electron beam diameters are much larger in the MIAMI facility than shown in the schematic. ....	156
<b>Figure 6.2:</b> Micrographs showing a virgin Si NW at a) zero-rotation zero-tilt position and b) the NW after 135° rotation and a x-tilt of -7° so that the ion beam is incident at 35° off normal. The scale bar is the same for both the images. ....	157
<b>Figure 6.3:</b> Ion implantation profiles calculated using SRIM for: (a) 9.5 keV Xe <sup>+</sup> ions in 50 nm thick Si at 35° off normal; and (b) 35 keV Ar <sup>+</sup> ions in 150 nm thick GaAs at 35° off normal. ....	158
<b>Figure 6.4:</b> Atomic displacement profiles calculated using SRIM for: (a) 9.5 keV Xe <sup>+</sup> ions in 50 nm thick Si at 35° off normal; and (b) 35 keV Ar <sup>+</sup> ions in 150 nm thick GaAs at 35° off normal. ....	159
<b>Figure 6.5:</b> Micrographs showing the tilt series of a Si NW: before irradiation (a–c) and after irradiation (d–f) to an end fluence of $1.9 \times 10^{16}$ ions.cm <sup>-2</sup> . The tilt image series demonstrates that the NW bent towards the ion beam. The scale bar is the same for all the images. ....	160

<b>Figure 6.6:</b> Graphs illustrating the matching of peak damage depth for: (a) 5 keV $\text{Xe}^+$ ions into 50 nm thick Si at $35^\circ$ off normal; and (b) 35 keV $\text{Ar}^+$ ions into 150 nm thick GaAs as calculated from SRIM.....	161
<b>Figure 6.7:</b> Ion implantation profiles calculated using SRIM for: (a) 5 keV $\text{Xe}^+$ ions into 50 nm thick Si at $35^\circ$ off normal; and (b) 35 keV $\text{Ar}^+$ ions into 150 nm thick GaAs at $35^\circ$ off normal. ....	162
<b>Figure 6.8:</b> Three-dimensional computer model of an inclined NW before (top) and after (bottom) undergoing ion-beam-induced bending. Comparison with the experimental result in figure 6.12 confirms that the inclination and bending direction of the NW have been correctly deduced and modelled.....	162
<b>Figure 6.9:</b> Micrographs showing a tilt image series for a Si NW before (a–c) and after irradiation (d–f) with 5 keV $\text{Xe}^+$ ions to a fluence of $2.2 \times 10^{15} \text{ ions.cm}^{-2}$ . The series reveals the ion-beam-induced bending direction to be away from the ion beam when irradiated. Scale bar is applicable to all images. ....	163
<b>Figure 6.10:</b> Micrographs showing a Si NW before (a) and (b) after with 9.5 keV $\text{Xe}^+$ ions to a fluence of $1 \times 10^{15} \text{ ions.cm}^{-2}$ . Scale bar is applicable to both images..	165
<b>Figure 7.1:</b> Graphs showing the distribution of damage of 7 keV $\text{Xe}^+$ ions in (a) 24 nm (b) 50 nm thick Si as calculated using SRIM. ....	167
In the first series of experiments, thin Si NWs of diameters ranging from 24–50 nm with one end attached to the grid and the other end in free space were selected for the irradiation experiments. The NWs were irradiated with 7 keV $\text{Xe}^+$ ions at normal incidence and the ion-beam-induced modifications were investigated. The damage and ion implantation profiles for 24 and 50 nm thick Si were calculated using SRIM and are shown in Figure 7.1 and Figure 7.2, respectively. The peak of the damage depth and $R_p$ for 7 keV $\text{Xe}^+$ ions into 24 nm Si lie at 5.8 nm and 10.5 nm, respectively. ....	167
<b>Figure 7.3:</b> Graphs showing the ion implantation profile of 7 keV $\text{Xe}^+$ ions in (a) 24 nm (b) 50 nm thick Si as calculated using SRIM. ....	168

<b>Figure 7.4:</b> Composite micrograph demonstrating the bending of a Si NW during irradiation with 7 keV Xe <sup>+</sup> ions. The bending curvature increases at higher fluences given in units of ions.cm <sup>-2</sup> . .....	169
<b>Figure 7.5:</b> Micrographs showing the tilt image series of a Si NW before (a to c) and after (d to f) irradiation with 7 keV Xe <sup>+</sup> ions at normal incidence to an end fluence of 3.2×10 <sup>16</sup> ions.cm <sup>-2</sup> . The scale bar shown in (f) applies to all images. ....	169
<b>Figure 7.6:</b> Bright-field images of a Si NW demonstrating a sputtering effect: (a) un-irradiated NW and (b) after irradiation to a fluence of 2.6×10 <sup>16</sup> ions.cm <sup>-2</sup> . The insets show the corresponding SAED patterns and the scale bar in (b) applies to both images. ....	170
<b>Figure 7.7:</b> Micrographs showing the ion-irradiation-induced structural deformation of a Si NW: (a) virgin NW and (b) after irradiation with 7 keV Xe <sup>+</sup> ions to a fluence of 3.2×10 <sup>15</sup> ions.cm <sup>-2</sup> . Insets show the corresponding SAED patterns demonstrating the partial amorphisation. Cracking defects are highlighted with red circles in (b). The scale bar in (b) also applies to (a). ....	170
<b>Figure 7.8:</b> Micrograph of a Si NW showing black-spot damage inside the NW highlighted with arrows after irradiation with 7 keV Xe <sup>+</sup> ions to a fluence of 4.4×10 <sup>16</sup> ions.cm <sup>-2</sup> . ....	171
<b>Figure 7.9:</b> Micrograph showing a bright-field image of a Si NW demonstrating the formation of bubbles following irradiation with 7 keV Xe <sup>+</sup> to a fluence of 4.4×10 <sup>16</sup> ions.cm <sup>-2</sup> . Greyscale levels have been enhanced to optimise the contrast of the bubbles. ....	172
<b>Figure 7.10:</b> Schematic of the procedure to observe a Si NW normal to the ion irradiation direction in the MIAMI facility geometry using a tilt-rotate TEM sample holder: (a) the sample is irradiated at an x-tilt of minus-32.5° and a rotation of 25° from the x-axis; and (b) the NW is tilted to plus-32.5° and rotated back to the x-axis for analysis. The NW is shown in red with a faceted surface representing the direction in which it was ion irradiated. The electron beam is shown in green and the ion beam in translucent blue. ....	174

<b>Figure 7.11:</b> Two-dimensional plots showing the (a) atomic displacements and (b) ion implantation in a 40 nm diameter Si NW obtained using the multislice SRIM method.....	175
<b>Figure 7.12:</b> Micrographs showing (a) bright-field and (b) dark-field images of a Si NW before irradiation captured at zero-rotation plus-32.5°-tilt, Inset is showing the corresponding diffraction pattern The scale bar in (b) applies to both images.....	175
<b>Figure 7.13:</b> Micrographs showing bright-field images of a Si NWs demonstrating the effect of sputtering: (a) before and (b) after irradiation with 7 keV Xe <sup>+</sup> ions to a fluence of $8.1 \times 10^{16}$ ions.cm <sup>-2</sup> . The scale bar in (b) applies to both images.....	176
<b>Figure 7.14:</b> Graphs showing: (a) DPA calculated from SRIM for 7 keV Xe <sup>+</sup> ion irradiation of Si to a fluence of $1.7 \times 10^{16}$ ions.cm <sup>-2</sup> ; and (b) a closer view of the tail of the damage profile with the dotted line indicating the required DPA to amorphise Si with Xe <sup>+</sup> ions at room temperature. ....	176
<b>Figure 7.15:</b> Micrographs showing (a) bright-field and (b) dark-field images of a Si NW at zero-rotation plus-30°-tilt after irradiation to measure the depth of the damage caused by 7 keV Xe <sup>+</sup> ions to a fluence of $1.7 \times 10^{16}$ ions.cm <sup>-2</sup> . The scale bar in (b) applies to both images.....	177
<b>Figure 8.1:</b> Schematic of a Si NW on a Mo grid.....	180
<b>Figure 8.2:</b> Histogram of Ra surface roughness measurements of the Si NWs. ....	185
<b>Figure 8.3:</b> Histogram of Ra surface roughness measurements of the molybdenum TEM grids. ....	185
<b>Figure 8.4:</b> AFM scanned image showing the (a) topography of a Si NW and (b) 3D view of the roughness of a typical Si NW.....	189
<b>Figure 8.5:</b> AFM scanned image showing the (a) topography of a Mo grid and (b) 3D view of the roughness of a typical Mo grid.....	189
<b>Figure 9.1:</b> Schematic of a NW of diameter, 2r, illustrating a bent section with a radius of curvature, R, and arc length, $\theta R$ . The volumes of the bent section on the outside, $V > R$ , and inside, $V < R$ , of R can be calculated using the expressions shown. ....	195



**Figure 9.2:** A typical Si NW bending irradiated with 6 keV Ne<sup>+</sup> ions Ne<sup>+</sup> ions to a fluence of 1.16×10<sup>16</sup> ions.cm<sup>-2</sup>. ..... 196

**Figure 9.3:** Example of a SRIM multislice calculation for 9.5 keV Xe<sup>+</sup> ion irradiation of a Si NW showing the distributions of: (a) vacancies; (b) interstitials; and (c) surpluses of vacancies and (d) interstitials..... 198

# 1 Introduction

## 1.1 Background

The invention of the solid-state transistor in 1947 by Shockley, Bardeen and Brattain opened up new horizons for the use of semiconductor technology [1], [2]. The first transistor was made using Germanium (Ge) and was known as a point contact transistor as shown in Figure 1.1 [3]. The invention of integrated circuits using Ge in 1960 revolutionised the semiconductor industry with the advantage of increased power to process information at reduced cost. The development of semiconductor devices continued to attract much interest and discrete devices like diodes, transistors and capacitors were fabricated into chips. Although the first transistors were made of Ge, it was realised later that silicon (Si) has some properties and advantages over Ge. Silicon subsequently became the dominant material in the semiconductor industry [4]. The miniaturisation of the technology continued and has held true the Gordon Moore's Law who predicted in his paper in 1965 that "number of transistors per unit area on an integrated chip doubles every two years" [5]. The first transistor developed was several mm<sup>2</sup> but the size reduced to  $\mu\text{m}^2$  in the 1970s [6].

The concept of Field Effect Transistors (FET) was a ground-breaking invention [7]. A FET is a four terminal device that consist of three metal electrodes referred as the gate, source and drain with a semiconductor substrate as the fourth contact. The source and drain are heavily doped regions of opposite conductivity type to the body (e.g. if the substrate is p-type then the source and drain are doped to be n-type). Current flows from source to drain when a voltage is applied on the gate electrode and thus a FET is referred to as a voltage controlled device. The flow of carriers can be controlled with the gate voltage which then controls the size and shape of the semiconducting channel between the source and drain. There are several main types of FET: junction FET (JFET); metal oxide FET (MOSFET); metal semiconductor FET (MESFET); and heterostructure FET (HFET). The most important type of FET

is the MOSFET in which a very thin oxide layer (e.g.  $\text{SiO}_2$ ) is formed between the gate and the substrate. The gate channel constitute current caused by either electrons or holes (usually current due to electrons in p-type substrate and vice versa).



**Figure 1.1:** The first transistor invented and assembled in 1947 at Bell Labs, USA. Reproduced from [3].

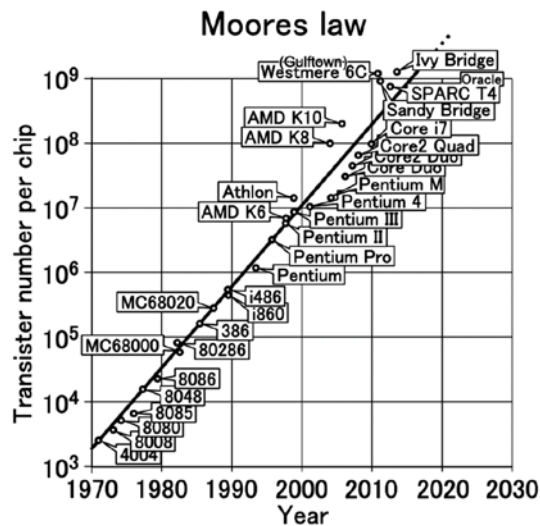


**Figure 1.2:** The graph is showing the progress of semiconductor technology and the adherence to Moore's Law. Reproduced from [8].

The first Si-based FET microprocessor called the 4004 was introduced by Intel and had 2300 transistors whilst current Intel microprocessors in 2016 such as the

Xeon-X7460 contain 1.9 billion [9]. The tremendous progress of the semiconductor industry over the years is demonstrated in Figure 1.2.

Silicon has been an attractive, dominant and versatile material in the semiconductor microelectronic industry due to its abundance, cost effectiveness and fundamental properties. The quest to continually miniaturise Si-based microelectronics poses challenges as the limits of current technologies are reached [10]. The challenges are classified into four broad categories: minimising gate and oxide thickness whilst avoiding leakage currents; heat dissipation due to the large number of devices per unit area; overcoming the limitations of lithographic techniques; and reducing the costs of fabrication, testing and production [11]. It is expected that the miniaturisation of conventional Si-based microelectronics can continue for a further five years but then there will be a need to replace the technology [12]. Therefore, research is underway to investigate and demonstrate novel materials to continue along the trend predicted by Moore's Law.

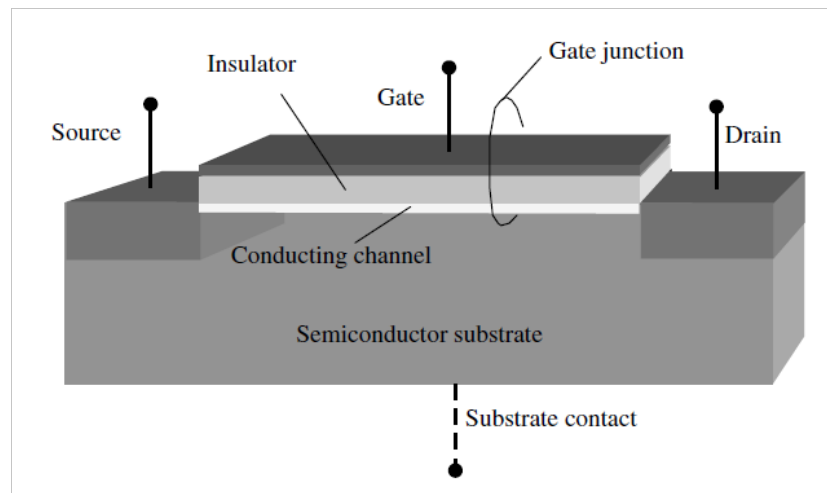


**Figure 1.3:** Schematic showing a four terminal field effect transistor illustrating the source, drain, gate and substrate. Reproduced from [13].

Researchers have proposed new materials and methods for future generations of nanoelectronics by adopting new ideas to continue with the miniaturisation of technology by overcoming the shortcomings of bulk Si [4]. For example: process-

induced-strained Si has been used as an alternative for the conducting channel as its charge carriers exhibit lower effective mass and hence increased mobility and current; high-k dielectric materials to allow the use of thinner gates; and the replacement of metal gate electrodes with polysilicon. Novel nanomaterials and non-planar device geometries have also been proposed [4].

Nanomaterials are of great importance in science and technology as the potential building blocks for the next-generation technologies [14], [15]. These include nanotubes (NTs) [16], [17], nanowires (NWs) [18], nanoparticles and quantum dots [14], [19], [20], [21], [22]. The large surface area-to-volume ratio together with associated quantum effects at the nanoscale causes these nanomaterials to show different physical properties compared to their bulk counterparts. For example, materials at the nanoscale can have lower melting points [23] and can demonstrate reduced lattice constants [24]. Some semiconducting nanomaterials have improved mechanical properties which may be attributed to a reduced numbers of defects [25]. The optical properties of semiconducting nanomaterials can be different from the bulk due to increased bandgaps [26]. Furthermore, some nanomaterials also demonstrate reduced electrical conductivity due to high surface scattering [25], [26]. In particular, semiconducting NWs are of interest for their unique properties and applications in multiple technologies [27].

An enormous amount of research has been dedicated toward silicon NWs (Si NWs) as a potential candidate for the next generation of nanodevices such as resonators, MOSFETs [28]–[32], nanogenerators [33] and sensors [34]. Silicon NWs are 1D nanomaterials with a cylindrical symmetry and a diameter usually not greater than 100 nm [35]. Silicon NWs have been demonstrated as a functional device element in Fin Field Effect Transistor (finFET) technology [36]. A finFET is a non-planar device built using silicon-on-insulator technology used in modern microprocessors and incorporates a gate wrapped around a thin Si fin. The NWs can serve as a channel in finFETs when connected between the source and drain. This device exhibits excellent carrier mobility and gate control properties. The fabrication of Si NWs with controlled diameter along with their compatibility with the current complementary metal oxide semiconductor (CMOS) technology are some of the advantages [37].

The applications of Si NWs are not limited to micro and nanoelectronics but could also be exploited in a range of fields. Thin Si NWs of diameters less than 10 nm have been developed as FET-based gas sensors for environmental monitoring [38]. The working principle of such devices is based on an electric field which influences the charge on the surface of the NWs and hence modulates the current in the channel. The resistivity of these NW-based sensors changes upon interaction with various gases and vapours such as NO<sub>2</sub>, NH<sub>3</sub> [39] and hydrogen [40]. Silicon NWs have been used as electrodes in rechargeable lithium-ion micro-batteries which demonstrated high capacity and long life for use in portable devices [41], [42]. Silicon NWs have also been demonstrated as efficient thermoelectric materials with higher thermoelectric efficiency due to their low thermal conductivity compared to bulk Si [43]. Thermoelectric materials could be used in automobiles or refrigerators for power generation. Further examples of applications of Si NWs include use as ultrasensitive biological sensors of proteins [44], gastric cancer biomarkers [45] and DNA [46].

The invention of the Transmission Electron Microscope (TEM) by German physicist Ernst Ruska in 1933 enabled materials characterisation with a much higher resolution than optical microscopy. *In-situ* ion irradiation with TEM provides an invaluable and versatile tool to explore the microscopic response of materials under irradiation. *Ex-situ* ion beam irradiation does not allow the possibility of observing dynamic and complex defect evolution and is limited to the investigation of the materials in the end-state. Although irradiation and characterisation can be performed in multiple steps, irradiating the samples in one instrument and transferring them to other equipment for characterisation is time consuming and there is a high risk of damage and/or contamination of the sample. Furthermore, it may be difficult to repeatedly return to the exact nanoscale area of interest in the TEM after each irradiation step especially if there are ion-beam-induced morphological changes. However, *in-situ* ion irradiations within TEM provides an excellent route to monitor the region of interest continuously during the ion irradiation process whilst maintaining the irradiation and sample conditions.

The history of TEM with *in situ* ion irradiation dates back to 1961 when Pashley and Presland [47] at Tube Laboratories in Cambridge (UK) observed black spot

damage in gold. They suspected that the damage may be caused by negative ions emitted from the tungsten filament of the electron gun. They further investigated this experimental result by using mass deflection coils to deflect the electrons but to allow any heavy ions to continue to the sample. Black spot damage was again introduced into the gold material even when the electrons were deflected. They concluded that the “*direct observation of ion damage in the electron microscope thus represents a powerful means of studying radiation damage*” [47]. In 1963, Howe *et al.* [48], [49] from Chalk River Nuclear Laboratories (Canada) carried out a series of irradiation experiments within the TEM by coating the electron beam filament to increase the flux of oxygen ions to irradiate the gold, aluminium and copper samples below 30 K. Furthermore, they developed a way to measure the ion beam flux by installing a Faraday cup in the TEM column in 1964 [50]. The first *in-situ* ion beam facility interfaced with a TEM was built in the Atomic Energy Research Establishment laboratory in Harwell (UK) [51].

*In-situ* ion irradiations with TEM are of great importance in helping to understand the underlying dynamic and complex processes of ion-solid interactions with real-time observations at different temperatures. This technique is applied to various technological challenges and in particular in nuclear and semiconductor research.

## 1.2 Thesis Overview

The current work is focused on understanding the underlying physics and mechanisms of ion-beam-induced modifications of Si NWs. *In-situ* ion irradiations experiments were carried out within the TEM. The ion irradiation caused atomic displacements and implantation in the nanowires. Multiple factors influence the outcome of these processes including ion energy, ion species, NW dimensions and irradiation geometry.

Ion implantation is a widely used processing technique for controlled doping with the aim of modifying materials to engineer desired properties. When an incident ion interacts with a target material, the ion may change its direction, energy and charge state while travelling through the target. During their journey through the target

material, the ions can create knock-on atoms which can themselves displace other atoms. This process continues until the ion and atoms come to rest or leave the target. The ions and the recoil atoms can cause a displacement of an atom from its lattice site if the transferred energy is greater than the displacement energy. In this way, the ion can cause crystal defects and morphological changes to the target.

The mechanisms for the bending of NWs under ion irradiation, have not yet been fully understood but have been explored by different authors [52], [53], [54] in the literature. The effect of ion irradiation on Si NWs has been explored in this study through *in-situ* TEM as this offers a novel technique to observe and characterize in real time the ion-irradiation-induced microstructural dynamic processes. This has allowed radiation damage including crystallographic defects, amorphisation and morphological changes of Si NWs to be explored in this work.

A literature review is presented in chapter 2 covering basic crystallography, defects in solids and specifically in Si. A review of radiation damage in NWs is presented with a particular emphasis on ion-irradiation-induced bending phenomena. Also of interest was the Van der Waals attraction of the NWs with the TEM support grid, mechanical and thermal properties which influence this interaction.

The experimental techniques are covered in chapter 3 including the basic principles of the instruments and techniques used for materials characterisation in this work. TEM has been extensively used and is discussed in detail. In particular, the Microscope and Ion Accelerator for Materials Investigations (MIAMI) facility is described as the main instrument used for this work. Atomic Force Microscope (AFM) is also discussed as it was also used to investigate the surface roughness of both Si NWs and the molybdenum (Mo) TEM grids.

The first results chapter builds on the literature review and experimental methods with the physics of atomic collision in solids leading into a description of the *Stopping and Range of Ions in Matter* (SRIM) Monte Carlo computer code. This forms the basis for the selection of ion beam irradiation conditions for the experiments design and the incorporation of SRIM into MatLab to extend it to non-planar geometries for application to NWs as part of this work.



The results of ion-beam-induced bending of Si NWs irradiated with 6 keV Ne<sup>+</sup> is presented in chapter 5. Tilt series and tomography of the un-irradiated and irradiated Si NWs were performed to determine the bending direction of NWs. Thermal annealing of Si NWs were also carried out and the results are presented.

Experiments specifically designed to match the irradiation conditions with results presented by Borschel *et al.* [55] are presented in chapter 6. In that work, they irradiated GaAs NWs using three different ion species (S, Xe and Ar) at different energies to explore the effects of irradiation conditions for NWs bending. As one of the principle papers on this phenomena in GaAs NWs, it was of particular interest to test the reproducibility, or not, in Si NWs.

Chapter 7 has been dedicated to investigating the ion-beam-induced modification of Si NWs specifically under processing conditions used in the microelectronic industry. Silicon NWs as potential candidates for FinFETs are being implanted by exposure to 5% arsine and 95% Xe plasma. For this reasons, these irradiation experiments were designed to investigate the effect of 7 keV Xe<sup>+</sup> ions. A combination of tilt-rotation procedure was developed to allow measurement of the damage depth using TEM techniques. Structural changes along with the plastic deformation and bubble evolution in the Si NWs were observed.

An important question for *in situ* TEM investigations of nanostructures is the temperature of a nanosized feature in only partial and indirect contact with a macroscopic sample-holder which is providing heating. In preparation for future computer modelling work to gain a better understanding of such systems to support the design and interpretation of this type of experiment, chapter 8 presents AFM results which has been used to characterise the contact surfaces of the TEM support grid and the Si NWs themselves. The geometry, materials and other considerations are discussed and a summary of the important input parameters for the modelling as identified in the literature review are also summarised.

Chapter 9 is a discussion drawing together the literature review and results collectively presented in the thesis. The main conclusions are directs for future work are summarised in chapter 10.

## 2 Literature Review

### 2.1 Introduction

Over the past three decades, an enormous amount of research has been directed toward nanoscience and nanotechnology resulting in the advancement of nanomaterials [56]–[58]. Scientific research has shown that nanoscale materials and structures have some unique differences compared to bulk materials including their thermal, mechanical, optical and electrical properties [59], [60]. Nanostructures are of great importance in science and technology and are considered as potential building blocks for the next generation of electronic devices [14], [15]. These include carbon nanotubes (NTs) [18], nanowires (NWs) [18], [61], nanoparticles and quantum dots [6]. Nanowires have been the subject of intense scientific research and of particular interest are semiconductor NWs [63]–[66].

Ion irradiation is the main processing technique for Si-based devices [67]. The current work is focused on understanding the underlying physics and mechanisms of ion-beam-induced modifications of single-crystalline Si NWs (e.g. defect formation, amorphisation) and subsequent recrystallisation during annealing. The ion irradiation can cause implantation, displacement of atoms and accumulation of damage potentially resulting in the amorphisation of the NWs depending on the conditions such as ion species, ion energy and fluence [68],[69], [70], [71].

Nanostructures range from zero-dimensions (0D) (e.g. quantum dots) through 1D (nanowires) to 2D materials (graphene) [72]. These distinctions reflect the geometry which can have significant implications for the physics of these materials [73]. Silicon NWs are either single-crystals, polycrystalline or amorphous and are usually up to 100 nm in diameter and with a length of a few microns [35]. Electronic devices based on Si NWs (e.g. solar cells and sensors) may have larger surface sensitivity compared to bulk devices due to their increased surface-to-volume ratio [38], [45],

[74], [75]. Mechanical properties of Si NWs are also influenced by their geometry [63], [76] and are also a useful platform for fundamental physics research [77]–[81].

Radiation-induced damage in crystalline silicon (c-Si), including the crystalline-to-amorphous (c-a) phase transformation has been an active area of investigation because of the use of ion implantation in semiconductor doping [82]. The aim of this work was to study and understand the fundamental science and mechanisms in Si NWs under ion irradiation.

## **2.2 Crystallography**

The field of science concerned with the atomic structure and ordering of solids (the regular periodic arrangements of atoms) is known as a crystallography.

### **2.2.1 Lattice Points**

A set of periodically repeated points in 3D space is called a lattice and each individual point is known as a lattice point [83], [84].

### **2.2.2 Lattice Vectors**

To describe the repetitive translational symmetry of crystals in 3D, three non-coplanar translation or lattice vectors are defined as  $\mathbf{a}$ ,  $\mathbf{b}$  and  $\mathbf{c}$  which make angles  $\alpha$ ,  $\beta$  and  $\gamma$  [85]. The lattice vectors and the relative angles are shown in Figure 2.1. In a cubic system, these translation vectors are orthogonal to each other.

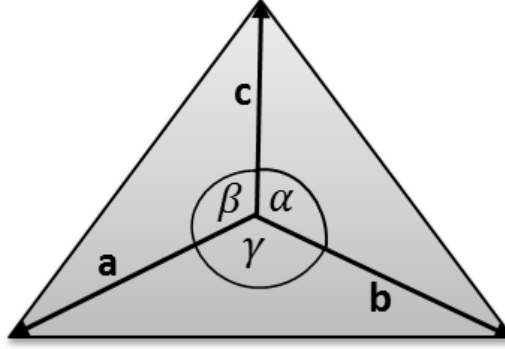


**Figure 2.1:** Translation vectors  $\mathbf{a}$ ,  $\mathbf{b}$  and  $\mathbf{c}$  with the angles  $\alpha$ ,  $\beta$  and  $\gamma$  between them.

The translation vector,  $\mathbf{R}$ , is defined as the sum of multiples of the vectors  $\mathbf{a}$ ,  $\mathbf{b}$  and  $\mathbf{c}$  in 3D space as given in Equation 2.1:

$$\mathbf{R} = n_1\mathbf{a} + n_2\mathbf{b} + n_3\mathbf{c} \quad \text{Equation 2.1}$$

where  $n$  is an integer.

### 2.2.3 Crystal Basis

The crystal basis is the simplest structure which can be translated by the lattice vectors to construct the entire crystal [85].

### 2.2.4 Primitive Unit Cell

The minimum volume of a crystal that contains only one lattice point is called a primitive unit cell. When these unit cells are stacked together in a repetitive fashion, they form an entire crystal. The periodic repetition of a primitive unit cell by translating the lattice vectors  $\mathbf{a}$ ,  $\mathbf{b}$  and  $\mathbf{c}$  occupies all space without leaving any voids and hence reproduce the entire crystal.

### 2.2.5 Conventional Unit Cell

The conventional unit cell is larger than the primitive unit cell and features all possible symmetries: rotational and reflectional. When a conventional unit cell is translated by the lattice vectors fills all space without leaving any voids.

## 2.3 Crystal System

The determination of the distinct unit cell in a 3D lattice categorises the crystal structures. The shape of the unit cell determines the appearance and physical properties of the crystals. There are seven primitive unit cells associated with the lattice symmetry (rotational and reflectional) and are categorised into seven crystal systems defined by **a**, **b**, **c** and  $\alpha$ ,  $\beta$  and  $\gamma$  (see Figure 2.2).

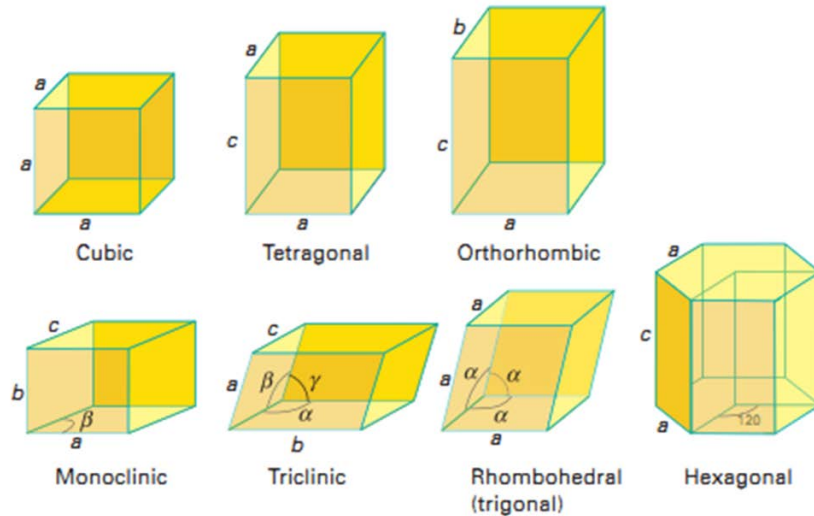


**Figure 2.2:** The seven crystal systems. reproduced from [86].

### 2.3.1 Bravais Lattice

In 1848, the French scientist August Bravais mathematically proved that there are 14 different ways to assemble lattice points in 3D space [87]. The seven crystal systems are primitive unit cells while for the others a non-primitive unit cell is employed to demonstrate the full lattice symmetry. The three cubic Bravais lattices are the simple cubic (SC), body centred cubic (BCC) and face centred cubic (FCC) [85].

### 2.3.2 Reciprocal Space

Reciprocal space is a framework in which the lattice vectors are the reciprocal of inter-planar spacing. It provides an alternative way to represent lattice vectors in terms of wavevectors,  $\mathbf{K}$  and is also known as k-space or momentum space. The lattice vectors  $\mathbf{a}$ ,  $\mathbf{b}$  and  $\mathbf{c}$  are represented with reciprocal lattice vectors  $\mathbf{a}^*$ ,  $\mathbf{b}^*$  and  $\mathbf{c}^*$ , respectively. Each reciprocal lattice vector is normal to two lattice vectors of the crystal and is illustrated in Equation 2.2:

$$\left. \begin{aligned} \mathbf{a}^* &= 2\pi \frac{\mathbf{b} \times \mathbf{c}}{\mathbf{a} \cdot \mathbf{b} \times \mathbf{c}} \\ \mathbf{b}^* &= 2\pi \frac{\mathbf{c} \times \mathbf{a}}{\mathbf{a} \cdot \mathbf{b} \times \mathbf{c}} \\ \mathbf{c}^* &= 2\pi \frac{\mathbf{a} \times \mathbf{b}}{\mathbf{a} \cdot \mathbf{b} \times \mathbf{c}} \end{aligned} \right\} \quad \text{Equation 2.2}$$

where  $\mathbf{a} \cdot \mathbf{b} \times \mathbf{c}$  is the volume of unit cell.

### 2.3.3 Coordination Number

When the lattice points are populated by atoms, the number of atoms touching a particular atom defines the coordination number of the crystal. The coordination number determines packaging efficiency and the lattice stability of the crystal. The SC unit cell has a coordination number of six whereas BCC and FCC are eight and twelve, respectively.

## 2.4 Face Centred Cubic System

In a FCC crystal structure, there is an atom at each vertex of the cube and one atom per face. There are four atoms per unit cell and coordination number is twelve in a FCC. A schematic representation of the FCC unit cell is shown in Figure 2.3:

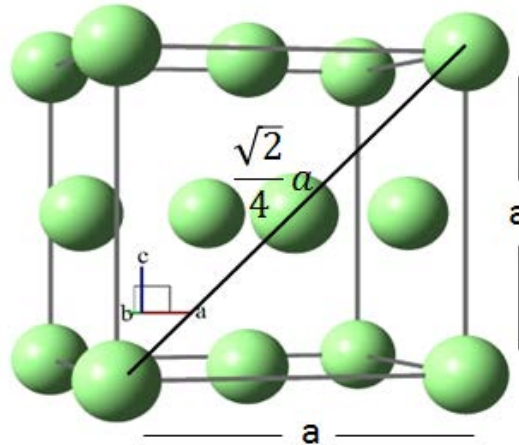


**Figure 2.3:** A representation of a conventional unit cell of FCC with lattice constant,  $a$ , made with Balls and Sticks software [88].

## 2.5 Miller Indices

The reciprocals of the intersections of a plane with the axes of a unit cell are used to define the Miller indices of that plane [89]. The Miller indices are used to describe the planes in a crystal system. The choice of origin in a crystal is arbitrary but once defined it determines the directions in the crystallographic system. Miller indices are represented with  $h$ ,  $k$ ,  $l$  and are the reciprocals of the fractions of the fundamental lattice vectors  $\mathbf{a}$ ,  $\mathbf{b}$  and  $\mathbf{c}$ , respectively. The following bracket notations are used for Miller indices: a lattice point is represented as  $(h, k, l)$ ; a plane is represented with parenthesis but without commas as  $(hkl)$ ; a direction with square brackets as  $[hkl]$ ; and a family of directions or planes as  $\langle hkl \rangle$  or  $\{hkl\}$ , respectively. Miller indices can be negative indicated with a bar on the index such as  $[h\bar{k}\bar{l}]$ .

### 2.5.1 Families of Directions and Planes

The directions and planes which are all equivalent because of the symmetry of the crystal are classified as family. All possible combinations of the  $\langle 100 \rangle$ ,  $\langle 110 \rangle$  and  $\langle 111 \rangle$  directions and the  $\{100\}$ ,  $\{110\}$  and  $\{111\}$  planes are given in Table 2.1:

**Table 2.1:** A table of all possible combinations of the  $\langle 100 \rangle$ ,  $\langle 110 \rangle$  and  $\langle 111 \rangle$  directions and the  $\{100\}$ ,  $\{110\}$  and  $\{111\}$  planes.

Family of Directions	Equivalent Directions in Family
$\langle 100 \rangle$	$[100] [010] [001] [\bar{1}00] [0\bar{1}0] [00\bar{1}]$
$\langle 110 \rangle$	$[110] [011] [101] [\bar{1}\bar{1}0] [0\bar{1}\bar{1}] [\bar{1}0\bar{1}]$ $[\bar{1}10] [0\bar{1}1] [\bar{1}01] [1\bar{1}0] [01\bar{1}] [10\bar{1}]$
$\langle 111 \rangle$	$[111] [\bar{1}\bar{1}1] [1\bar{1}\bar{1}] [11\bar{1}] [\bar{1}\bar{1}\bar{1}] [\bar{1}1\bar{1}]$ $[1\bar{1}\bar{1}] [\bar{1}\bar{1}\bar{1}]$
$\{100\}$	$(100) (010) (001) (\bar{1}00) (0\bar{1}0) (00\bar{1})$
$\{110\}$	$(110) (011) (101) (\bar{1}\bar{1}0) (0\bar{1}\bar{1}) (\bar{1}0\bar{1})$ $(\bar{1}10) (0\bar{1}1) (\bar{1}01) (1\bar{1}0) (01\bar{1}) (10\bar{1})$
$\{111\}$	$(111) (\bar{1}\bar{1}1) (1\bar{1}\bar{1}) (11\bar{1}) (\bar{1}\bar{1}\bar{1}) (\bar{1}1\bar{1})$ $(\bar{1}\bar{1}\bar{1})$



## 2.6 Distance between Planes (d–Spacing)

The distance between  $(hkl)$  planes is called the d-spacing,  $d_{hkl}$ . Consider a plane with Miller indices  $(hkl)$  parallel to the equivalent plane passing through origin, O. As shown in Figure 2.4, the  $(hkl)$  plane intercepts the three perpendicular crystallographic axis (Oa, Ob, Oc) at  $\frac{a}{h}$ ,  $\frac{b}{k}$  and  $\frac{c}{l}$ , respectively. The distance between the planes  $OP = d_{hkl}$  and  $\alpha$ ,  $\beta$  and  $\gamma$  are the angles which OP makes with the axes.

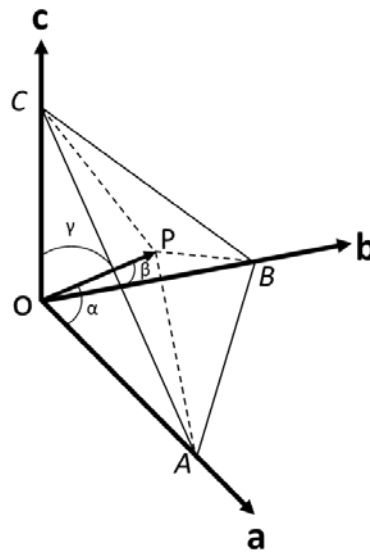


**Figure 2.4:** Vector diagram to illustrate the derivation of  $d_{hkl}$ .

Applying the rules for Miller indices to Figure 2.4 gives:

$$\left. \begin{aligned} OA &= \frac{a}{h} \\ OB &= \frac{b}{k} \\ OC &= \frac{c}{l} \end{aligned} \right\} \quad \text{Equation 2.3}$$

Applying trigonometry using triangles OPA, OPB and OPC gives:

$$\begin{cases} \cos\alpha = \frac{OP}{OA} \\ \cos\beta = \frac{OP}{OB} \\ \cos\gamma = \frac{OP}{OC} \end{cases} \quad \text{Equation 2.4}$$

Using the following trigonometric rule for rectangular systems:

$$\cos^2 \alpha + \cos^2 \beta + \cos^2 \gamma = 1 \quad \text{Equation 2.5}$$

Then substituting values of  $\cos \alpha$ ,  $\cos \beta$  and  $\cos \gamma$  from Equation 2.4 and using  $OP = d_{hkl}$  gives:

$$d_{hkl}^2 \left( \frac{h^2}{a^2} + \frac{k^2}{b^2} + \frac{l^2}{c^2} \right) = 1 \quad \text{Equation 2.6}$$

$$d_{hkl} = \frac{1}{\sqrt{\frac{h^2}{a^2} + \frac{k^2}{b^2} + \frac{l^2}{c^2}}} \quad \text{Equation 2.7}$$

This formula used to calculate d-spacings is valid for cubic, tetragonal and orthorhombic systems. For any cubic system, the direction  $[hkl]$  is perpendicular to the plane  $(hkl)$ . The interplanar spacing is largest for the  $\{001\}$  planes and decreases for increasingly higher-order planes.

## 2.7 Structural Properties of Si

Silicon is a member of group IV in the periodic table. The structure of Si is diamond-like FCC and atoms form covalent bonds with four neighbours at the vertices of a tetrahedron making an angle of  $109.47^\circ$  between each other [90], [91]. The average bond length of c-Si is 2.34–2.36 Å [92], [93] and the atomic density of Si is  $5.0 \times 10^{22}$  atoms.cm<sup>-3</sup> [94], [95].

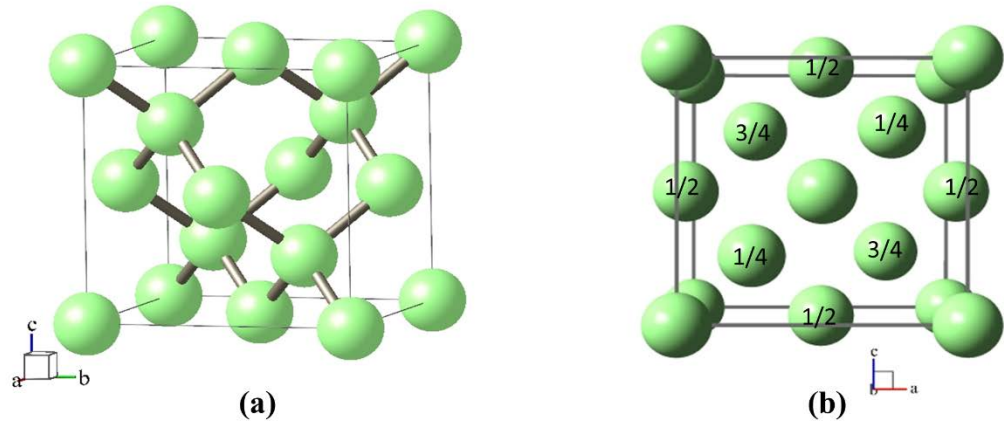


**Figure 2.5:** (a) Schematic view of a Si conventional unit cell containing 14 atoms as FCC structure (b) along [001] created using Balls and Sticks software [88].

The crystal structure of Si is shown in Figure 2.5. in which atoms are periodically arranged and are characterised by a long-range order between them. In amorphous Si (a-Si), atoms lose the long-range order through distortion of the bond angle but maintain the fourfold coordination. Amorphous Si is composed of three-, five-, or seven- membered rings along with six-member ring as found in the perfect crystal [96]. The example structure of a-Si is shown in Figure 2.6:

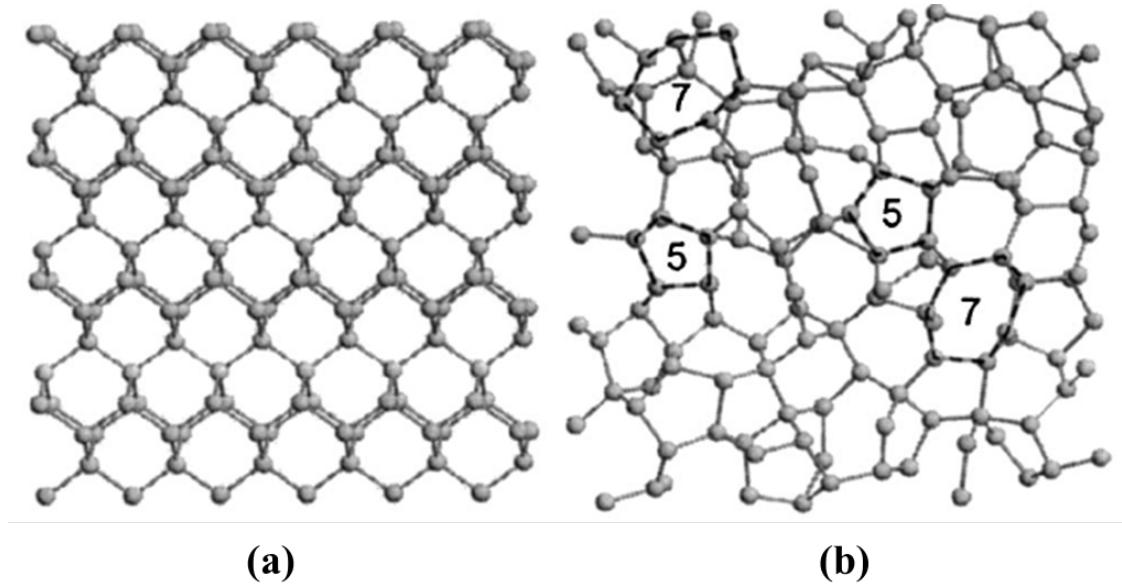


**Figure 2.6:** (a) Perfect crystalline structure of c-Si {110} with six-member rings in which each central atom bonding with four atoms at the vertices of a tetrahedron; and (b) a-Si with 5 and 7 member rings and long range order is lost. Reproduced from [96].

## 2.8 Atomic Collisions in Solids

When a material is irradiated with an ion beam, the incident ions can transfer their energy to the target atoms [70]. The target atoms may then be displaced from their lattice sites and then go on to collide with other atoms in the target material. Such collision processes continue until all recoil atoms come to rest or exit the sample. The details of these processes are discussed in more detail in chapter 4.

## 2.9 Taxonomy of Defects by Dimensionality

Structural defects in crystals are classified relative to their dimensionality as discussed below. Defects are characterised as localised disruptions in the regularity of the lattice. The internal energy of the system increases as a consequence of the existence of defects which may produce strain inside the crystalline [97], [98].

### 2.9.1 Point Defects

Defects involving just one missing or extra atom (i.e. a vacancy or interstitial, respectively) are known as point defects. The point defects are either intrinsic (i.e. native) or extrinsic (i.e. impurity) atoms. Examples of point defects include:

- i. Mono-vacancies
- ii. Mono-interstitials
- iii. Substitutional atoms

If two point defects combine, it is possible to form:

- iv. Di-vacancies
- v. Di-interstitials
- vi. IV pairs

#### 2.9.1.1 Mono-vacancies and Mono-interstitials

The simplest point defect is a vacancy. A vacancy is defined as a vacant lattice site in a crystal and is called a mono-vacancy when it occurs in isolation. Vacancies are either inherited (imperfect crystal) or may introduced into the material by ion irradiation or atomic vibrations. Thermal energy increases at higher temperatures thus increasing the vacancy population as there are more chance of atoms jumping from their lattice sites due to atomic vibrations and thus increasing the randomness in a material [46]. The mono-vacancy in its various charge states ( $V^{++}$ ,  $V^+$ ,  $V^0$ ,  $V^-$  and  $V^{--}$ ) [99], [100] can be monitored experimentally using electron paramagnetic resonance, deep level transient spectroscopy or positron annihilation spectroscopy [101]. If the lattice atom that is displaced during vacancy formation comes to rest in a non-lattice site is known as an interstitial. Interstitials could be the intrinsic atoms (native to the crystal) or extrinsic atoms (non-native to the crystal) may cause compressive stress in the surrounding crystal [102].

### 2.9.1.2 Substitutional Atom

A substitutional atom is an extrinsic atom that could be introduced by a process such as ion implantation and replaces an atom on a lattice site of the crystal as shown in Figure 2.7. A substitutional atom could be bigger or smaller than the matrix atoms and may cause stress in the surrounding lattice. However, if the size of the substitutional atom is bigger (or smaller) than size of the parent lattice atoms it may apply a compressive (or tensile) force on the surrounding atoms [102].

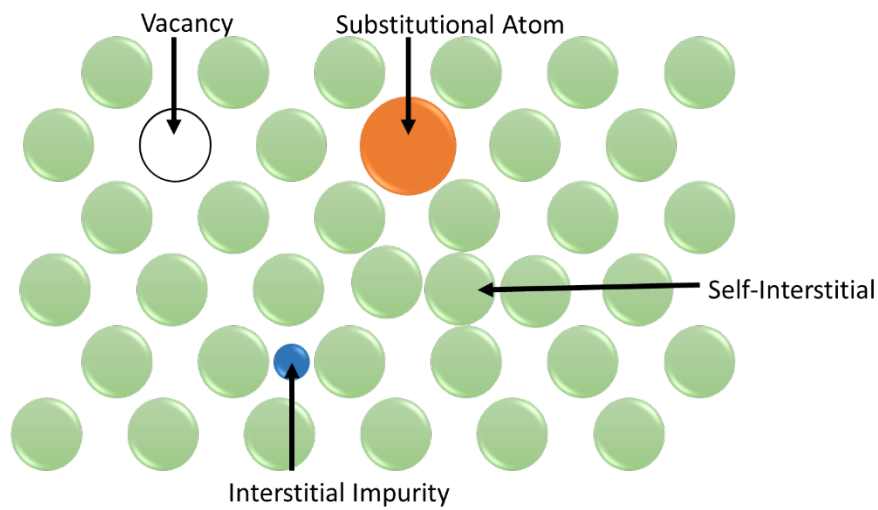


**Figure 2.7:** Schematic illustration of point defects in a crystal.

### 2.9.1.3 Di-vacancies

The agglomeration of two individual vacancies is known as a di-vacancy. Di-vacancies may form in the material by ion irradiations when incident particle transfers sufficient energy to displace two neighbouring atoms from the lattice sites [103]. The population of di-vacancies increases at high temperature and are mobile at  $\sim 250^\circ\text{C}$  [104]. Di-vacancies is a stable defect at room temperature and may combine with other point defects to produce extended defects (e.g. dislocation loops). The crystalline structure of di-vacancies in Si is shown in Figure 2.8:

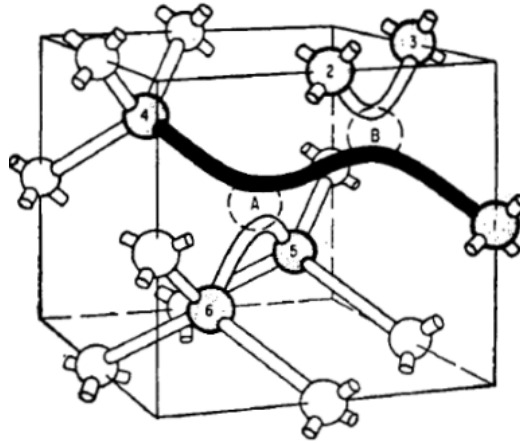


**Figure 2.8:** Crystalline structure of a di-vacancy in silicon. Reproduced from [105].

### 2.9.2 Frenkel Defect and IV Pair

Frenkel defect is an interstitial-vacancy defect formed in crystals by displacing an atom from its lattice site to an interstitial site. This defect is associated with a primary atom originally displaced from the same lattice and a vacancy created at its parent lattice site. When a vacancy interacts with an interstitial, annihilation is not inevitable as there is an energy barrier to overcome. Thus, a metastable defect is formed known as an interstitial-vacancy (IV) pair or bond defect [106]. The IV pair induces disorder in the crystal lattice and when present in sufficient numbers may be able to render the crystal amorphous [96].

### 2.10 Defects in Silicon

In a-Si, the atoms have no long-range order and may contain many defects including: point defects [96], Si-Si strained bond [107], floating bonds [108], dangling bonds [109]. Dangling bonds are broken covalent bonds where an Si atom is under coordinated while in a floating bond the Si atom is over coordinated. Defect accumulation in a-Si changes bond lengths which increases the free energy of the system [110]–[112]. Many other properties such as optical [113], [114], vibrational

[110], [115], [116] and electron spin density [107], [109], [117] also change due to amorphisation.

The reconfiguration of unsatisfied covalent bonds in Si is responsible for the different possible charged states mentioned above. However, the  $V^{-}$ ,  $V^{++}$  and  $V^0$  charge states are dominant in n-type, p-type and intrinsic Si, respectively. G. D. Watkins [100] has extensively studied the isolated defects produced in Si following cryogenic electron irradiation. Mono-vacancies in Si are mobile at room temperature [118] and the disappearance in electron paramagnetic resonance (EPR) spectra during isochronal annealing has been reported at  $\sim 70$  K in n-type, 150 K in p-type and  $\sim 200$  K in intrinsic Si (see Figure 2.9). The activation energy for vacancy migration in Si has been reported to be  $0.18 \pm 0.02$  eV for  $V^{-}$  in n-type,  $0.32 \pm 0.02$  eV for  $V^{++}$  in p-type and  $0.45 \pm 0.04$  eV for  $V^0$  in intrinsic Si [100].

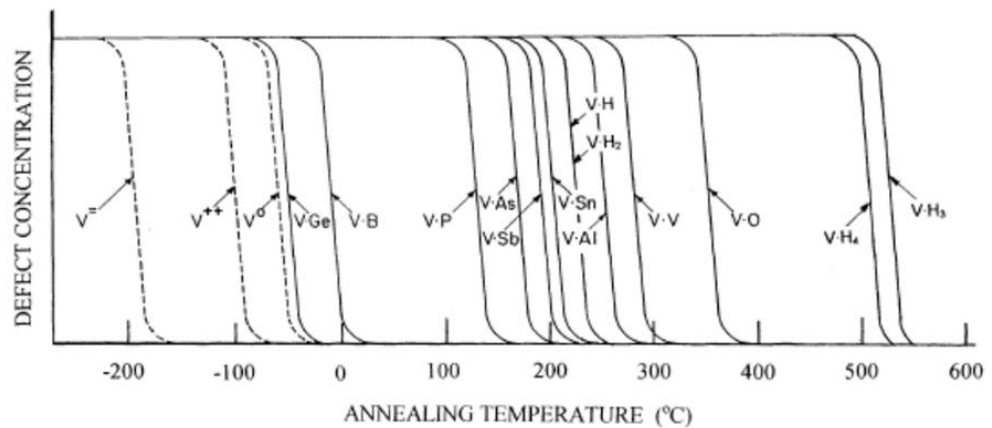


**Figure 2.9:** Vacancy type defect annealing in Si is shown with dotted lines during 15 min isochronal annealing. Reproduced from [100].

In the experiments reported by Watkins [100], no mono-interstitial was observed in the EPR spectra in electron irradiated p-type Si at cryogenic temperature (4.2 K). The only observed interstitial-type defects which were identified were trapped interstitials at impurities thus suggesting the interstitials are highly mobile at low



temperatures. However, low levels of interstitial defect survival were observed in n-type Si. The migration of interstitials in n-type Si was not evident until ~140–175 K where trapped interstitials were again observed. In contrast to the vacancies, interstitial atoms are weakly bonded and have an activation energy for migration of between 0.08 to 0.57 eV [118]–[120].

Di-vacancies in Si are formed either by electron or ion irradiations and are immobile at room temperature [120]. The di-vacancies in Si becomes active at a temperature ~125°C for proton and neutron irradiations and ~250°C for electron irradiations [120], [121]. The activation energy for migration of di-vacancies for electron irradiated Si was found to be ~1.3 eV [122]. Agglomeration di-vacancies in Si may lead to large clusters known as vacancy clusters. Such vacancy clusters in Si are formed between 400–500°C and annealed out at ~ 600°C [120].

Di-interstitials in Si are formed either by migration and agglomeration of mono-interstitials or by rapid relaxation following a collision cascade caused by displacing irradiation (see chapter 4). Larger collections of interstitials are known as interstitial clusters. Interstitial clusters are formed in Si and were found as a stable defect up to temperature of ~500°C [123]. Di-interstitials can be detected using EPR spectroscopy and become mobile at ~150°C with an activation energy for migration of between 0.18 and 0.7 eV [124]–[126]. The activation energy for migration of tri-interstitial clusters in Si has been reported to be 1.6 eV [127] from MD simulations but in other work it was reported to be as low as ~0.2 eV [128].

IV pair in Si is a combination of vacancy and interstitial and are regarded as primary defects generated. The accumulation of IV pairs leads to the amorphisation and results of MD simulations has proved that when IV pair accumulation reaches ~25% in Si [126] it renders the crystal amorphous.

## **2.11 Ion-beam-Induced Amorphisation**

### **2.11.1 Introduction**

When energetic ions are bombarded into crystalline materials, they deposit energy into the target through nuclear and electronic interactions (discussed in detail in Chapter 4). The deposited energy by the ions during these interactions may cause the atoms to be displaced from their lattice sites and cause defects (e.g. vacancies and interstitials). The volume of material disrupted in this way may contain amorphous materials and/or damaged crystalline material. There are many models of ion-beam-induced amorphisation proposed in the literature [129]–[131]. However, ion-beam-induced amorphisation can be attributed to one of the two basic mechanisms (or combination of the two) of damage accumulation – namely homogenous and heterogeneous processes which are discussed below in detail.

### **2.11.2 Homogenous Amorphisation**

Homogenous amorphisation from ion irradiation can be ascribed by a parameter known as critical free-energy,  $E_c$ , or defect density [132]. The defects are built up uniformly throughout the crystal in the irradiated region until it reaches sufficient level to cause a transition from the crystalline state to the energetically favourable amorphous state.

In this model, defects are distributed homogeneously in the irradiation-induced collision cascades. This damage accumulation increases the free energy of the crystal system as the fluence increases and when the deposited energy rises above a critical value then a spontaneous transition from the crystalline to amorphous state occurs [96]. The  $E_c$  required for amorphisation of Si to occur has been reported as  $5 \times 10^{23}$  eV.cm<sup>-3</sup> [133], [134]. The fluence required for amorphisation based on a critical energy model can be calculated from the known  $E_c$  using Equation 2.8 [132]:

$$\varphi \frac{v}{X_m} = E_c \quad \text{Equation 2.8}$$

where  $\varphi$  (ions.cm<sup>-2</sup>) is the critical fluence for amorphisation,  $E_c$  (eV.cm<sup>-3</sup>) is the critical energy density deposited by the ions,  $X_m$  (cm) is the depth over which Si is 90% damaged and  $v$  (eV) is energy deposited per ion.

However, Baranova *et al.* [135], [136] suggest in 1975 that point defect density is not sufficient to induce a transition to an amorphous phase but the critical radius,  $R_{cr}$ , of the damage is also important. If the defect density is higher than the critical defect density in one region but the size of the damaged zone is smaller than  $R_{cr}$  then a transformation to an amorphous state may occur but it then quickly recrystallises via dynamic annealing. The dynamic annealing can be suppressed at low temperatures and amorphisation can be achieved more rapidly as the defects will be less mobile.

In summary, homogenous amorphisation based on a defect density model is dependent on the ion beam parameters. However, other experimental conditions such as sample temperature also play a major role for amorphisation. The  $E_c$  required for amorphisation is strongly dependent on the irradiation conditions and could be achieved quickly at low temperature by suppressing the dynamic annealing [132].

### 2.11.3 Heterogeneous Amorphisation

In heterogeneous amorphisation, each ion entering the crystal may produce a local amorphous zone with its displacement spike which overlap with zones created by other ions to form a continuous amorphous layer in the crystal [7], [27]–[29].

An ion-beam-induced heterogeneous amorphisation model was proposed by Morehead and Crowder [141] by assuming an amorphous cylindrical core of radius,  $R_0$ , around an ion trajectory within each ion cascade as shown in Figure 2.10:

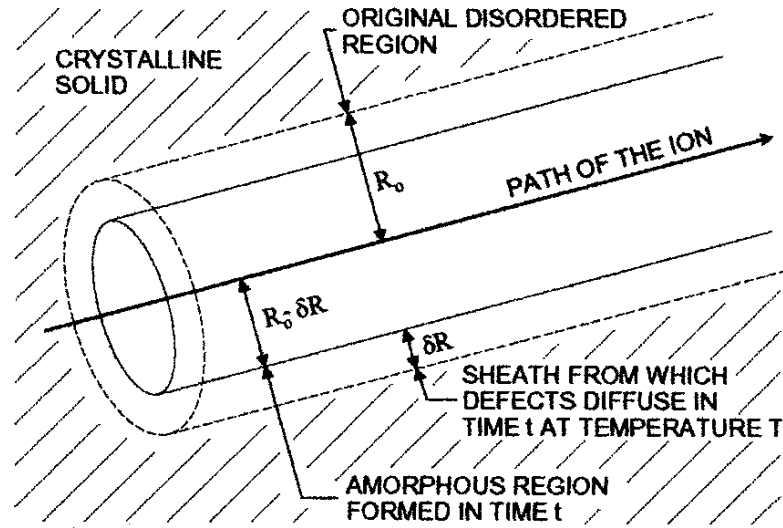


**Figure 2.10:** Cylindrical model of radius,  $R_0$ , for the volume surrounding the path of an ion track.  $\delta R$  is the sheath for out-diffusion of defects and  $R_0 - \delta R$  is the stable amorphous core. Reproduced from [138].

In this model,  $R_0$  is defined by the energy deposited through nuclear collisions per unit path length. A certain proportion of vacancies or other point defects may diffuse over length  $R_0$  in time,  $t$ , at temperature,  $T$ , thereby reducing the size of the amorphous core by  $\delta R$  through dynamic annealing processes. The stable radius of the amorphous core then reduces to  $R_0 - \delta R$ . The formation of a continuous amorphous layer proceeds by overlapping of these residual damaged regions. Heavier ions may produce amorphous pockets of large volume (greater  $R_0$ ) within the cascade and may not require overlapping. The formation of an amorphous layer by overlapping of damage zones can be described by Equation 2.9 based on a kinetic theory described by the Johnson–Mehl–Avrami equation for phase transformations (see Equation 2.10):

$$F = 1 - \exp(-V \cdot D) \quad \text{Equation 2.9}$$

$$F = 1 - \exp(-K_{\text{temp}}\Phi^n)$$

*Equation 2.10*

where  $F$  is the amorphous fraction;  $V$ , is the amorphous volume per ion;  $D$  is the ion dose (ions.cm<sup>-3</sup>);  $n$  is an exponent describing the 3D growth;  $\Phi$  is the fluence (ions.cm<sup>-2</sup>) and  $K_{\text{temp}}$  is the temperature dependent parameter (cm<sup>2</sup>.ions<sup>-1</sup>).

#### **2.11.4 Nucleation Limited Model of Amorphisation**

The nucleation limited model suggests a two stage nucleation process for amorphisation: i) production of suitable sites for the accumulation of defects and ii) the interaction of point defects with these sites to produce an amorphous phase [126]. The favourable sites for this process are free surfaces [142], grain boundaries [143] and c-a interfaces [144], [145].

The defect accumulation at these nucleation sites during irradiation may produce complex defects which increase the free energy of the system until the crystal collapses into the amorphous phase [96]. The growth or shrinkage of the amorphous volume depends on the ion fluence and temperature of the substrate. Gibson [105] has extended the Morehead and Crowder [141] model of heterogeneous amorphisation by assuming the overlapping of individual cascades as a requirement for amorphisation as described in Equation 2.11:

$$F = 1 - \sum_{k=0}^{m-1} \frac{(V \cdot D)^k}{k!} \exp(-V \cdot D)$$

*Equation 2.11*

where  $m$  is the number of overlapping cascades required for amorphisation. For single hit amorphisation within a cascade which requires no overlapping,  $m = 1$  and Equation 2.11 reduces to Equation 2.9.

## 2.12 Amorphisation of Silicon

There are many ways to amorphise c-Si including: ion irradiation [107], [138], [146], [147], surface scratching [148] and indentation [149]. Phase transformation of c-Si to a-Si due to ion irradiation has attracted much attention from researchers over the last fifty years [150] because of the importance of ion implantation for the manufacture of semiconductor devices [96]. The mechanisms which best describe the amorphisation of Si under ion irradiation will depend on the exact experimental conditions under consideration taking into account various experimental factors. In particular, ion species and energy are important as these are the key determinants of collision cascade size and density [126].

Since ion irradiation induces defects in the material, the defect concentration increases with fluence and when this concentration in the irradiated Si exceeds a certain threshold value, it may cause amorphisation in the c-Si. When Si is irradiated with heavy ions, the amorphisation could be achieved following the heterogeneous mechanism proposed by Morehead and Crowder [141] and no overlapping is required [151]. Furthermore, heavy ions produce greater total damage resulting in lower fluences being required to reach  $E_c$  for amorphisation. However, the situation is different when Si is irradiated with light ions, the amorphisation is better described by a homogenous mechanism. A mixed homogenous and heterogeneous defects nucleation could also lead to an amorphisation in Si.

### 2.12.1 Defect-based Models

#### 2.12.1.1 Di-vacancies and Di-interstitial Pairs

Motooka [152] introduced a model based on the defect accumulation of di-vacancies and di-interstitial (D-D) pairs for the amorphisation of Si using molecular dynamics (MD). A combination of di-vacancies and a di-interstitials may distort the local atomic configuration of atoms in c-Si from perfect six-member rings to five- and seven-member rings as shown schematically in Figure 2.11: when a di-vacancy was introduced at position 1 and 2 in the six-member ring (ring of atoms 1–6), atom 6

was replaced by a  $\langle 100 \rangle$  split interstitial Motooka [152] calculated the bond angle and length, radial distribution function and density of states as a function of the number of D-D pairs. The results were in good agreement with experiments [153], [154] and it was concluded that complete amorphisation occurs when D-D pairs per atom exceed 2% or approximately two D-D pairs are introduced into the FCC cubic lattice [155], [156].

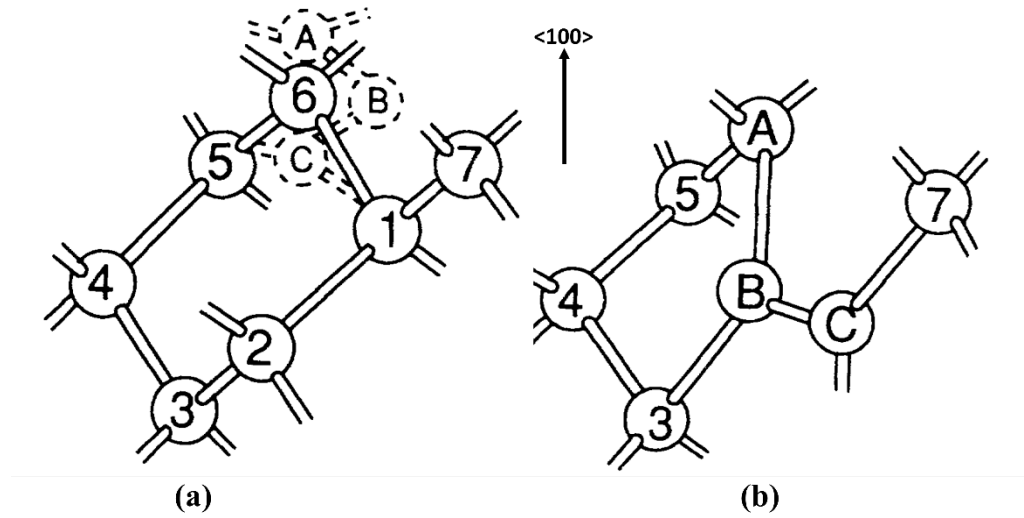


**Figure 2.11:** Schematic representations of: (a) the c-Si structure showing the six-membered rings with a  $\langle 100 \rangle$  split di-interstitial shown by the dotted bonds and atoms labelled A, B and C; (b) the local atomic rearrangement after the introduction of a D-D pair with atoms 3, 4, 5, A and B forming a five-member ring and atoms 3, B and C are part of a 7 member ring. Reproduced from [152].

#### 2.12.1.2 IV Pair or Bond Defects

Tang *et al.* [93] have proposed a model for amorphisation based on a metastable IV pair defect by carrying out tight binding simulations of self-diffusion and recombination of vacancies and interstitials. Since the IV pair can be formed by the local rearrangement of bonds within the crystal without any addition or removal of atoms, it is also referred to as a bond defect. In c-Si, it may distort the structure by

introducing five- and seven-member rings but preserve the fourfold coordination. These odd member rings are the characteristic of amorphous phase when present in sufficient numbers [157]. The stability of the defect in Si was determined by Tang *et al.* to have a lifetime of hours at room temperature. The atomic structure of an IV pair (or bond defect) is shown in Figure 2.12:

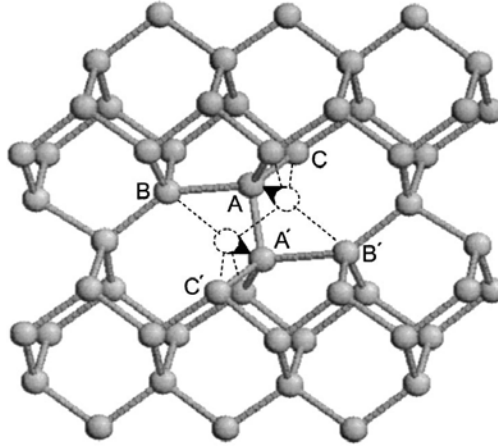


**Figure 2.12:** Atomic structure of the IV pair: dotted lines indicate the atoms and bonds in a perfect Si crystal; arrows at atoms A and A' show the direction of displacement of the atoms from their sites in the perfect lattice; the bonding between atoms A and A' is switched between B and B'. Reproduced from [93].

Stock *et al.* [158] worked on the modelling of IV pairs using MD and deduced that bond defects can be generated not only by the incomplete recombination of vacancies and interstitials, but also through head-on collisions with energetic ions. In another MD study carried out by Stock *et al.* they observed that IV pairs could be created using ballistic processes. In such a case, the formation of an IV pair does not require any pre-existing vacancy or interstitials within the lattice and may be considered as a primary defect caused by ion irradiation [159].



## **2.13 Recrystallisation**

The phenomenon in which amorphous regions in a material are recovered with introduction and nucleation of existing or new grains by the depositing energy is called recrystallisation.

### **2.13.1 Annealing**

Ion-beam-induced defects may be removed by thermal annealing. Thermal annealing can be performed using different methods e.g. annealing in a tube furnace, rapid thermal annealing (RTA) and thermal spike annealing [82], [118], [160]. In these techniques, the crystal does not change its state of matter but rather remains solid unlike other crystallisation processes such as floating zone crystal growth.

Recrystallisation can be achieved by heating amorphous material via thermal annealing. Crystalline Si has lower free energy as compared to a-Si; this is due to the fact that a-Si has a disordered arrangement of atoms and bonds [161]. The distorted bonds (i.e. distorted in length and/or angle) in a-Si are less thermodynamically stable as compared to c-Si. Thermal annealing thus provides a driving force to rearrange the unstable atoms into the form of a regular crystal [162] and can be verified, for example, in a TEM via the DP. The transition from a metastable amorphous phase could be achieved either through solid phase epitaxial growth (SPEG) or random nucleation growth (RNG) which are discussed below. During these processes, the dopants (i.e. impurities introduced into the material) can become electrically activated.

### **2.13.2 Solid Phase Epitaxial Growth**

In 1968, Meyer *et al.* [163] proposed the SPEG process. This process involves the growth of a crystal layer into an amorphous region under thermal annealing which recovers the amorphous region while maintaining the solid phase. The semiconductor industry uses the RTA technique to cause this process to remove amorphous material

created during ion implantation of a semiconductor substrate [162]. The activation energy for recrystallisation for Si using SPEG is  $\sim 2.4$  eV [162] to 2.7 eV over the temperature range of  $\sim 480$ – $1350^\circ\text{C}$  [164].

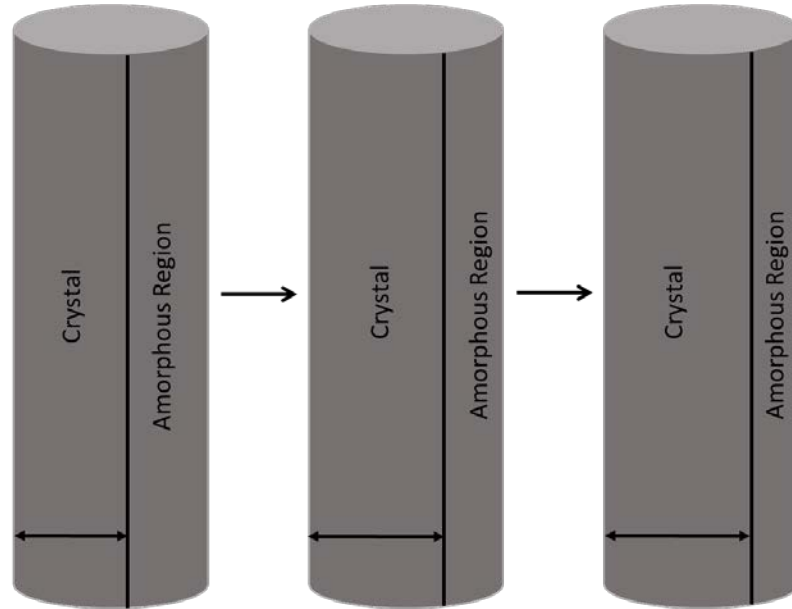


**Figure 2.13:** Schematic representation of SPEG recrystallisation of a Si NW. Crystal-amorphous interface region shown as thick black line moving from left to right during thermal annealing.

### 2.13.3 Random Nucleation Growth

Recovery of an amorphous phase into a crystalline phase achieved without a crystalline template is known as RNG. The randomly orientation crystalline seeds within the material grow resulting in a randomly orientated polycrystalline materials. For Si, RNG starts above a temperature range of  $\sim 650$ – $1350^\circ\text{C}$  [164] and is governed by an activation energy of  $\sim 4$  eV [162], [164].

### 2.13.4 Regrowth Rate and Orientation Dependence

Csepregi *et al.* [165] have reported the orientation dependence of the re-growth of a-Si when irradiated with self-ions. They reported in their paper that the re-growth rate of Si with different orientations varied and proposed that orientation dependence is inversely proportional to atomic density of a plane i.e. {100} Si with an area density (number of atoms per unit area on the plane) of  $6.78 \times 10^{14}$  atoms.cm<sup>-2</sup> has the fastest regrowth rate whilst {111} Si with an atomic density of  $7.83 \times 10^{14}$  has the slowest regrowth rate (see Figure 2.14). The re-growth rate of {100} family of planes was 25 times faster than {111} family of planes. To explain their observations [46], they invoked a simple bond-breaking model originally proposed by Spaepen [166] in 1978 and discussed further in § 2.13.5.1.

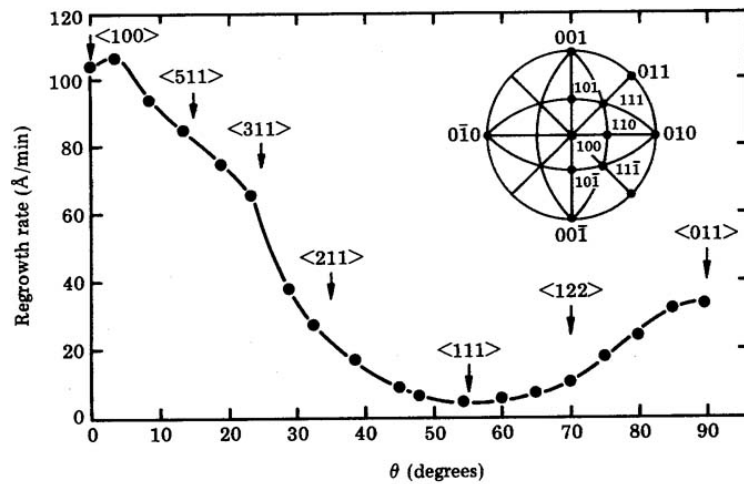


**Figure 2.14:** Graph illustrating the regrowth rate of amorphous silicon is orientation dependant. It can be seen that regrowth is fastest for the <100> direction whilst it is slowest for the <111>. Reproduced from [46].

### 2.13.5 Solid Phase Epitaxial Growth Models

A number of models for the kinetics of solid phase epitaxial growth for recrystallisation have been proposed in the literature by various researchers [167], [168],[169]–[171]. Amorphous Si consists of five-, six-, seven- and eight-membered

rings and is a phase of Si with well-defined thermodynamic properties [132]. Francesco *et al.* [171] and Rossano *et al.* [172] proposed that a-Si possesses free energy  $\sim 0.12 \text{ eV.atom}^{-1}$  greater than that of c-Si which acts as a driving force to transform the a-Si phase into the c-Si phase. The a-Si phase is metastable at room temperature and recrystallisation occurs when subjected to temperatures higher than  $450^\circ\text{C}$  [173]. Olson and Roth [55] demonstrated that the growth rate in SPEG follows an Arrhenius-like behaviour over a growth rate range of more than six orders of magnitude with single activation energy of  $2.68 \pm 0.05 \text{ eV}$ .

#### **2.13.5.1 Atomistic Models**

The atomistic of the SPEG model involve the rearrangement of atoms in the amorphous phase using the crystalline region as a template. It has been proposed by Csepregi *et al.* [165] that for a crystal to regrow along [110] ledges, an atom must fulfil the necessary condition to have two nearest neighbours at the interface which are already in crystalline phase. Spaepen and Turnbull invoked that SPEG is mediated by bond breaking and reordering that leads to the regrowth of the amorphous layer onto the crystal along [110] ledges. The formation and migration energies for dangling bond in Si has been reported to be  $2.246 \text{ eV}$  and  $0.43 \text{ eV}$ , respectively, [166], [167]. Another study carried out by Narayan [174] suggested that the mass transportation of excess interstitials from the amorphous region to the crystalline region may be a regrowth mechanism for SPEG.

#### **2.13.5.2 IV Pair Recombination**

IV pair recombination has been modelled by Stock *et al.* [158] using MD and kinetic Monte Carlo simulations [175]. They demonstrated that IV pairs recombine during annealing and in so doing facilitating the recrystallisation process. Different values of activation energy for recombination of vacancy and interstitial have been reported in the literature with a minimum of  $0.43 \text{ eV}$  [176] MD simulations and a maximum of  $1.32 \text{ eV}$  [177] using ab initio method.

## 2.14 Bending of Semiconductor Nanowires under Ion Irradiation

The mechanisms for the bending of NWs under ion irradiation, have not yet been fully understood but have been explored by different authors [55], [178]–[183] in the literature.

Borschel *et al.* [55] investigated the alignment of semiconductor NWs under ion irradiation. They irradiated GaAs using three different ion species ( $S^+$ ,  $Xe^+$  or  $Ar^+$ ) at different energies between 30–620 keV to explore the effects of irradiation conditions (i.e. ion mass, energy and fluence) on NW bending. They reported that when NWs are irradiated with lower energy ions (30, 35, 70 and 80 keV), the projected range of ions (discussed in detail in Chapter 4) is less than half the diameter of the NWs and the defects are concentrated in the irradiated side of the NWs. They suggested that ion-beam-induced defects lead to a volume expansion due to the interstitial atoms. As the volume expansion is in the irradiated side of the NW it thus produces a bending in the ion beam direction and the NW bends away from the ion beam. Based on calculations using the 3d TRIM Monte Carlo code [184], at higher energies (210 and 620 keV  $Xe^+$  ions), the projected range of the ion increases and they stop in the backside of the NWs where damage predominantly accumulates. Borschel *et al.* [55] proposed that excess vacancies lie in irradiated side while excess interstitial atoms in the unirradiated of the NW due to forward knock-on scattering in the collision cascade. This spatial distribution of vacancies and interstitials results in the contraction and expansion in the volume of the irradiated and unirradiated side of the NW. This expansion and contraction then generates compressive and tensile stress in the regions of excess interstitial and vacancies, respectively. Thus causing bending the NWs towards the direction of the ion beam in high-energy ion irradiations. This bending mechanism of the NWs is illustrated in Figure 2.15 by considering the two sides of the NW. For medium-energy ion implantation where the range of ions is in the middle of the NW, it was suggested by Borschel *et al.* [55] that the range of the ions increases or decreases during downward and upward bending of the NWs because of the change of inclination, respectively. Therefore producing defects deeper into the NW and causing the alternate bending of the NW.

In another study, Borschel *et al.* [181] explored the effects of 30 keV Ga ions on ZnO NWs using a focused ion beam (FIB) miller. The NWs were irradiated with varying energies and fluences and alternating directions of bending could be induced. The ZnO NWs bending was attributed to the compressive and tensile stresses because of the expansion and contraction of volume due to the interstitials and vacancies, respectively.

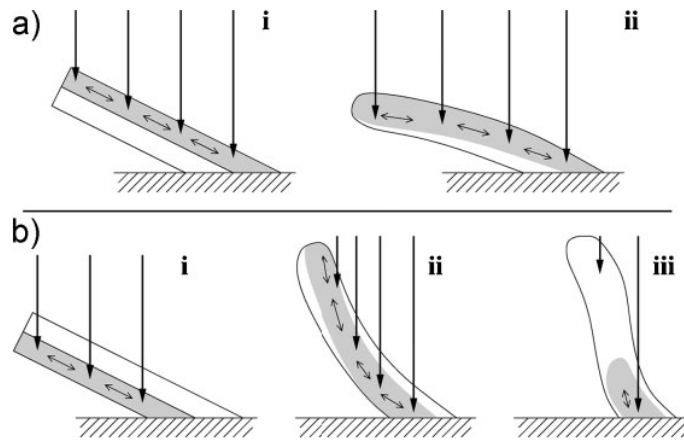


**Figure 2.15:** Schematic of semiconductor NWs bending under ion irradiation: a) downward bending; b) upward bending. Arrows show the ion beam direction. Reproduced from [55].

Pecora *et al.* [180] carried out a study on the ion beam induced bending of Si NWs. Silicon NWs were fabricated through an electron beam evaporation technique in such a way that the upper part of the NWs were tapered (i.e. the NWs had a thicker base than tip). NWs with three different crystallographic orientations of (111), (110) and (100) were grown on a (111) Si substrate. The (111)-oriented NWs were perpendicular while (110) and (100)-oriented NWs were  $35^\circ$  and  $54^\circ$  to the substrate, respectively. The samples were irradiated with 45 keV  $\text{Ge}^+$  ions perpendicular to the substrate in such a way that it made an angle of  $45^\circ$  with the NWs. They reported no change in the structural features of the NWs at a fluence of  $5 \times 10^{14} \text{ ions.cm}^{-2}$ . At fluences above  $5 \times 10^{14} \text{ ions.cm}^{-2}$ , the inclined NWs were

observed to bend while no change was observed in the (111) NWs which were perpendicular to the substrate. Further increasing the ion fluence up to  $2.5 \times 10^{15}$  ions.cm<sup>-2</sup> caused no further structural modification contrary to the reported behaviour of other semiconductor NWs in which the bending increased with increasing ion fluence [180], [185], [186].

In another study Pecora *et al.* [185] investigated the amorphisation, bending and recrystallisation of Si NWs. The samples were irradiated *ex-situ* with 45 keV Ge<sup>+</sup> ions perpendicular to the substrate and were characterised using SEM and TEM. They reported that ion irradiation induced bending of Si NWs was directly related to the amorphisation process. The bending occurred only in those regions which were fully amorphised. They used a viscoelastic spike model to explain the NW deformation. The model assumed thermal expansion during propagation of an ion inside the material which induces anisotropic heating around the ion trajectory. Thermal expansion then generates shear stress and relaxes resulting in expansion and contraction in the direction perpendicular and parallel to the ion beam, respectively, to maintain a constant volume. This effect requires amorphous material and has not been observed in crystalline materials due to the lack of shear sites [187].

The role of the c-a interface in NW bending has also been explored by Pecora *et al.* [185]. It was observed that Si NWs bent only when they were fully amorphous (i.e. no c-a interface). They suggested that the presence of crystallinity in the NWs acts as a strong constraint against NWs bending.

Romano *et al.* [188] reported the irradiation of crystalline germanium (Ge) NWs of diameter ~50 nm with 30 keV Ga<sup>+</sup> ions at 45° off-normal. The *in-situ* irradiation experiments were carried out in a FIB-SEM system and structural characterisation was performed *ex-situ* using TEM. They reported that the NWs bent towards the ion beam experiencing tensile stresses due to a density change due to amorphisation. They observed that the NW bending direction could be repeatedly reversed when irradiated from the opposite side. They also ruled out ion hammering effects as these would require a negative thermal expansion coefficient to account for the tensile stresses. They suggested a viscoelastic flow as a key mechanism for the bending the NWs.

Jun *et al.* [179] irradiated Si NWs with 30 keV Ga<sup>+</sup> ions implantation at normal incidence in a FIB-SEM system. They observed the Si NWs bent towards the ion beam and proposed that amorphisation induced tensile stresses was a driving mechanism in line with the conclusions of Romano *et al.*

Rajput *et al.* [189] fabricated the Si NWs using FIB milling and the structural characterisation was carried out using TEM. The polycrystalline Si NWs were irradiated with 16 keV Ga<sup>+</sup> ions at 54° off-normal using FIB-SEM system. They observed the immediate bending of NWs under ion irradiation and subsequently reverse bending of the NWs when they align parallel to the ion beam direction. They reported that the NWs bent towards the ion beam experiencing void-induced stress generation and dynamic annealing of ion-beam-induced defects. Further, explaining the sputtering and redistribution of atoms produce compressive stresses causing the irradiated surface of the NW to shrink. This shrinkage of surface thus cause deformation and the NWs to bend towards the ion beam direction. MD simulations of NWs were carried out by Rajput *et al.* to support the proposed bending mechanism under ion irradiation.

Kimin *et al.* [179] has irradiated the Si NWs with 30 keV Ga<sup>+</sup> ions at normal incidence in FIB-SEM system. They proposed that stresses induced under ion irradiation due to possible dynamic annealing of the amorphous zones as an underlying mechanism of NWs bending. They repeated the experiment to gallium nitride (GaN) and ZnO NWs and to verify the bending direction and found the NWs bend towards the ion beam direction.

There has been no consensus on the underlying mechanisms of ion-beam-induced bending of NWs in the literature. Since NWs are considered as potential candidates for future nanodevices, the understanding of ion-beam-induced modifications e.g. doping, manouvering and plastic deformation are important for the manufacture of such devices.



## **2.15 Van Der Waals Forces**

The Si NWs used in this work were dispersed onto Mo TEM grids by the method described in detail in chapter 4. The Si NWs adhere to the TEM grid with the help of Van der Waals (VDW) forces as discussed below. These forces are of particular interest for chapter 8 in which the input parameters required for modelling the Si NWs onto the TEM grid has been discussed.

### **2.15.1 Introduction to Van der Waals Forces**

Van der Waals forces are non-covalent intermolecular forces consisting of three components: the Keesom, Debye and Dispersion forces [190]. The Keesom force arises due to electrostatic interaction between charges, permanent dipoles, quadrupoles and multipoles [191]. The second component is the Debye force which is due to interactions between a permanent dipole and an induced dipole [190]. The third and most important contribution is the dispersion or London force (temporary dipoles) and is always present because it originates from the continuous electron motion which forms temporary dipoles. These three forces of different origins are proportional to  $1/r^6$  (where  $r$  is the separation distance between two atoms or molecules). Different models have been proposed in the literature [192], [193] to quantify the VDW interaction between two bodies which depends on the contact area and these adhesive forces.

### **2.15.2 Microscopic and Macroscopic Models**

Derjaguin and Hamaker [194], [195] developed a macroscopic model to calculate the VDW forces between two spheres and a sphere and a flat surface [81]. This model was based on the assumption that the potential between atoms is additive and the interaction between two bodies may be obtained via integration over their geometric shapes. As VDW forces are anisotropic, non-additive (the forces between two molecules can be affected by the presence of other molecules) and influenced by retardation effects described elsewhere in the literature [196].

Lifshitz [197] developed a microscopic model of VDW forces based on quantum field theory. In that model, each body was treated as a continuum with certain dielectric properties. It incorporated many body effects which were neglected in the Hamaker's macroscopic model [196]. Subsequent papers in the literature proposed different models by improving the Lifshitz model and found the power law dependencies remained the same for each geometrical configuration [198], [199]. The strength of VDW interactions is based on material properties and defined with a constant known as the Hamaker constant,  $A$  (joules). The only difference between the Lifshitz (microscopic) and Hamaker (macroscopic) model is the way the Hamaker constants are calculated for different materials.

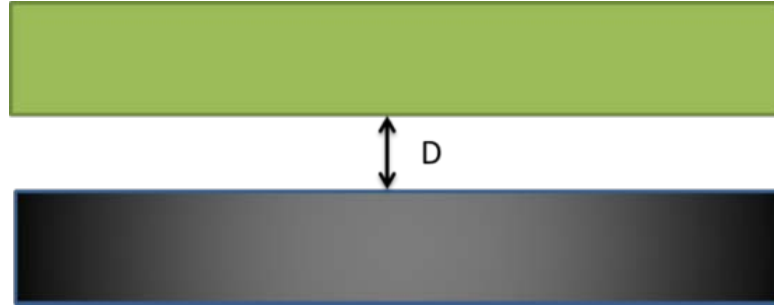


**Figure 2.16:** Schematic of two flat planes interacting at a distance,  $D$ .

The VDW force per unit area between two flat surfaces, as shown in Figure 2.16, can be calculated through Equation 2.12 [196], [200], [201]:

$$F_{\text{plane-plane}} = -\frac{A}{6\pi D^3} \quad \text{Equation 2.12}$$

Where  $D$  is the distance between two interacting surfaces and  $A$  is the Hamaker constant defined in Equation 2.13. The minimum distance at which the VDW forces are measured is called the equilibrium distance between the atoms below which the chemical forces dominate [194].

$$A = \pi^2 C \rho_1 \rho_2 \quad \text{Equation 2.13}$$

where  $C$  is the constant in the atom-atom pair potential and  $\rho_1, \rho_2$  are the number of atoms per unit volume in materials 1 and 2. Typical values of  $A$  for most materials in vacuum are about  $10^{-20}$  J. The values of the Hamaker constant for various materials have been taken from the literature and are presented in Table 2.2:

**Table 2.2:** *Experimental and theoretical values of Hamaker constant values for different material systems.*

Materials (in Vacuum)	Experimental Value ( $\times 10^{-20}$ J)	Theoretical Value ( $\times 10^{-20}$ J)
W-TiO <sub>2</sub>	$40 \pm 10$ [23]	30 [23]
W-TiO <sub>2-x</sub>	$31 \pm 7$ [23]	30 [23]
W-MgO		18 [23]
W-SiO <sub>2</sub>	$13 \pm 2$ [23]	13 [23]
C(diamond)-SiO <sub>2</sub>	13.7 [25]	
KCl- SiO <sub>2</sub>	5.94	
PbS- SiO <sub>2</sub>	5.37 [25]	
$\beta$ -Si <sub>3</sub> N <sub>4</sub> -SiO <sub>2</sub>	10.8 [25]	
ZnS- SiO <sub>2</sub>	9.69 [25]	
TiO <sub>2</sub> - SiO <sub>2</sub>	9.46 [25]	
6H-SiC- SiO <sub>2</sub>	12.6 [25]	
PTFE-SiO <sub>2</sub> (in Nitrogen)	4.87 [15], 7.60 [24]	4.87-6.17 [24]
Ag-SiO <sub>2</sub>	12.92 [24]	11.42-18.2 [24]
Cu-SiO <sub>2</sub>	14.10 [24]	11.60-16.73 [24]
TiN-SiO <sub>2</sub>	8.80 (in Nitrogen) [15]	10.10-12.04 [15,24]
SiO <sub>2</sub> -SiO <sub>2</sub> (in Nitrogen)	7.20 [15,24]	6.55-6.96 [15,24]

The VDW force based on Lifshitz theory (macroscopic model) between a sphere and a plane, as shown in Figure 2.17 is given by Equation 2.14 [196], [202], [203]:

$$F_{\text{sphere-plane}} = -\frac{AR}{6D^2} \quad \text{Equation 2.14}$$

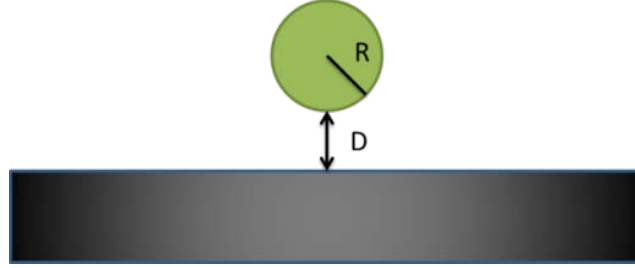


**Figure 2.17:** Schematic of a sphere and a plane interacting at a distance,  $D$ .

The VDW forces per unit length between a cylinder and a flat surface, as shown in Figure 2.18, can be calculated through the following Equation 2.15 [191], [204]:

$$F_{\text{cylinder-plane}} = -\frac{A\sqrt{R}}{8\sqrt{2}D^{5/2}} \quad \text{Equation 2.15}$$

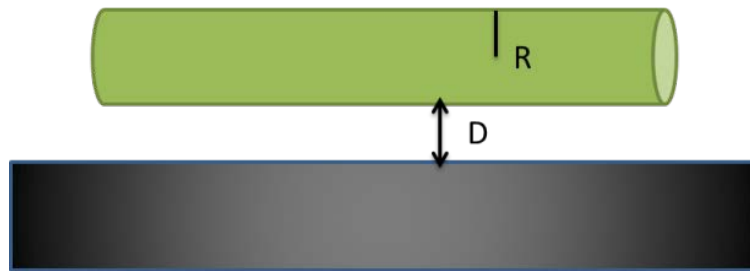


**Figure 2.18:** Schematic of a cylinder and a plane interacting at a distance,  $D$ .

## 2.16 Force Measurement Techniques

Atomic force microscopy (AFM) is a valuable tool for measuring interaction forces as small as  $10^{-18}$  N [205] allowing the long-range VDW forces between the tip of a AFM and a sample to be measured. The interaction between the tip and the sample under investigation is measured by monitoring the deflection of the free end of the cantilever by a laser beam using the beam bounce back method. The laser beam reflects off the cantilever onto a position sensitive photodiode. The deflection of the cantilever is recorded during the scan period and used to gather information on the surface such as the topography. The movement of the tip over a sample is controlled by a piezoelectric material known as scanner.

The sample is scanned with a sharp tip attached at the end of a cantilever. When the cantilever is brought into contact with the sample, the microfabricated tip of the cantilever deflects due to the close range forces between the tip and surface. This deflection is commonly measured using a laser beam reflected off the cantilever [206].

The earliest experimental work to measure the VDW forces using a surface force apparatus (the forerunner of the modern AFM) was done by Derjaguin and Israelchivili [194], [207]. At a large tip-to-sample distance, there exists a weak interaction between atoms. This interaction force increases with decreasing distance between the tip and the sample until the electrostatic force dominates as the electrons repel each other. This repulsion decreases the attractive force by reducing the distance between the atoms and reaches zero when the interatomic distance is about the length of a typical chemical bond (approximately 0.2 nm) [208], [209]. The distance  $D$  is typically taken to be 0.35 nm for the purposes of calculating the VDW force [193], [196], [202].

When the AFM measurements are performed in air, the capillary forces increase the adhesion. Weisenhorn *et al.* [210] were the first to purpose to perform measurements in water to avoid capillary forces [196]. However, experimentally-measured total adhesion through AFM at the minimum  $D$  between the tip and surface is composed of the VDW, dielectrophoretic (force experienced by a dielectric particle in non-uniform electric field) and image forces [203].

Nancy *et al.* [211] probed the VDW forces by AFM between tungsten-graphite and tungsten-gold in air by measuring the cantilever deflection due to the tip-sample interaction. They estimated the force acting on the tungsten tip of radius 100 nm at a distance of 5 nm from the sample (graphite) position to be  $0.2 \times 10^{-9}$  N. However, the magnitude of force increases with decreasing tip-sample distance and at 0.2 nm the force was  $133 \times 10^{-9}$  N. In another study, Nancy *et al.* [212] presented similar results to estimate the magnitude of the attractive and adhesive forces using a tungsten tip on mica, graphite,  $\text{Al}_2\text{O}_3$  and other materials. The force-displacement curve of a tungsten tip on graphite is shown in Figure 2.19

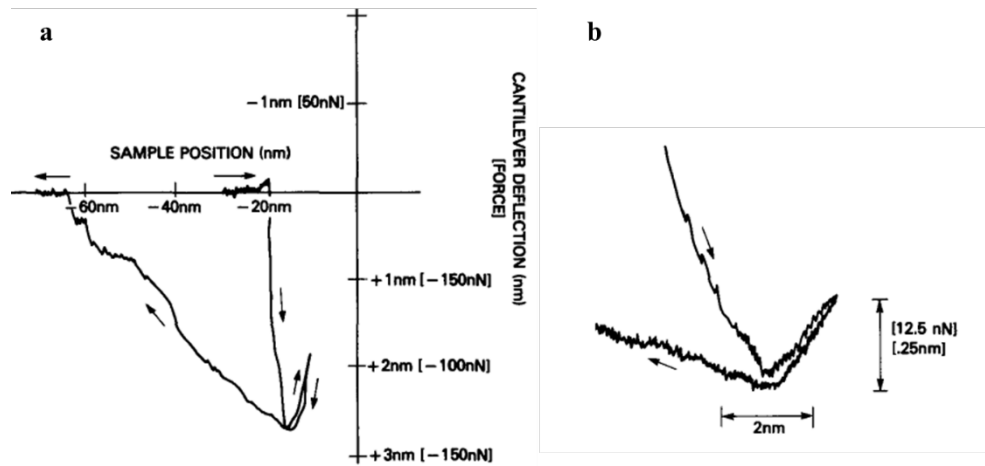


**Figure 2.19:** Force-displacement curve for interactions between a tungsten tip and a graphite sample obtained by AFM. The cantilever is under extremely-light load which is completely due to surface forces. Reproduced from [211].

Goodman *et al.* [213] calculated the VDW force for a variety of tip-sample systems using AFM and demonstrated the importance of  $D$ . For metal-metal tip-sample systems, the reported values for VDW forces were  $\sim 20 \times 10^{-9}$  N for a tip of radius 100 nm at  $D = 1$  nm. The magnitude of the force went up to  $120 \times 10^{-9}$  N when  $D = 0.4$  nm and AFM then operates in the repulsive mode.

Alley *et al.* [214] have estimated and compared the adhesion force for Si in the presence of air (Si-air-Si) system using uncoated and coated Si tips and their contributions in imaging surface roughness. Silicon tips were coated in octadecyltrichlorosilane (OTS) and the magnitude of the adhesion forces were compared to the uncoated tips. The measurements were performed with a cantilever tip radius of 5 nm. The force displacement curves were obtained for uncoated/coated and different Si surfaces. The adhesion forces  $(6.9 \pm 2) \times 10^{-9}$  N and  $(4.5 \pm 0.8) \times 10^{-9}$  N were reported for hydrophilic and hydrophobic Si, respectively. While very small adhesion forces  $(1.2 \pm 0.3) \times 10^{-9}$  N and  $(4.5 \pm 0.8) \times 10^{-9}$  N were reported for OTS coated tips for hydrophilic and hydrophobic Si, respectively. They reported that image resolution can be enhanced by coating the AFM tip with OTS yielding very low adhesive forces. Komvopoulos [30] suggested this small adhesion is mainly due to the VDW forces.

Stifter *et al.* [215] investigated the VDW adhesion forces and proposed that the Lennard-Jones force acted alongside the capillary forces between the tip and the sample surface when AFM measurements were made in air. The Lennard-Jones force (the force between two uncharged molecules or atoms) is a combination of the VDW forces and Pauli repulsive force (due to the overlapping of electron clouds). They calculated the adhesion forces and their dependence as a function of  $D$ , tip radius,  $R$ , relative humidity and contact angle. The comparison of different forces measured by Stifter *et al.* with  $R = 20$  nm using  $A = 0.04 \times 10^{-19}$  J and  $3.0 \times 10^{-19}$  J are shown in Figure 2.20. Stifter *et al.* [215] has also investigated the force dependence on the  $R$  and the results are shown in Figure 2.21. As the tip radius increases, the contact area between the tip and sample surface increases and hence the resultant adhesion forces increase.

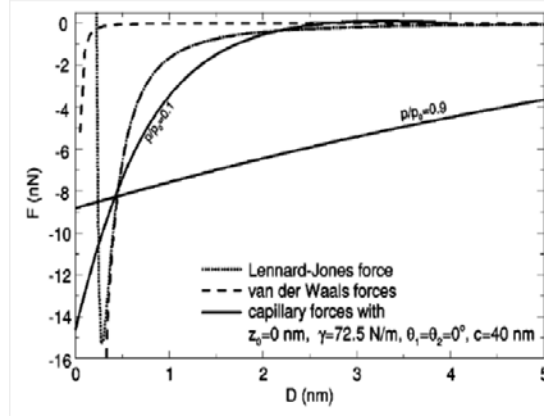


**Figure 2.20:** Graph showing a comparison between the Van der Waals and capillary forces as a function of distance,  $D$ . Reproduced from [215].

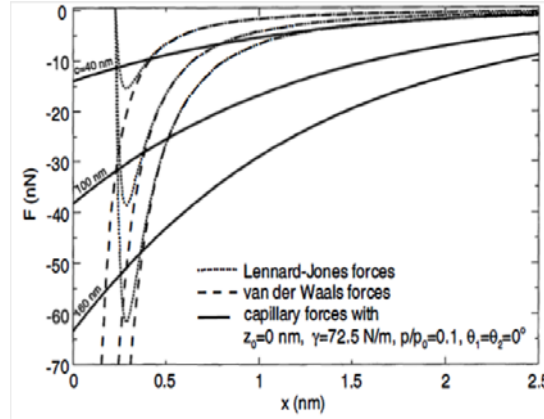


**Figure 2.21:** Force-displacement curve for surface forces as a function of tip radius. The parameters used to plot Fig. 2.20 are the:  $A = 3.0 \times 10^{-19}$  J and  $R = 20$  nm. Reproduced from [215].

Michael *et al.* [203] performed measurements in ultra-high vacuum using scanning tunnelling microscopy and estimated the VDW force using the Lifshitz model (Equation 2.14) as the dominant force involving the picking up of small Ni clusters on highly ordered pyrolytic graphite (HOPG). They used an idea of overcoming the adhesive force of the Ni nano clusters on HOPG by reducing the tip-cluster distance (increasing the attractive force between tip and cluster). The force-distance curve involved in the controlled picking-up of Ni clusters describes the tip-cluster distance at which pick-up occurs. A curve of  $F$  against separation was



obtained

using

$A = 4 \times 10^{-19}$  J, a radius of Ni cluster of 5.9 nm at a minimum distance  $D = 0.30$  nm and is shown in Figure 2.22:

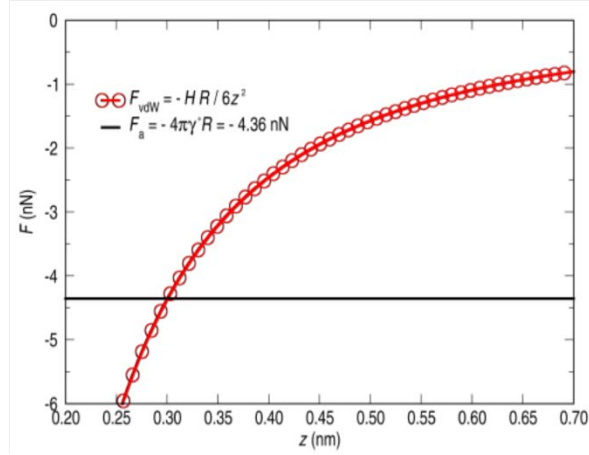


**Figure 2.22:** Graph showing the force-displacement curve plotted using Equation 2.14. The adhesion force ( $F_a = -4.36$  nN, solid black line) and Van der Waals forces (open red circles) involved in the picking-up process of Ni clusters on HOPG. Reproduced from [203].

## 2.17 Mechanical Properties of Nanowires

Mechanical properties of different nanomaterials [26], [216], [17] have been investigated in the literature and found to be different from the bulk equivalents. Nanoscale material properties strongly depend on the sample dimensions [59]. The experimentally measured elastic properties (e.g. Young's modulus) of NWs and nanotubes have been found to be diameter dependent [216], [17], [182], [217]. However, there is no definitive consensus about how the Young's modulus relies on NW geometry and diameter. Some literature suggest that the Young's modulus of NWs increases with decreasing diameter [216], [17], [182] but an inverse trend has also been reported in other work [65]. This effect may attributed to the elastic properties of nanoscale structures which have high surface-to-volume ratios [59]. As is well known, the effects of surface tension is significant for fluids and relatively

unimportant for bulk materials since the outside surface does not play a key role in deciding material properties in the latter [218].

The mechanical properties of NWs have been extensively studied using different experimental and computational techniques [216], [217], [219], [15], [65]. For example: the surface effects on mechanical properties of NWs as a function of surface-to-volume ratio have been reported in the literature [220], [221], [76]; diameter dependent elastic properties of NWs have been studied using different numerical methods including molecular dynamic simulations [222],[223],[224]; and finite element methods [224], [225], [226].

Xian *et al.* [59] performed theoretical investigations on the effects of applying force to GaN NWs for the three different cases of: a cantilever (fixed at one end); simply supported (fixed at ends which are free to rotate); and clamped NWs (fixed at both ends with no rotation allowed) [59]. They estimated the Young's modulus by incorporating the Timoshenko beam theory which accounts for the effects of transverse shear deformation when cross-sections of the beam (i.e. cantilever) is no longer perpendicular to the neutral axis of the cantilever where the tension or compression occurs during bending. The Young's modulus for clamped lead (Pb) NWs increases to nearly twice that of its bulk value as the NW diameter decreased from 200 to 50 nm. This reported trend agrees with the results obtained experimentally in [227] and is shown in Figure 2.23a. However, a reverse trend was observed for cantilevered GaN NWs for which the Young's modulus decreased gradually for NWs less than 80 nm in diameter. The authors explained their results in terms of positive surface tension increasing the deflection for cantilevered NWs and decreasing the deflection for clamped NWs which behave like softer and stiffer materials, respectively. For Si NWs, a similar trend has been observed where the Young's modulus of clamped NWs is greater than that of cantilevered NWs.

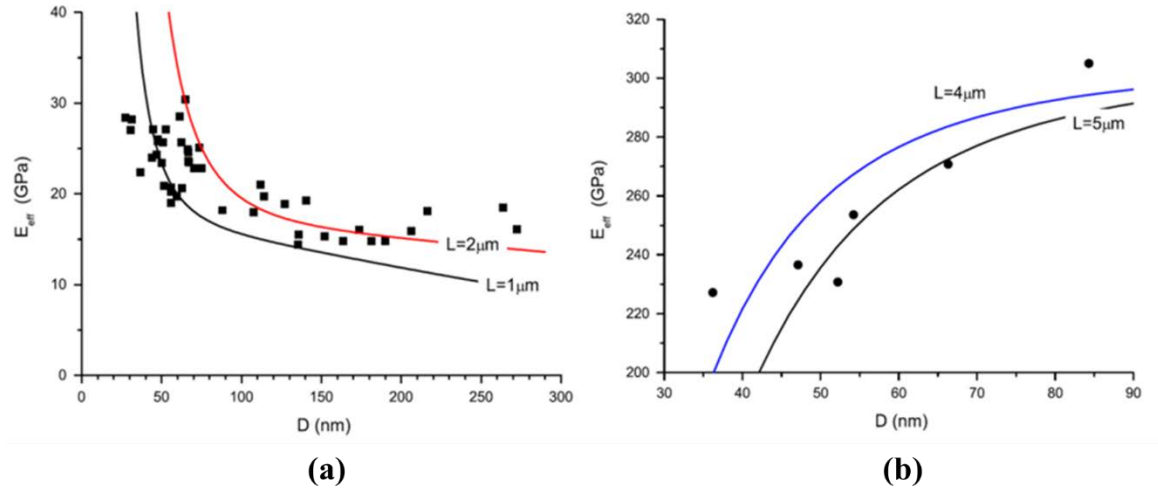


**Figure 2.23:** Young's modulus dependence on the diameter of NWs obtained using atomic force microscopy: (a) increasing with decreasing diameter for clamped Pb NWs; and (b) decreasing with decreasing diameter for cantilevered GaN NWs. The curves are the best fit for the experimental data. Reproduced from [59].

Atoms on the surface of the NWs are under-coordinated as they have no neighbouring atoms outside the NWs. Therefore they have a low electron density on the surface and experience asymmetrical coulomb interactions [221]. H.A. Wu [217] investigated the mechanical properties of Cu NWs and calculated the Young's modulus, yield strength and deformation of NWs using MD simulations. The MD simulations showed that the Young's modulus of Cu NW is not constant in the strain range of 0–0.15 as illustrated in Figure 2.24 and the authors suggested that this may arise from inhomogeneity in the cross-section of the rectangular shaped NW which resulted from surface effects.

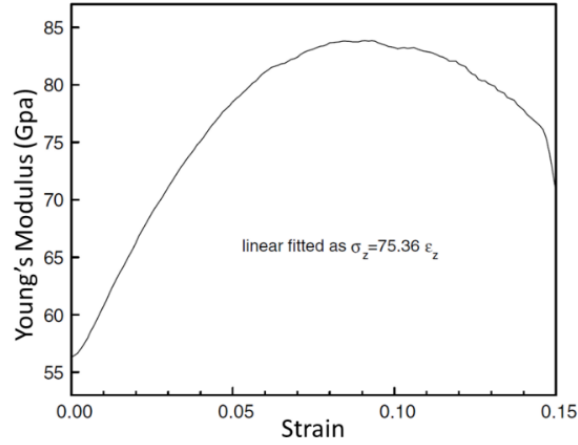


**Figure 2.24:** Young's modulus of strained Cu NWs calculated using MD simulations. Reproduced from [217].

### 2.17.1 Young's Modulus Dependence on Nanowire Diameter

Kang *et al.* [228] performed MD simulation studies on Si NWs of small diameters ranging from 3–7 nm at temperatures from 100–1200 K. The bare NW (without a hydrogen or passive oxide layer) simulations were set up such that the NWs had an aspect ratio of 1:10 (diameter: length). Circular cross-sections of [110]-orientated NWs from this study are shown in Figure 2.25.

Kang *et al.* [228] performed MD simulations to estimate the Young's modulus of Si NWs as a function of NW diameter and crystallographic orientation. They reported that the modulus decreases as the diameter decreases and is orientation dependent. The modulus for [110]-oriented Si NWs is always less than that of [111] orientated as illustrated in Figure 2.26. For the Young's modulus of the [110]- and [111]-oriented NWs of 2 nm diameter, this reduction was 28% and 33% from that of the bulk values of 154 GPa and 168 GPa, respectively.

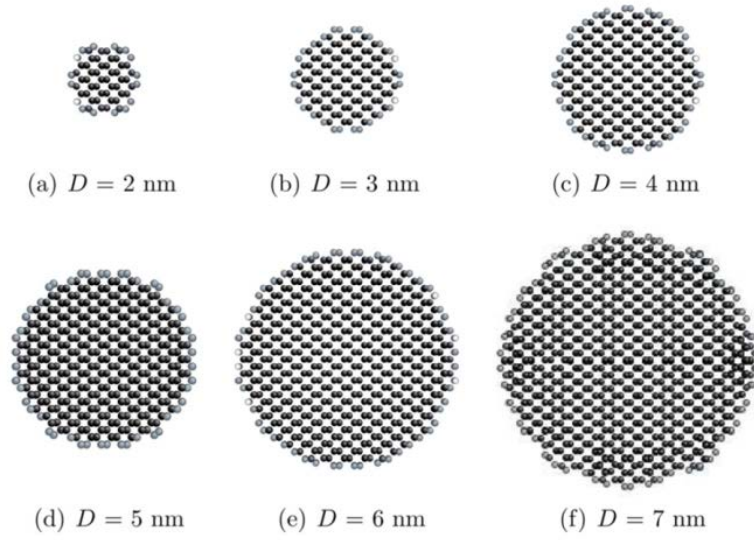


**Figure 2.25:** Circular cross-sections of  $[110]$ -oriented Si NWs of different diameters used for MD simulations. Surface atoms have higher energy than inner atoms after relaxation. Reproduced from [228].

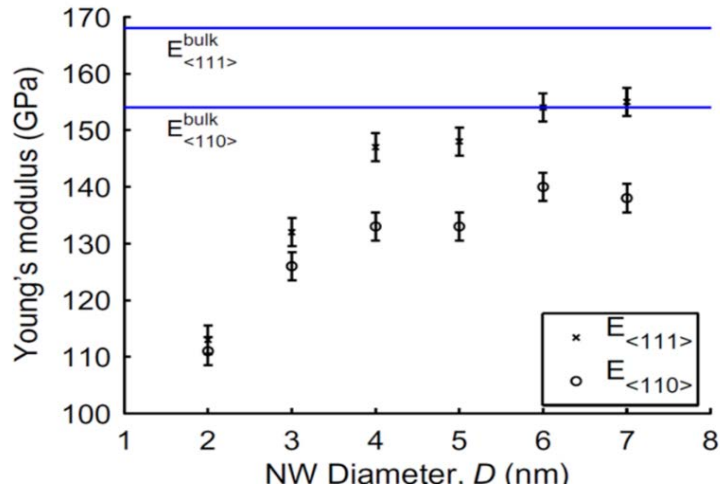


**Figure 2.26:** Results of MD simulations for Young's modulus of  $[111]$  and  $[110]$ -oriented Si NWs as a function of diameter and compared with bulk Si. The Young's modulus for both orientations decreases as a function of diameter. Reproduced from [228].

The same trend of decrease in Young's modulus of Si NWs was observed by Lee and Rud [63] using density functional theory. They reported a 26% decrease in Young's modulus of [100]-oriented NWs compared to the bulk value of 122.5 GPa at room temperature. Another study reported different values for the Young's modulus of Si NWs using different simulation methods ranging from 53–120 GPa for 12–20 nm diameter but following the same trend of the modulus decreasing with diameter [228].

Liang *et al.* [220] employed MD simulations of Cu NWs to explore Young's modulus dependence on the diameter. The modulus along different orientations was calculated and compared with bulk Cu. For thicker NWs, Young's modulus is in good agreement with the bulk value, but significant deviation has been observed for the thin NWs as shown in the Figure 2.27:

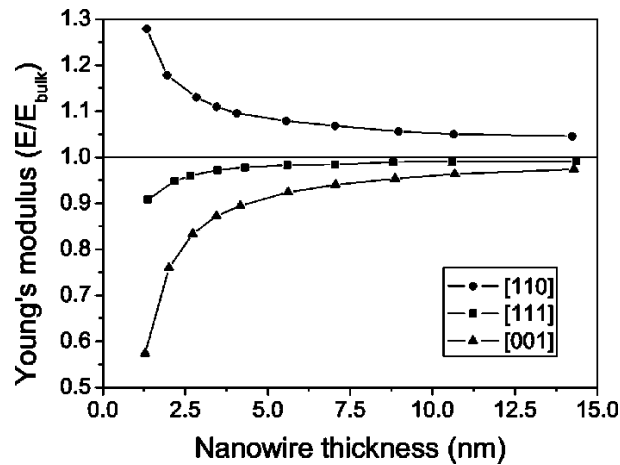


**Figure 2.27:** MD simulation results of the Young's modulus for [100]-, [110]- and [111]-oriented Cu NWs with values for the bulk indicated by horizontal line. For larger diameter NWs, the surface compressive strain is smaller and therefore the value of the Young's modulus is closer to the bulk. Reproduced from [220].

Wu *et al.* [217] reported the Young's modulus dependence on the diameter for Cu NWs ranging from 1.62–9.18 nm using MD simulations. It can be seen from the

results shown in Figure 2.28 that the Young's modulus increases with increasing diameter until it becomes equal to the bulk value of 85 GPa [217].

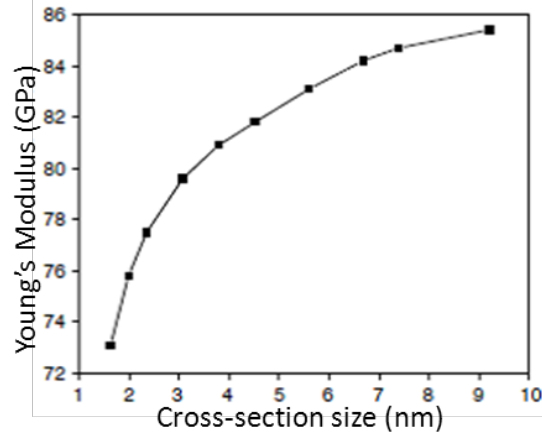


**Figure 2.28:** Diameter dependence of Young's modulus for Cu NWs obtained using the MD simulations. Reproduced from [217].

Young's modulus has been found to be diameter and orientation dependent and decreases by decreasing the diameter of the NWs. Young's modulus for thin Si NWs decreases with decreasing the diameter below 20 nm but above that thickness it tends to the value for bulk Si (154–168 GPa [228]).

### 2.17.2 Temperature Effects

Kang *et al.* [228] carried out MD simulations to generate stress-strain curves for Si NWs at different temperatures to study the fracture strength of Si NWs as shown in Figure 2.29. The slope of the stress-strain curve at zero strain gives the Young's modulus of the Si NWs and has been observed to decrease with increasing temperature. Kang *et al.* also observed that Young's modulus decreases with decreasing diameter as illustrated in Figure 2.29 (b):

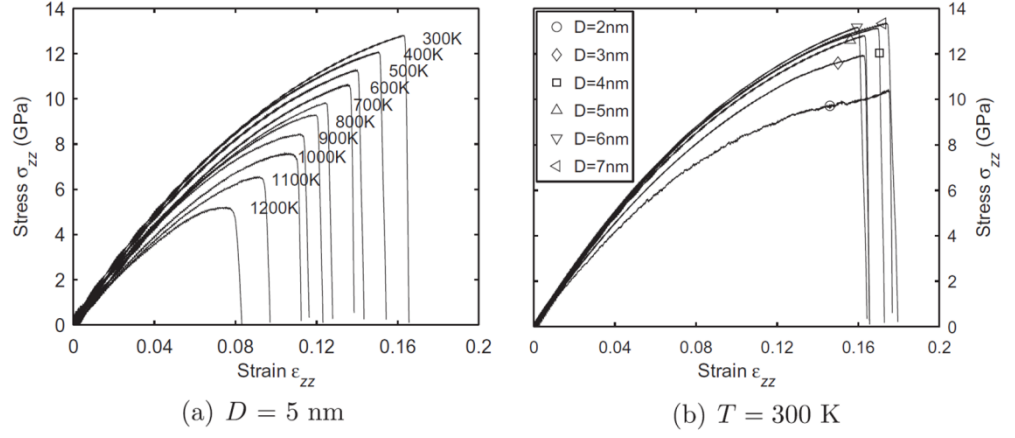


**Figure 2.29:** Graphs showing results of MD simulations: a) stress-strain curve for 5 nm Si NWs at different temperatures illustrating the decrease in stress as temperature increases; and b) tensile stress-strain curves for Si NWs of different diameters at room temperature. Reproduced from [228].

Using MD simulations, Wu *et al.* [217] also showed that the elastic modulus of Cu NWs decreases almost linearly with increasing temperature from 0–500 K [13] as shown in Figure 2.30.

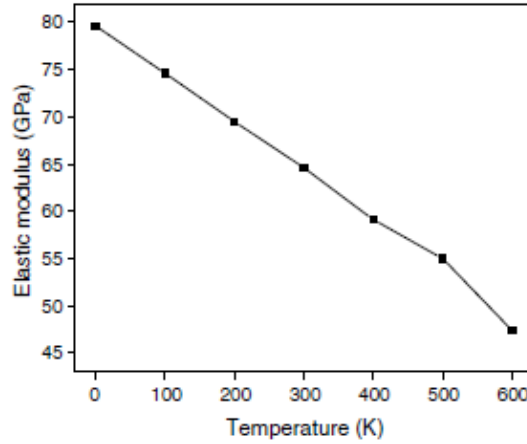


**Figure 2.30:** Variation in the Young's modulus of Cu NWs against temperature obtained using MD simulations. Reproduced from [217].



### 2.17.3 Temperature Effects

Kang *et al.* [228] carried out MD simulations to generate stress-strain curves for Si NWs at different temperatures to study the fracture strength of Si NWs as shown in Figure 2.31. The slope of the stress-strain curve at zero strain gives the Young's modulus of the Si NWs and has been observed to decrease with increasing temperature. Kang *et al.* also observed that Young's modulus decreases with decreasing diameter as illustrated in Figure 2.31 (b):

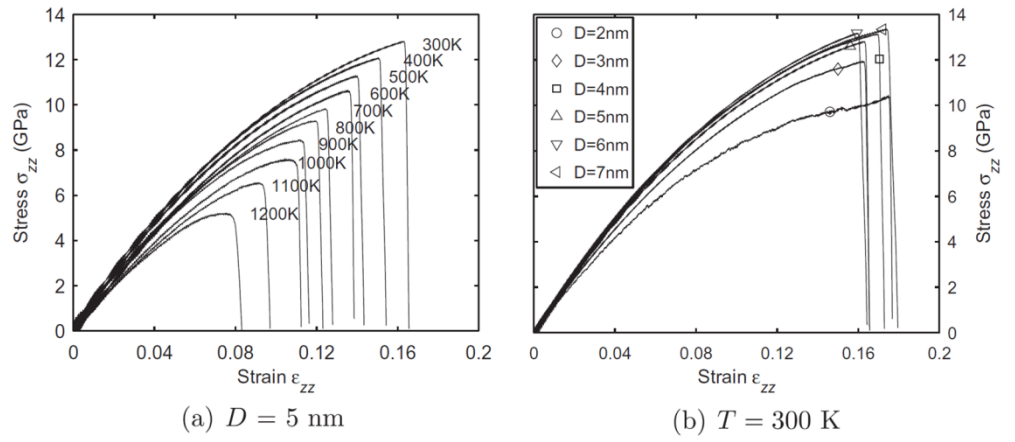


**Figure 2.31:** Graphs showing results of MD simulations: a) stress-strain curve for 5 nm Si NWs at different temperatures illustrating the decrease in stress as temperature increases; and b) tensile stress-strain curves for Si NWs of different diameters at room temperature. Reproduced from [228].

Using MD simulations, Wu *et al.* [217] also showed that the elastic modulus of Cu NWs decreases almost linearly with increasing temperature from 0–500 K [13] as shown in Figure 2.32.

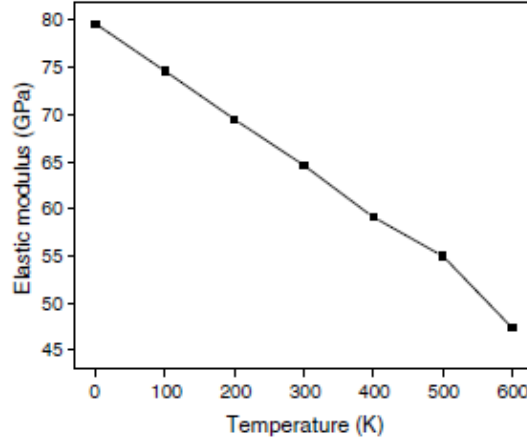


**Figure 2.32:** Variation in the Young's modulus of Cu NWs against temperature obtained using MD simulations. Reproduced from [217].

## 2.18 Thermal Conductivity of Silicon Nanowires

Thermal conductivity in materials is dominated by atomic vibrations: the transportation of random motion of thermal energy via phonons [229]. Thermal conductivity of materials depends in part on the mean free path of the phonons and at the nanoscale increases in scattering events (resulting in a shorter mean free path) reduce the thermal conductivity [54]. Fourier's law of heat conduction can be used to relate the heat flux,  $Q$ , as shown in Equation 2.16 [230].

$$Q = -k_t A \nabla T \quad \text{Equation 2.16}$$

where  $A(\text{m}^2)$  is the area,  $\nabla T$  is the local temperature gradient ( $\text{K} \cdot \text{m}^{-1}$ ) and  $k$  is thermal conductivity ( $\text{W} \cdot \text{m}^{-1} \cdot \text{K}^{-1}$ ) and is defined by Slack [231] in the Equation 2.17:

$$k_t = \frac{1}{3} C v \lambda' \quad \text{Equation 2.17}$$

Here  $C$  is the specific heat capacity ( $\text{J} \cdot \text{kg}^{-1} \cdot \text{K}^{-1}$ ),  $v$  is the speed of sound ( $\text{m} \cdot \text{s}^{-1}$ ) in the material and  $\lambda'$  (m) is the mean free path of phonons. The classical Equation 2.17

is valid for materials of thickness equal to or greater than the wavelength of phonons [232].

Silicon is the dominant semiconductor material in microelectronics and optoelectronics but the high thermal conductivity of bulk Si ( $142 \text{ W.m}^{-1}.\text{K}^{-1}$  [30–32]) prevents its use in thermoelectrics. As the physical properties of Si at the nanoscale are different from the bulk material, Si-based nanostructures also possess different thermal conductivity properties as reported in literature [66], [233]–[239]. At dimensions of less than the  $\lambda$  of phonons ( $\sim 300 \text{ nm}$  for Si at room temperature [54]), phonon scattering is strongly enhanced by a range of mechanisms such as boundary scattering [240] and interface scattering [241].

Thermal conductivity and thermal contact resistance can be measured by various characterisation techniques: scanning thermal microscopy [232], [242]–[245], four point probe method differential scanning calorimetry [228], [53], [233], [246] and the  $3\omega$  method [247], [245], [248].

In the laser flash method a sample is heated on one side with a laser pulse and the temperature rise is measured at the backside of the sample as a function of time [249].

Scanning thermal microscopy is a version of AFM (see details in Chapter 4) in which a cantilever tip scans the sample in contact mode [243]. Heat flow between the tip and the sample changes the temperature of the tip which is monitored to create a thermal image using a thermometer.

Differential scanning calorimetry is a technique which utilises a reference material of well-known thermal conductivity and tracks the changes in heat capacity,  $C_p$ , of the sample as a function of temperature [250]. The changes in  $C_p$  required to heat or cool the reference material are recorded as a function of heat flow.

The  $3\omega$  method is used as a characterisation technique to measure the thermal conductivity of thin dielectric films [248]. In this method, a single metal strip deposited on the specimen is used as both a heater and thermometer. Alternating current voltage is applied to excite the heater at a frequency  $\omega$  which heats the surface of the dielectric film at frequency  $2\omega$ . Since the resistance of metal increases

with temperature, the periodic heating generates temperature oscillations which in turn produce oscillations in the electrical resistance of the metal strip. The voltage drop across the metal strip has a small component at  $3\omega$  which can be used to measure the temperature oscillations and therefore the thermal response of the dielectric film and substrate [251].

Bux *et al.* [252] have reported the experimental thermal conductivity of nanostructured bulk Si (made of clustered nanoparticles) to be  $6.3 \text{ W.m}^{-1}.\text{K}^{-1}$  at room temperature using the laser flash method. Boukai *et al.* [253] reported a very low value of thermal conductivity ( $0.76 \text{ W.m}^{-1}.\text{K}^{-1}$ ) at room temperature for 10 nm diameter Si NWs. They measured  $k'$  by applying a thermal load across the ends of the NW via current and thermoelectric voltage was recorded as a function of temperature difference. Hochbaum *et al.* [236] found that surface roughness has a significant effect on the thermal conductivity of NWs and reported thermal conductivity to be  $1.6 \text{ W.m}^{-1}.\text{K}^{-1}$  at room temperature for 52 nm diameter Si NWs with rough or porous surfaces. Zhang *et al.* [233] have extensively investigated the dependence of thermal conductivity on the surface morphologies of rough and porous Si NWs fabricated using a metal-assisted chemical-etching method. In this method an electrochemical reaction takes place between the semiconductor surface, hydrofluoric acid and hydrogen peroxide in the presence of a noble metal which can result in different surface morphologies. They measured the thermal conductivity with the laser flash technique (see Figure 2.33) and differential scanning calorimetry reporting that surface morphologies have significant effect on the thermal conductivities at the nanoscale. Silicon NWs were grown on both sides of etched p-type and n-type Si wafers to form sandwich-structured composites (SSCs) [233]:

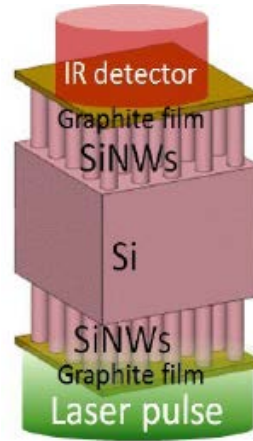


**Figure 2.33:** Sandwich-structured composites (SSCs) of SiNWs/Si/SiNWs grown on both sides of a Si wafer by etching. Conduction of heat introduced by the laser pulse was detected on the opposite side of the SSC as shown. Reproduced from [233].

The thermal conductivity of porous Si NWs measured with this technique was lower than for the rough Si NWs and Zhang *et al.* [233] attributed this due to phonon boundary scattering and pore-interface phonon scattering. Thermal conductivity of Si NWs were found to decrease with increasing etch time which also increased the NW length and surface roughness. For p-type Si NWs, pores or rough surfaces achieved with different etch time of 30 and 120 min, demonstrated thermal conductivities of 12.06 and 13.50  $\text{W.m}^{-1}.\text{K}^{-1}$ , respectively [233]. For an etching time of 240 min, thermal conductivity of n-type SSC and p-type SSC was reported to be 37.69 and 7.12  $\text{W.m}^{-1}.\text{K}^{-1}$ , respectively. These measured values are lower than the thermal conductivity of lightly doped n-type and highly doped p-type bulk Si having 122.8 and 81.47  $\text{W.m}^{-1}.\text{K}^{-1}$ , respectively [233]. Furthermore, the thermal conductivity of rough n-type and porous p-type Si NWs was found to decrease with increasing etch time and for 240 min etch time was reported as low as 8.48 and 1.68  $\text{W.m}^{-1}.\text{K}^{-1}$ , respectively [233].

### 2.18.1 Thermal Conductivity of Silicon Dioxide

Silicon dioxide ( $\text{SiO}_2$ ) thin films have excellent physical and electrical properties for gate insulators compared to the bulk form and are regarded as an important dielectric material in advanced semiconductor technologies [254]. Thermal conductivity measurements on thin  $\text{SiO}_2$  films have been a subject of intense research driven by the miniaturisation of electronic devices [40–44] as heat transportation by conduction in  $\text{SiO}_2$  used as an insulating film in integrated circuits affects the device stability and performance [52].

The thermal conductivity of  $\text{SiO}_2$  layers depends on the method of fabrication [232]. These methods include thermal oxidation, sputtering, chemical vapour deposition (CVD), low pressure CVD and plasma-enhanced CVD [232].

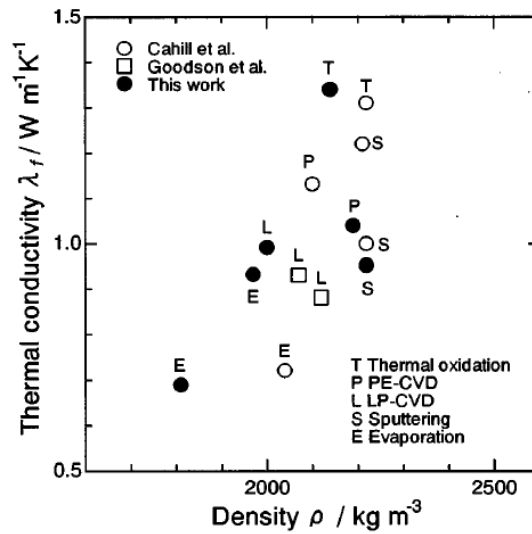


**Figure 2.34:** Thermal conductivity dependence of  $\text{SiO}_2$  films on different preparation techniques. Reproduced from [247].

The different processes result in different atomic densities of  $\text{SiO}_2$  and affect thermal conductivity as shown in Figure 2.34 and summarised in Table 2.3[255].

**Table 2.3:** Properties of SiO<sub>2</sub> films on Si substrates. Reproduced from [255].

Preparation	Conditions	Thickness (nm)	Refractive Index at 675 nm	Density (Kg.m <sup>-3</sup> )
Thermal Oxidation	Source-Atmosphere containing O <sub>2</sub> and H <sub>2</sub> O  Temperature-1100 °C	50-1000	1.46	2140
PE-CVD	Source- Si(OC <sub>2</sub> H <sub>5</sub> ) <sub>4</sub> , Temperature- 450 °C	50-520	1.46	2100
Low-pressure CVD	Source- Si(OC <sub>2</sub> H <sub>5</sub> ) <sub>4</sub> , Temperature- 700 °C	470	1.44	2000
Sputtering	Method- rf magnetron sputtering	20-580	1.47	2220
Ion-planting evaporation	Method- rf magnetron sputtering	1000	1.46	1970
EB evaporation	Method- rf magnetron sputtering	600	1.45	1810

Thermal conductivity of nanoscale thin SiO<sub>2</sub> films is substantially lower than the bulk which is 1.4 W.m<sup>-1</sup>.K<sup>-1</sup> at room temperature [52]. Callard *et al.* [232] measured the thermal conductivity of SiO<sub>2</sub>-Si system by scanning thermal microscopy and from this experimental data  $k_{\text{eff}}$  for SiO<sub>2</sub> films thickness of 50–1000 nm was extracted using FE modelling. Their reported modelling results were that  $k_{\text{eff}}$  decreases with reducing thickness as shown in Figure 2.35. Using Equation 2.17 an

intrinsic thermal conductivity and resistance of 1000 nm SiO<sub>2</sub> were calculated to be  $1.31 \pm 0.11 \text{ W.m}^{-1}.\text{K}^{-1}$  and  $6.8 \pm 0.35 \times 10^{-8} \text{ m}^2.\text{K.W}^{-1}$ , respectively [232].

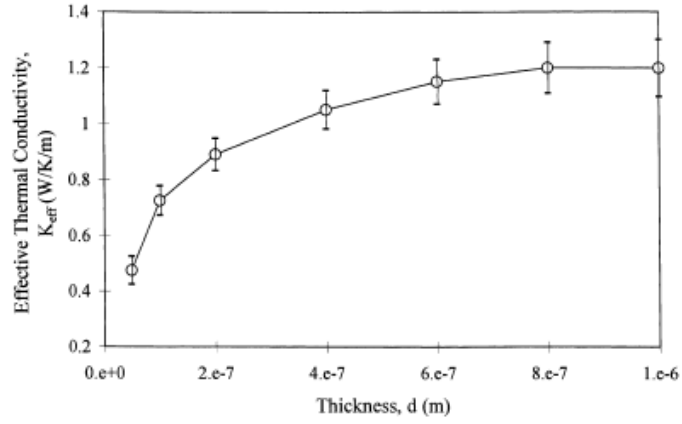


**Figure 2.35:** Dependence of effective thermal conductivity on thickness of SiO<sub>2</sub> films obtained from FE modelling. Reproduced from [232].

Tsuneyuki *et al.* [247] used the  $3\omega$  method to measure the thermal conductivity of SiO<sub>2</sub> thin films prepared by different procedures. The thermal conductivity of SiO<sub>2</sub> as a function of  $d$  is shown in Figure 2.36 from their work. The thermal conductivity of SiO<sub>2</sub> decreased significantly below a thickness of 250 nm and was found to be independent of the growth process below a thickness of 150 nm [247].



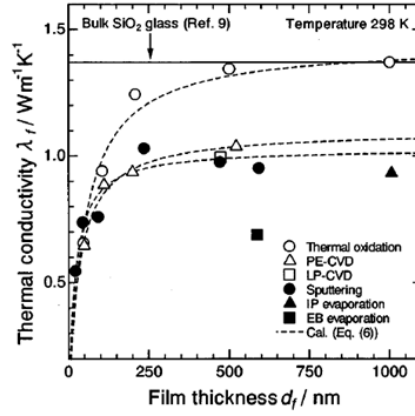


**Figure 2.36:** Thermal conductivities of SiO<sub>2</sub> films as a function of film thickness,  $d$ , measured using the  $3\omega$  method. The solid line indicates the bulk value. Reproduced from [247].

A wide range of values for thermal conductivity for Si NWs has been reported in the literature which are significantly different from bulk Si. The values were found dependent on the diameter and surface morphologies of the NWs. Silicon NWs used in the experiments reported in this work were typically of 50 nm and had a passive oxide (SiO<sub>2</sub>) layer of 2–4 nm. The thermal conductivities of 48 nm and 52 nm diameter, rough Si NWs, has been reported to be 1.6 W.m<sup>-1</sup>.K<sup>-1</sup> [233] and 1.2 W.m<sup>-1</sup>.K<sup>-1</sup> [256], respectively. The thermal conductivity of SiO<sub>2</sub> on the nanoscale were also found to have a significant difference from bulk value of 1.4 W.m<sup>-1</sup>.K<sup>-1</sup> [52] and found to be thickness dependent which tends to decrease for film thickness below 250 nm [247]. Thermal conductivity of SiO<sub>2</sub> for 8.5 nm and 2 nm thick SiO<sub>2</sub> film found to be 0.4 W.m<sup>-1</sup>.K<sup>-1</sup> [242] and 0.2 W.m<sup>-1</sup>.K<sup>-1</sup> [257], respectively.

## 2.19 Summary

A literature review is presented in this chapter 2 covering basic crystallography, defects in solids, amorphisation and recrystallisation mechanisms specifically in Si. A review of ion irradiation damage in NWs is presented with a particular emphasis on ion-beam-induced bending phenomena. Hamaker constant to calculate VDW

attraction of the NWs with the TEM support grid has been discussed in detail. Also were of interest the mechanical and thermal properties of Si NWs and SiO<sub>2</sub> as an input parameter for FE modelling of NWs.

## **3 Experimental Methods**

### **3.1 Introduction**

TEM has been a versatile instrument for the characterisation of materials at the micro and nano scale since its invention in 1931 [258]. Ion-beam-induced irradiation effects in materials have been widely studied and characterised using TEM. This chapter deals with the sample preparation, instrument construction, experimental techniques and software that have used to obtain experimental results for this thesis.

### **3.2 Sample Preparation**

Commercially available polydispersed Si NWs were obtained from Sigma Aldrich, UK (product number 731498). The polydispersed NWs were selected as they offer a variety of different lengths and diameters. The NWs were supplied in powder form and deposited onto TEM grids by the method described below.

The Si NWs were suspended in ethanol by agitating in an ultrasonic bath for ~90 minutes until the NWs were evenly dispersed in the solution. The solution was deposited onto 400 hexagonal-mesh Mo TEM grids using a syringe. The samples were left at room temperature until the ethanol had evaporated leaving the NWs adhered to the Mo grid via the Van der Waals forces. Samples were then loaded into a TEM holder for characterisation and irradiation. Two TEM sample holders were used in the irradiation experiments: a Gatan heating holder model 652; and a JEOL rotation holder model EM–BSR. Silicon NWs samples were screened using a JEOL JEM-2000FX TEM and NWs of different lengths and diameters were observed typically ranging from 1–5  $\mu\text{m}$  in length and 20–100 nm in diameter.

The reason to choose the Mo grid rather than a conventional copper grid in these experiments was due to the following facts that at high temperatures: migration of carbon atoms into Si may change the electrical and mechanical properties of the Si; carbon atoms form blobs on the surface of Si NWs which may change the surface physics; carbon atoms could stick with the tantalum washers of the heating holder due to which sample may stuck.

When selecting a NW for an experiment, three criteria had to be met in addition to it having the required length and diameter: it had to be attached to the grid at only one end so it would be free to exhibit any ion-beam-induced bending; it had to be located in a position on the grid so as to allow it to be manipulated into a suitable orientation relative to the ion beam using the TEM goniometer and sample holder; and it had to be free of obstructions such as the grid and other NWs so as to avoid ion beam shadowing effects and to allow effective observation over a range of goniometer tilts to facilitate tomography.

### **3.3 Transmission Electron Microscopy**

In TEM, an electrons are generated using an electron source and accelerated through a high voltage. An electromagnetic condenser lens is used to manipulate the beam onto the sample. The beam then interacts with the sample and some of the electrons are transmitted through the sample. An objective lens forms a DP and image in its back focal plane and image plane, respectively. Depending on the mode of operation of TEM, either the DP or image can be selected and magnified by the intermediate lens. Finally, the projector lens performs a final magnification onto the detector. The detector is often a phosphor screen, a scintillator coupled to a charge-coupled device (CCD) or an electron sensitive film.

### **3.4 Physics of Electrons Moving in an Magnetic Field**

When an electron with velocity,  $\mathbf{v}$ , enters a magnetic field,  $\mathbf{B}$ , it experiences a Lorentz force,  $\mathbf{F}$ , given by Equation 3.1:

$$\mathbf{F} = q(\mathbf{v} \times \mathbf{B})$$

Equation 3.1

where  $q$  is the charge on an electron ( $e = 1.6 \times 10^{-19}$  C).

The direction of  $\mathbf{F}$  that an electron experiences in a magnetic field can be determined from the left-hand rule and is perpendicular to both  $\mathbf{v}$  and  $\mathbf{B}$ . In the left-hand rule, the Thumb points in the direction of  $\mathbf{F}$  acting on an electron when the index finger points in the direction of  $\mathbf{B}$  and the middle finger in the direction of  $\mathbf{v}$  as shown in Figure 3.1:

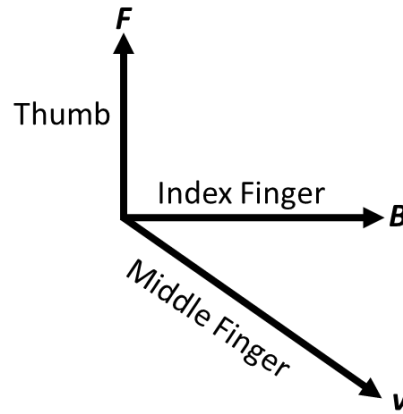


**Figure 3.1:** A vector diagram of a left-hand rule to determine the direction of the Lorentz force,  $\mathbf{F}$ , in a magnetic field,  $\mathbf{B}$ , acting on a charged particle moving with velocity,  $\mathbf{v}$ .

The force experienced by electrons moving with velocity,  $\mathbf{v}$ , in a magnetic field,  $\mathbf{B}$ , is given by Equation 3.2:

$$F = evB \sin \theta$$

Equation 3.2

When an electron enters the magnetic field at  $\theta = 90^\circ$ , Equation 3.2 becomes:

$$F = evB$$

Equation 3.3

The electrons move on a circular path when entering the magnetic field at  $90^\circ$  to  $\mathbf{B}$ . The centripetal force required to move an electron on a circular path of radius,  $r$ , is given by Equation 3.4:

$$\mathbf{F} = \frac{m\mathbf{v}^2}{r} \quad \text{Equation 3.4}$$

Combining Equation 3.3 and Equation 3.4, it is possible to calculate the radius when the electron is acted on by the Lorentz force:

$$r = \frac{m\mathbf{v}}{e\mathbf{B}} \quad \text{Equation 3.5}$$

When  $\mathbf{v}$  of electrons is perpendicular to  $\mathbf{B}$ , they move in a circular path and motion of electrons in  $\mathbf{B}$  is shown in Figure 3.2. The situation is different when electrons travel in  $\mathbf{B}$ , with  $\mathbf{v}$  at some angle,  $\theta$ , then  $\mathbf{v}$  of the electrons can be separated into x and y components,  $\mathbf{v}_x$ , and  $\mathbf{v}_y$ , as shown in Figure 3.2. The force acting along component  $\mathbf{v}_x$  (parallel to  $\mathbf{B}$ ) is zero while force along  $\mathbf{v}_y$  (perpendicular to  $\mathbf{B}$ ) change in time as direction of  $\mathbf{v}$  changes in  $\mathbf{B}$  and cause the electrons to move in spiral path. The force experienced by the electrons entering  $\mathbf{B}$  with  $\mathbf{v}$  at an angle  $\theta$  in a TEM column results in a spiral (helical) path moving along the z-axis as illustrated in Figure 3.3:

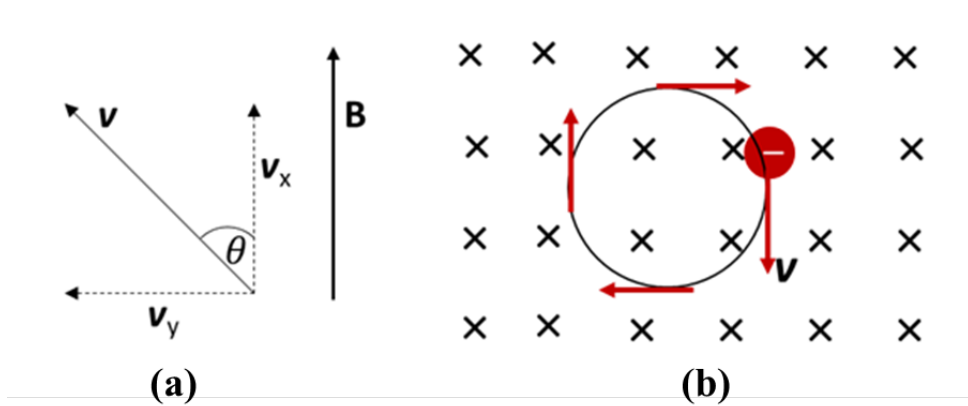


**Figure 3.2:** Schematics showing: (a) a breakdown of the velocity vector,  $\mathbf{v}$ , into its components,  $\mathbf{v}_x$ , and  $\mathbf{v}_y$  with the direction of the magnetic field,  $\mathbf{B}$ , parallel

to  $v_x$ ; (b) an electron with  $v_y$  entering in  $\mathbf{B}$  (into paper) following a circular motion. The direction of the force acting on the electron has been found from left hand rule.

In a TEM, electrons are accelerated through a voltage,  $V$ , gaining kinetic energy (KE),  $E$ . The potential difference (eV) is related to the KE given in Equation 3.6:

$$E = eV = \frac{mv^2}{2} \quad \text{Equation 3.6}$$

where  $m$  is the mass of the electron and  $v$  is the velocity.

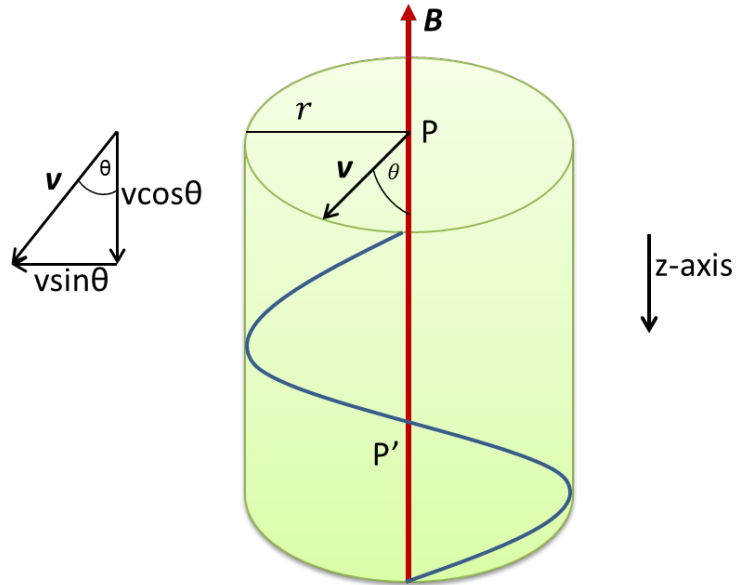


**Figure 3.3:** Schematic of the trajectory of an electron with velocity,  $v$ , entering a homogenous magnetic field,  $\mathbf{B}$ , at an angle,  $\theta$ . The parallel and perpendicular components of  $v$  relative to  $\mathbf{B}$  are shown. In a TEM, electrons follow a helical path of radius,  $r$ , through magnetic field,  $B$ , entering through point  $P$  and exiting at  $P'$ . The  $z$ -axis indicates the optical axis of the TEM. Redrawn and adapted from [259].

The momentum,  $\mathbf{p}$ , given to the electrons moving with  $\mathbf{v}$  is given by Equation 3.7:

$$\mathbf{p} = m\mathbf{v} \quad \text{Equation 3.7}$$

Substituting  $\mathbf{v}$  from Equation 3.6 into Equation 3.7 gives:

$$\mathbf{p} = m\mathbf{v} = (2meV)^{1/2} \quad \text{Equation 3.8}$$

The wavelength of electrons accelerated through  $V$  can be calculated using Equation 3.9:

$$\lambda = \frac{h}{\mathbf{p}} = \frac{h}{(2meV)^{1/2}} \quad \text{Equation 3.9}$$

The accelerating voltage typically used in a TEM are from 80–400 keV. At 100 keV, the electrons move at  $\sim 50\%$  the speed of light,  $c$  ( $\sim 1.6 \times 10^8 \text{ m}^{-1}.\text{s}^{-1}$ ) and so the relativistic effects needs to be considered. To account for relativistic effects, rest mass,  $m_0$ , have to be used to calculate  $\lambda$  and Equation 3.9 is modified to Equation 3.10 below:

$$\lambda = \frac{h}{[(2m_0eV)(1 + \frac{eV}{2m_0c^2})]^{1/2}} \quad \text{Equation 3.10}$$

A typical wavelength of 100 keV and 200 keV electrons in TEM is  $3.70 \times 10^{-12} \text{ m}$  and  $2.51 \times 10^{-12} \text{ m}$ , respectively.

### 3.4.1 Deflection of Electron Beam

Magnetic fields are used to shift and tilt the electron beam relative to the optical axis in TEM. The angle of deflection,  $\varepsilon$  (using small angle approximation), in  $\mathbf{B}$  acting over a length,  $L$ , can be obtained by the Equation 3.11:



$$\varepsilon = \frac{eLB}{mv} \quad \text{Equation 3.11}$$

where  $L$  (m) is the length of path in  $\mathbf{B}$  (T) of the current carrying coil to deflect an electron beam [259].

### 3.5 Introduction to Elastic Scattering

A collision between two bodies in which total kinetic energy is conserved is known as an elastic collision or scattering event. Electrons experience both elastic and inelastic scattering by the atoms in the sample. In this section, the elastic scattering is described.

#### 3.5.1 Interaction Cross-Section

The interaction cross-section,  $\sigma$ , is the probability of an electron undergoing a scattering event with an atom. A large interaction cross-section means that an atom presents a larger target to the electrons and thus it is more likely to scatter them. The  $\sigma$  for a single isolated atom is defined in Equation 3.12 with an effective radius,  $r$  (m):

$$\sigma_{atom} = \pi r^2 \quad \text{Equation 3.12}$$

where  $\sigma_{atom}$  is measured in units of  $\text{m}^2$ .

There are two types of interaction cross-section: the nuclear cross-section ( $r = r_{\text{nuc}}$ ) and the electronic cross-section ( $r = r_{\text{elec}}$ ). These cross-sections depend on the energy of the incident electrons, atomic weight of the target atom,  $Z$ , and the angle of scatter,  $\theta$ . The elastic scattering radius,  $r$ , of a single atom for these two types of scattering have the following form:

$$r_{\text{nuc}} = \frac{Ze}{V\theta} \quad \text{Equation 3.13}$$

and

$$r_{\text{elec}} = \frac{e}{V\theta} \quad \text{Equation 3.14}$$

From Equation 3.13 and Equation 3.14, it can be seen that  $\sigma_{\text{atom}}$  is a function of  $Z$ ,  $V$  and  $\theta$  for nuclear scattering and is a function of  $V$  and  $\theta$  for electronic scattering.

For higher-energy electrons, the probability of scattering decreases as electrons move more quickly through the same volume and thus are less likely to interact with the target atom. For higher  $Z$ , there is a greater probability of electron being scattered by a nucleus.

### 3.5.2 Differential Cross-Section

The interaction of the incident electron beam with a target scatters the electrons over a range of angles. The differential cross-section,  $d\sigma(\theta)/d\Omega$ , gives the probability of electron scattering at an angle  $\theta$  in per unit solid angle,  $\Omega$ . It is important as it also represents a measure of the proportion of the incident intensity scattered at an angle  $\theta$  per unit  $\Omega$ .

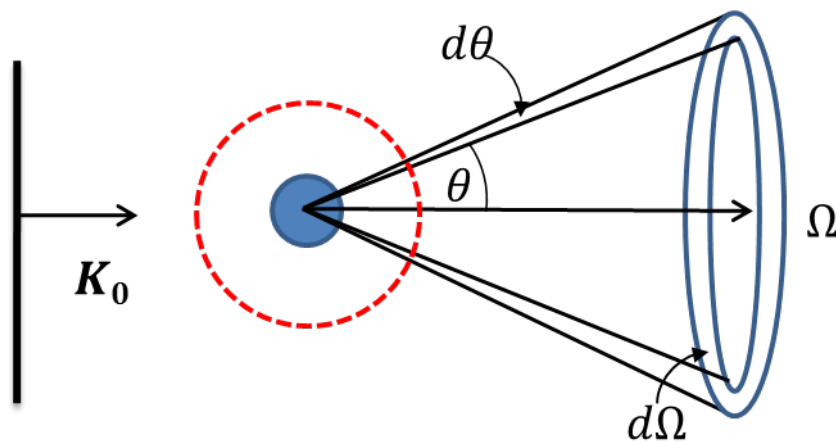


**Figure 3.4:** Schematic of a plane wave,  $K_0$ , interacting with an atom (blue circle) and scattered as a spherically wave (dashed red circle). Redrawn and adapted from [259].

The incident beam of wave vector,  $\mathbf{K}_0$ , interacting with a single atom with a scattering cross-section,  $\sigma(\theta)$ , is scattered at all angles in  $\Omega$  is shown in Figure 3.4. The relationship between a scattered angle,  $\theta$ , and  $\Omega$  is given by Equation 3.15:

$$\Omega = 2\pi (1 - \cos \theta) \quad \text{Equation 3.15}$$

Differentiating Equation 3.15 with respect to  $\theta$  gives:

$$d\Omega = 2\pi \sin \theta d\theta \quad \text{Equation 3.16}$$

For a single atom, the differential cross-section is given by:

$$\frac{d\sigma(\theta)}{d\Omega} = \frac{1}{2\pi \sin \theta} \frac{d\sigma}{d\theta} \quad \text{Equation 3.17}$$

As  $\theta$  varies from 0 to 180° (i.e. 0 to  $\pi$  radians),  $\sigma$  can be calculated by integrating Equation 3.17:

$$\sigma_{\text{atom}} = \int_0^\pi d\sigma = 2\pi \int_0^\pi \frac{d\sigma}{d\Omega} \sin \theta d\theta \quad \text{Equation 3.18}$$

### 3.5.3 Total Probability of Scattering

Equation 3.12 gives the  $\sigma_{\text{atom}}$  for a single isolated atom. If the specimen consists of  $N$  atoms per unit volume, the total cross-section is given by:

$$\sigma_{\text{total}} = N\sigma_{\text{atom}} \quad \text{Equation 3.19}$$

where  $N = \rho N_o / A$  and  $N_o$  is Avogadro's number (atoms.mole<sup>-1</sup>),  $\rho$  is the density (kg.m<sup>-3</sup>) and  $A$  is the atomic weight (kg.mol<sup>-1</sup>) of the scattered atom.

By substituting the value of  $N$  in Equation 3.19, the probability of scattering the electron beam with a sample of thickness,  $t$ , can be defined as shown in Equation 3.20:

$$\sigma_{\text{total}}t = \frac{N_o\sigma_{\text{atom}}}{A}(\rho t) \quad \text{Equation 3.20}$$

where  $\rho t$  defines the mass-thickness of the specimen.

### 3.5.4 Mean Free Path

Mean free path,  $\lambda'$ (m), is a measure of the average distance the electron travels between two successive collisions in a target. For an electron to experience only one scattering event, it is very important to have a thin sample. For thicker samples, the probability of more than one scattering event increases and this is termed plural or multiple scattering. The mean free path depends on the scattering cross-section of the atoms and is described in Equation 3.21:

$$\lambda' = \frac{1}{\sigma_{\text{total}}} \quad \text{Equation 3.21}$$

## 3.6 Atomic Scattering Factor

The atomic scattering factor,  $f(\theta)$ , relates the differential cross-section to the amplitude of the beam,  $|f(\theta)|$ . The square of  $|f(\theta)|$  gives the intensity of the electron beam,  $|f(\theta)|^2$ :

$$\frac{d\sigma(\theta)}{d\Omega} = |f(\theta)|^2 = \text{Intensity} \quad \text{Equation 3.22}$$

The differential cross-section relates the intensity of the scattered electron beam at an angle  $\theta$ . The scattering cross-section  $\sigma(\theta)$  and atomic scattering factor  $f(\theta)$  depend on wavelength,  $\lambda$ , scattering angle,  $\theta$ , and atomic mass,  $Z$ .

### 3.6.1 The Structure Factor

The scattered amplitude by a unit cell of a crystal structure is given by the structure factor,  $F(\theta)$ .  $F(\theta)$  is defined as the sum of  $f(\theta)$  (i.e. the scattering amplitude from individual atoms) over all the atoms in the unit cell. For a unit cell of  $n$  atoms with position coordinates  $(x, y, z)$ , the structure factor  $F(\theta)$  is defined by multiplying the exponential of the phase angle at the  $n^{\text{th}}$  atom in the unit cell,  $\psi_n$ , with the  $f(\theta)$ :

$$F(\theta) = \sum_{i=1}^n f_i(\theta) e^{i\psi_n} \quad \text{Equation 3.23}$$

The phase angle can be described by a dot product of the scattered wave vector,  $\mathbf{K}$ , from a single atom and the position vector,  $\mathbf{r}_n$  of the  $n$ th atom:

$$\psi_n = 2\pi \mathbf{K} \cdot \mathbf{r}_n \quad \text{Equation 3.24}$$

$$\begin{aligned} \psi_n = 2\pi \mathbf{K} \cdot \mathbf{r}_n &= 2\pi(h\mathbf{a}^* + k\mathbf{b}^* + l\mathbf{c}^*) \cdot (x_n\mathbf{a} + y_n\mathbf{b} + z_n\mathbf{c}) \\ &= 2\pi(hx_n + ky_n + lz_n) \end{aligned} \quad \text{Equation 3.25}$$

where  $h, k$  and  $l$  are the Miller indices,  $\mathbf{a}^*$ ,  $\mathbf{b}^*$  and  $\mathbf{c}^*$  are the reciprocal lattice vectors,  $\mathbf{a}$ ,  $\mathbf{b}$  and  $\mathbf{c}$  are the lattice vectors,  $x$ ,  $y$  and  $z$  are the fractional coordinates of the  $n^{\text{th}}$  atom.

Substituting  $\psi_n$  from Equation 3.25 into the Equation 3.23 gives the following expression for  $F(\theta)$ :

$$F_{hkl}(\theta) = \sum_i^n f_i(\theta) e^{2\pi i(hx_n + ky_n + lz_n)} \quad \text{Equation 3.26}$$

$F_{hkl}(\theta)$  gives the intensity of the  $hkl$  reflections and thus can be used to identify the forbidden reflections for which  $F_{hkl}(\theta) = 0$ .

### 3.7 Coherent Elastic-Scattering and Bragg's Law

When an electron does not lose any energy and maintains its phase after scattering by an atom, it is said to have undergone coherent elastic-scattering. This can be illustrated as shown in Figure 3.5 by considering a plane wavevector of an electron,  $\mathbf{K}_0$ , scattering at an angle  $2\theta$  forming a diffracted wavevector,  $\mathbf{K}_d$ .

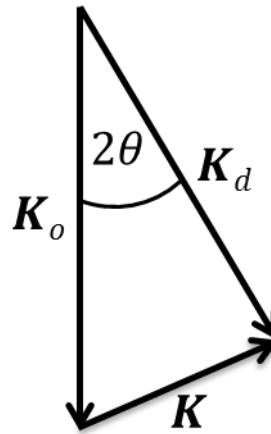


**Figure 3.5:** A vector diagram illustrating an incident wave vector,  $\mathbf{K}_0$ , diffracted wavevector,  $\mathbf{K}_d$ , and the resulting wavevector,  $\mathbf{K}$ , in going from  $\mathbf{K}_0$  to  $\mathbf{K}_d$ .

In the case of elastic scattering, the magnitude of the incident and diffracted wavevectors are the same and equal to the reciprocal of wavelength,  $\lambda$ .

$$\mathbf{K}_d = \mathbf{K}_0 + \mathbf{K} \quad \text{Equation 3.27}$$

Consider two atomic planes separated by a distance,  $d$ , as illustrated in Figure 3.6. Electrons in planewaves of wavelength,  $\lambda$ , are scattered at different planes at angle,  $\theta$ .

The wave travels an additional distance from point A to point B to point C compared to in Figure 3.6. Rearranging Equation 3.27:

$$\mathbf{K} = \mathbf{K}_d - \mathbf{K}_o$$

Equation 3.28

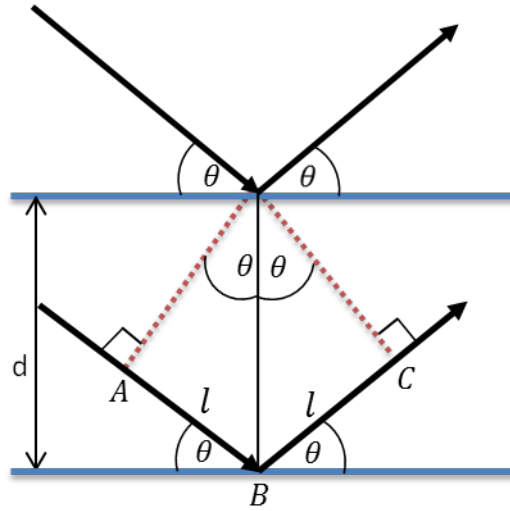


**Figure 3.6:** A schematic of plane wave scattered at an angle,  $2\theta$ , by atomic planes separated by a distance,  $d$ .

From trigonometry, it can be shown that  $AB = BC$  and the path difference between the two planes separated by  $d$  is given by:

$$AB = BC = d \sin \theta$$

Equation 3.29

$$AB + BC = 2d \sin \theta$$

Equation 3.30

Constructive interference occurs when the path difference between two beams is an integral multiple of the wavelength. The angle at which the scattered waves give rise to constructive interference is called Bragg angle,  $\theta_B$ , and diffraction occurs when the Bragg condition is (sufficiently) satisfied.

$$2d \sin \theta_B = n\lambda$$

Equation 3.31

### 3.7.1 Deviation Parameter ( $s_g$ )

It is possible to excite a reflection when the Bragg condition (Equation 3.31) is not exactly satisfied. In such a situation,  $\theta$  deviates from the perfect  $\theta_B$ , and a new vector is introduced to define the deviation from the perfect Bragg condition. This parameter is known as deviation parameter,  $s_g$ , as shown in the Figure 3.7.

$$\mathbf{K} = \mathbf{g} + \mathbf{s}_g \quad \text{Equation 3.32}$$

The wavevector,  $\mathbf{K}$ , is equal to the diffraction vector,  $\mathbf{g}$ , when  $s_g = 0$  – i.e. when the Bragg condition is exactly satisfied.

### 3.7.2 Incoherent Elastic-Scattering

In incoherent elastic-scattering, the particles do not lose energy but do change their phase relative to the incident beam. In fact, the incident electrons do lose some energy by transferring it to the target atom, but this energy loss is negligible. Thus, in incoherent elastic-scattering the electrons have the same wavelength and so they are scattered at the same Bragg angle,  $\theta_B$ .

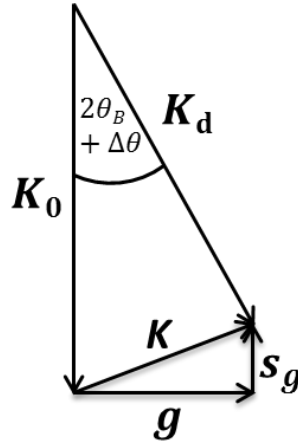


**Figure 3.7:** Vector diagram for diffraction deviating from the perfect Bragg angle,  $\theta_B$ , by  $\Delta\theta$  showing the deviation parameter,  $s_g$ .



When  $\mathbf{s}_g \neq 0$ , the Bragg condition is not satisfied and  $\mathbf{K} \cdot \mathbf{s}_g$  is positive or negative when  $\theta > \theta_B$  and  $\theta < \theta_B$ , respectively.

### 3.7.3 Kikuchi Lines

The spots in a DP are formed by the coherently elastically scattered electrons from sets of atomic planes which are on or close to their respective Bragg conditions. Incoherent elastically scattered electrons can be diffracted by planes with which they satisfy the Bragg condition but these electrons do not share a common incident direction. In this case, constructive interference occurs in two cones termed Kossel cones (see Figure 3.8). The intersection of these cones with the back focal plane of the objective lens creates slight parabolas which are visible in the DP and these are termed Kikuchi lines.

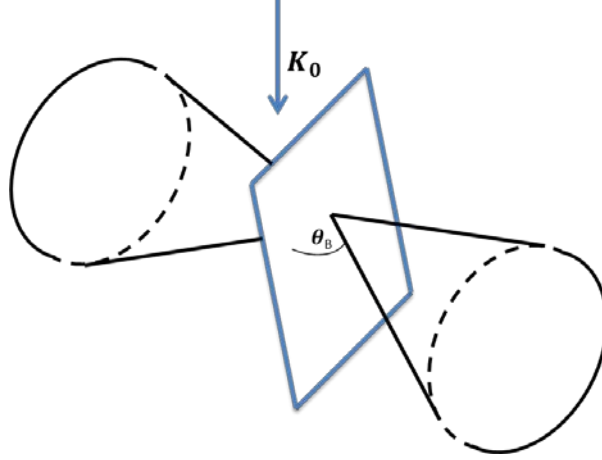


**Figure 3.8:** Incoherently elastically scattered electrons diffracting at the Bragg condition forming a pair of Kossel cones. Adapted from [259].

### 3.7.4 Ewald Sphere

The Ewald sphere is a geometrical construction in reciprocal space (i.e. in which the lattice vectors are the reciprocal of inter-planar spacing) with a radius equal to the reciprocal of the electron wavelength. Where the sphere intersects reciprocal lattice points corresponds to the reflections seen in the DP. However because dimensions in

reciprocal space are the inverse of real space dimensions, the reciprocal lattice points are elongated in the direction in which the TEM sample is thin. This elongated “points” are termed relrods.

As shown in Figure 3.9, the wavevectors  $\mathbf{K}_0$  and  $\mathbf{K}_d$  extend from the centre of Ewald sphere, C, to point O which is the origin of the reciprocal lattice. Tilting the sample or the electron beam rotates the reciprocal lattice relative to the Ewald sphere, changes the intersection of the two and hence the DP.

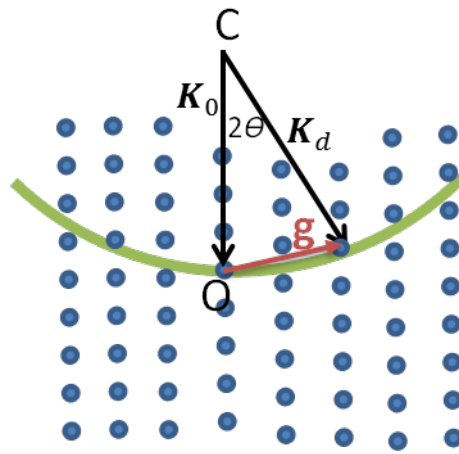


**Figure 3.9:** Construction of Ewald sphere with incident beam,  $\mathbf{K}_0$ , and Bragg diffracted beam,  $\mathbf{K}_d$ , forming an angle of  $2\theta_B$ .

### 3.8 Electron Sources

Two types of electron sources can be used to generate electrons in a TEM: a thermionic source or a field emission gun (FEG). Thermionic sources normally emit from a tungsten (W) filament or lanthanum hexaboride ( $\text{LaB}_6$ ) crystal which is heated using electrical current. The electrons leave the tip of the source when sufficient thermal energy is provided to overcome the work function of the material and are accelerated by the positive potential down the column. A negative voltage is applied to an electrostatic lens called a Wehnelt cap. A FEG source uses an electric field to extract electrons by establishing a high potential difference between emitter

and the electrode. A FEG source is more expensive than thermionic source but offer greater brightness, coherence and longer lifetimes than thermionic sources [259].

### 3.8.1 Wehnelt Cap

The Wehnelt cap was invented by a German physicist Arthur Rudolph Berthold Wehnelt in 1902 [260] and performs the extraction from the filament. The Wehnelt cap is an electrostatic lens surrounding the electron source and condenses the extracted electrons emitted from the filament. The purpose of the Wehnelt cap is to focus and control the electrons. A negative bias is applied to the Wehnelt relative to the filament and makes a first crossover of the electron beam in a TEM above the anode and focuses the electron beam into the condenser lens system. The anode then accelerate the electrons to high velocities. A schematic of the filament, Wehnelt cap and anode is shown in Figure 3.10:

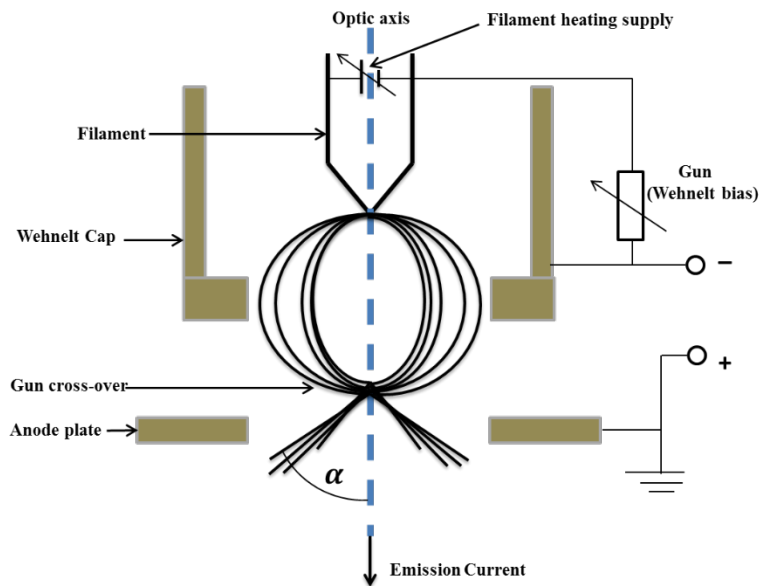


**Figure 3.10:** Schematic of the filament, Wehnelt cap and anode for a tungsten thermionic electron source (redrawn from [259]).

### 3.9 Electromagnetic Lens in TEM

In a TEM, the electromagnetic lenses are made of soft iron poles composed of many small copper windings. A strong  $\mathbf{B}$  is produced in these lenses by applying a current through the copper windings. The magnetic field act as a convex lens in TEM and bring the electrons back to the optic axis. Traditional optical lenses have a fixed focal length,  $f$  (i.e. the distance from centre of lens to the crossover where the rays meet on the optic axis after passing through the lens is called focal length,  $f$ ) but in electromagnetic lenses  $f$  can be varied by changing the current. A typical electromagnetic lens used in a TEM is shown in Figure 3.11:

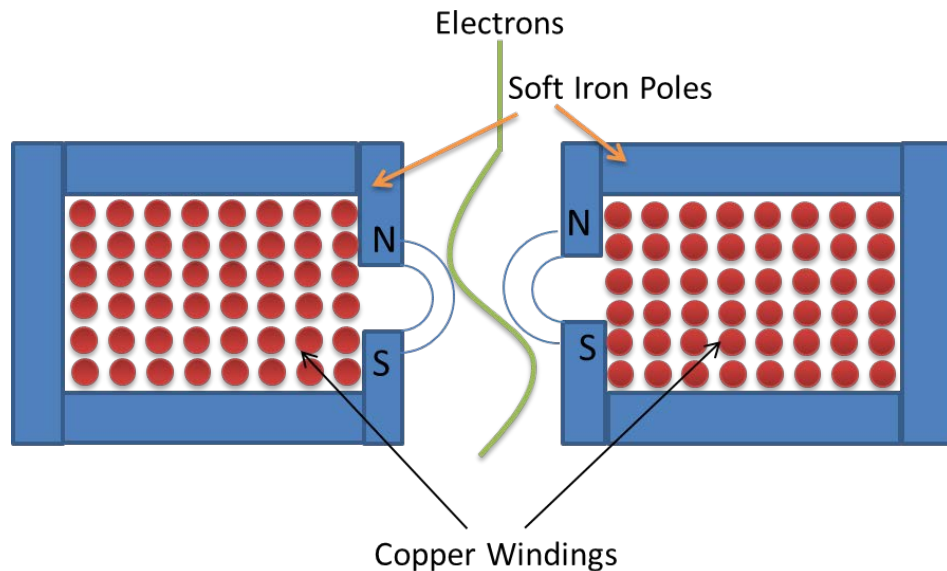


**Figure 3.11:** Schematic cross-section of an electromagnetic lens used in a TEM. Redrawn from [259].

After being generated, the electron beam passes through the lens system of the TEM column. Electromagnetic lenses are used in a TEM to modify the path of electrons and focus the electron beam through the sample and onto a detection device. There are a number of lenses in a typical TEM column (see Figure 3.12) and these are described below.

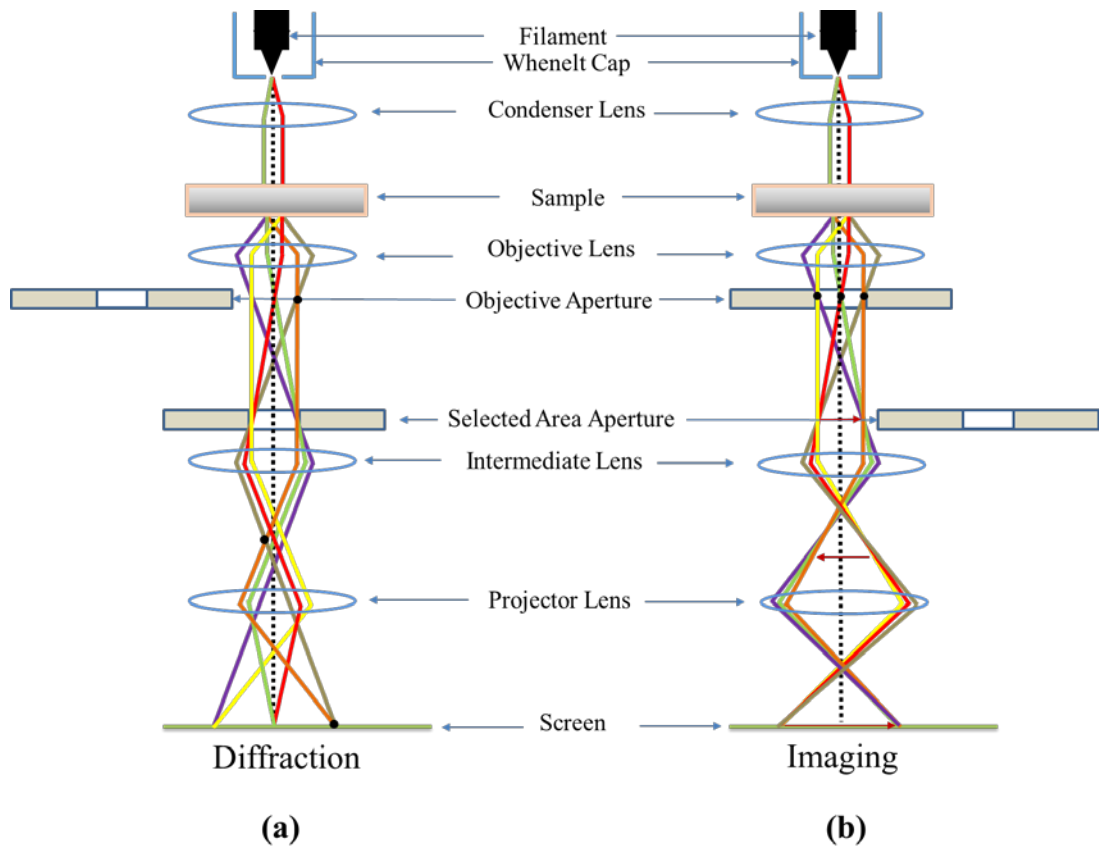


**Figure 3.12:** Schematic ray diagrams for a TEM operating in (a) diffraction mode and (b) imaging mode. Redrawn from [259].

### 3.9.1 Condenser lens

The main purpose of the condenser lens system ( $C_1$ ,  $C_2$  and  $C_3$ ), in a TEM is to focus the electrons and control the spot size at sample position. This also allows the area of illumination to be adjusted to give the required intensity at different magnifications. The range of rays gathered by a condenser lens are described by a semi-angle,  $\beta$ , which are converged at a point on the optical axis making a convergence semi-angle,  $\alpha$ , as shown in Figure 3.13.

The condenser lens  $C_1$  is used to form a crossover of electron beam existing the Whenelt cap and control the spot size (diameter of the beam). Strong  $C_1$  is used to

make to small probe size at the sample while weak  $C_1$  produce large spot size at the sample and is shown in Figure 3.14. When The  $C_2$  lens is used to adjust the illumination or brightness of the electron beam at the sample. The condenser lens  $C_3$  is used to control the  $\alpha$  and allow a near parallel condition on the sample position, a condition when beam is coherent and produce good quality images with best contrast and DP.

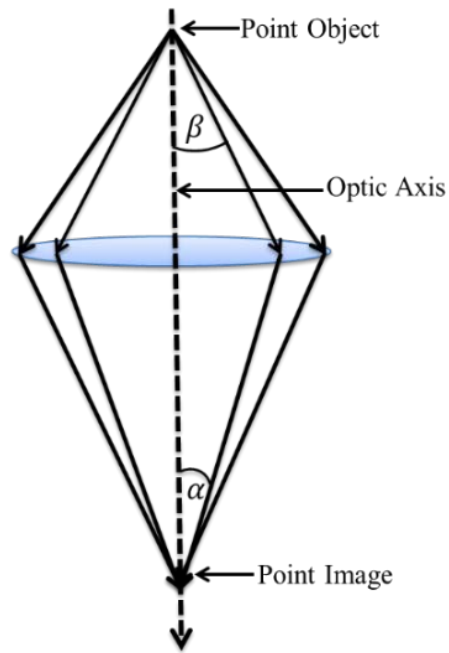


**Figure 3.13:** Schematic ray diagram for a single condenser lens showing the collection semi-angle,  $\beta$ , and convergence semi-angle,  $\alpha$ . Redrawn from [259].

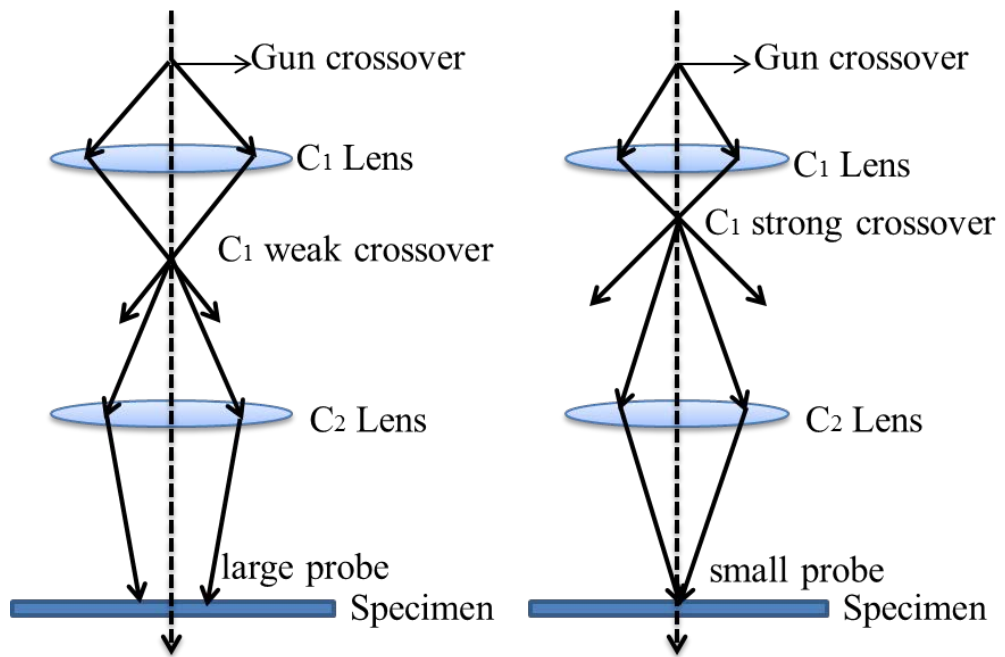


**Figure 3.14:** Schematic ray diagram of a double-lens condenser system: (a) weak condenser lens forms a broader probe on the specimen, (b) strong condenser lens makes a sharper probe on the specimen. Redrawn from [259].

### 3.9.2 Objective Lens

The objective lens is considered to be the most critical lens of the TEM optics and is the primary imaging system which focuses the electrons exiting the bottom of the sample and generates a DP and an image. The objective lens forms a DP on its back focal plane and an image on an image plane. The image is underfocused when the object plane of the objective lens is above the sample and overfocused when it is below. All lenses after the objective lens in the TEM column are used to subsequently magnify the output of the objective lens.

### 3.9.3 Intermediate Lenses

The intermediate lens system in a TEM magnifies the image and DP formed by the objective lens and works in two modes. In diffraction mode, the lens is focused on the back focal plane of the objective lens where the DP is formed. In imaging mode,

the image plane of the objective lens becomes the object plane of the intermediate lens which then magnifies the image.

### 3.9.4 Projector Lens

Projector lens focuses at the back focal plane of the intermediate lens as an object plane and project the images or DP onto the device used for electron detection.

### 3.10 Deflectors

Deflectors in a TEM are used to deflect the electron beam relative to the optical axis. Deflectors are often made up of pairs of electromagnets as shown in Figure 3.15. There are normally four such pairs in a deflector to allow the electron beam to be tilted and shifted in the  $x$  and  $y$  directions. The pole pieces have a curved geometry to provide a uniform magnetic field. For example, the condenser deflectors are used to tilt and shift the electron to control the position and incidence angle at the sample position.

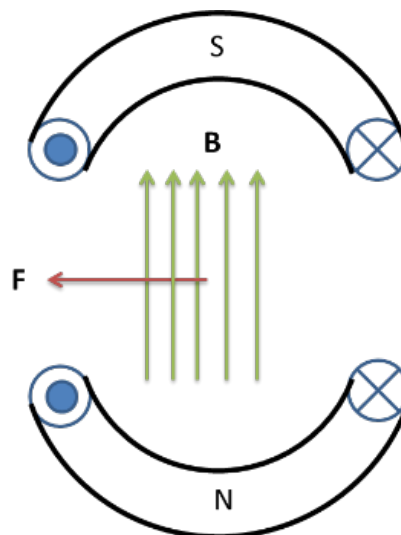


**Figure 3.15:** Schematic top-down view of a deflector illustrating the direction of the magnetic field,  $\mathbf{B}$  (green) and magnetic force,  $\mathbf{F}$  (red) while the direction of



*the electron beam is into the paper. The windings of the coil are shown in blue. Redrawn from [259].*

To shift the beam, the beam is first deflected by some angle,  $\phi$ , and then by an equal and opposite angle to deflect it back such that final beam is moved relative to the specimen without changing  $\phi$ .

To tilt the beam, the first set of deflectors change the direction of the beam by an angle  $\phi$  and the second set of deflectors brings the beam back to optical axis by applying twice the deflection – i.e.  $2\phi$  [4]. In order to move the beam across the sample without changing the angle of incidence or to tilt the beam without changing the position on the sample, careful alignment of deflection coils is necessary by setting the pivot points as discussed in section 3.10.1. The schematic of beam shift and tilt is shown in Figure 3.16:

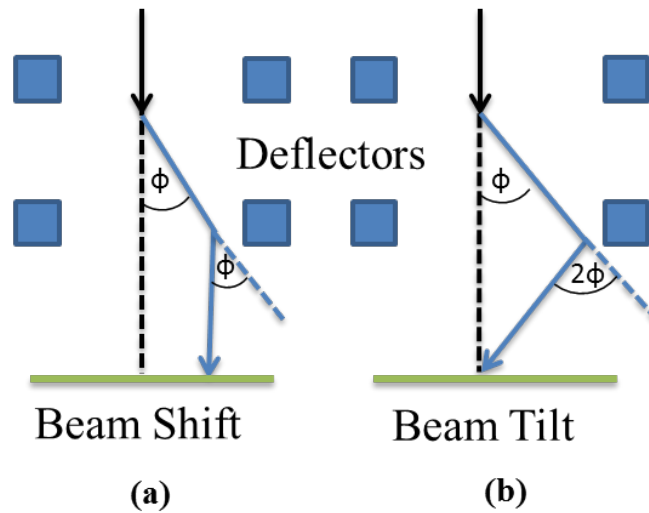


**Figure 3.16:** Schematics demonstrating the use of condenser deflectors to (a) shift and (b) tilt the electron beam onto the specimen. Black dashed line shows the incident electron beam along the optical axis.

### **3.10.1 Pivot Points**

Pivot points play an important part in TEM alignment through a pair of deflection coils. The electron beam shift and tilt procedures are decoupled from each other and hence a pure shift and pure tilt can be obtained in TEM by setting the pivot points such that electron beam pivots at those points analogous to seesaw. If the pivot points are not adjusted the two beams are separated laterally onto the phosphorous screen. Pivot shift points and tilt points are adjusted by deflecting the electron beam with wobbler and minimising the movement in diffraction and image mode, respectively. A wobbler is a mechanism in which an electron beam switched rapidly back and forth between the negative and positive voltage applied to deflector coils or simply the alternating current [261].

### **3.10.2 Voltage and Current Centring**

The fluctuations added in the objective lens current or accelerating voltage of TEM distorts the image (i.e. spirally enlarges and shrinks). The centre of this image distortion is known as objective current and accelerating voltage centre. These effects can be adjusted by bringing back the objective current centre and accelerating voltage centre along the optical axis with the help of double deflectors. Due to the small fluctuations in the objective lens current this alignment is not normally performed. Although small fluctuations in high voltage in TEM are small ( $<10^{-6}$ ) in TEM, accelerating voltage centre is aligned for optimum imaging [259].

## **3.11 Astigmatism**

Astigmatism arises from non-uniformity in a magnetic lens caused by machining defects of the soft-iron pole pieces which can result in imperfections in the cylindrical symmetry down the bore. Contamination is another source of astigmatism which is mainly due to hydrocarbons and sputtered material on the aperture diaphragm and other surfaces which can charge up producing a localised electric field to deflect the electron beam. Other factors which could induce stigmatisms are

the sample contamination and magnetic samples. Condenser astigmatism causes the electron beam on the sample to deviate from a perfect circle. Objective astigmatism results in preferential magnification of the image in certain directions and thus induces distortion. In the TEM this problem is reduced by the use of stigmators. The radius,  $r_{\text{ast}}$ , can be defined by Equation 3.33.

$$r_{\text{ast}} = \beta \Delta f \quad \text{Equation 3.33}$$

where  $\Delta f$  is the change in focal length.

### 3.12 Stigmators

Stigmators are small octupoles which are used to rectify the astigmatism (i.e. electrons experience a non-uniform  $\mathbf{B}$  and are preferentially deflected) induced in a TEM either due to the defects at the time of manufacturing of the polepieces of the magnetic lenses, apertures or even contamination which can build-up the electrostatic charge. Stigmators are used both in the condenser lens and in the objective lens. The condenser stigmator provides compensating field to make a uniform  $\mathbf{B}$ . Astigmatism produce streaking effects and due to objective astigmatism the shape of the beam distorts from circle to oval or ellipsoidal. Objective stigmator finally align the deflected beam onto the optic axis and it converges to a perfect circle. The typical octupoles stigmator used in many TEMs is shown in Figure 3.17:

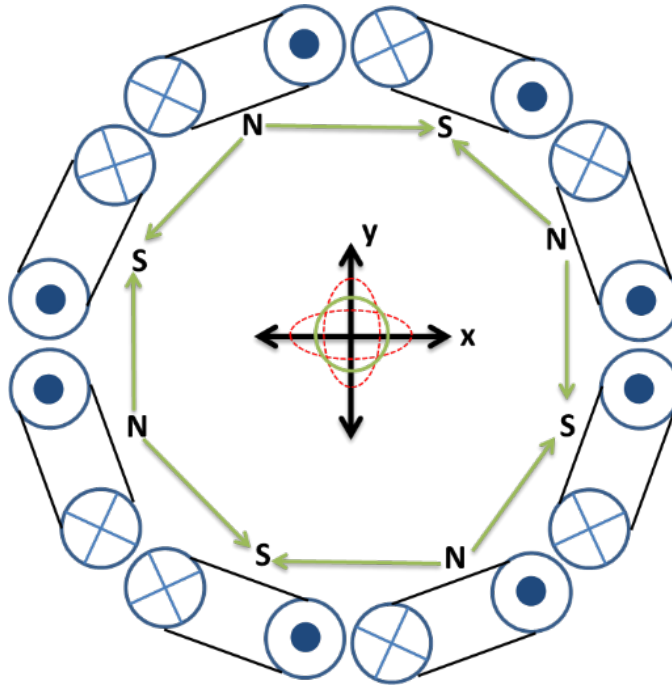


**Figure 3.17:** Schematic of a stigmator used in TEM. The windings of the coils are illustrated with blue lines while the direction of the magnetic fields is indicated with green solid arrows. Astigmatism in the electron beam is illustrated by the red dashed ellipsoids and the green circle indicates the ideal beam shape once astigmatism is corrected. Reproduced from [262].

### 3.13 Apertures

Aperture strips are normally made of metal such as platinum (Pt) or Mo. In a TEM, a hole typically of a few microns in diameter on this metal strip is called an aperture and the surrounding metal is called a diaphragm which blocks the electrons progressing down the TEM column. A choice of different apertures sizes (from ten to hundreds of microns) is normally available in a TEM for optimum use.

#### 3.13.1 Condenser Aperture

The condenser aperture is used to select the angular range of electrons incident on the specimen. A large aperture is used to get greater intensity at the sample position whereas a smaller aperture restricts the electrons to those nearer the optical axis

where the aberrations (see section 3.15) are less. A suitable selection of aperture is important to obtain optimum imaging conditions.

### **3.13.2 Objective Aperture**

The objective aperture in a TEM is used to select the direct or diffracted electron beam from a crystalline sample for the purpose of image formation. The objective aperture is inserted into the back focal plane of the objective lens.

### **3.13.3 Selected Area Aperture**

A selected area aperture is used to form a DP of a particular area of interest in a TEM specimen. A DP captured using a selected area aperture is called a selected area electron diffraction (SAED) pattern. The selected area aperture is inserted into the image plane of the objective lens.

This aperture sits in the image plane of an objective lens. It is sometimes called a virtual aperture because it lies in the image plane rather than the object plane of the objective lens.

## **3.14 Detection Devices**

The viewing screen in a TEM is usually coated with a phosphor which is doped to emit green light of wavelength 550 nm which is at the peak response of the human eye to visible light. This makes it easier for the TEM operator to observe the image especially if contrast is low. The final magnified image formed by the projector lens is projected onto a detection device e.g. a charge-coupled device (CCD), image plates or films. The detection device directly collect electrons and transfer the real-time image and DP on a computer screen or film.

### 3.15 Aberrations

Aberrations in the optical system can come from lens imperfections introduced during manufacturing, apertures, the sample, the sample holder and contamination of any of these. There are three types of aberration namely chromatic, spherical and astigmatic. The aberrations can greatly reduce the performance of a TEM. In order to get optimal performance from a microscope these aberrations need to be corrected.

#### 3.15.1 Airy Disk

The concept of an airy disk is important as it describes how much a microscope image distorts from a point source of light. Hence, the dot appears as a disk made up of concentric circles due to diffraction and whose intensity is receding from centre. The central spot with maximum intensity is known as an airy disk [5].

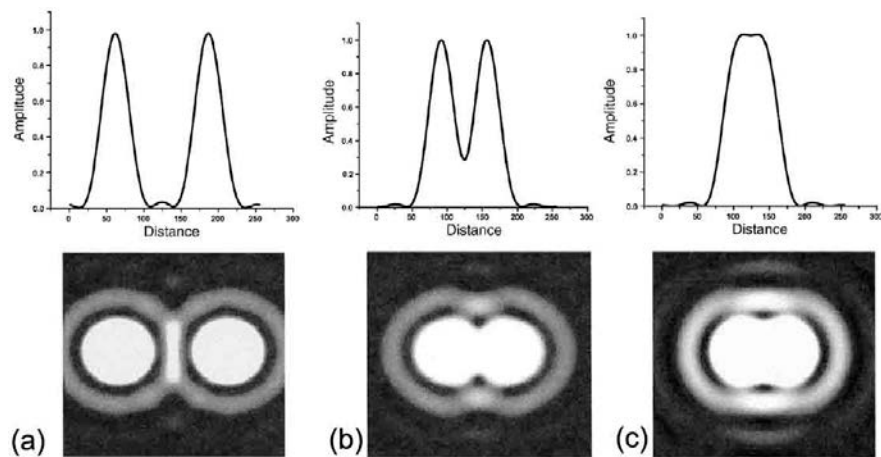


**Figure 3.18:** The intensity profile of images of two point sources: a) when the points are resolvable and airy disks are not overlapping; b) the two point sources are close and the airy disks are overlapping but are at the limit of resolvability; and c) airy disks are overlapping as points are too close and hence cannot be resolved. Reproduced and adapted from [4].

The Rayleigh criterion refers to the limit of the theoretical resolution,  $r_{th}$ , of a TEM defined as the ability to distinguish two point sources (see Equation 3.34). The points are at the limit of being distinguishable if the maxima of intensity of one aligns to the minima of intensity of the other disk. Under the Rayleigh criterion, the two points cannot be resolved if the dip in sum of the intensity profiles is above 80% of maximum intensity. The resolution of a TEM is limited by the radius of the Airy disk and is given by the following Equation 3.34 [259].

$$r_{th} = \frac{1.22 \lambda}{\beta} \quad \text{Equation 3.34}$$

where  $\lambda$  is the wavelength of the electrons and  $\beta$  is the collection semi-angle of the lens.

### 3.15.2 Spherical Aberration

The aberration caused by imperfections in the geometry of a lens is known as spherical aberration. This causes off-axis parallel rays not to coincide at same point on the optical axis after passing through the lens due to the inhomogeneity in the lens. As a result, the image of a point object forms a disk of finite size. The radius,  $r_{sph}$ , of the disk due to spherical aberrations is defined as:

$$r_{sph} = C_s \beta^3 \quad \text{Equation 3.35}$$

### 3.15.3 Chromatic Aberration

The electron beam extracted from the source is not monochromatic and contains electrons with a range of energies. Instabilities of the accelerating-voltage power supply can change the wavelength of the extracted electrons and energy losses in the sample also adds to the energy spread. This effect is greater in thicker samples because the electrons undergo more scatter. However, the dispersion of electron energies due to modern power supplies,  $\Delta E$ , is very low and typically one part in million:

$\sim 1$  eV for a LaB<sub>6</sub> filament and  $\sim 0.1$  eV for a FEG source [259]. The electrons of lower energy are deflected more strongly towards the optical axis and thus a point object is imaged as a disk. The radius,  $r_{\text{chr}}$ , of the disk due to chromatic aberrations is defined by Equation 3.36:

$$r_{\text{chr}} = \frac{C_c \Delta E}{E_0} \beta \quad \text{Equation 3.36}$$

where  $C_c$  is the coefficient of chromatic aberration,  $E_0$  is the energy of the electrons extracted from the electron source and  $\Delta E$  is the spread in energies.

### 3.16 Imaging Techniques

#### 3.16.1 Bright Field Imaging

The bright field (BF) imaging technique utilises the direct electron beam (i.e. the electrons undeflected by the sample) to produce an image. The objective diaphragm blocks the electrons outside the aperture. A ray diagram illustrating BF imaging is shown in Figure 3.19:

#### 3.16.2 Dark Field Imaging

The dark field (DF) imaging technique utilises a diffracted electron beam to produce an image. The electron beam is tilted such that the diffracted beam is brought onto the optic axis and passes through the objective aperture whilst the diaphragm blocks the other electrons. The DF imaging technique is illustrated by the ray diagram shown in Figure 3.20.



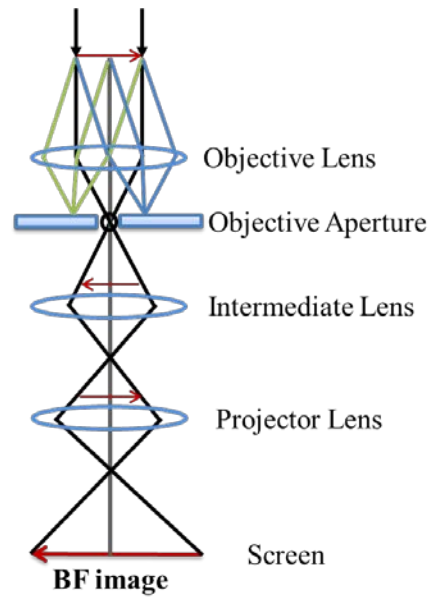


**Figure 3.19:** A schematic ray diagram of BF imaging in a TEM.

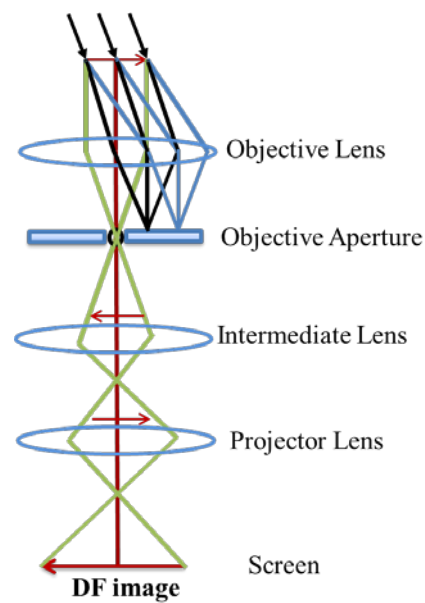


**Figure 3.20:** A schematic ray diagram of DF imaging in a TEM.

### 3.16.3 Two-Beam Conditions

Two beam is an imaging condition acquired by tilting the sample away from down zone (i.e. where multiple reflections are excited in the DP) such that only the direct beam and one diffracted beam are strongly excited. The two-beam condition is

widely used in the imaging of crystallographic defects. This technique allows the forming of BF and DF images with a particular  $g$ .

### **3.17 The MIAMI Facility**

#### **3.17.1 Introduction**

The Microscope and Ion Accelerator for Material Investigations (MIAMI) facility is a unique resource in the UK combining an *in-situ* ion beam system with a TEM to study the irradiation of materials. The MIAMI laboratory has the capability of delivering ions of gasses or self-ions with energies ranging from 500 eV to 100 keV [263]. The facility enables the study of the complex and dynamic effects which can occur during the irradiation of materials as the damage evolves. The resulting investigations can be helpful in understanding the underlying atomistic physics of advanced and functional materials for practical applications. This type of facility is one of only two in Europe and of around twelve globally [263].

#### **3.17.2 Overall Design of the MIAMI Facility**

The MIAMI facility has been equipped with a JEOL JEM-2000FX to characterise the dynamic effects of radiation damage in materials captured using a 4 mega pixel CCD camera model ORIUS SC2000. The overall design of MIAMI consists of various components as shown in Figure 3.21. It consists of an ion source to generate the ion beam, a profile monitor to beam shape, a bending magnet to deflect the beam onto the angle required to enter the TEM, a post-acceleration tube which can accelerate the ions to higher energies if required and finally an electrostatic deflection system inside the TEM to bring the beam onto the sample position. The ion beam also passes through XY steerers and an einzel lens followed by second beam profile monitor before entering the TEM. Once the ion beam has entered the TEM, it passes through two separate skimming apertures which are used to align the beam and monitor the current during irradiation [263].

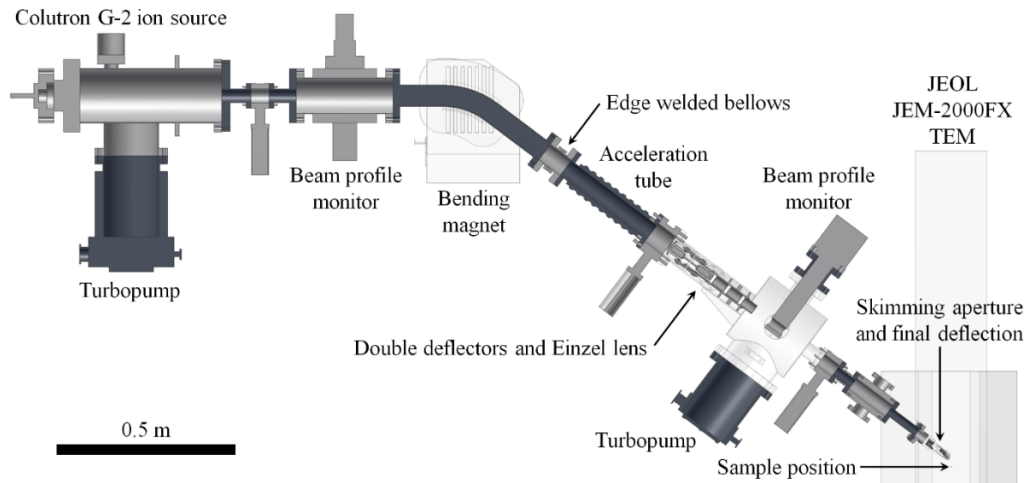


**Figure 3.21:** *MIAMI facility layout and transport system for ion beam. Reproduced from [263].*

### 3.17.3 Ion Source

The ion source is considered to be the heart of the ion beam system. The MIAMI facility is equipped with a Coultron G-2 ion source (see Figure 3.22) which is capable of producing singly-charged ions of energies 0.5 to 10 keV [264]. The ion source produces high beam-currents for light ions (e.g.  $\text{He}^+$ ). The ion source sits inside an ion gun which also features vertical defectors, an einzel lens, a Wien filter and a stigmators for beam adjustment [263], [264].

### 3.17.4 Beam Transport

#### 3.17.4.1 Bending Magnet

A bending magnet is used in the MIAMI facility to deflect the ions through an angle of  $37^\circ$  below the horizontal. This brings the ion beam onto the correct trajectory to enter the port on the TEM. The bending magnet also acts as a mass-energy selection device for the ion beam before entering into the post-acceleration system and is shown in Figure 3.23.

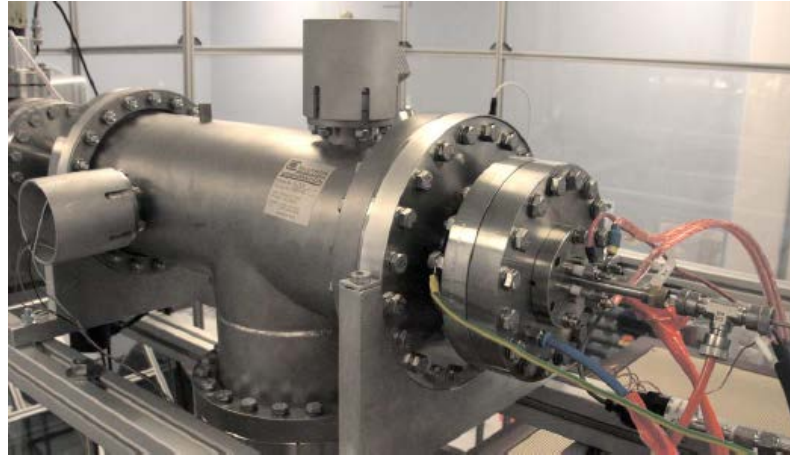


**Figure 3.22:** *The Colutron G-2 ion source installed in the MIAMI facility. Reproduced from [263].*

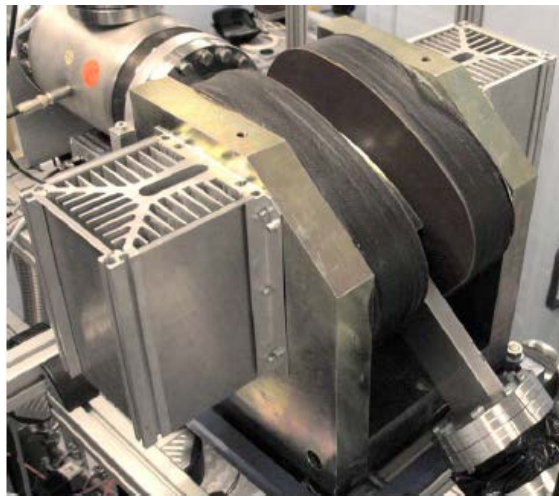


**Figure 3.23:** *The bending magnet used in the MIAMI facility to deflect the ions through  $37^\circ$  (reproduced from [263]).*

#### 3.17.4.2 Post-Acceleration Tube

The post-acceleration tube is used to accelerate the ions to higher energies if desired after passing through the bending magnet. It consists of nine voltage stages

connected to a resistor chain and is capable of accelerating the ion beam up to a maximum energy of 100 keV and is shown in Figure 3.24.



**Figure 3.24:** *The nine-stage acceleration tube to accelerate the ion beam to higher energies if required. The white rings are ceramic used for the purpose of insulation between the acceleration stages (reproduced from [263]).*

#### **3.17.4.3 Einzel Lens and Double Deflectors**

An Einzel lens and a deflection system is employed in the MIAMI system between the post-acceleration tube and the TEM for additional focusing and positioning of the ion beam. The Einzel lens is comprised of three sequential metal cylindrical electrodes and a voltage is applied to the second electrode relative to the other two grounded electrodes to focus the ions [5]. Double deflectors can be used to shift and/or tilt the beam as desired. The einzel lens and deflectors system employed in the MIAMI facility are shown in Figure 3.25.

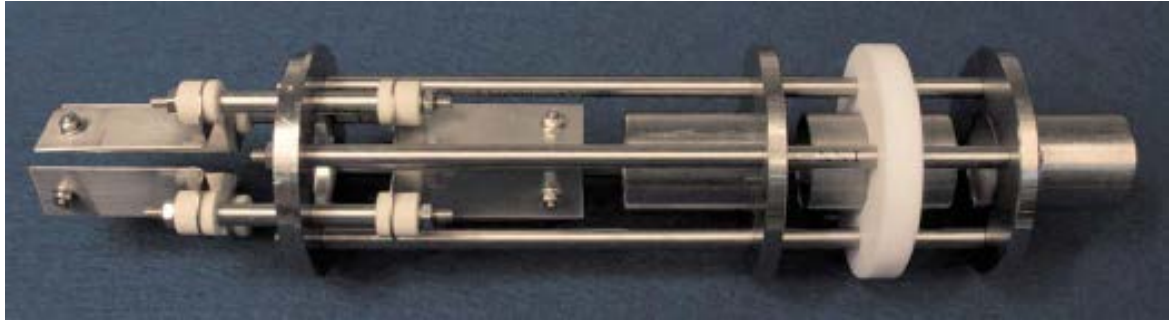


*Figure 3.25: Einzel lens (right) with deflectors (left) used in the MIAMI facility. Reproduced from [263].*

#### **3.17.4.4 Final Deflection**

An electrostatic deflection system which bends the ion beam onto the sample position in the microscope is known as the final deflection system. It consists of two horizontal and two vertical deflection plates (see Figure 3.26).

An equal and opposite voltage are applied to the plates in order to have the ion beam follows the zero-potential line. An aperture is placed at the exit of the final deflection system to shield the electron beam of the TEM from the electric field and insulating surfaces. The MIAMI facility has been tested from zero to the maximum voltage of the final deflection system to check for any interference due to the electrostatic field with TEM imaging but no such degradation has been observed [263].

#### **3.17.5 Beam Profile Monitors**

A helical wire sweeps across the ion beam as it passes through the chamber and emits secondary electrons which are collected as a current proportional to the ion beam intensity in two orthogonal directions. This current is amplified and displayed on an oscilloscope. For this purpose, two National Electrostatic Corporation beam profile monitors are installed in the MIAMI facility. The first beam profile monitor is immediately after the ion source and the second is installed on the beam line chamber before entering into the TEM [263].

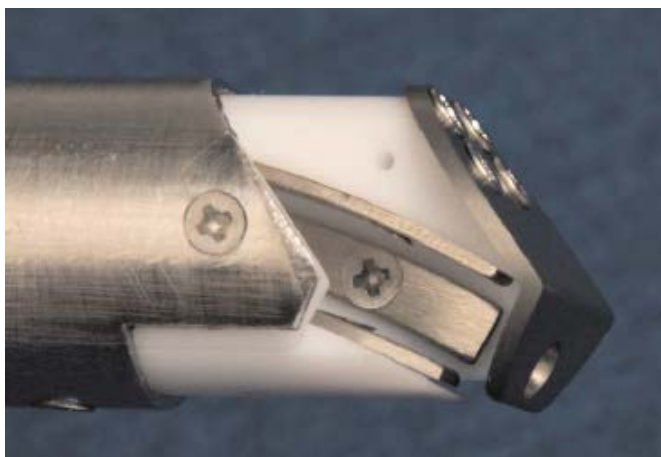


**Figure 3.26:** Final deflection system used in the MIAMI facility to provide an electrostatic field to the ion beam entering the TEM (reproduced from [263]).

### 3.17.5.1 Skimming Diaphragm

A skimming diaphragm is designed and installed before and after the final deflection system to measure the ion beam current. The pre-skimming diaphragm placed before the final deflection system ensures that a well-aligned ion beam enters into the final deflection system on the zero-potential line [263]. The skimmers are a valuable tool to monitor any change in the ion beam flux during the irradiation experiments.

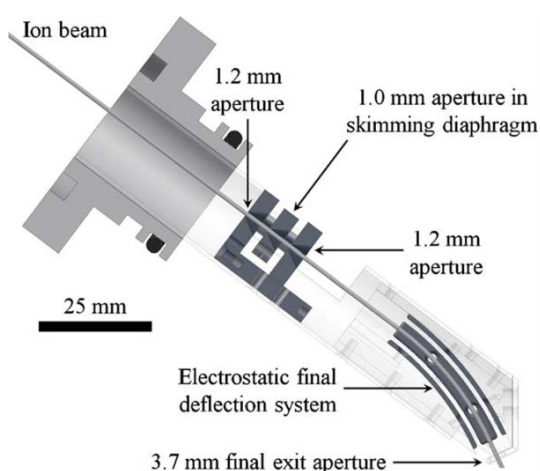


**Figure 3.27:** Skimming diaphragm between two apertures ensuring that the ion beam enters the final deflection system of the MIAMI on zero- potential line. Reproduced from [263].

### 3.17.6 Current Metering Rod

The current metering rod (CMR) is a device which is used to measure the electron and ion beam current at the sample position. It consists of three metal plates with insulating layers between them. The top plate is a diaphragm with a small 40  $\mu\text{m}$  diameter entrance aperture at the sample position. The middle plate has a relatively large aperture and is maintained at minus  $-60\text{ V}$  to suppress secondary electrons. The third is a detector plate that collects the current which is read using a picoammeter. The electron beam in the TEM can be detected using the CMR thus allowing the entrance aperture to be manoeuvred to the sample position using the  $x$  and  $y$  specimen shift controls.

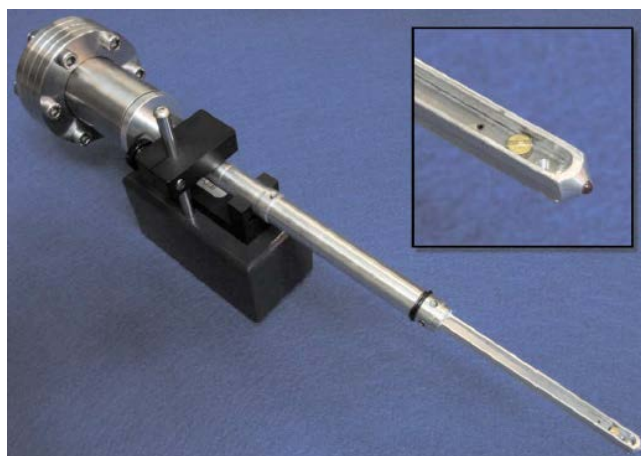


**Figure 3.28:** *The current metering rod to align and measure the ion beam current in a TEM (adapted from [263]).*

### 3.18 Atomic Force Microscope

The atomic force microscope was first developed by Binnig and Quate [205] in 1986 and was capable of measuring forces as small as  $10^{-18}\text{ N}$ . An AFM is capable of examining bulk samples with flat or rough surfaces and investigations may be performed in air or liquid. An AFM incorporates a sharp tip of radius less than 10 nm integrated into the end of a cantilever (dimensions  $\sim 100\text{ }\mu\text{m}$ ) to image the shape of a



surface in 3D [265]. Depending on the mode of operation, the tip of the cantilever may or may not touch the surface of sample under investigations and measures small force between the sample and the probe.

### 3.19 Working Principle of AFM

As the sample is scanned by the cantilevered tip in the AFM, the interatomic potential between the tip and the surface causes the cantilever to deflect up and down. The bending of the cantilever and thus the force,  $F$ , is measured and can be described using Hook's law (Equation 3.37):

$$F = -k.x \quad \text{Equation 3.37}$$

where  $k$  is spring constant of the cantilever and  $x$  is the deflection. The spring constant of cantilevers used in AFM for imaging varies from  $10 \text{ mN.m}^{-1}$  to  $100 \text{ N.m}^{-1}$  [265]. The schematic of the working principle of AFM is shown in Figure 3.29:

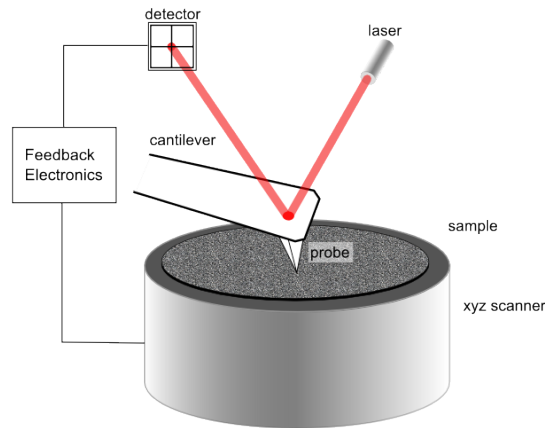


**Figure 3.29:** A schematic of AFM operation. Interaction between the tip and the sample is measured by monitoring the deflection of the free end of the cantilever by a laser beam shown in red. The laser beam reflects off the cantilever onto a position sensitive photodiode. *Reproduced from [266].*

### **3.19.1 Modes of Operation**

AFM can be operated in three different modes: contact mode, tapping mode and non-contact mode.

#### **3.19.1.1 Contact Mode**

The tip of the cantilever contacts the surface of the specimen and strong repulsive forces causes the cantilever to bend. The distance between the tip and sample is maintained by a feedback loop which applies a voltage on the piezoelectric tube to adjust the height of the cantilever. The force can be measured by monitoring the change in the cantilever deflection using Hook's law given in Equation 3.37.[206].

#### **3.19.1.2 Tapping Mode**

Tapping force microscopy is a technique in which the tip of the cantilever oscillates at a frequency close to its resonance frequency. The tip gently touches the surface of the sample under investigation. The force on the tip changes with the tip-sample distance and the resonance frequency is dependent on this distance. The amplitude of the cantilever is maintained by a feedback loop and the force is measured by recording the deflections correspond to the changes in cantilever vibration (i.e. amplitude of oscillation). The advantage of tapping mode over contact mode is that the tip interacts with the surface only once in every oscillation which reduce the frictional forces and does not damage the surface as much. Imaging of fragile samples, polymer surfaces and biological samples are performed with tapping mode [267].

#### **3.19.1.3 Non-Contact Mode**

In a non-contact mode, the cantilever oscillates at a frequency above its resonance frequency near the surface of the sample such that the tip of the cantilever does not contact the surface. This mode utilises the attractive forces between the tip and

sample surface, which reduce the amplitude of vibration, to gather data on the surface topology. A feedback loop maintains the constant amplitude or frequency by adjusting the distance between the tip and sample surface. This mode of operation preserves the sample surface and extends the lifetime of the AFM tip. [268].

### **3.20 Artefacts in AFM images**

Atomic force microscopy is not only limited to image morphology of a surface but widely used for determining the magnetic structures, friction measurement and surface charge distributions [269]–[271]. Artefacts are the features appear in the image that are not real [272], [273]. The artefacts introduced in the AFM images may perturb the measurements. It is important to recognise and minimise the source of artefacts [274]–[281]. The artefacts which appear in AFM imaging may originate from the probing tip, scanning system, external vibrations, thermal gradients, feedback circuitry and image processing software [282], [283].

#### **3.20.1 Probing Tip Artefacts**

The geometry and dimension of the probe used for measuring the features may introduce artefacts into an AFM image. The accurate imaging of lateral dimension depends on the sharpness and inclination angle of the tip used. If the radius of curvature of the tip is greater than the features of the image (e.g. nanotube and nanosphere), the scanning probe overestimates the lateral dimensions (see Figure 3.30) [282], [284]. Measurements taken with conical tips produce images with fewer artefacts than pyramidal tips [283]. If the tip cannot reach the sidewalls of valley, the AFM tip then underestimates the details of the sample such as size and depth (see Figure 3.30) [283]. However, the height of the object to be measured is independent of the geometry of the tip [283]. The probe artefacts can be minimised by using a sharp tip with a radius of curvature much less than the details of the image being measured. The effect has been illustrated schematically in Figure 3.31. A damaged or contaminated AFM tip may produce blurred images [283]. Shadows or double image can also appear in images and described as double tip effects [5], [283]. While

imaging flat samples featuring fine details with large tips, the image can contain artefacts known as tip self-imaging due to the sidewall angle of the tip as illustrated in Figure 3.31.

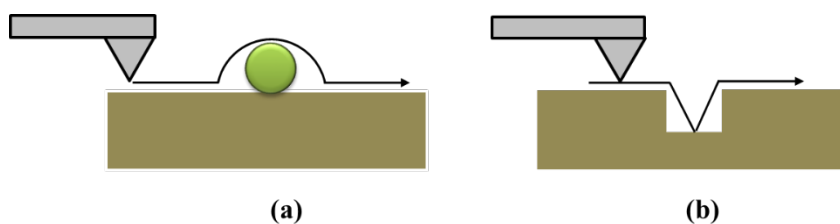


**Figure 3.30:** Schematic of how an artefact can be introduced by a large diameter tip: (a) overestimating and (b) underestimating the lateral dimensions. Arrow shows the scanning direction and trace. Redrawn from [8].

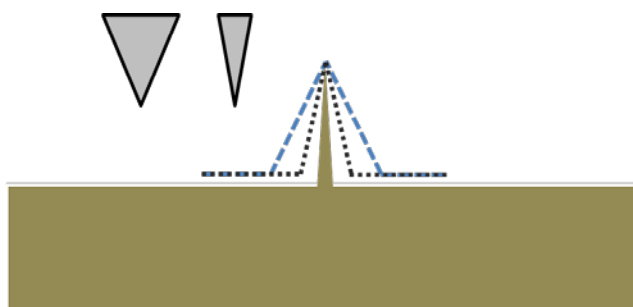


**Figure 3.31:** Schematic showing the traces of two tips with different sidewall angles. The side walls cause broadening of the lateral dimensions in the image. Redrawn from [283].

### 3.20.2 Scanner Artefacts

Atomic force microscopy uses a piezoelectric scanner that moves the probe in three dimensions (x, y, and z). The geometry of the tip and the scanner may introduce artefacts into AFM images. The most frequent artefacts are edge overshoot, edge elevation, thermal drift and creep as discussed below.

Piezoelectric ceramics are capable of moving the tip by very small distances by applying a linear voltage [284]. Edge overshoot artefact arises in AFM imaging due to hysteresis of the piezoelectric scanner that moves the cantilever in the z-direction (see Figure 3.32). The artefact can be seen in the narrow hills and valleys at the edges of the image and can be minimised by slowing down the scanning speed [283].

Edge elevation is another artefact in AFM imaging and can be caused by the tip-sample attractive forces [282]. The probe in an AFM moves in a curved path over the surface and cause bows in the imaging. If the tip-sample angle is not perpendicular, a tilt is introduced. If the bows and tilts are larger than the features of interest, then the artefacts can be rectified in post processing of the images by subtracting the background bows and tilt and this is called levelling or flattening [284].

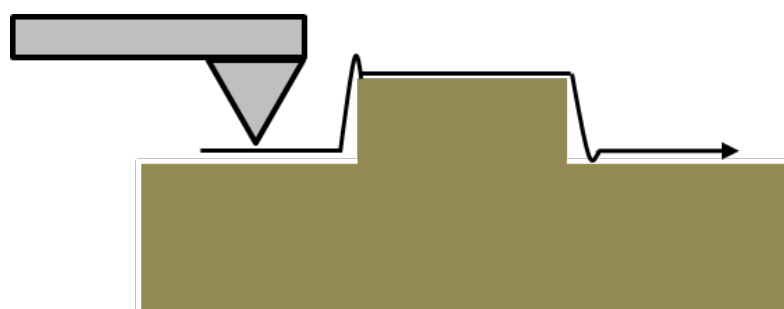


**Figure 3.32:** Schematic of edge overshoot caused by a fast scan speed. Arrow shows the scanning direction and trace. Redrawn from [282].

Thermal drift and creep of the AFM cantilever caused by the laser or by contact with the sample may introduce artefacts [282]. These artefacts distort the straight lines into curved lines in the AFM imaging as shown in Figure 3.33 and 3.34. This artefact can be minimised by using a fast scan speed, sample position sensors and improved feedback control loops [282].

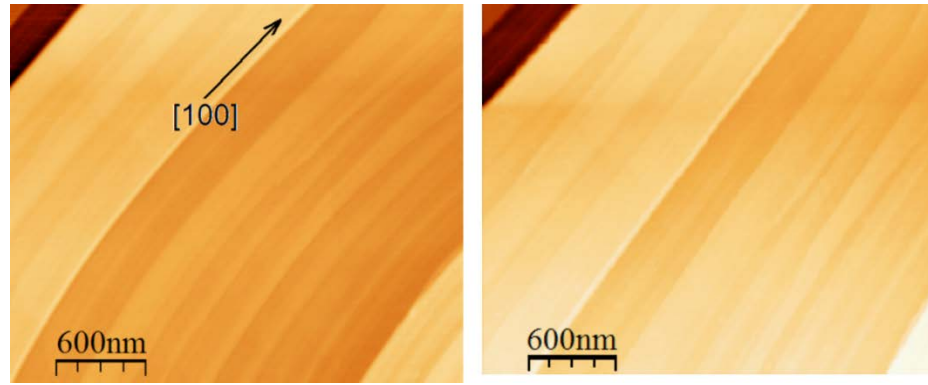


**Figure 3.33:** A topographic image of LiF crystal surface showing distortions due to thermal drift (left) with bowing apparent in the bottom of the image. The image without thermal drift (right). Reproduced from [282].

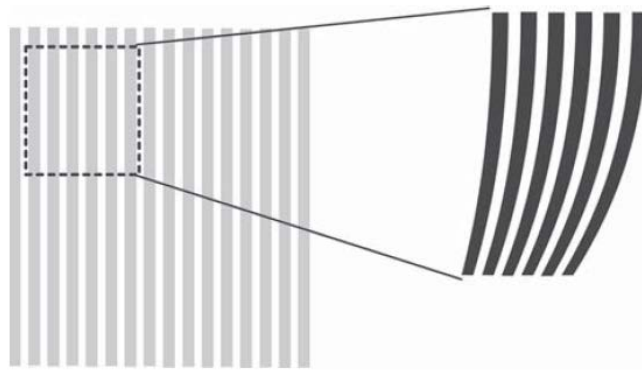


**Figure 3.34:** Distortion of features in an AFM image caused by creep. Reproduced from [283].

### 3.20.3 Features along the Scan Direction

Sometimes, triangular and oval features appear along the scan direction which can be due to the high set point, low amplification and high scanning speed [279]. Furthermore, irregular edges and dips can appear along scan direction and are due to a large amplitude of the cantilever and small set point, respectively [279]. Also, plastic deformation of the sample can cause vertical ridges to appear in the scan direction when imaging in contact mode [285].

#### 3.20.4 External and Internal Noise

Mechanical noise arises from factors such as acoustic vibrations, floor vibrations, electromagnetic interference and temperature fluctuations which can introduce artefacts into the image [14]. Furthermore, electronic noise caused by the piezoelectric scanner, amplifiers and optical systems may lead the probe to vibrate and cause artefacts. External noises may influence the texture, sensitivity and resolution of the AFM [282], [286]. Such noise can be removed from AFM images with image enhancement techniques by using proper filtering – for example, 2D Fourier filtering [287].

#### 3.21 Experimental Method for Irradiation of Nanowires

Experiments were carefully designed to study and explore the ion irradiation induced modifications of Si NWs. A rotation holder offers a way to bring any NW randomly dispersed onto the sample grid to a desired orientation by tilting and rotating. This may be either the orientation relative to the electron beam and/or the ion beam within the geometry of the MIAMI facility. Single crystalline NWs with one end attached to the grid side and other end in free space were selected for the ion irradiation experiments to explore the bending phenomenon.

Before irradiation, the selected NW was first rotated to align its axis with the x-axis of the TEM (and hence also the x-axis of the rod) at *zero-tilt* (i.e. an x-tilt of  $0^\circ$ ). This position of the NW will be referred to as *zero-rotation zero-tilt* position. The NW was then rotated  $45^\circ$  degrees from *zero-rotation zero-tilt* position such that such that ion beam was directed normal to the axis of the Si NW under investigation. This position of the NW will be referred as *zero-tilt plus  $45^\circ$ -rotation* and is shown in Figure 3.35:

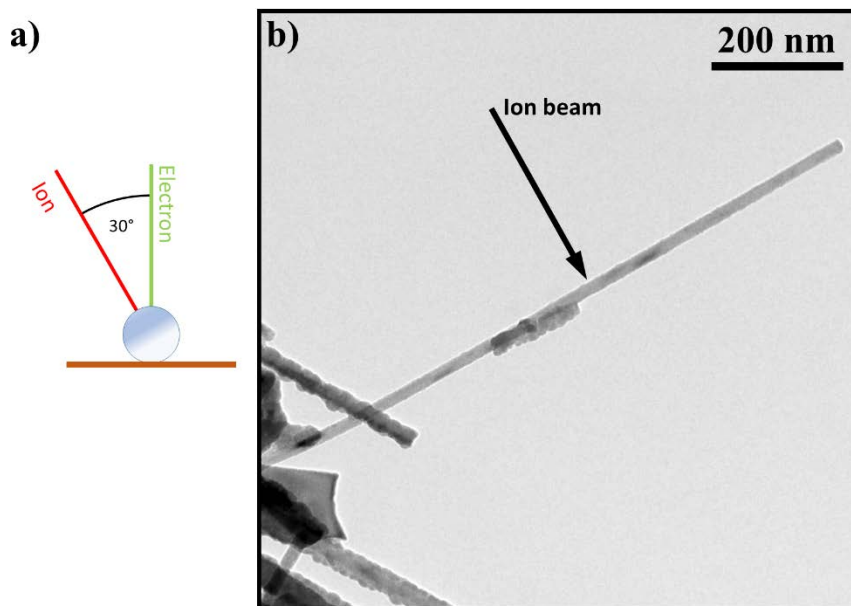


**Figure 3.35:** (a) A schematic representation of an electron beam and ion beam in the MIAMI facility and (b) a bright-field image of the NW at zero-tilt plus 45°-rotation such that the ion beam is at normal incidence.

### 3.21.1 Tilt Image Series of Nanowires

At *zero-rotation* a tilt image series of the NW was captured before and after the irradiations to determine the bending direction by tilting the sample to *plus-45°* and *minus-45°* (x-tilt) by rotating the goniometer anti-clockwise (ACW) and clockwise (CW), respectively. This tilt operation will be referred to as *zero-rotation plus-45°-tilt* and *zero-rotation minus-45°-tilt*. BF-TEM images and the corresponding SAED patterns were recorded.

SolidWorks modelling was carried out to demonstrate the tilt image series and is shown in Figure 3.36. The top view (a–c) is showing the images captured along the electron beam direction (i.e. z-direction of TEM) demonstrating the tilt series to reveal and hide the NW curvature by rotating the goniometer (x-tilt). The bottom row (d–e) is illustrating the view along x-direction of TEM (x-tilt) demonstrating the NW in the images bent upwards in the TEM.



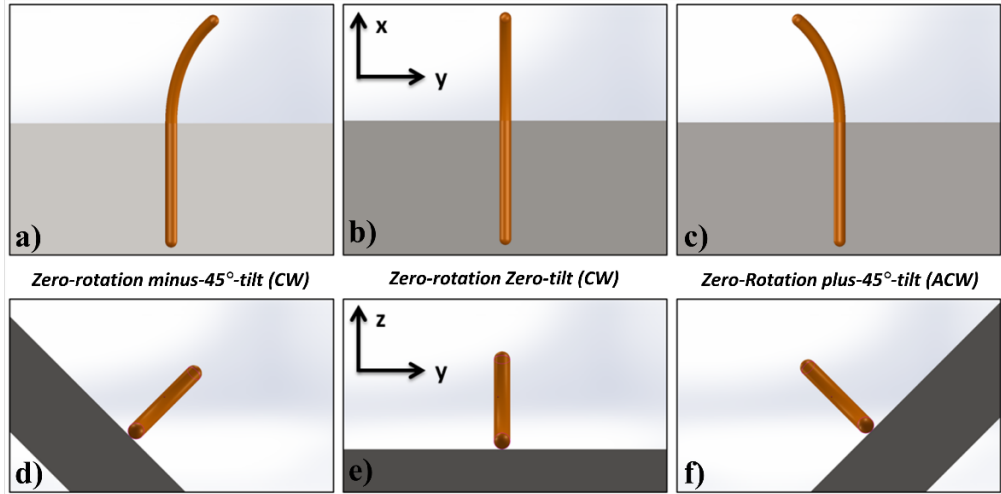


**Figure 3.36:** Schematics demonstrating the tilt image series performed before and after the irradiation experiments to determine the bending direction of the Si NWs. A representation of the NW as seen by the electron beam in the TEM along the z-axis is shown in (a) to (c). The representation of the Si NW as seen from the x-axis of the TEM is illustrated in (d) to (f).

### 3.21.2 Determination of Angle of Inclination of Nanowires

It was observed during the capture of the pre-irradiation tilt image series that some of the NWs were not lying flat on the grid and instead were inclined relative to the support grid. This was due to the random nature of the sample preparation via dispersion onto the grid. Although such inclination can introduce an additional complication into the experimental method and analysis, due to the scarcity of ‘ideal’ NWs it was still desirable to use these if they were otherwise of appropriate length, of appropriate diameter, protruding into free space and suitably located to avoid ion and electron beam shadowing effects. Trigonometry was used to calculate the pitch (angle of inclination from the horizontal xy-plane) of the NWs using the tilt image series.

The method for the calculation of the angle of inclination,  $\alpha'$ , of the NWs can be derived as follows. Let  $a = 1$  be the projected length of the NW in the xy-plane at zero-tilt,  $b$  be the projected length at plus-45°-tilt and  $\beta'$  be the angle between  $a$  and

$b$  as showed in Figure 3.37 from which the distance,  $c$ , was calculated using trigonometry.

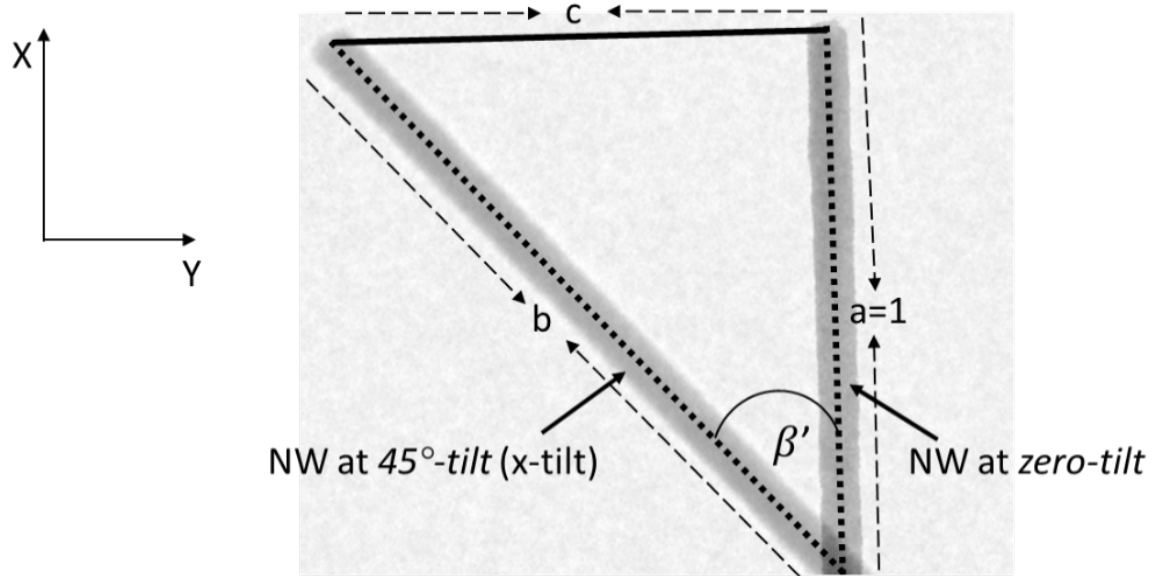


**Figure 3.37:** Overlaid images of a Si NW at zero-tilt and plus-45°-tilt where  $a$  and  $b$  are the projected length at these two tilts, respectively.

From Figure 3.37 it can shown:

$$c = a \tan \beta' \quad \text{Equation 3.38}$$

Now consider the same NW viewed in the  $yz$ -plane of the TEM and let  $d$  be the projected length of the NW in the  $yz$ -plane as shown in.Figure 3.38:

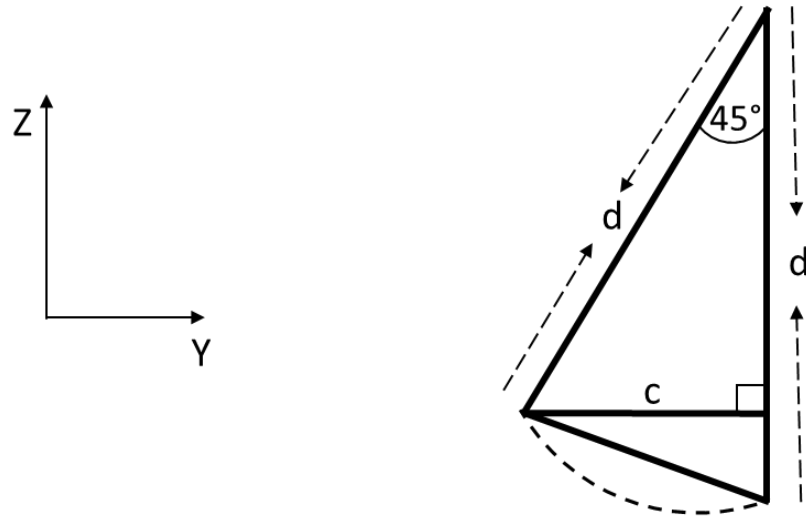


**Figure 3.38:** Trigonometry of NW undergoing  $45^\circ$   $x$ -tilt viewed in  $yz$ -plane of the TEM.

From Figure 3.38 it can be shown:

$$\sin 45^\circ = \frac{c}{d} \quad \text{Equation 3.39}$$

Now consider the NW viewed in the  $xz$ -plane of the TEM. Let  $N$  be the true length of the NW in the  $xz$ -plane and  $\alpha'$  be the angle of inclination as shown in Figure 3.39:

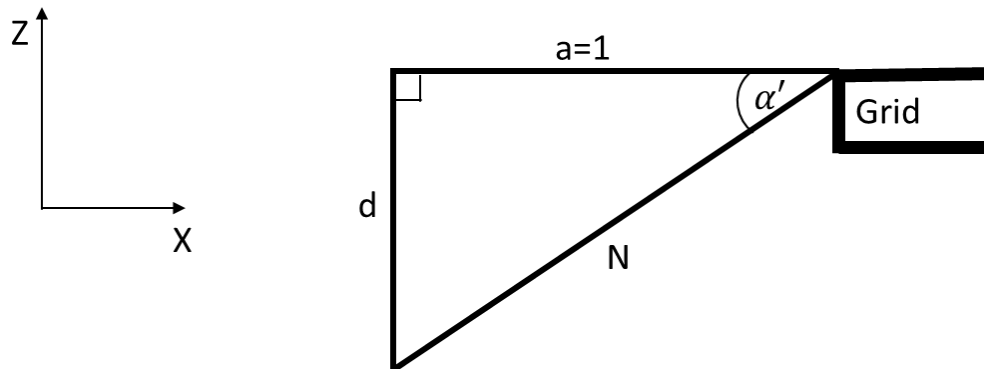


**Figure 3.39:** Trigonometry of the NW as seen in  $xz$ -plane of the TEM.

Now an expression for  $\alpha'$  can be derived by solving the three triangles shown in Figure 3.37, 3.38 and 3.39. From Figure 3.39:

$$\tan \alpha' = \frac{d}{a} \quad \text{Equation 3.40}$$

Substituting Equation 3.38 into 3.39 and rearranging gives:

$$d = \frac{c}{\sin 45^\circ} = \frac{\tan \beta'}{\sin 45^\circ} \quad \text{Equation 3.41}$$

Substituting in Equation 3.41 and  $a = 1$  gives:

$$\tan \alpha' = \frac{\tan \beta'}{\sin 45^\circ} \quad \text{Equation 3.42}$$

Finally, rearranging gives an expression of the angle of inclination,  $\alpha'$ , in terms of  $\beta'$  which can be measured from the tilt image series as illustrated in Figure 3.37:

$$\alpha' = \tan^{-1} \left( \frac{\tan \beta'}{\sin 45^\circ} \right) \quad \text{Equation 3.43}$$

### 3.22 Summary

*In-situ* TEM was extensively used to investigate the ion irradiation induced modifications of Si NWs at MIAMI facility. Therefore the operation of the TEM and MIAMI facility has been discussed in detail. AFM was also used to measure surface roughness of Si NWs and Mo grids and thus has been discussed in this chapter. Experimental methods to irradiate Si NWs at normal

incidence and the procedure to capture tilt image series to determine bending direction of NWs has also been discussed.

## 4 Ion Irradiation Calculations

### 4.1 Introduction

Stopping and Range of Ions in Matter (SRIM) is a package of software that is capable of performing calculations of the interactions of an energetic ion with a target [288]. SRIM is currently the most commonly used software to calculate the displacement of atoms, ion range and stopping power (energy loss) in matter. The underlying physics to calculate the energy losses is based on quantum mechanics and Monte Carlo computer code is based on the binary collision approximation (discussed in 4.3). Monte Carlo is a computational technique that utilises random numbers to run the same calculations multiple times in order to build up statistics on how a system behaves – for example, collision events, atomic displacements, ion range, number of vacancies and interstitials generated etc. The SRIM code can estimate the stopping and range of ions with energies from 10 eV to 2 GeV/amu [289] and employs a screened Coulomb potential to treat nuclear collisions and this can increase the computation speed by 50 times over some other methods [289].

### 4.2 Ion-Solid Interactions

When an incident particle of energy  $E_0$  enters a target material, it can undergo a collisions and an energy,  $E$ , is transferred to a target atom. If  $E$  is less than the minimum displacement energy,  $E_{d-\min}$ , then the target atom is not displaced but rather vibrates about its lattice site and dissipates the energy as phonons. If the amount of transferred energy is greater than the  $E_{d-\min}$  of the target material, an atom can be displaced from its lattice site. The probability of a displacement occurring as a function of the energy transferred to it is shown schematically in Figure 4.1, where  $E_{d-\min} < E_d < E_{d-\max}$ .  $E_d$  is defined as the average displacement energy. The maximum

energy which can be transferred to a lattice atom can be calculated through Equation 4.1:

$$E_{\max} = \frac{4Mm}{(M + m)^2} E_0 \quad \text{Equation 4.1}$$

where  $M$  is the mass of the target atom,  $m$  is the mass of the incident particle and  $E_0$ , is the energy of an incident particle.

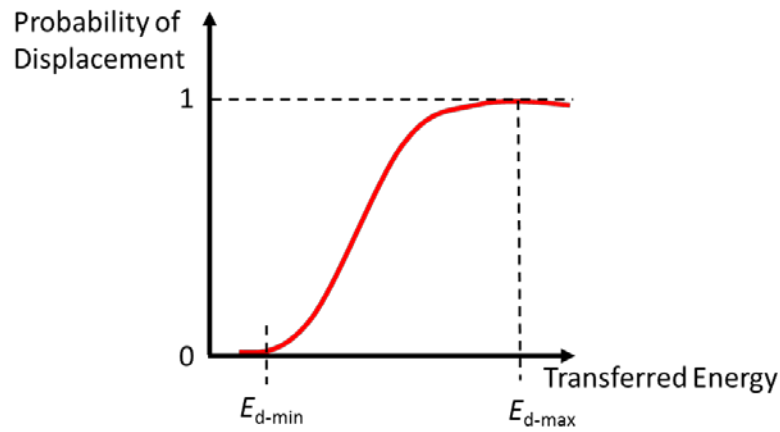


**Figure 4.1:** A schematic showing the probability of an atomic displacement occurring when the energy transferred to the target atom is between the minimum,  $E_{d-\min}$ , and maximum,  $E_{d-\max}$ , displacement energies. Redrawn from [262].

A target atom displaced from its original lattice site and set into motion is called a primary knock-on atom (PKA). This atom travels with an initial energy and can then collide with other atoms causing subsequent displacements until it comes to rest. The PKA loses energy through interactions with other atoms and electrons, and may either come to rest at an interstitial position or combine with a vacancy in the target material.

#### 4.2.1 Collision Cascades

If the energy transferred to a target atom in an elastic collision is greater than  $E_d$ , the collision results in the displacement of the atom from its lattice site. This PKA is created in  $10^{-18}$  s [290] can go on to collide with other atoms and produce secondary knock-on atoms, tertiary knock-on atoms and so on as long as the imparted energy in each collision is greater than  $E_d$ . The process continues until all the energetic particles drop below the energy at which they can induce further atomic collisions and come to rest. All the collisions initiated by an incident particle constitute what is termed a collision cascade with knock-on atoms initiating sub-cascades. The energy of each knock-atom decreases with each subsequent collision and it finally comes to rest at an interstitial position or is captured by an empty lattice site in the target material thus producing defects (for example, vacancies, interstitials etc.) along its path in the material [141].

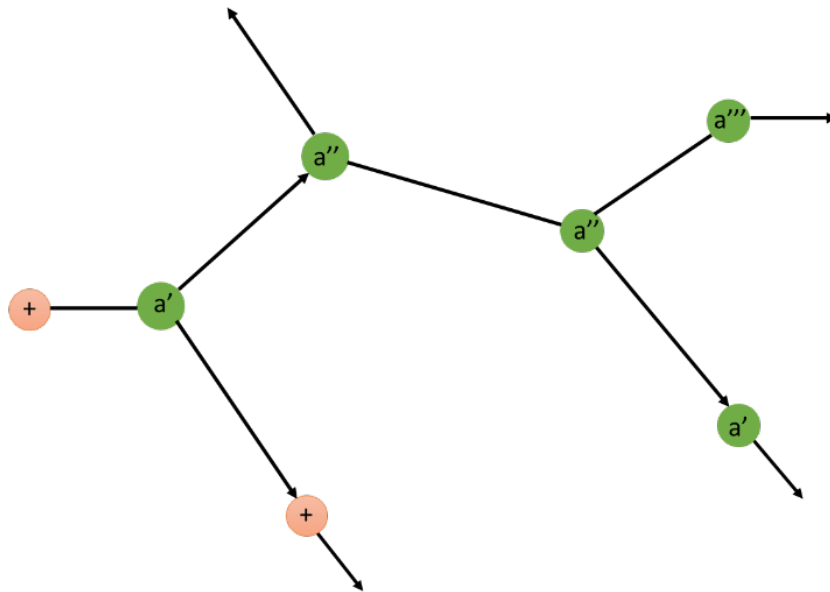


**Figure 4.2:** A schematic showing a single atomic collision leading to the formation of a cascade: an incident ion with  $E_0 > E_d$  displaces a target atom from its lattice site becoming a PKA,  $a'$ ; a PKA with  $E - E_d > E_d$  produces a secondary knock-on atom,  $a''$ ; and in turn  $a''$  produces a tertiary knock-on atom,  $a'''$ , and so on. This process continues in the material until atoms lose energy and come to rest or exit the target.



#### 4.2.2 Displacement Spike

When the energy of an energetic particle drops below a critical energy,  $E_c$ , the mean free path between collisions approaches the interatomic spacing in the material and a region can be formed along the ion trajectory where nearly every atom is displaced from its lattice site [291]–[294]. This results in a highly disrupted region where a significant proportion of the atoms are displaced. This event is referred to as a displacement spike and occurs over approximately  $10^{-13}$  s [294]. Brinkman has described the displacement spikes as a depleted zone with a high concentration of vacancies at the core surrounded by the displaced interstitials [293] as illustrated in Figure 4.3:

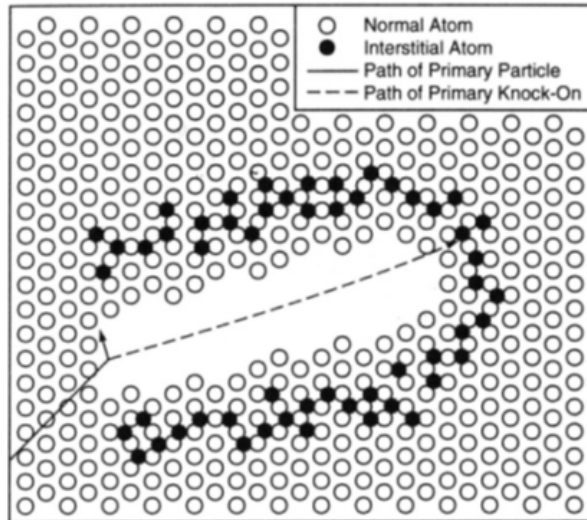


**Figure 4.3:** Schematic illustration of a displacement spike (reproduced from [295]).

#### 4.2.3 Thermal Spike

A large amount of energy is deposited into a region affected by a displacement spike. This rapid lattice heating is referred to as a thermal spike and requires about  $10^{-12}$  s [296], [297] before the vibrational energy distribution of the atoms can be described by Maxwell-Boltzmann statistics and the concept of temperature applied. A thermal spike can form a local region where the “temperature” is greater than the melting

temperature of the material. However, the time period is so short that actual melting may not occur in all cases. The heat energy released through a thermal spike can facilitate defect migration, agglomeration and annihilation.

#### 4.2.4 Stopping Power

The incident particles and recoil atoms dissipate energy during their motion in the material through nuclear collisions (elastic) and electronic collisions (inelastic) which are discussed in sections 4.2.6 and 4.2.5. These energy losses can be described by the stopping power or energy loss,  $S(E)$ , defined by the amount of energy transferred per unit length,  $x$ , in the material. (Equation 4.2)

$$S(E) = \left( -\frac{dE}{dx} \right) \quad \text{Equation 4.2}$$

where  $S(E)$  is measured in  $\text{J.m}^{-1}$  or  $\text{eV.m}^{-1}$ .

#### 4.2.5 Elastic Energy Loss (Nuclear Stopping)

The slowing down of an energetic atom due to an elastic transfer of energy to a target atom is known as a nuclear collision. Nuclear collisions are most likely to dominate over electronic stopping at lower energies and can be treated using the BCA in which one energetic atom interacts with one target atom. The incident ion changes its direction and loses energy in each collision. However, this approximation breaks down for heavier ions at low energies where  $\lambda'$  approaches the interatomic spacing.

#### 4.2.6 Inelastic Energy Loss (Electronic Stopping)

Energetic particles moving through a material experience a Coulomb force due to interactions between their electrons and those of the target. This causes a continuous energy loss which can be thought of as a type of drag force known as electronic energy loss or electronic stopping,  $S_e$ . Electrons may escape their host atom due to this inelastic interaction if the energy transferred to the electron is greater than its

ionisation energy. Electronic stopping can dominate over nuclear stopping at higher energies because of high velocity of electrons and small interaction cross-section. The schematic in Figure 4.4 illustrates the process of energy loss by electronic stopping resulting in a decrease in energy of the ion.

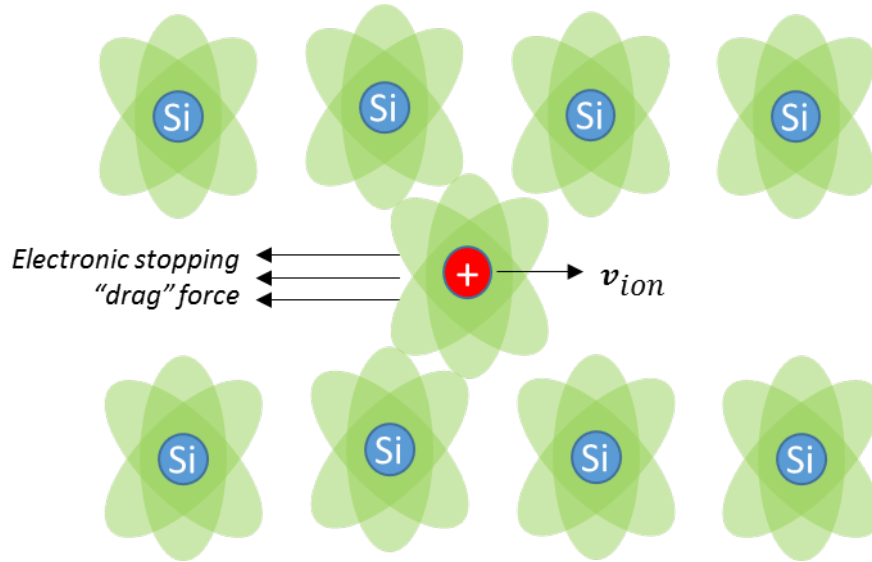


**Figure 4.4:** A schematic of the energy loss due to electronic stopping of an ion moving with velocity,  $v_{ion}$ , through a target.

#### 4.2.7 Total Stopping Power

The sum of total energy lost by an incident ion in the target material due to the electronic and nuclear stopping is referred to as the total stopping power,  $S(E_{tot})$  (Equation 4.3). The two stopping powers are treated differently by SRIM with nuclear stopping being approximated a series of binary collisions and electronic stopping as a continuous slowing. The prominence of the two types of stopping powers as functions of energy are illustrated in Figure 4.5.

$$S(E_{tot}) = -\frac{1}{N} \left[ \frac{dE_{tot}}{dx} \right] = S_e + S_n \quad \text{Equation 4.3}$$

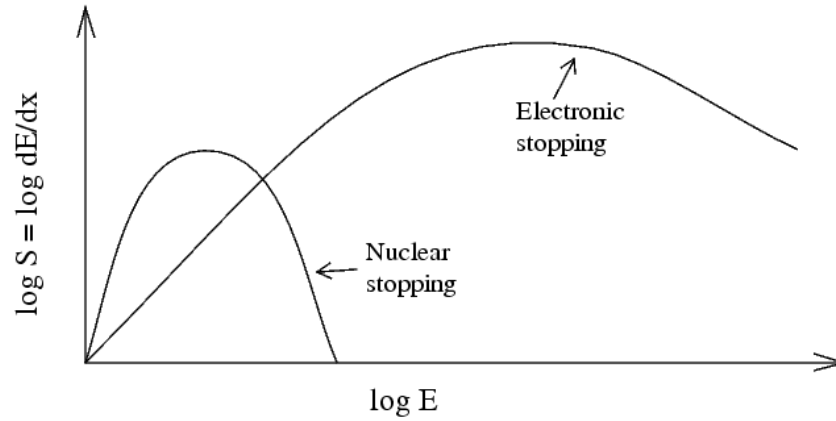


**Figure 4.5:** Comparison between the electric and nuclear stopping powers: nuclear stopping power curve dominates at lower energies (typically between 10–100 keV) while electronic stopping is dominant at higher energies (typically MeV energies). Reproduced from [298].

#### 4.2.8 Range of Ions

The total distance travelled by an ion in a material depends on the energy losses it experiences (i.e. the combination of electronic and nuclear stopping). The rate of energy loss is proportional to the total stopping cross-section [292], [294]. Since ions can be deflected during the scattering process, the total distance travelled by the ion in the target material is likely not to be the same as the depth (i.e. distance from surface of entry) as shown in Figure 4.6. The range of implanted ions in the target material depends on the mass, energy and angle of incidence of the incoming ion as well as the composition, density and temperature of the target (however, in SRIM all calculations are performed at 0 K [289]). The mean free path is reduced when ions are slowed down in a target material and ultimately the ion may dissipate so much energy that  $\lambda'$  approaches the interatomic spacing of the target material.

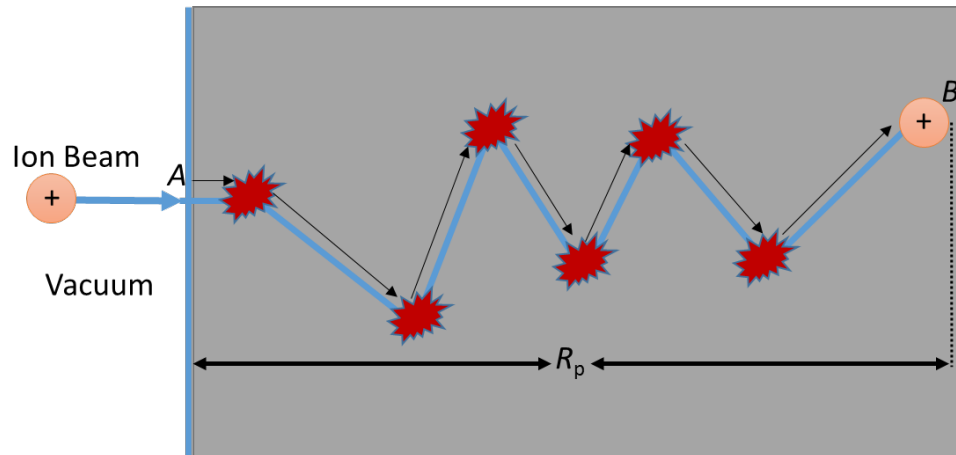


**Figure 4.6:** Schematic of an ion begin scattered during a series of collisions with the target atoms illustrating how the actual range of the ion and the path length (distance from A–B) can differ. In other words, the projected range,  $R_p$ , is different from the path length,  $R$ .

#### 4.2.9 Channelling

In crystalline materials, atoms are arranged in rows between which can be open pathways called channels. If an ion finds itself travelling along one of these channels then the probability of a nuclear collision is reduced. Therefore the crystallographic orientation of the target can affect the penetration of an incident ion and this is called a channelling effect. When an ion enters a channel, the electrons of the ion and of the surrounding atoms repel each other so as to guide the ion along the open pathway. Channelled ions are less likely to collide with target atoms (i.e. have nuclear collisions) and therefore lose energy more slowly resulting in a greater range in the material as illustrated in Figure 4.7. The channelling of ions depends on the surface of the target material (for example impurities and surface disorder due to oxidation may cause scattering), temperature of the substrate and most importantly the angle of incidence relative to the crystal structure [299]. However, SRIM does not take into account the crystal structure of the material and so does not model channelling effects [289].

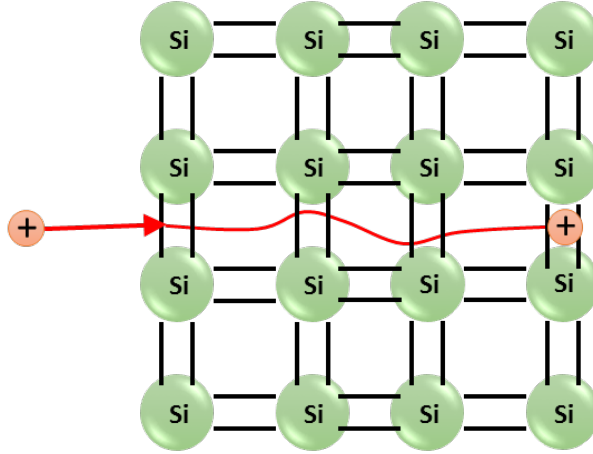


**Figure 4.7:** A schematic showing an ion being channelled in Si. The channelled ion may experience glancing collisions and will lose energy due to the electronic drag force but the probability of nuclear collisions is reduced.

### 4.3 Binary Collision Approximation

The binary atomic collision approximation treats the interaction of one ion or recoil atom with one target atom. The BCA is used in SRIM in combination with the Monte Carlo technique treating successive collisions as binary collisions. A seed is used to set off the random number generator in SRIM which then decides the free flight path,  $F$ , and impact parameter for each collision. The flight path is given by Equation 4.4:

$$F = \frac{e^{-\frac{1}{\lambda'}}}{\lambda'} \quad \text{Equation 4.4}$$

where  $\lambda'$  is the average distance between two successive collisions and can be determine using Equation 4.5:

$$\lambda' = \frac{1}{N\sigma} \quad \text{Equation 4.5}$$

where  $N$  is the atomic density of the target material in  $\text{atoms.m}^{-3}$  and  $\sigma$ , is the scattering cross-section ( $\text{m}^2$ ) which is a measure of the probability of a collision. Equation 4.6 gives the parameters which determine  $\sigma$ :

$$\sigma \propto \left( \frac{Z_1 Z_2 e^2}{4E} \right) \left( \frac{4}{\sin^4 \theta} \right) \quad \text{Equation 4.6}$$

where  $Z_1$  and  $Z_2$  are the atomic numbers of the particles involved in the collision;  $\theta$  is the scattering angle relative to the direction of incident particle; and  $E$  is energy of the impacting atom.

The energy transferred to the target atom and the deflection of the projectile during a collision can be calculated by knowing the impact parameter,  $P$  and projectile energy. SRIM uses an analytical formula to evaluate the atom-atom scattering known as the Magic Formula given in Equation 4.7 which determines the angle of scatter for both incident and recoil atoms and as illustrated in Figure 4.8.

$$\cos \frac{\theta}{2} = \frac{\rho_1 + \rho_2 + \delta_1 + \delta_2 + P'}{\rho_1 + \rho_2 + r_0} \quad \text{Equation 4.7}$$

where:  $\theta$  is the scattering angle;  $\rho_1$  and  $\rho_2$  are the radii of the projectiles;  $r_0$  is the distance of closest approach;  $\delta_1$  and  $\delta_2$  are the correction terms for different atomic potentials; and  $P' = P/a$ , where  $a$  is the universal screening length to reduce  $P$ .

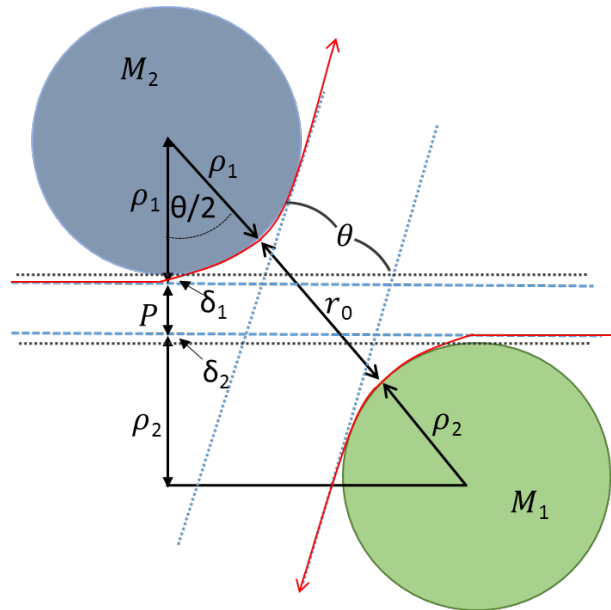


**Figure 4.8:** A collision between two atoms of mass  $M_1$ , and  $M_2$ , drawn schematically in a centre-of-mass system: a “scattering triangle” is used to calculate the scattering angle,  $\theta$ . The triangle is composed of are the distance of closest approach,  $r_0$ , between the atoms, the radii of projectiles,  $\rho_1$  and  $\rho_2$ , and the correction terms,  $\delta_1$  and  $\delta_2$ , for different atomic potentials.

#### 4.3.1 The SRIM Monte Carlo Computer Code

SRIM allows the user to change and select various input variables. These include the  $E_d$ , the angle of incidence,  $\theta$ , the phase of the target material, density, lattice energy, surface binding energy, number of ions, ion species and type of calculation. SRIM is capable of calculations for multi-layered targets (up to eight layers) with complex compositions. SRIM does not take into account the crystal structure of the material and calculates the damage for an implantation at 0 K [289].

SRIM uses the Monte Carlo method to distribute collisions along trajectories with a straight flight path assumed between them [289]. This procedure is applied for the ion itself and then every displaced target atom. For each collision, the impact parameter is calculated and the smallest deflections in the trajectory of the ion due to glancing collisions are ignored. If the energy transferred is greater than  $E_d$  then the atom is displaced. After a collision, if the remaining energy of the displacing atom is less than  $E_f$  and the energy of the displaced atom is greater than  $E_d$  then the displacing atom is considered to have replaced the displaced atom. In the case of the ion this is considered to be implanted or if the displacing atom is a target atom then this is considered to be a replacement collision. SRIM records the positions of vacancies (displacements), interstitials (knock-ons which have come to rest), replacement collisions (vacancies filled by displacing atom) and ions which have come to rest. The code is run until the energies of the ion and displaced atoms leave the target or are below a final cut off energy,  $E_f$  (for example, SRIM uses 2 eV for Si). Electronic energy loss is considered as a constant effect in the SRIM calculations.

For high energy particles, typically with energy is  $>100$  keV/amu, the impact parameter,  $P$  (see Figure 4.8) is small, and collisions that causes scattering  $> 1^\circ$  are



rare and so the treatment in SRIM is different to increase computational efficiency. The free flight path,  $L$ , (see Equation 4.4) for higher energies is calculated as the distance between collisions which would result in a displacement and thus non-displacing collisions are ignored. In addition, SRIM performs a check on  $L$  that the electronic energy loss is less than 5% of the ion energy between collisions. For the lowest energy particles, the mean interatomic spacing,  $N^{-1/3}$ , is used instead of  $L$ .

### 4.3.2 Types of Damage Calculation

SRIM offers several calculation modes which can be selected depending on the information required and offer trade-offs between their computational speeds and the quality of the statistics they produce. These modes are discussed below.

#### 4.3.2.1 Ion Distribution and Quick Calculation of Damage

This type of calculation estimates the damage produced by the incident ions using a quick statistical method based on the Kinchin-Pease (K-P) model [300]. This mode of calculation in SRIM estimates the distribution of ions in the material, energy loss and transfer to recoil atoms, as well as the number of backscattered and transmitted ions. This mode does not include replacement collisions and sputtering. The Monte Carlo is not run for every recoil but rather the number of displacements,  $N_d$ , is calculated by the revised K-P formula using Equation 4.8:

$$N_d = \begin{cases} 0 & \text{when } E < E_d \\ \frac{0.8E}{2E_d} & \text{when } E > 2E_d \end{cases} \quad \text{Equation 4.8}$$

where  $E$  is the PKA energy.

#### 4.3.2.2 Detailed Calculation of Damage with Full Damage Cascades

This mode of calculation in SRIM calculates the displacement damage in detail and the Monte Carlo code is run for every recoil until its energy drops below  $E_f$ .

#### **4.3.2.3 Monolayer Collision Steps**

This mode of calculation uses the Monte Carlo method in such a way so as to allow a collision in each monolayer of the target. The concept of free flight path is therefore not employed in this type of calculation. However, this causes the computational time be much longer for this type of calculation.

#### **4.3.2.4 Calculation of Surface Sputtering**

This mode of calculation is similar to the monolayer collision steps mode and is used to better estimate sputtering. It allows the user to analyse sputtering plots and their variation as a function of surface binding energy.

#### **4.3.2.5 Other Methods of Calculations**

Further to the calculation modes described above, SRIM can also calculate the damage caused by the cascades of other particles such as electrons, photons or neutrons and ions of different starting energies or with varying angle of trajectories to the target surface.

### **4.4 SRIM Outputs**

The number of displacements produced by the ions and recoil atoms in the target material can be obtained from the outputs of SRIM using Equation 4.9:

$$\text{Displacements} = \text{Vacancies} + \text{Replacement Collisions} \quad \text{Equation 4.9}$$

The number of interstitials in SRIM calculations is a bit less than the number of vacancies. This is due to the fact that SRIM only considers those ions and recoil atoms which do not leave the target and when a recoil leaves the target it reduces the number of interstitial by one:

$$\text{Vacancies} = \text{Interstitials} + \text{Atoms Exited Target}$$

*Equation 4.10*

The SRIM output files are generated and stored. These give information on such things as the: distribution of displacements; distribution of stopped ions; ion and recoil atom energy loss; sputtering; and phonon generation etc. The data can be displayed within SRIM in 2D or 3D plots as well as being exported to third-party software for further analysis.

Statistical data is accumulated on the ion-solid interactions by repeatedly running the Monte Carlo code to determine the average statistical projected range and damage profile with a maximum accuracy of  $\approx 5\%$  [289].

## **4.5 Modelling Radiation Damage in Nanowires Using SRIM**

### **4.5.1 Threshold Displacement Energy of Silicon**

The average kinetic energy needed to remove an atom from a lattice site is known as threshold displacement energy,  $E_d$ . When the transferred energy,  $E$ , is greater than  $E_d$ , an atom acquires sufficient energy to leave its lattice site and a Frenkel pair is created. It has remained as a difficult task to determine  $E_d$  due to its anisotropic nature. A wide range of experimental and computational values from 12.5 to 25 eV is reported in the literature [167], [301]–[307]. The accepted values for  $E_d$  in Si is typically 20 eV [308] and has thus been used for the SRIM calculations in this thesis.

### **4.5.2 Multislice SRIM Method**

SRIM is able to calculate damage profiles for planar and layered surfaces but not for other geometries such as a cylindrical NW. Therefore, the damage and implantation caused by an ion beam were modelled by developing the multislice approach discussed below using SRIM version 2013. An example of a SRIM input file and the MatLab code are presented in Appendix A.

For the first version of this custom implementation of SRIM, the circular NW cross-section was divided into 11 slices which were calculated individually in SRIM and manually processed in a spreadsheet. This approach was then developed using MatLab to automate the running of SRIM and processing of the data allowing the number of slices to be increased to 100. Each slice corresponds to a rectangle with a length equal to the chord length,  $x$ , at the corresponding position across the circle. These slices are shown schematically in Figure 4.9. The calculation of  $x$  for each slice was performed using the Pythagoras theorem as defined in *Equation 4.12*. A dummy gas of H with the minimum allowed density of  $10^{-7} \text{ g.cm}^{-3}$  was used for slices for which  $x$  was less than  $2r$  in order to maintain the length scale in the SRIM output files.

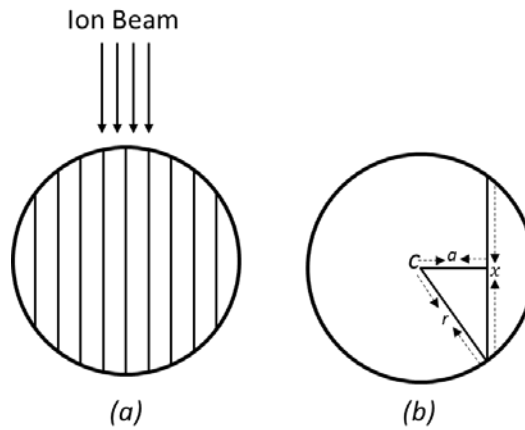


**Figure 4.9:** Diagram showing: (a) division of NW geometry into multiple slices to allow application of SRIM calculations; and (b) calculation of chord length,  $x$ , at distance,  $a$ , from centre,  $C$ , of a NW of radius,  $r$ , used to determine target thickness for the input parameters for the corresponding SRIM calculation.

$$\left(\frac{x}{2}\right)^2 = (r^2 - a^2) \quad \text{Equation 4.11}$$

$$x = 2\sqrt{(r^2 - a^2)}$$

*Equation 4.12*

where  $x$  is the chord length to be calculated,  $r$  is the radius of the NW being considered and  $a$  is the perpendicular distance from the centre of the circle to the chord.

The ion-beam-induced displacements and implantation profiles in the NW were obtained from SRIM using this multislice approach and the results are shown in Figure 4.10. Two-dimensional plots of damage and implantation profiles as well as the local excesses of interstitials and vacancies were generated from the resulting datasets.

The first version of this approach used the “Detailed calculation of damage with full damage cascades” option and input parameters of  $E_d = 15$  eV,  $N = 5 \times 10^{22}$  atoms.cm<sup>-3</sup>,  $E_{\text{surf}} = 4.7$  eV and  $E_{\text{lattice}} = 2$  eV. In the latter implementation within Matlab,  $E_{\text{surf}} = 0$  eV and  $E_{\text{lattice}} = 0$  eV were used as proposed by Stoller *et al.* [309] and a more appropriate value of  $E_d = 20$  eV [308] was used.

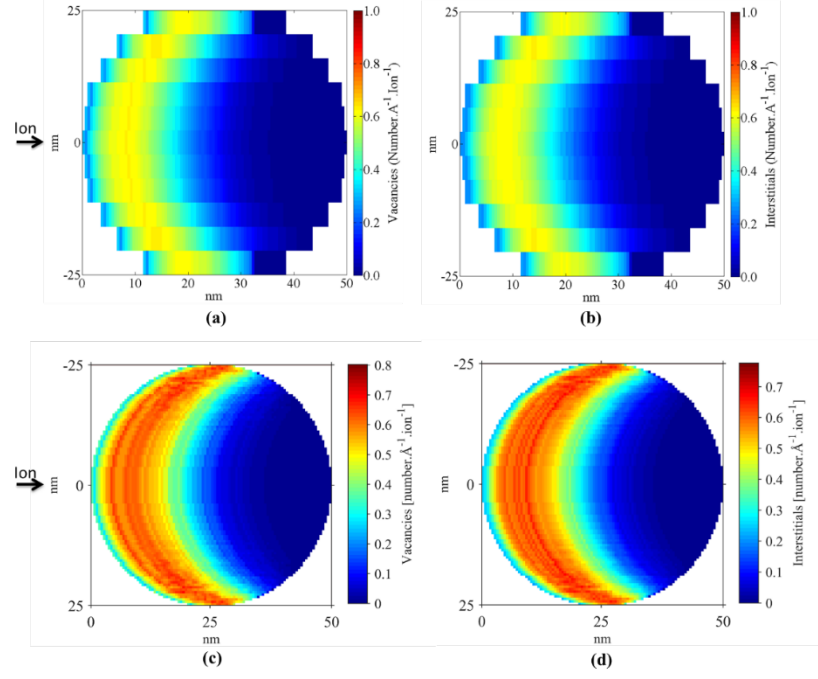


**Figure 4.10:** Plots of vacancies (a, c) and interstitials (b, d) created by 6 keV  $\text{Ne}^+$  ions incident upon a 50 nm Si NW obtained using the multislice SRIM method. The results of the first implementation of this approach are shown in (a) and (b) with the results of the improved MatLab code is shown in (c) and (d).

#### 4.6 Selection of Ion Irradiation Conditions

Ion irradiation can cause displacement of atoms and accumulation of damage ultimately potentially resulting in the amorphisation of a NW. However, the probability of the ions being implanted into the NW and the amount of damage they cause both vary as complicated functions of ion species, energy, NW composition and NW diameter. Implanted ions may perturb the damage accumulation and/or recrystallisation processes under study. Therefore, it is desirable to design irradiation conditions for experiments to achieve maximum damage with the minimum amount of implanted ions.

For this purpose, calculations of the displacement per ion for different ions at different energies were obtained using SRIM-2013. The displacements per atom (DPA) threshold for the ion-irradiation-induced amorphisation of Si in the keV regime was obtained from the literature for different noble gases [59-61]. The noble

gases have complete in outermost shells of electrons and are thus chemically stable and hardly react with other elements. The threshold DPA for amorphisation is defined as the minimum displacement per atom required for amorphisation in the target material. Based on the threshold DPA values, the threshold fluence for amorphisation was obtained by considering the following Equation 4.13:

$$Fluence = DPA \times Atomic\ Density \times \frac{Depth\ of\ Amorphous\ Layer}{\frac{Displacements}{Ion}\ in\ Amorphous\ Layer}$$

*Equation 4.13*

Once the threshold fluence for amorphisation of Si was calculated using Equation 4.13, the atomic percentage of implanted gas at the threshold was obtained for different energies and for different thickness of Si. Figure 4.11 shows plots of percentage of ion implantation against ion energy for various Si NW thicknesses from 30 to 100 nm.

Threshold DPA for amorphisation at room temperature has been obtained from literature. However, for the NWs bending experiments, different irradiation conditions were employed either to confine the damage in the first half of the NW or to extend the damage and range of the ions from middle to the second half of the NWs and the specific irradiation conditions are discussed in detail in the result chapters 5–7.

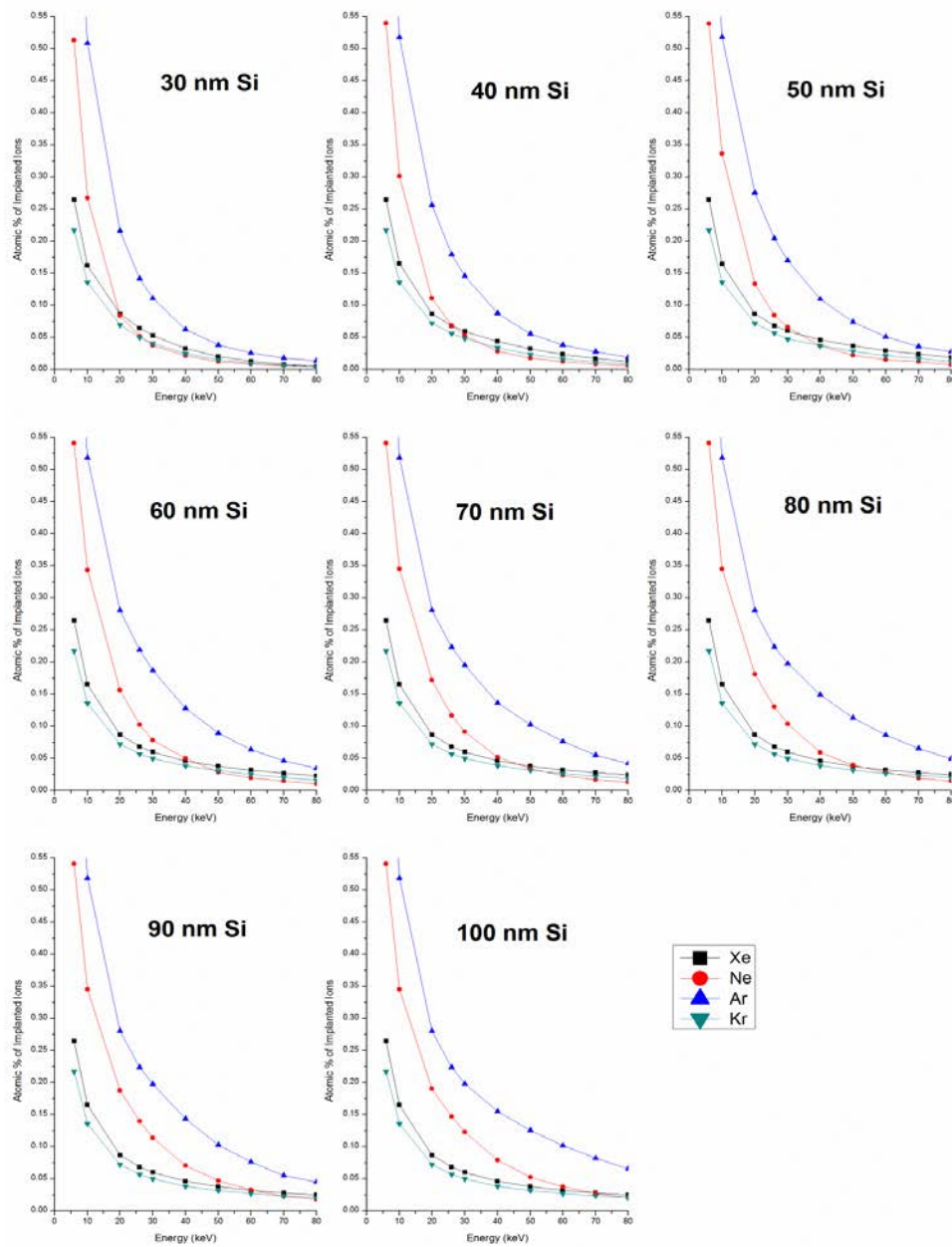


**Figure 4.11:** Atomic percentages of ion implantation at amorphisation against ion energy in different thickness of Si calculated using SRIM.

## 4.7 Summary

Ion solid interaction has been discussed in detail. SRIM is the most widely used open software to estimate damage and ion implantation in materials but is



applicable for flat surfaces. Physics of SRIM and different modes of calculation in SRIM has been discussed. To estimate the ion-beam-induced damage and ion implantation in NWs a multislice SRIM method has been introduced and a MatLab code has been developed to automate SRIM for non-planar geometries. The calculation of ion irradiation conditions was then performed using this approach and two-dimensional surface plots of NWs were produced to better understand the ion-beam-induced damage and ion implantation in NWs.

## 5 Bending of Silicon Nanowires

### 5.1 Introduction

The fabrication of NWs can be performed by a variety of physical and chemical methods as described in Chapter 2. These methods do not provide complete control of the morphology and alignment of the NWs during the growth process. Therefore, post-growth methods are often required to modify these parameters. In the literature, different authors have proposed various methods to control the alignment of NWs by suspending them in solution such as the blown bubble film technique [310] or by electrophoresis [311]. Ion irradiation effects on materials and nanostructures have been widely studied in the literature [105], [133], [145], [312], [313] and have been used to control the morphology, alignment and orientation of NWs [96], [105], [134]. This technique has certain advantages over the other methods reported in the literature [310], [311] to modify NWs because a large area could be irradiated. Furthermore, ion irradiation can be applied to modify NWs independently of the fabrication method and without the necessity to suspend the NWs in solution. The ion-beam-induced bending phenomenon first being reported by Stichtenoth *et al.* [314] as an unwanted effect while doping GaAs NWs with  $\text{Zn}^+$  ions.

This chapter deals with *in-situ* ion irradiation experiments within a TEM to study the bending, amorphisation and recrystallisation of Si NWs. The real-time dynamic and complex behaviour of defects produced in the materials under a range of irradiation conditions can be investigated through such experiments.

A series of *in-situ* irradiation experiments were carried out with  $\text{Ne}^+$  or  $\text{Xe}^+$  ion beams at room temperature to investigate the bending behaviour of Si NWs using the MIAMI facility at the University of Huddersfield. Here, the results of 6 keV and 60 keV  $\text{Ne}^+$  ion irradiations at room temperature whilst the  $\text{Xe}^+$  ion experiments, which

are specifically tailored towards practical industrial applications, are covered later in Chapters 6 and 7.

## 5.2 Ion Irradiation Conditions

The experiments were designed using the SRIM–2013 Monte Carlo code [288] (discussed in section 4.3.1) to explore the ion irradiation induced modification of Si NWs. The operating electron beam energy of the TEM was set to 100 keV in the experiments reported in this thesis because of the known effect of electron-beam-induced recrystallisation of isolated amorphous pockets in Si and may perturb the amorphisation experiment [315]. The recrystallisation rate of amorphous pockets in Si decreases with increasing electron beam energy from 50 keV and a minima has been reported at ~100 keV [315]. Silicon NWs with diameters of  $50 \pm 5$  nm were irradiated at room temperature with 6 keV or 60 keV  $\text{Ne}^+$  ion beams to confine the peak damage in first half of the NW and to fully amorphous NWs for recrystallisation (discussed in section 4.6), respectively. The angle of incidence of the ion beam was normal to the axis of NW in these experiments except where noted as otherwise.

The estimated projected range,  $R_p$ , of ions for 6 keV  $\text{Ne}^+$  ions in 50 nm of Si was calculated to be ~15.8 nm and is less than half the diameter of the NW. The distribution of the displacements and ion implantation (or range of the ions) caused by the  $\text{Ne}^+$  ions in 50 nm thick Si is illustrated in Figure 5.1. The total number of atomic displacements was calculated by summing up the vacancies and replacement collisions as per *Equation 4.9*.

The number of vacancies produced in the Si was calculated using SRIM and *Equation 4.10*. The Si recoil atoms estimated by SRIM are the sum of the interstitials and the replacement collisions. The number of interstitials can be calculated from the following *Equation 5.1*:

$$\text{Interstitials} = \text{Si Recoils} - \text{Replacement Collisions} \quad \text{Equation 5.1}$$

The distribution of vacancies and interstitials calculated through SRIM are shown in Figure 5.2.

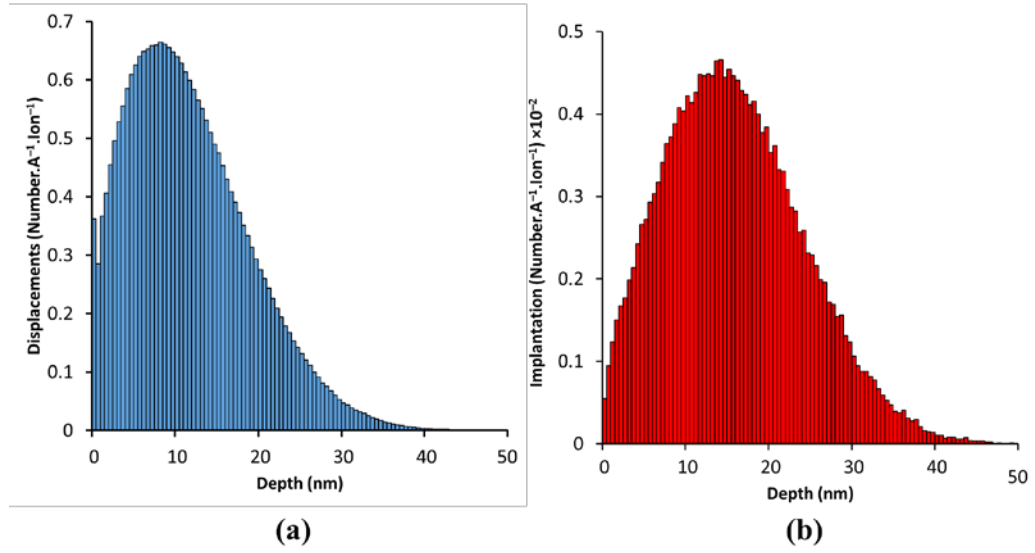


**Figure 5.1:** Distribution of the (a) atomic displacements and (b) ion implantation caused by 6 keV  $\text{Ne}^+$  ions in 50 nm thick Si obtained using SRIM [288].

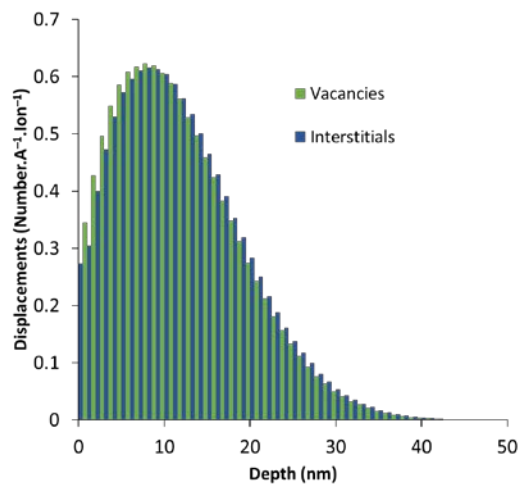


**Figure 5.2:** Vacancy and interstitial distributions in 50 nm thick Si irradiated with 6 keV  $\text{Ne}^+$  obtained using SRIM [288].

Two-dimensional surface plots for the total number of displacements, vacancies and interstitials caused by 6 keV  $\text{Ne}^+$  ions in a 50 nm diameter Si NW were created using SRIM and MatLab as described in chapter 4 and are shown in Figure 5.3 and 5.4:

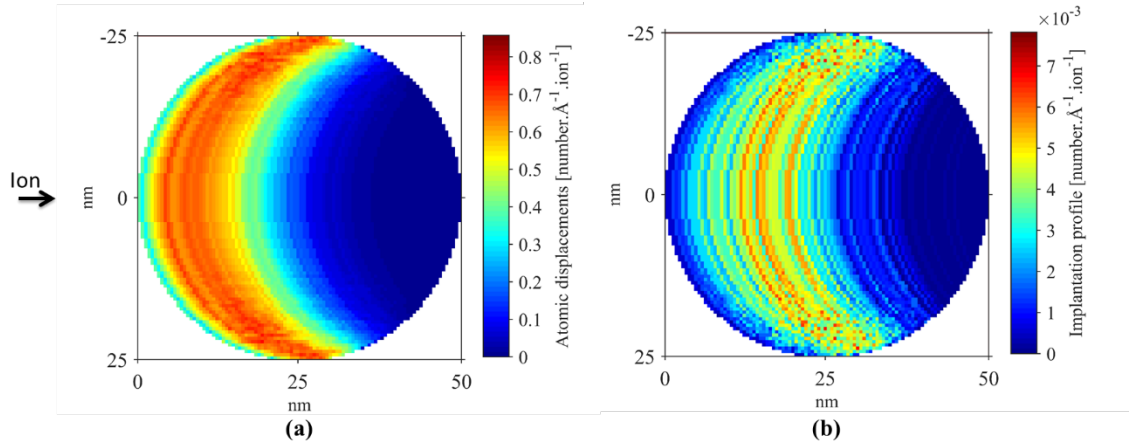


**Figure 5.3:** Two-dimensional representations of (a) displacement distribution and (b) ion implantation in a 50 nm diameter Si NW irradiated with 6 keV  $\text{Ne}^+$  ions.

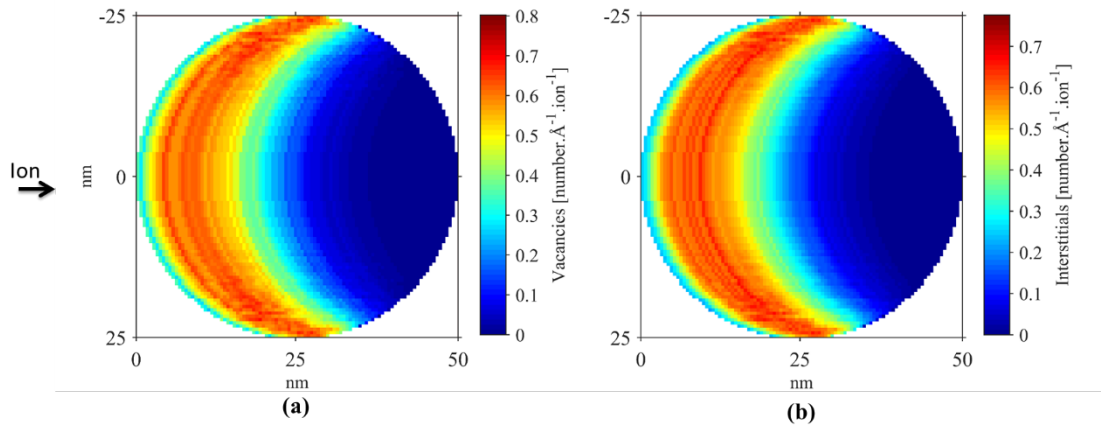


**Figure 5.4:** Two-dimensional representation of (a) vacancies and (b) interstitials created by 6 keV  $\text{Ne}^+$  ions in a 50 nm diameter Si NW.

For the amorphisation experiments on Si NWs, ion irradiation conditions were designed using SRIM to produce maximum damage with minimal ion

implantation. The selections of ion irradiation conditions are discussed in detail in Chapter 4. It was found from the results summarised in Figure 4.11 that 60 keV  $\text{Ne}^+$  ions were the most appropriate choice to produce maximum damage with the minimum amount of implanted ions for 50 nm thick Si. In order to produce 0.9 displacements per atom (the threshold dose for amorphisation of Si with  $\text{Ne}^+$  [316]), the threshold fluence for the amorphisation of 50 nm Si with a 60 keV  $\text{Ne}^+$  ion beam has been calculated to be  $8.2 \times 10^{14} \text{ ions.cm}^{-2}$ . The ion irradiation induced damage and ion implantation profiles for 60 keV  $\text{Ne}^+$  ions in 50 nm diameter Si NWs obtained from the multislice SRIM calculations are shown in Figure 5.5 and 5.6, respectively.

It has been shown in the SRIM results that 60 keV  $\text{Ne}^+$  ions cause significant damage in the Si compared to 6 keV  $\text{Ne}^+$  ions (see Figure 5.5). Range of 60 keV  $\text{Ne}^+$  ions in Si was calculated using SRIM to be  $\sim 129 \text{ nm}$  but the diameter of the typical NW used in irradiation experiments was  $\sim 50 \text{ nm}$ . This means that 60 keV  $\text{Ne}^+$  ions can produce a significant damage to transform the crystalline NW into amorphous.

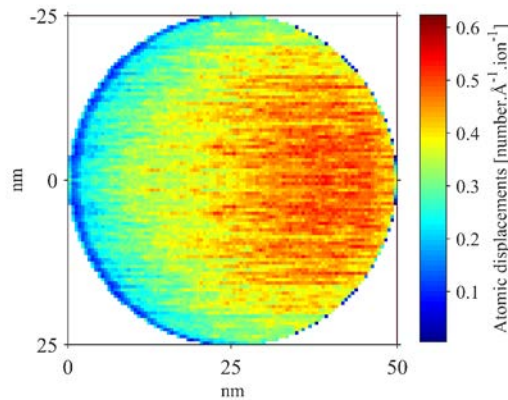


**Figure 5.5:** Distribution of displacement caused by 60 keV  $\text{Ne}^+$  ions in 50 nm diameter Si NW calculated using the multislice SRIM method.

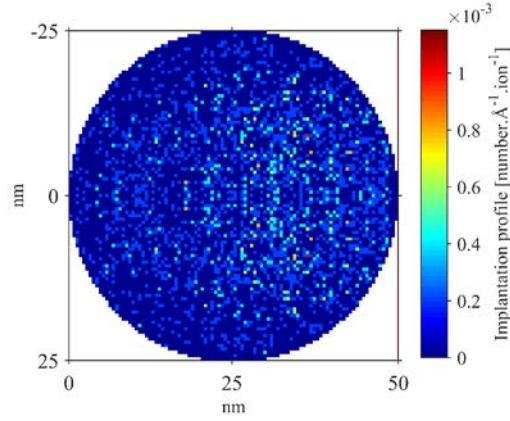


**Figure 5.6:** Ion implantation profile of 60 keV  $\text{Ne}^+$  ions in 50 nm diameter Si NW calculated using the multislice SRIM method.

Ion irradiation conditions were designed with 6 keV  $\text{Ne}^+$  ions to confine the peak damage in first half of the NW to investigate the NWs bending. In second stage, experiments were designed to subsequently irradiate the bent NW with 60 keV  $\text{Ne}^+$  to achieve fully amorphous phase to explore the behaviour of bent NWs upon thermal annealing.

### 5.3 Procedure for Nanowire Bending Experiments

Silicon NWs were irradiated at normal incidence in these experiments following the procedure discussed in chapter 3. However prior to irradiation, the NW was brought back to the *zero-rotation zero-tilt* position. The NW was then orientated to *zero-rotation minus-30°* by rotating the goniometer CW and a SAED pattern was captured as shown in Figure 5.8. As the ion beam forms an angle of 30° to the electron beam in the MIAMI facility and the NW was orientated normal to the ion beam during irradiation, this SAED pattern corresponded to the crystallographic orientation of the NW as seen by the ion beam. This information could be used to explore the possibility of channelling having occurred should this be required in post-analysis. This tilt-rotation procedure is illustrated in Figure 5.7.

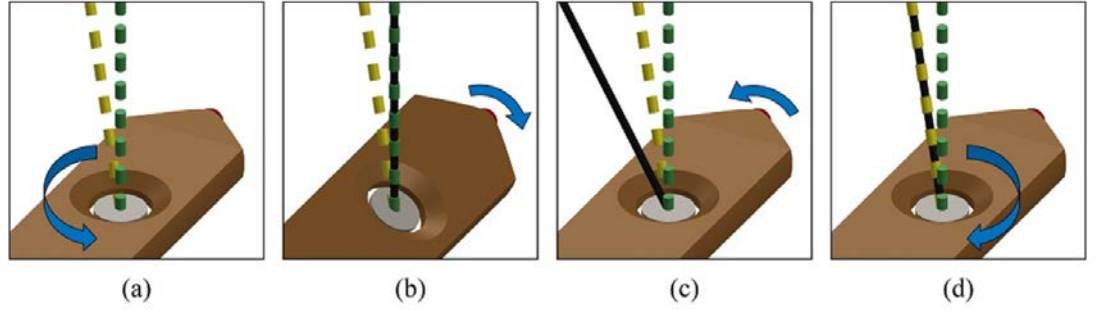


**Figure 5.7:** Illustration of the tilt and rotate procedure with the electron beam (shown in green) and the ion beam (shown in yellow): a) the selected NW is rotated to align with the x-axis of the TEM; b) the NW is then tilted to  $-30^\circ$  to capture the SAED corresponding to the crystallographic direction in which the irradiation will subsequently be performed (represented by a solid black line); c) the NW is next tilted back to the zero position; and d) is rotated to plus- $45^\circ$  such that the ion beam is normal to the axis of the NW.

To get the NW into the desired orientation for irradiation, it was tilted back to the *zero-rotation zero-tilt* position and rotated *plus- $45^\circ$*  CW so that it became oriented normal to the ion beam. This position will be referred to *zero-tilt plus- $45^\circ$ -rotation*.

After irradiation, the procedures described above were repeated to capture the corresponding post-irradiation images and SAED patterns.

## 5.4 Ion Irradiation Experimental Results

### 5.4.1 Bending of Silicon Nanowires

Silicon NWs were irradiated at the *zero-tilt plus- $45^\circ$ -rotation* position with 6 keV  $\text{Ne}^+$  ions at room temperature to fluences in the range from  $3.7 \times 10^{15}$  to  $1.7 \times 10^{17}$  ions. $\text{cm}^{-2}$ . The NWs irradiated all had diameters of  $50 \pm 5$  nm and were observed to bend during the *in-situ* ion irradiation experiments. The damage caused by the 6 keV  $\text{Ne}^+$  beam predominantly accumulates in the irradiated side of the NW and the



majority of the implanted ions are also confined in the first half of the NW as shown in the Figure 5.3.

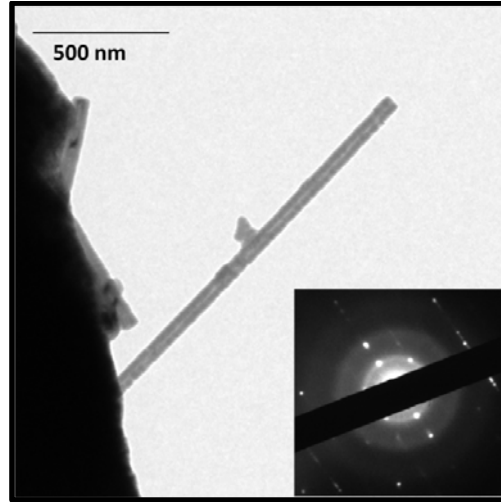


**Figure 5.8:** A SAED pattern captured during the tilt-rotation procedure illustrated in Figure 5.7 showing the crystallographic direction presented to the ion beam.

It was observed during all these irradiation experiments performed with  $\text{Ne}^+$  ions that the Si NWs demonstrated bending. A typical example of a Si NW irradiated with a 6 keV  $\text{Ne}^+$  ion beam to a fluence of  $5.2 \times 10^{16} \text{ ions.cm}^{-2}$  is shown in Figure 5.9.

The virgin and bent Si NW at *zero-rotation zero-tilt* is shown in Figure 5.9 b and e, respectively. The tilt series of the NW was performed and is shown in Figure 5.9 reveals that the NW bend towards the ion beam under these irradiation conditions. This is contrary to the results obtained by Borschel *et al.* [55] in which the GaAs NWs were irradiated with either 35 keV  $\text{Ar}^+$  or 30 keV  $\text{S}^+$  ions. Since  $R_p$  for the 6 keV  $\text{Ne}^+$  ions in 50 nm Si is less than half the diameter of the NWs, the majority of the ions stopped in the irradiated side of the NW. In this situation, according to the conclusions of Borschel *et al.* [55], the NW should bend in the opposite direction relative to the ion beam (i.e. away).

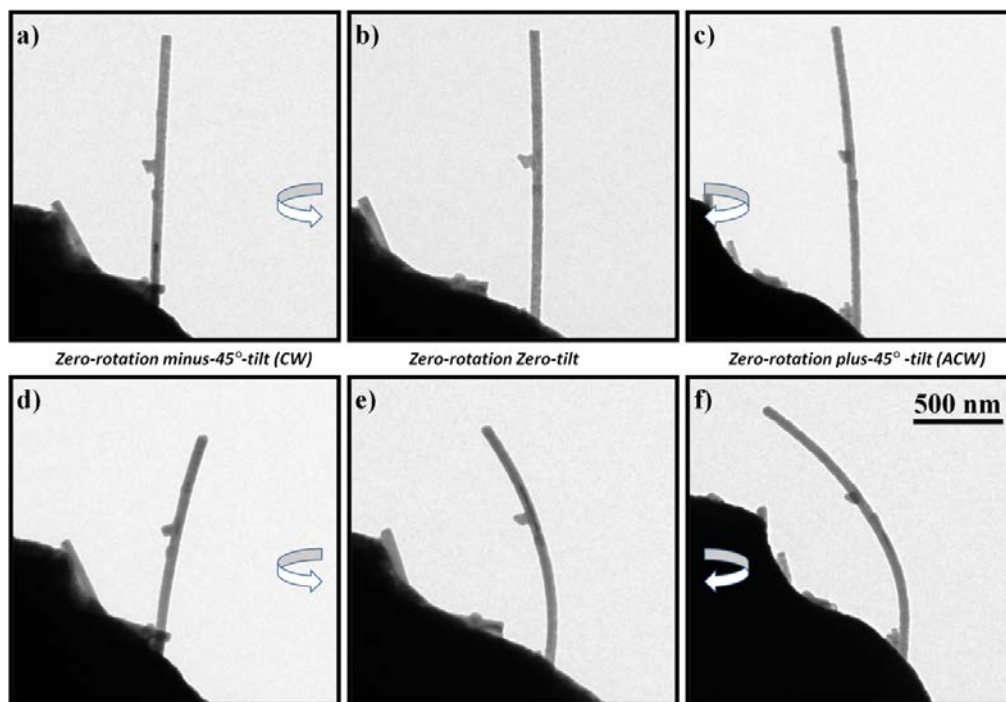


**Figure 5.9:** Micrographs showing the tilt image series of an Si NW before (a to c) and after (d to f) ion irradiation. The series was captured by tilting the NW at plus-45° (c and f) and minus-45° (a and d) about the x-axis of the TEM. The NW was irradiated with 6 keV Ne<sup>+</sup> ions to an end fluence of  $5.2 \times 10^{16}$  ions.cm<sup>-2</sup>. The scale bar in f) applies to all images.

Ion-irradiation induced bending phenomenon is a plastic deformation and NWs remained bent when observed few months after irradiation. It was also observed that the NWs undergo bending as soon as the ion irradiation was started and therefore before any amorphous material could have accumulated. This is contrary to the behaviour reported in [185] that bending occurred only in those NWs which were fully amorphous. A BF-TEM image of one of the irradiated NW with the corresponding SAED pattern is shown in Figure 5.10 which clearly demonstrates that the Si NW bending before acquiring a fully amorphous phase.

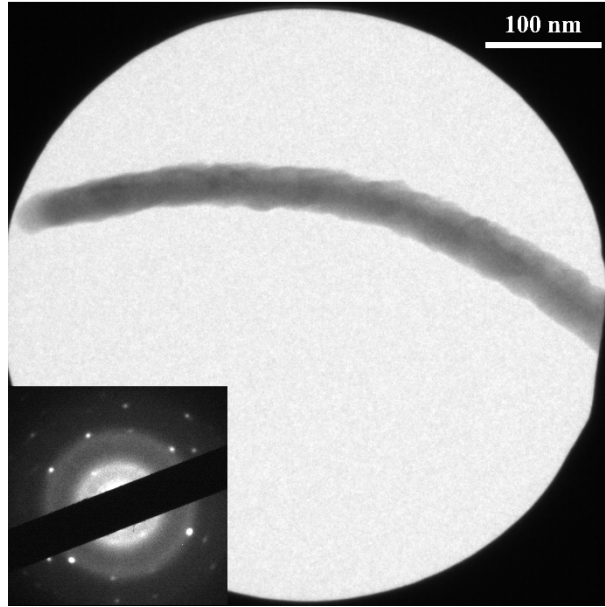


**Figure 5.10:** A BF-TEM image of the bent Si NW irradiated with 6 keV Ne<sup>+</sup> ions to a fluence of  $1.1 \times 10^{16}$  ions.cm<sup>-2</sup>. The inset shows the SAED pattern with intense bright spots clearly demonstrating the residual crystallinity.

A typical example of a bent Si NW after irradiation with 6 keV Ne<sup>+</sup> ions to a fluence of  $3.5 \times 10^{16}$  ions.cm<sup>-2</sup> is shown in Figure 5.11b. In order to investigate the behaviour of the bent NWs (Figure 5.11b) when subsequently irradiated for a second time from the back side, the grid was removed from the microscope, flipped (turned upside down) and remounted in the rotation holder. The flip operation was necessary to irradiate the NW from back side because of the holder limitations and potential ion beam shadowing effect. Also, the holder had a nominal range of rotation angles of  $\pm 180^\circ$  but slip during operation can prevent access to the full range of rotation.

For the experiment shown in Figure 5.11, unfortunately the bent NW from the first irradiation step was lost and so an adjacent NW from the same area was used for the second irradiation. The loss of the original NW was probably due to it becoming detached from the grid during the flip operation or because other material shifted into a position so as to create an obstruction. Once flipped, the bent NW was then rotated such that the ion beam was normal to the axis of the NW at its base. The angle of incidence of the ion beam was measured from the bottom of the NW which was attached to the grid and demonstrated no bending probably due to shadowing effects

from the grid. The NW was then irradiated from the opposite side to the original irradiation at normal incidence with 6 keV  $\text{Ne}^+$  ions to a fluence of  $3.0 \times 10^{16} \text{ ions.cm}^{-2}$ . It was observed during this irradiation that the bent NW first straighten and then continue bending towards the ion beam as shown in the image sequence in figure 5.13.

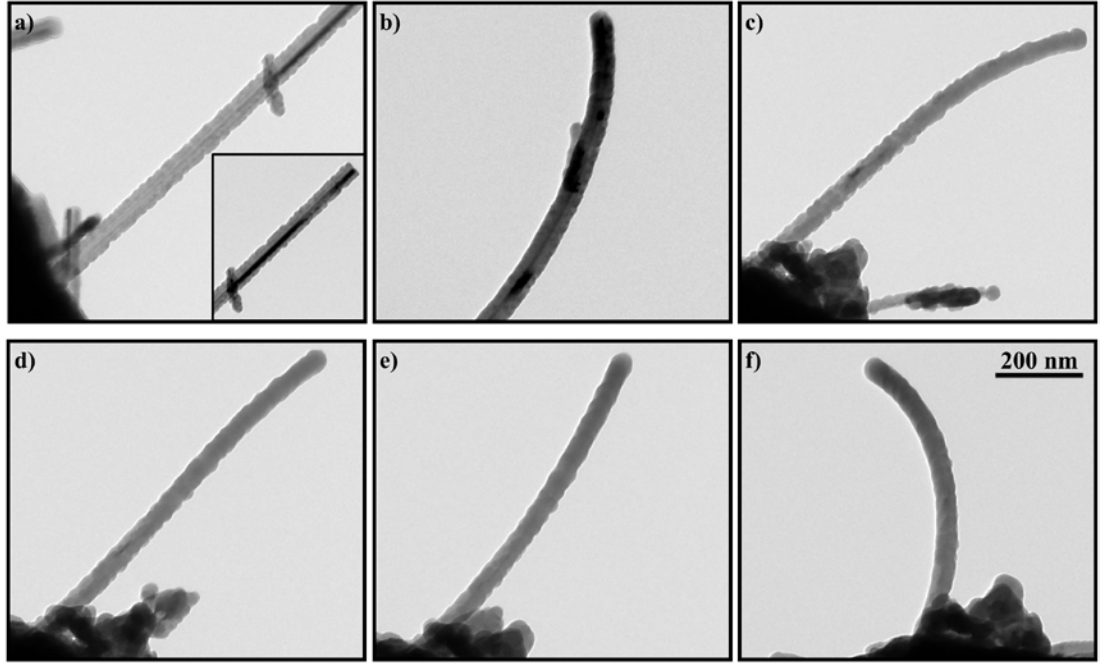


**Figure 5.11:** Micrographs showing a Si NW undergoing bending when irradiated with 6 keV  $\text{Ne}^+$  ions: (a) virgin NW with inset showing tip of NW; (b) the NW bends towards the ion beam during irradiation to a fluence of  $3.5 \times 10^{16} \text{ ions.cm}^{-2}$ ; (c) the sample was flipped to allow irradiation from the opposite side; (d) a bent NW demonstrates straightening when subsequently irradiated from the opposite side to a fluence of  $1.3 \times 10^{16} \text{ ions.cm}^{-2}$ ; and (e–f) continued to bend back towards the ion beam. The fluences for (e) and (f) are  $1.6 \times 10^{16}$  and  $2.4 \times 10^{16} \text{ ions.cm}^{-2}$ , respectively. The scale bar in (f) applies to all images.

In the irradiation experiments carried out with the pre-irradiated bent NWs, it has been observed that NWs which had previously experienced ion-beam-induced bending in one direction would bend in the reverse direction when irradiated from the opposite side. In so doing, the bent NWs first straightened (Figure 5.11d) and then continued to bend towards the ion beam direction (Figure 5.11e–f). The ion-beam-induced bending direction of the NWs were confirmed at each step by obtaining a tilt image series. It has therefore been demonstrated that the ion-beam-induced bending under these conditions was towards the ion beam and that not only could the NWs be straightened using ion irradiation but that the bending direction could actually be reversed.

#### 5.4.2 Fully Amorphous Silicon Nanowires

The bent Si NWs which contained radiation damage after irradiation with 6 keV Ne<sup>+</sup> ions were fully amorphised by further irradiation with 60 keV Ne<sup>+</sup> ions. The objective of this was to create fully amorphous NWs with which to explore the process of recrystallisation during annealing.

An example of a typical Si NW shown in Figure 5.12a was then bent under 6 keV Ne<sup>+</sup> ion irradiation as shown in Figure 5.12b. The bent NW was then irradiated with 60 keV Ne<sup>+</sup> ions at room temperature to a fluence of  $6.1 \times 10^{15}$  ions.cm<sup>-2</sup> which is seven times higher than the threshold fluence ( $8.2 \times 10^{14}$  ions.cm<sup>-2</sup>) calculated for amorphisation of 50 nm thick Si with 60 keV Ne<sup>+</sup> ions. At a fluence of  $6.1 \times 10^{15}$  ions.cm<sup>-2</sup>, the 60 keV Ne<sup>+</sup> ions will produce on average ~ 4.5 DPA in 50 nm thick Si with a minimum of ~2 DPA at the lowest point of the damage profile. Thus causing the complete amorphisation of the Si NW as the threshold dose for amorphisation with keV Ne<sup>+</sup> ions is 0.9 DPA [316].

The SAED patterns shown in Figure 5.12 demonstrate the transformation of the crystalline diffraction spots into amorphous rings and that the crystal phase could no longer be detected at a fluence of around  $3 \times 10^{15}$  ions.cm<sup>-2</sup>. Irradiation was continued to twice the fluence required to remove the diffraction spots to ensure complete amorphisation had been achieved.

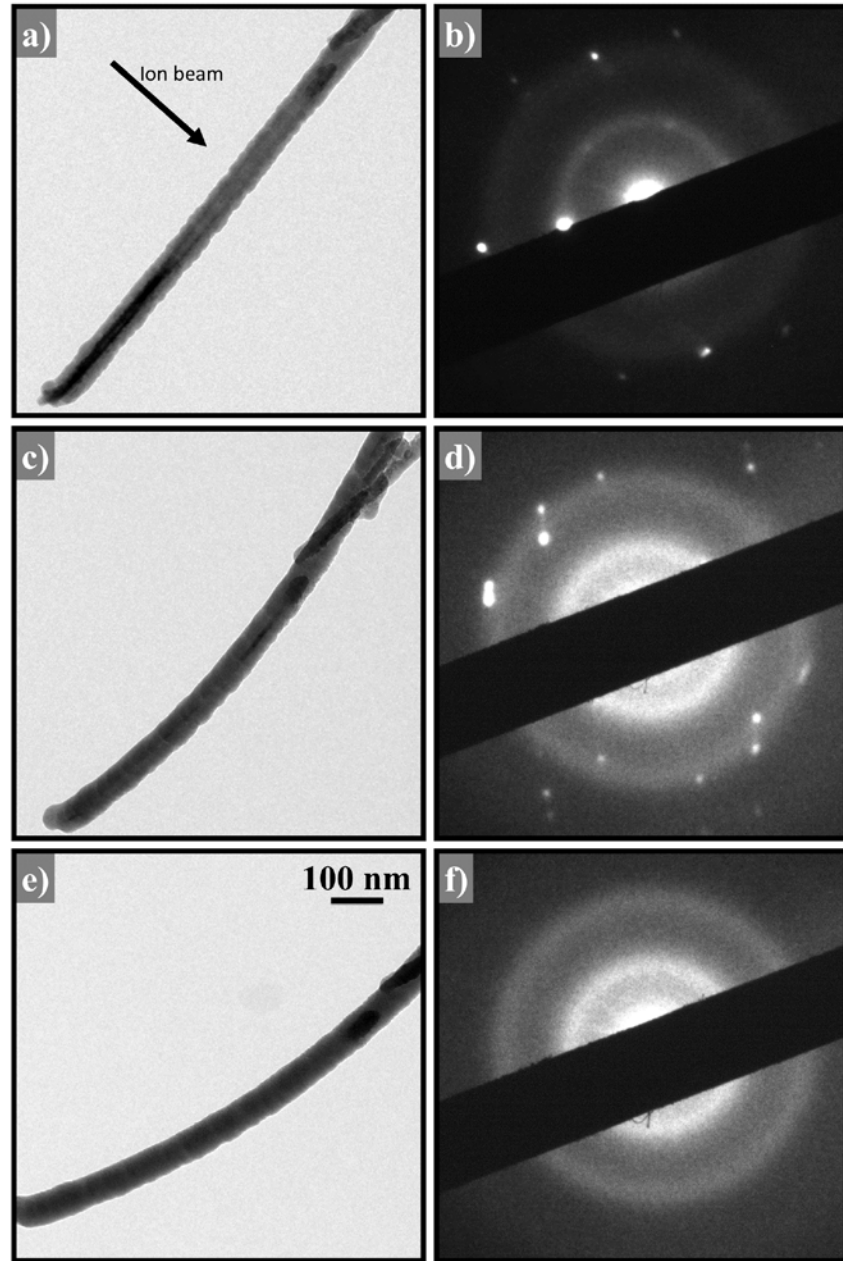


**Figure 5.12:** BF-TEM images showing a Si NW at zero-tilt plus-45°-rotation: (a) virgin NW with corresponding SAED pattern shown in (b); (c) irradiated with 6 keV  $\text{Ne}^+$  ions to a fluence of  $5.2 \times 10^{16} \text{ ions.cm}^{-2}$  shows bending of the NW with corresponding SAED pattern shown in (d) demonstrating the residual crystallinity; (e) fully amorphous NW irradiated with 60 keV  $\text{Ne}^+$  ions to a fluence of  $6.1 \times 10^{15} \text{ ions.cm}^{-2}$ ; and (f) the absence of any detectable crystallinity is confirmed in the corresponding SAED pattern. The scale bar is the same for all images.

Although the theoretical considerations above predicted that amorphisation should have been achieved at a lower fluence, the varying angle of incidence along the bent NW would have influenced the range of the 60 keV  $\text{Ne}^+$  ions into the Si resulting in higher fluences being required to fully amorphise material towards the tail of the damage distribution. In other words, higher angles of incidence in the bent section of the NW would have increased the effective thickness of the NW. Furthermore, the known recrystallisation effects of the electron beam, although minimised at 100 keV [317], may also have played a role in increasing the effective amorphisation fluence.

## **5.5 Recrystallisation of Silicon Nanowires**

Having been amorphised, the Si NWs were recrystallised by thermal annealing. The temperature was ramped directly from room temperature to 400°C in the first instance with a ramp rate of 20°C.min<sup>-1</sup>. The temperature was then ramped at the same rate from 400°C to 600°C pausing in increments of 50°C in order to facilitate the acquiring of BF images and DPs. After 600°C, the temperature ramp was continued with dwells at increments of 20°C until no further recrystallisation was detected in the DP with increasing temperature. A dwell time of 10 minutes was kept constant between each stage in the temperature ramp to allow the sample to stabilise. The temperature ramp used in these experiments is plotted against the time in Figure 5.13.

Thermal annealing was able to recover the damage produced by the 6 keV and 60 keV  $\text{Ne}^+$  ion irradiation in the NWs by inducing a transition from the amorphous to the crystalline phase. Recrystallisation into single crystal and/or, polycrystalline material were observed in the thermal annealing experiments. A range of activation temperatures were observed during the annealing experiments. Some of the irradiated NWs recovered at temperatures as low as 550°C but for others the recrystallisation temperature was higher up to a maximum of 740°C. Typically, recrystallisation was found to occur around 640°C.

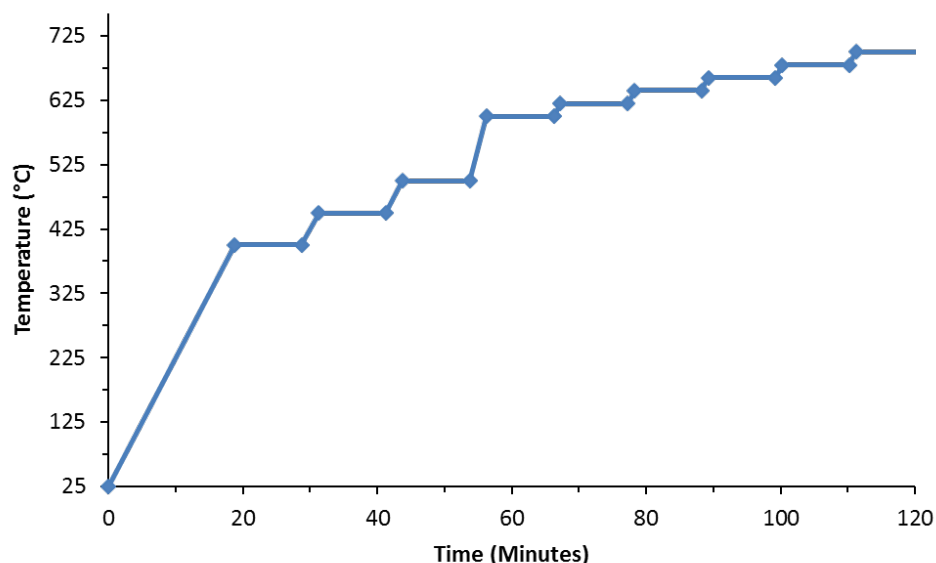


**Figure 5.13:** Graph showing the temperature ramp versus time used to monitor the recrystallisation of amorphous Si NWs. The temperature increment was reduced above 400°C and then again above 600°C to allow the recrystallisation of the NWs to be monitored more closely.

No correlation has been found between the diameter of the NWs and recrystallisation temperature as measured by the thermocouple of the heating sample holder. Furthermore, the NWs which were bent under ion irradiation were found to remain bent after thermal annealing contrary to the results reported in [53]. An example of typical Si NW which was bent using irradiation with 6 keV Ne<sup>+</sup> ions and then subsequently amorphised with 60 keV Ne<sup>+</sup> ions before recrystallisation via thermal annealing is shown in Figure 5.14.

Recrystallisation in Si is thought to occur via one of the two mechanisms (discussed in Chapter 5): bond rearrangement at the c–a interfaces or IV pair recombination [174], [175]. Polycrystalline growth has been attributed to RNG in which crystallites randomly nucleate in the amorphous material and grow until they intersect with a neighbouring crystallite or surface.



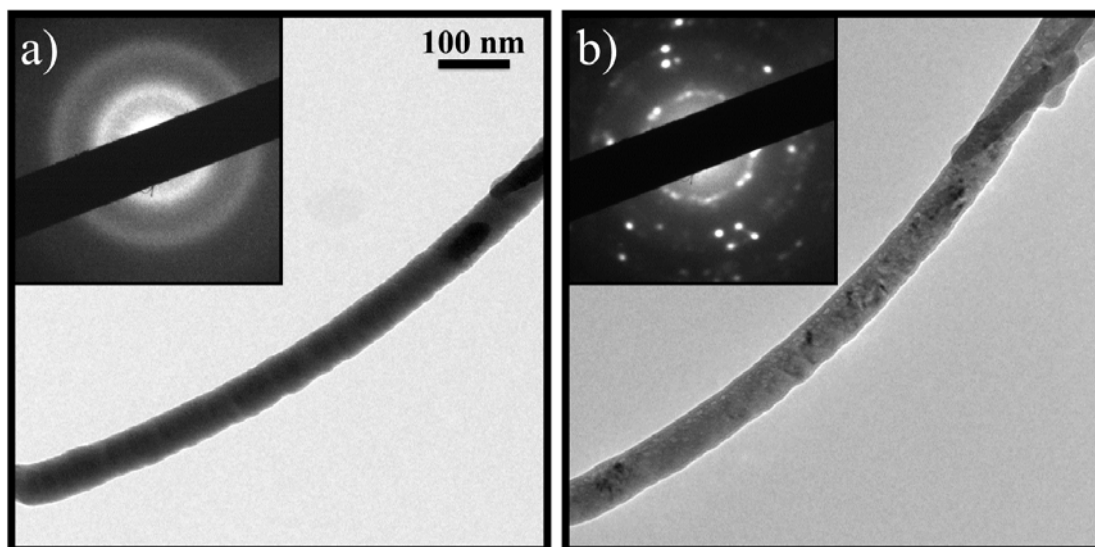


**Figure 5.14:** Micrographs showing: (a) amorphous Si NW after 60 keV Ne<sup>+</sup> ion irradiation to a fluence of  $6.1 \times 10^{15}$  ions.cm<sup>-2</sup>; and (b) recrystallisation of the Si NW achieved through thermal annealing to 720°C. The insets show the corresponding SAED patterns with amorphous rings transitioning into a pattern featuring bright spots indicative of a significant single crystalline region in combination with rings characteristic of polycrystalline material. This suggests that the recrystallisation occurred via a mixture of SPEG and RNG.

The insets show the corresponding SAED patterns with amorphous rings transitioning into a pattern featuring bright spots indicative of a significant single crystalline region in combination with rings characteristic of polycrystalline material. This suggests that the recrystallisation occurs via a mixture of RNG and SPEG. A typical example of mixed growth recovery is shown in Figure 5.14 illustrating mixed growth with intense bright spots reflecting the SPEG and RNG due to the less intense spots around the amorphous rings.

In these experiments, the Si NWs were not straightened after thermal annealing regardless of whether SPEG, RNG or mixed regrowth (SPEG and RNG) occurred. This is again contrary to results described previously in the literature [185] where bent Si NWs have been reported to straighten upon thermal annealing.

Another interesting phenomenon observed during thermal annealing was the increased bending in some of the already-bent Si NWs. This is again contrary to the results described previously in the literature [185] that the bent NWs straighten upon thermal annealing.

## 5.6 Summary

*In-situ* ion-irradiation-induced bending of Si NWs was observed under 6 keV and 60 keV Ne<sup>+</sup> ions. It has been observed that NWs starts bending immediately after irradiation and does not require a fully amorphous state as reported in [185]. Tilt image series was performed to determine the bending direction of NWs. Already bent NWs were subsequently irradiated with 60 keV Ne<sup>+</sup> ions to create fully amorphous NWs. Amorphous NWs were then recrystallised to explore the effect of straightening upon thermal annealing. However no straightening of fully amorphous bent NWs was observed during these experiments.

## 6 Comparative Experiments to Borschel

### 6.1 Introduction

Silicon NWs have been observed to bend when irradiated with an ion beam. They were observed to bend towards the ion beam when irradiated with 6 keV  $\text{Ne}^+$  ions which is opposite to the behaviour of GaAs NWs irradiated with different ions (35 keV  $\text{Ar}^+$  or 30 keV  $\text{S}^+$ ) reported by Borschel *et al.* [318]. As that is a key publication in the literature on the topic of ion-irradiation-induced bending of semiconductor NWs, the objective of the experiments presented in this chapter was to explore the ion-irradiation-induced bending of Si NWs under comparable conditions.

Borschel *et al.* [318] identified the distribution of point defect accumulation as a driving mechanism for semiconductor NW bending [318]. The GaAs NWs reportedly bent towards the ion beam when the range of the ions was less than half the diameter of the NW and vice versa. Ion-beam-induced bending of semiconductor NWs and the underlying physics of the phenomenon is still not well understood in the literature and different authors [179]–[181], [185], [188], [318]–[320] have reported various mechanism to support their observations. Therefore, it was of interest to use the Si NWs and *in-situ* techniques of the current work to reproduce the conditions used by Borschel *et al.* [318] in an attempt to reproduce that study in Si.

The GaAs NWs reported on in [318] were irradiated whilst still attached to their growth substrate with different species ( $\text{Ar}^+$ ,  $\text{S}^+$  and  $\text{Xe}^+$  ions), at different energies (35 keV  $\text{Ar}^+$ , 30 keV  $\text{S}^+$  and 210 keV  $\text{Xe}^+$ ) and characterised *ex-situ* using scanning electron microscope. The GaAs NWs used in the experiments carried out by Borschel *et al.* were grown  $35^\circ$  off the substrate and were irradiated normal to the substrate (i.e.  $35^\circ$  off normal to the NW axis) [318]. The lower energy ions (35 keV  $\text{Ar}^+$  and 30 keV  $\text{S}^+$ ) were chosen by Borschel *et al.* to confine the damage caused by the ion beam in the irradiated side of the NWs while higher energies were used to accumulate the damage in the backside of the NWs. The ion irradiation conditions

for the experiments reported in this chapter were designed using SRIM by matching the damage depth,  $R_p$ , and DPA with the lower energy irradiation experiments of Borschel *et al.* [55]. The displacement energy,  $E_d$ , for Ga and As was found to have a wide range from 9 eV to 18 eV in the literature [321]–[325]. However, the most recent work of Follies [325] gives a value of 15 eV and this was used for the SRIM calculations presented here.

It was found that 5 keV and 9.5 keV  $\text{Xe}^+$  ion irradiation of 50 nm Si gave the best match for 35 keV  $\text{Ar}^+$  ion irradiation of 150 nm GaAs in terms of the peak damage depth and  $R_p$ , respectively. It was not possible to exactly match the irradiation conditions in terms of both the peak damage depth and  $R_p$  in a single irradiation because of the different atomic and physical properties of GaAs and Si. Therefore two sets of experiments using the two energies were performed. Furthermore, the incident angle reported in Borschel *et al.* [55] was initially incorrectly entered into SRIM as  $55^\circ$  from normal in the calculations used to design these experiments. However, repeat SRIM calculations using the correct value of  $35^\circ$  show that the errors introduced by this mistake was 10.5%. However, for the actually irradiation experiments reported here the angle of incidence was correctly set to be the same as in the work of Borschel *et al.* (i.e.  $35^\circ$  off normal to the NW axis).

## 6.2 Establishing Nanowire Orientation to Irradiate $35^\circ$ off Normal

A combination of appropriate tilt and rotation was utilised in the MIAMI facility to irradiate at  $35^\circ$  off the normal to the NW axis. To do this, the axis of a chosen NW was aligned with the x-axis of the rod. Next, the NW was rotated by  $45^\circ$  about the z-axis in the xy-plane of the TEM such the ion beam direction was normal to the axis of the NW (i.e. a *zero-tilt plus-45°-rotation* position). The NW was then further rotated  $90^\circ$  from such that the ion beam was  $30^\circ$  off the normal to the NW axis and  $60^\circ$  off the NW axis itself. The NW was finally x-tilted to *minus-7°* to achieve an ion beam angle of  $35^\circ$  off normal to the NW axis. The tilt angle of  $\beta_{\text{tilt}} = -7^\circ$  was calculated using Equation 6.1. A schematic representation of the ion beam making an angle with the NW of  $35^\circ$  off normal in the geometry of the MIAMI facility is shown in Figure 6.1.

$$\beta_{\text{tilt}} = \sin^{-1} \left( \frac{\sin 5^\circ}{\cos 135^\circ} \right)$$

Equation 6.1

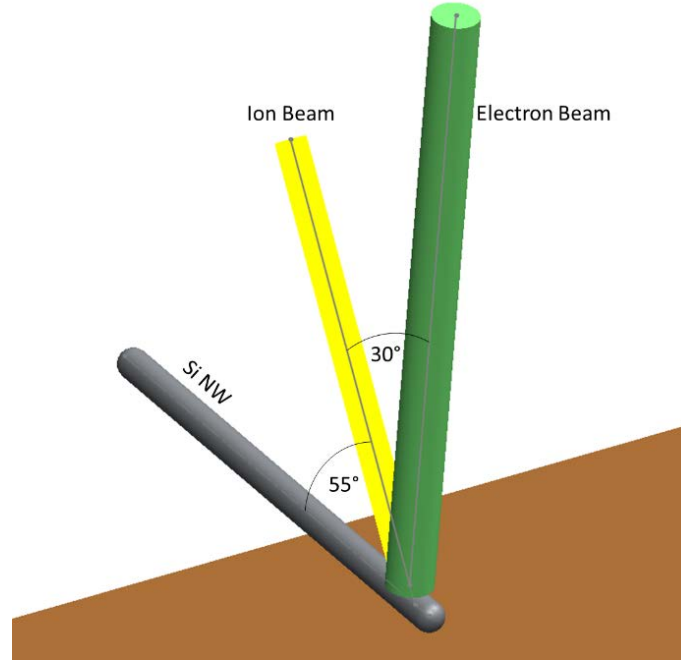


**Figure 6.1:** Schematic showing a Si NW which has been rotated  $135^\circ$  from the  $x$ -axis and  $x$ -tilted by  $-7^\circ$  to give an angle with the NW of  $35^\circ$  off normal in the geometry of the MIAMI facility. The ion and electron beam diameters are much larger in the MIAMI facility than shown in the schematic.

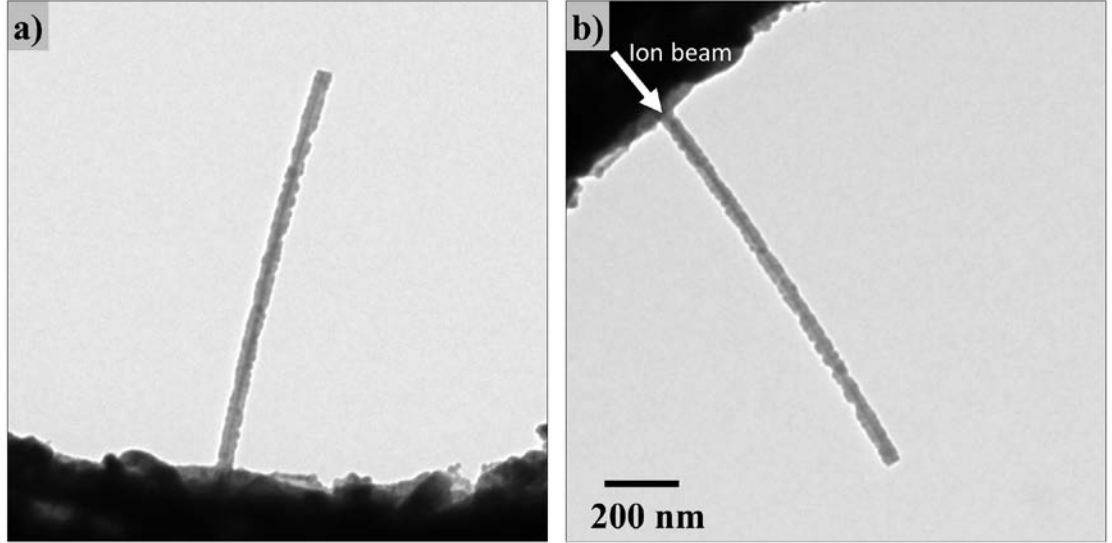


**Figure 6.2:** Micrographs showing a virgin Si NW at a) zero-rotation zero-tilt position and b) the NW after  $135^\circ$  rotation and a  $x$ -tilt of  $-7^\circ$  so that the ion beam is incident at  $35^\circ$  off normal. The scale bar is the same for both the images.

### 6.2.1 Ion Range Matching

In the experiments designed to match ion range, the ion species and energy were selected using SRIM to irradiate 50 nm thick Si NWs such that the  $R_p$  of the ions matched with the 35 keV  $\text{Ar}^+$  ions used to irradiate 150 nm GaAs NWs in the work of Borschel *et al.* [55] The  $R_p$  for 35 keV  $\text{Ar}^+$  ions into 150 nm GaAs was found to be 17.2% of the thickness when irradiated at  $35^\circ$  off normal. The  $R_p$  for 9.5 keV  $\text{Xe}^+$  ions into 50 nm Si was calculated to be 20.0% of the NW thickness at  $35^\circ$  off normal. The slight mismatch in these ranges is for the reasons explained above. The ion implantation profiles and damage caused by 9.5 keV  $\text{Xe}^+$  ions into 50 nm thick Si

and 35 keV  $\text{Ar}^+$  ions into 150 nm thick GaAs are shown in Figure 6.3 and

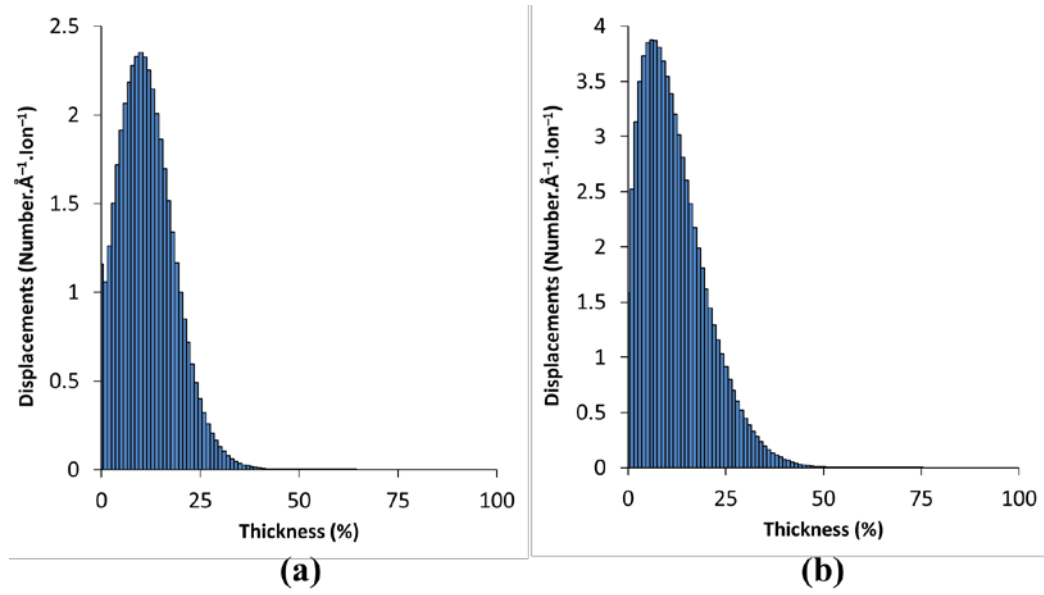
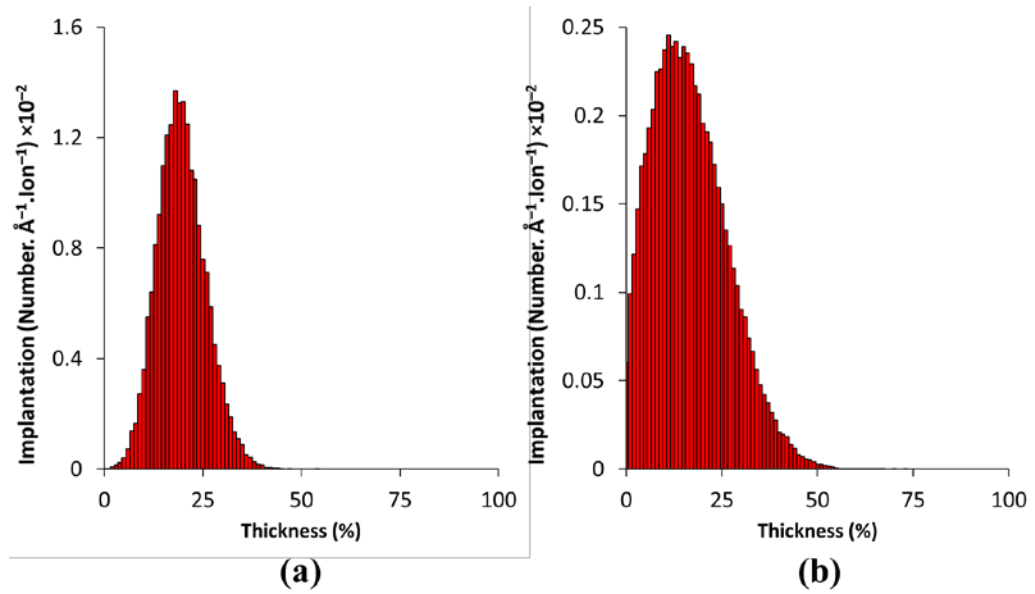
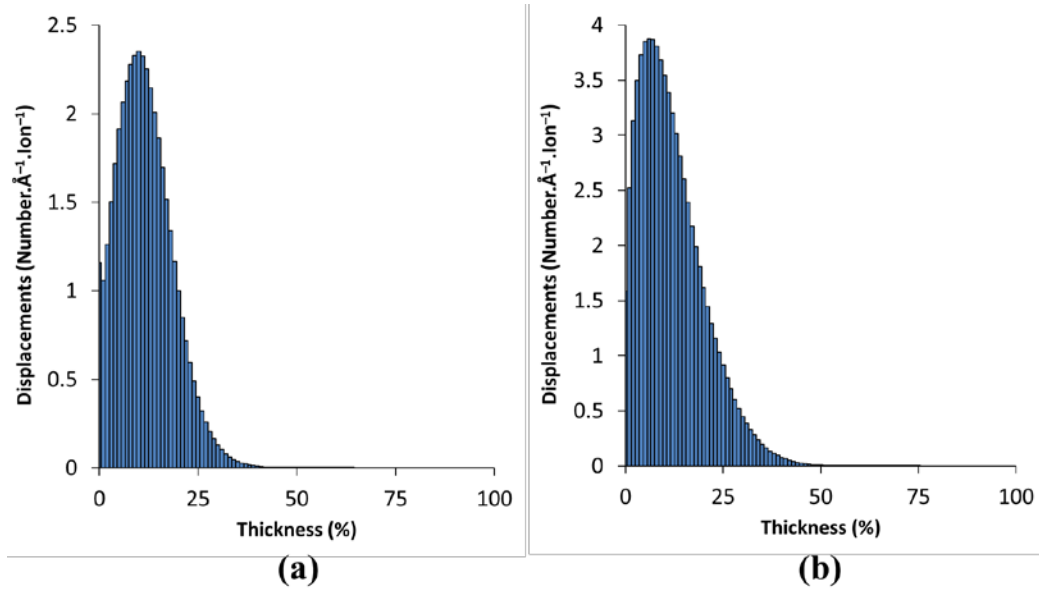


Figure 6.4, respectively.



**Figure 6.3:** Ion implantation profiles calculated using SRIM for: (a) 9.5 keV  $\text{Xe}^+$  ions in 50 nm thick Si at 35° off normal; and (b) 35 keV  $\text{Ar}^+$  ions in 150 nm thick GaAs at 35° off normal.



**Figure 6.4:** Atomic displacement profiles calculated using SRIM for: (a) 9.5 keV  $\text{Xe}^+$  ions in 50 nm thick Si at  $35^\circ$  off normal; and (b) 35 keV  $\text{Ar}^+$  ions in 150 nm thick GaAs at  $35^\circ$  off normal.

Single-crystalline Si NWs of  $50 \pm 2$  nm diameter were irradiated with 9.5 keV  $\text{Xe}^+$  ions at room temperature to end fluences ranging from  $4.4 \times 10^{15}$  to  $2.8 \times 10^{17}$  ions. $\text{cm}^{-2}$ . As in the other experiments presented in the current work, it was observed that as soon as the ion beam is incident on the NW it started to bend and continued to bend as the fluence was increased. For the purpose of acquiring tilt image series after irradiation, the Si NWs were first rotated back from the irradiation position ( $135^\circ$ -rotation minus- $7^\circ$ -tilt) to the initial position (zero-rotation zero-tilt). BF-TEM images of the NWs with corresponding SAED patterns were captured before, during and after the irradiations. Figure 6.5 shows a typical Si NW irradiated with 9.5 keV  $\text{Xe}^+$  ions at  $35^\circ$  off normal to an end fluence of  $1.9 \times 10^{16}$  ions. $\text{cm}^{-2}$ . The results revealed that the Si NWs bend towards the ion beam when irradiated under these conditions which is contrary to the results reported by Borschel *et al.* [318].



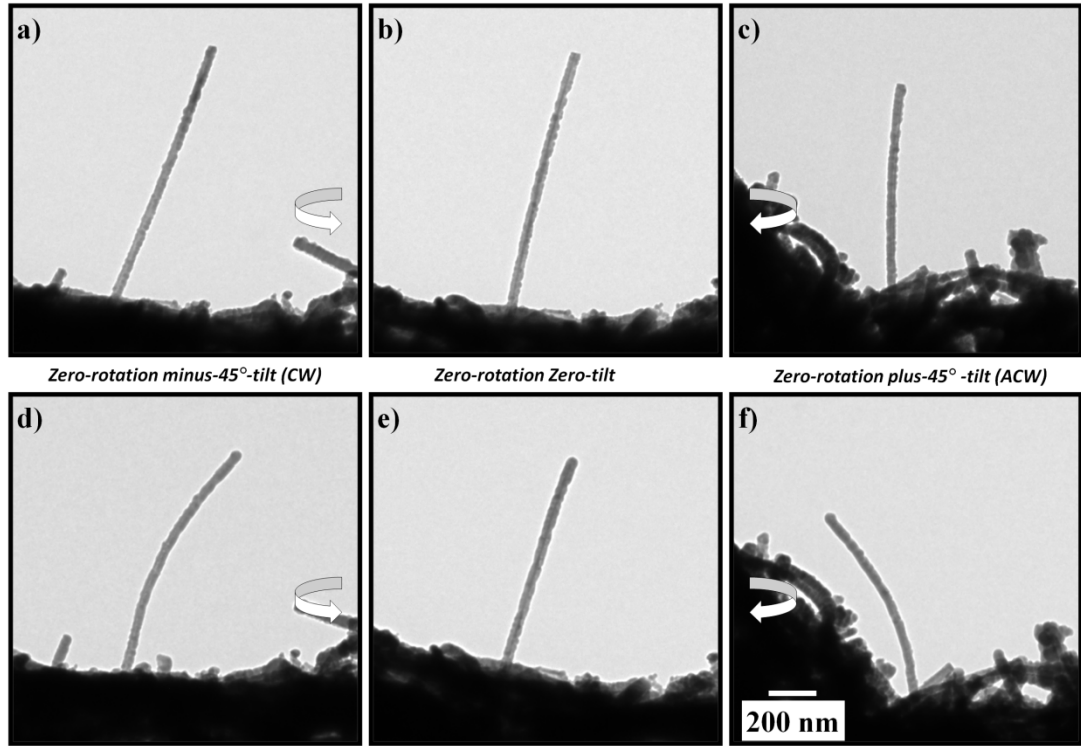


**Figure 6.5:** Micrographs showing the tilt series of a Si NW: before irradiation (a–c) and after irradiation (d–f) to an end fluence of  $1.9 \times 10^{16} \text{ ions.cm}^{-2}$ . The tilt image series demonstrates that the NW bent towards the ion beam. The scale bar is the same for all the images.

### 6.2.2 Peak Damage Depth Matching

A suitable selection of ion energy was made by running SRIM to match the peak damage in 50 nm Si with the peak damage caused by a 35 keV  $\text{Ar}^+$  ions into 150 nm GaAs at  $35^\circ$  off normal. The peak damage caused by a 5 keV  $\text{Xe}^+$  ions into 50 nm Si ( $\sim 8\%$  of the NW thickness) was found closely approximated to the peak damage caused by 35 keV  $\text{Ar}^+$  ions into GaAs ( $\sim 7\%$ ) as shown in Figure 6.6:

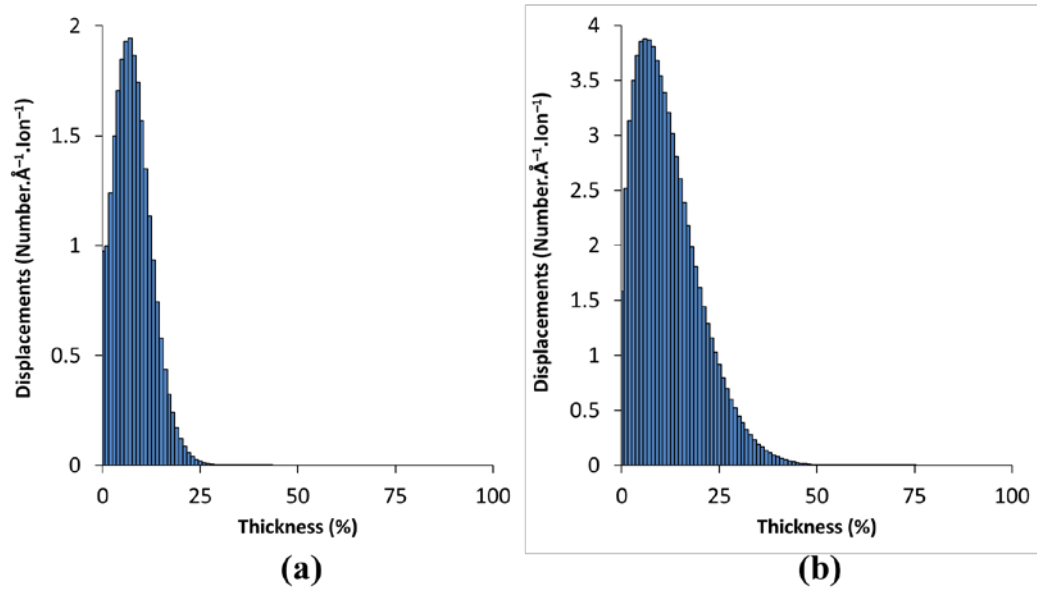


**Figure 6.6:** Graphs illustrating the matching of peak damage depth for: (a) 5 keV Xe<sup>+</sup> ions into 50 nm thick Si at 35° off normal; and (b) 35 keV Ar<sup>+</sup> ions into 150 nm thick GaAs as calculated from SRIM.

Although not the parameter which was targeted in these experiments designed to match the peak damage depth, the  $R_p$  for 5 keV Xe<sup>+</sup> ions into 50 nm Si was 14.7% of the thickness, which is slightly less than the  $R_p$  for 35 keV Ar<sup>+</sup> ions into 150 nm GaAs at 17.2 % of the thickness. The corresponding implantation profiles are shown in Figure 6.7.

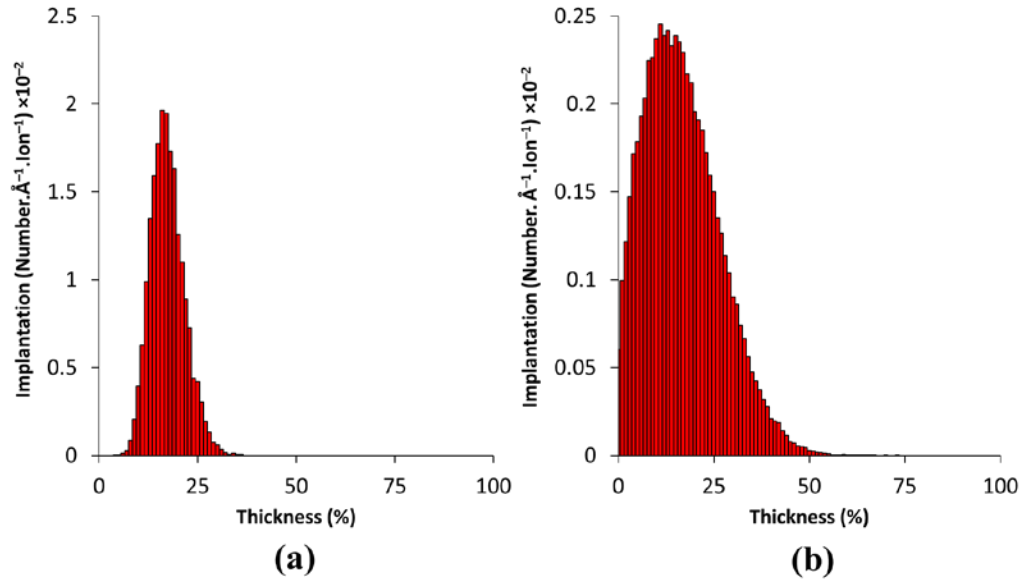


**Figure 6.7:** Ion implantation profiles calculated using SRIM for: (a) 5 keV  $\text{Xe}^+$  ions into 50 nm thick Si at  $35^\circ$  off normal; and (b) 35 keV  $\text{Ar}^+$  ions into 150 nm thick GaAs at  $35^\circ$  off normal.

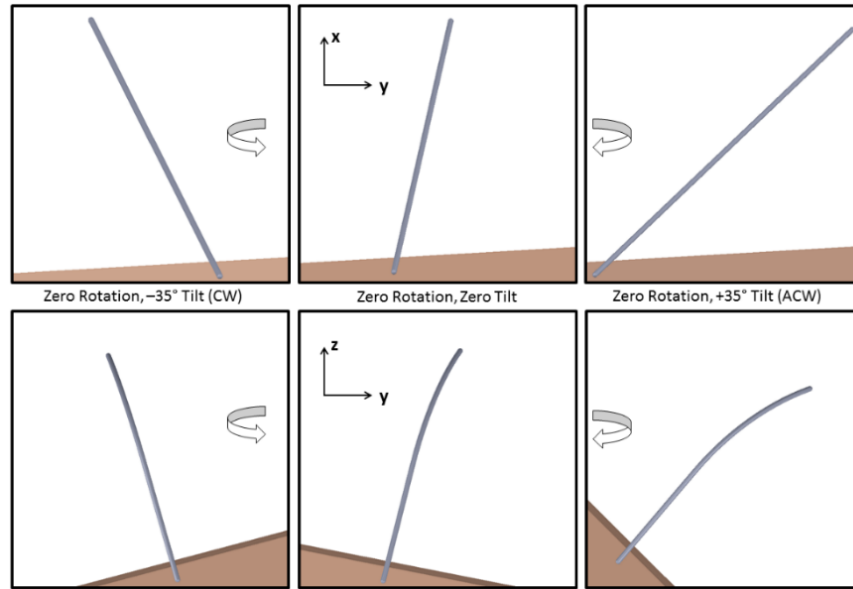


**Figure 6.8:** Three-dimensional computer model of an inclined NW before (top) and after (bottom) undergoing ion-beam-induced bending. Comparison with the experimental result in figure 6.12 confirms that the inclination and bending direction of the NW have been correctly deduced and modelled.

The Si NW shown in Figure 6.9 was irradiated with 5 keV Xe<sup>+</sup> ions to a fluence of  $2.2 \times 10^{15}$  ions.cm<sup>-2</sup> and significant bending of the NW was observed. The tilt image series of the Si NWs after irradiation revealed the interesting result that it had bent away from the ion beam under irradiation (see Figure 6.9) which was opposite to the behaviour of the NWs irradiated with 9.5 keV Xe<sup>+</sup> ions and thus in agreement with Borschel *et al.*

In order to understand the complex combination of inclination and bending as observed in a tilt image series, a three-dimensional computer model (Figure 6.8) of such a NW on a grid was constructed to recreate the images captured in the TEM (Figure 6.9). The initial inclination was calculated using Equation 3.43. As can be seen, the 3D model matches well with the experimental images confirming that the inclination and bending direction of the NW have been correctly deduced and modelled.

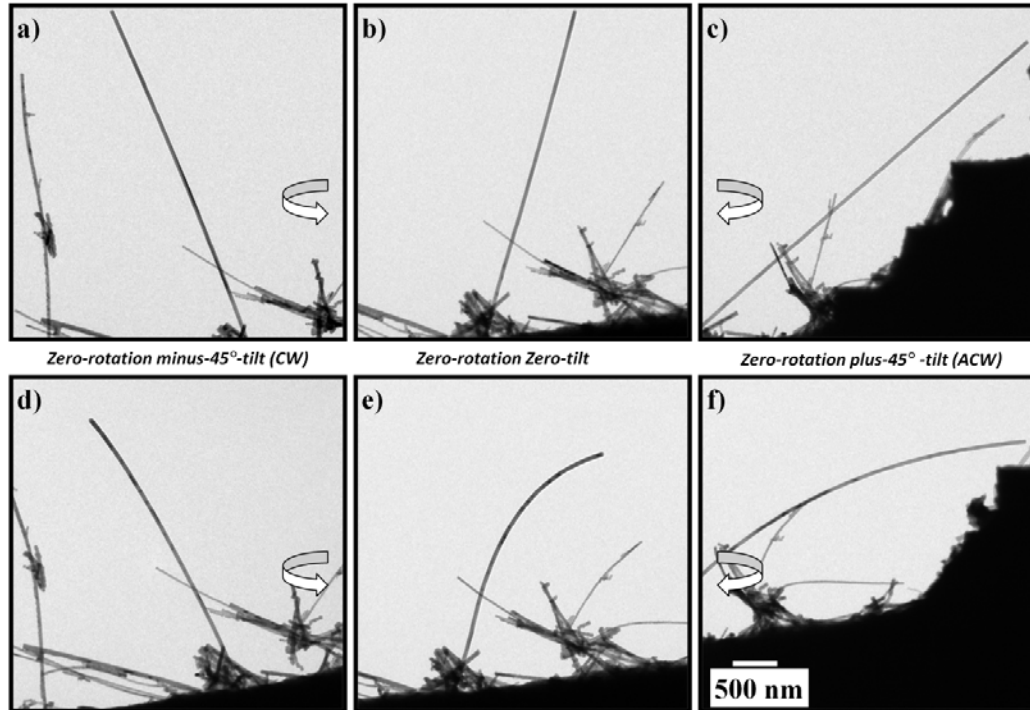


**Figure 6.9:** Micrographs showing a tilt image series for a Si NW before (a–c) and after irradiation (d–f) with 5 keV Xe<sup>+</sup> ions to a fluence of  $2.2 \times 10^{15}$  ions.cm<sup>-2</sup>. The series reveals the ion-beam-induced bending direction to be away from the ion beam when irradiated. Scale bar is applicable to all images.

### 6.2.3 DPA Matching

Ion irradiation experiments on Si NWs were also designed to match the maximum DPA value in the experiments carried out by Borschel *et al.* [318] in which GaAs NWs were irradiated with 35 keV  $\text{Ar}^+$  ions to a fluence of  $10^{15} \text{ ions.cm}^{-2}$  and a typical example is shown in Figure 6.10.

**Table 6.1:** Ion irradiation conditions to match the end DPA.

NW Material	Diameter (nm)	Ion	Energy (keV)	$\theta$	End Fluence (ions.cm <sup>-2</sup> )	End DPA
GaAs	150	$\text{Ar}^+$	35	35°	$10^{15}$	1.6
Si	50	$\text{Xe}^+$	9.5	90°	$10^{16}$	1.6

A fluence of  $10^{15} \text{ ions.cm}^{-2}$  causes 1.6 DPA averaged across the 150 nm of GaAs. In order to produce 1.6 DPA in Si, a typical Si NW of 50 nm diameter was irradiated with 9.5 keV  $\text{Xe}^+$  at a fluence of  $10^{16} \text{ ions.cm}^{-2}$ . Under these conditions, it was again found that the NWs bent towards the ion beam contrary to the results of Borschel *et al.*

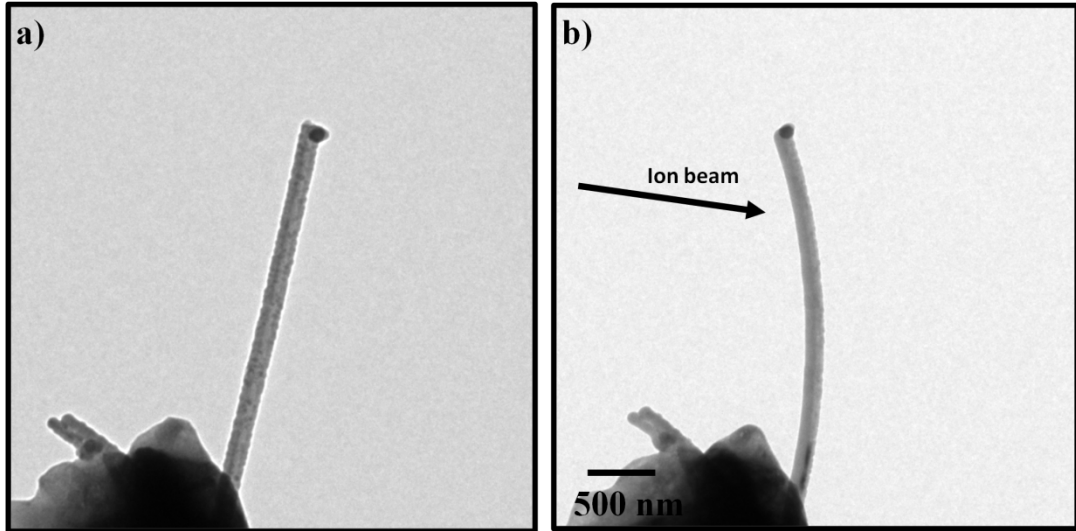


**Figure 6.10:** Micrographs showing a Si NW before (a) and (b) after with 9.5 keV  $\text{Xe}^+$  ions to a fluence of  $1 \times 10^{15} \text{ ions.cm}^{-2}$ . Scale bar is applicable to both images.

### 6.3 Summary

In this Chapter, the Si NWs were irradiated with 5 keV and 9.5 keV  $\text{Xe}^+$  ions at  $35^\circ$  off normal whilst matching the peak damage depth and  $R_p$  with the GaAs NW experiments reported by Borschel *et al* [318]. Under these conditions, the Si NWs were observed to bend away from the ion beam when irradiated with 5 keV  $\text{Xe}^+$  ions and towards the ion when irradiated with 9.5 keV  $\text{Xe}^+$  ions. These findings are contrary to Borschel in the 5 keV case but not in the 9.5 keV case. The Si NWs were also observed to bend towards the ion beam when irradiated with 9.5 keV  $\text{Xe}^+$  ions in experiments designed to match the end DPA to the GaAs NW experiments of Borschel. Furthermore, the angle dependence on the bending direction was also explored by irradiating the Si NWs with the same energies (i.e. 5 keV and 9.5 keV  $\text{Xe}^+$  ions) at normal incidence. From the results of *in-situ* ion irradiation experiments it has been found that bending towards the ion beam does not necessitate a 50% implantation threshold as proposed by Borschel *et al*.

## 7 Industrial Semiconductor Processing Conditions

### 7.1 Introduction

The continuing miniaturisation of semiconductor technology has posed challenges for the physical limits of devices such as gate length and thin oxide thickness as predicted by the International Technology Roadmap for Semiconductors [326]. Si-based electronic devices have revolutionised the world with fast circuit performance but the continuation of their development requires ever greater reductions in their capacitance and an increasing number of transistors per  $\text{cm}^2$  [327], [328]. Researchers are developing new materials and technological processing techniques for the next generation of microelectronic devices [329]. Nanowire Field Effect Transistors (FETs) are proposed structures in which a planar channel is replaced with NWs of semiconductor materials such as Si, Ge, AlN, InN or GaP [330]–[333]. Silicon NWs are among the potential candidates to replace the current Si-based devices in the microelectronics industry because of their compatibility with the existing complementary metal-oxide-semiconductor technology and excellent properties such as high carrier transport and robustness against short channel effects [334], [335].

Ion implantation has been a major processing technique for Si-based microelectronics to introduce dopants due to its reproducibility of concentration and ion range [67], [82], [336]. When an ion beam is incident on a wafer, it can induce charging of the surface and current can flow through the device under fabrication causing damage [337]. Therefore, wafer charging control is necessary and this can be achieved using a plasma deposition (PLAD) system. In PLAD, a high-density low-energy ion plasma is used to control wafer charging by providing a flux of electrons over the surface [337].

Silicon NWs of diameter 24–40 nm are being used in the finFET technology industry and are implanted using a PLAD system with a (~5%) arsine plasma in a (~95%) support gas of  $\text{Xe}^+$  ions [338]. In PLAD, a typical implant of 7 keV  $\text{Xe}^+$  ions to a fluence of  $3.2 \times 10^{15} \text{ ions.cm}^{-2}$  is used in industry during wafer charging control [338]. However, the effect of these 7 keV  $\text{Xe}^+$  ions on thin NWs (for example, atomic displacements, NW bending and bubble formation etc) used for fins is not fully understood and is under investigation [338]. Therefore, *in-situ* ion irradiation experiments with 7 keV  $\text{Xe}^+$  ions were carried out to investigate the modification of Si NWs and the results are presented in this chapter.

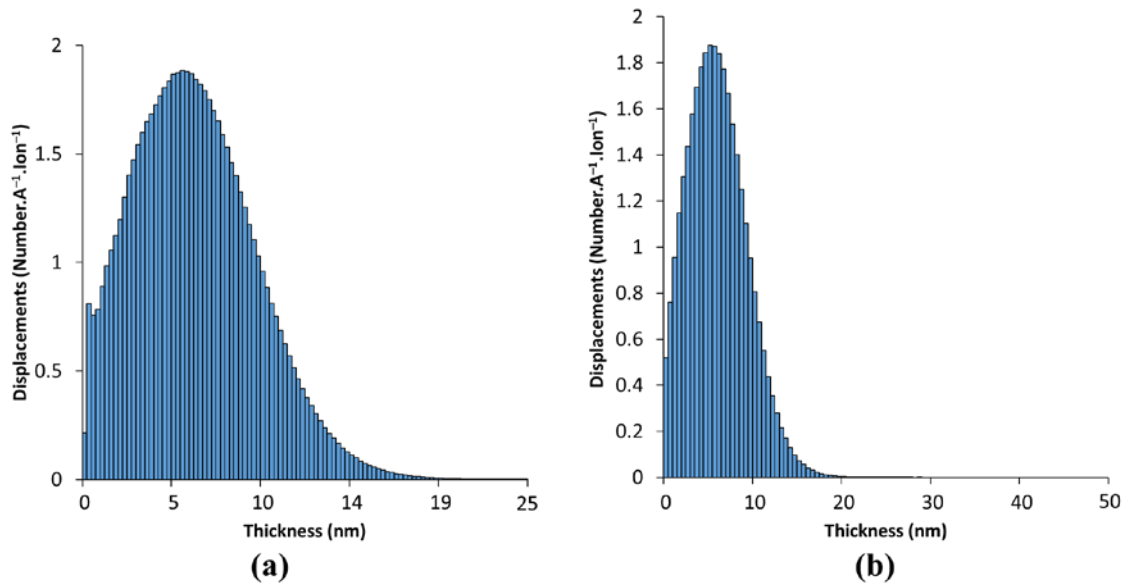


**Figure 7.1:** Graphs showing the distribution of damage of 7 keV  $\text{Xe}^+$  ions in (a) 24 nm (b) 50 nm thick Si as calculated using SRIM.

## 7.2 Structural Defects and Plastic Deformation

In the first series of experiments, thin Si NWs of diameters ranging from 24–50 nm with one end attached to the grid and the other end in free space were selected for the irradiation experiments. The NWs were irradiated with 7 keV  $\text{Xe}^+$  ions at normal



incidence and the ion-beam-induced modifications were investigated. The damage and ion implantation profiles for 24 and 50 nm thick Si were calculated using SRIM and are shown in Figure 7.1 and Figure 7.2, respectively. The peak of the damage depth and  $R_p$  for 7 keV  $\text{Xe}^+$  ions into 24 nm Si lie at 5.8 nm and 10.5 nm, respectively.

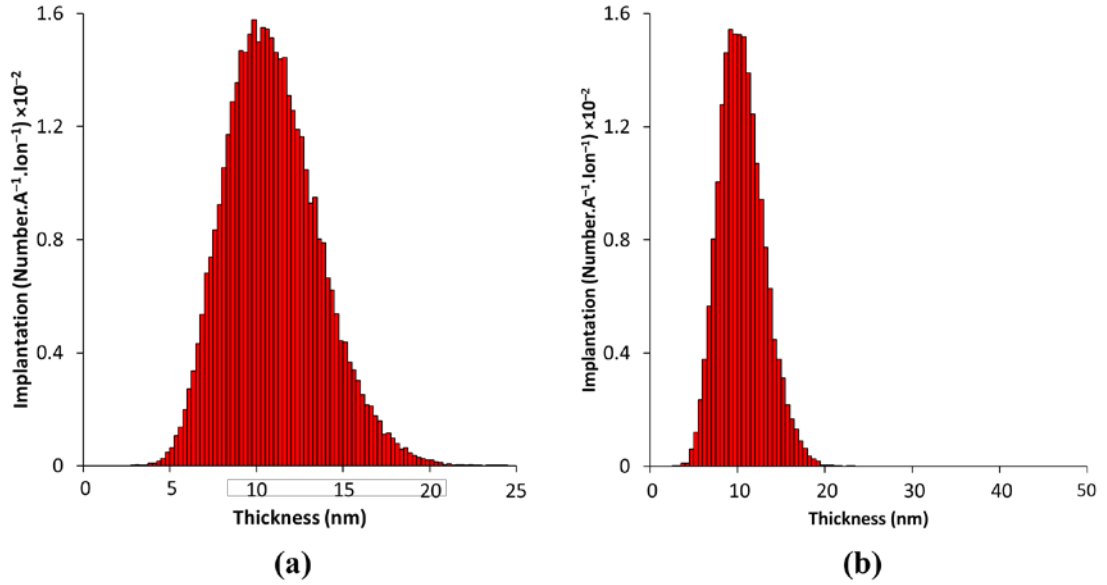


**Figure 7.3:** Graphs showing the ion implantation profile of 7 keV  $\text{Xe}^+$  ions in (a) 24 nm (b) 50 nm thick Si as calculated using SRIM.

The NWs underwent a significant amount of bending during irradiation these conditions. The immediate bending of the NWs upon exposure to ion irradiation again demonstrates the fact that the Si NWs undergo bending before acquiring a fully amorphous state contrary to the results reported by Pecora *et al.* [180], [339]. An example of a NW bending during irradiation is shown in the Figure 7.4.

The results of the tilt image series revealed that Si NWs of diameters between 24–40 nm bend towards the ion beam (see Figure 7.5) while an opposite trend (i.e. bending away from the ion beam) was observed for 50 nm NWs when irradiated under the same conditions. Tomography of some of the NWs was also performed after irradiation from *plus-45°* to *minus-45°* with an increment of  $3^\circ$  in which a BF

image with corresponding SAED pattern were captured for each step to observe the structural changes.

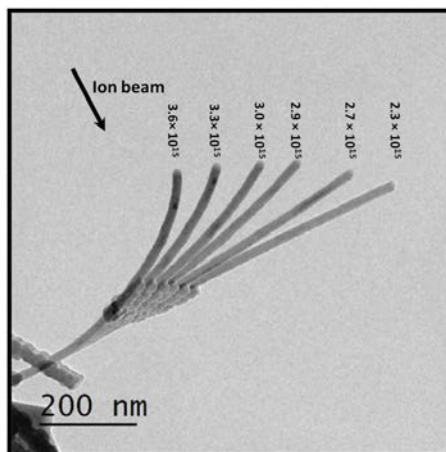


**Figure 7.4:** Composite micrograph demonstrating the bending of a Si NW during irradiation with 7 keV  $\text{Xe}^+$  ions. The bending curvature increases at higher fluences given in units of  $\text{ions.cm}^{-2}$ .

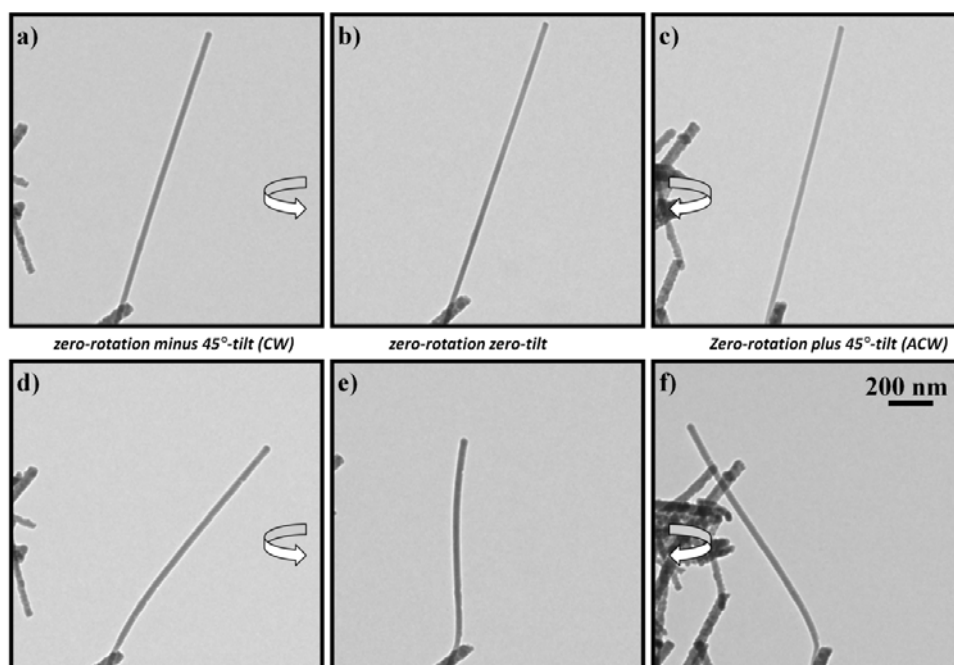


**Figure 7.5:** Micrographs showing the tilt image series of a Si NW before (a to c) and after (d to f) irradiation with 7 keV  $\text{Xe}^+$  ions at normal incidence to an

end fluence of  $3.2 \times 10^{16}$  ions.cm<sup>-2</sup>. The scale bar shown in (f) applies to all images.

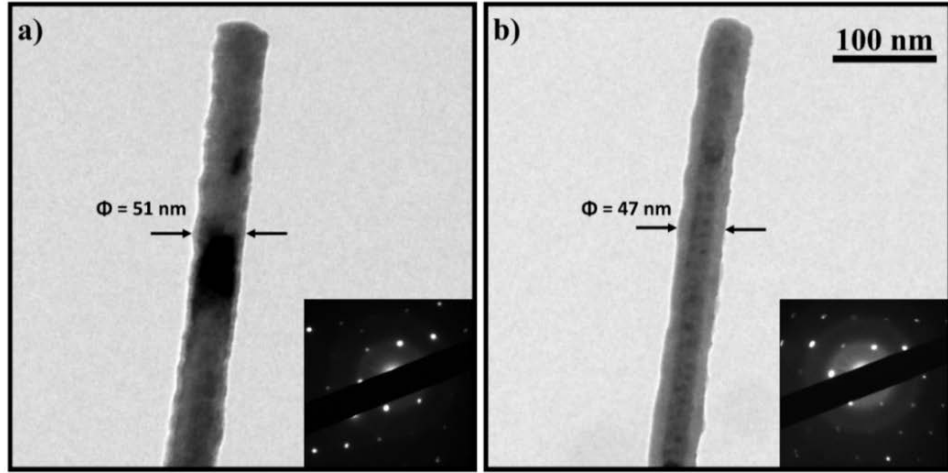


**Figure 7.6:** Bright-field images of a Si NW demonstrating a sputtering effect: (a) un-irradiated NW and (b) after irradiation to a fluence of  $2.6 \times 10^{16}$  ions.cm<sup>-2</sup>. The insets show the corresponding SAED patterns and the scale bar in (b) applies to both images.

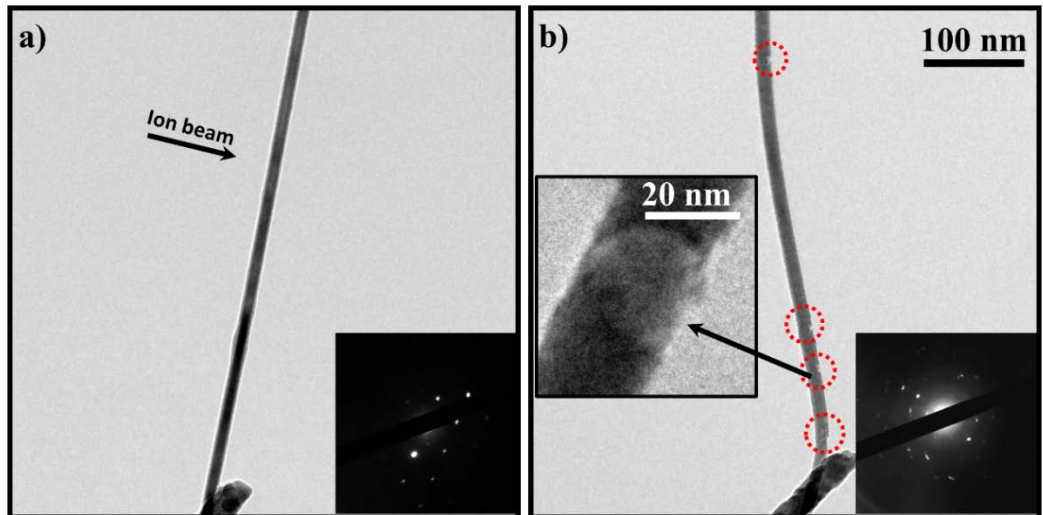


**Figure 7.7:** Micrographs showing the ion-irradiation-induced structural deformation of a Si NW: (a) virgin NW and (b) after irradiation with 7 keV Xe<sup>+</sup> ions to a fluence of  $3.2 \times 10^{15}$  ions.cm<sup>-2</sup>. Insets show the corresponding SAED

*patterns demonstrating the partial amorphisation. Cracking defects are highlighted with red circles in (b). The scale bar in (b) also applies to (a).*

In addition to the bending, it was also observed during the irradiation experiments that the Si NWs underwent surface modifications. The structural modifications were observed in the BF images and the corresponding SAED patterns. The NWs were rendered partially amorphous by the irradiation as confirmed from the faded spots and amorphous rings in the DPs as shown in Figure 7.7. Thinning of the NWs was also observed (see Figure 7.6) after the irradiations and may be attributed to the degree of sputtering achieved at higher fluences. A cracking defect was observed on the un-irradiated side of the NWs which had undergone bending during the irradiation and is highlighted with red dotted circles in Figure 7.7b. Finally, ion irradiation induced black-spot damage was observed in the Si NWs and are shown in Figure 7.8:

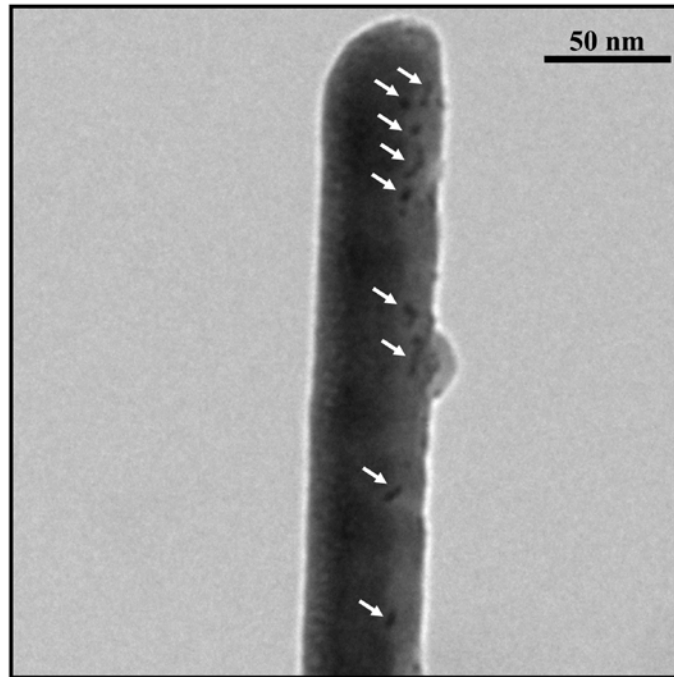


**Figure 7.8:** Micrograph of a Si NW showing black-spot damage inside the NW highlighted with arrows after irradiation with 7 keV  $\text{Xe}^+$  ions to a fluence of  $4.4 \times 10^{16} \text{ ions.cm}^{-2}$ .

### 7.3 Xenon Bubbles in Silicon Nanowires

The formation of small  $\text{Xe}^+$  bubbles in Si NWs was observed following irradiation to a high fluence at room temperature. It has been reported in the literature that nucleation of Xe bubbles during irradiation. Since the maximum range of 7 keV  $\text{Xe}^+$  ions is  $\sim 20$  nm in Si (see Figure 7.3b), the implanted  $\text{Xe}^+$  ions may become trapped at vacancy sites and form bubbles. The bubbles were observed using Fresnel contrast imaging in the TEM by defocusing the objective lens and are shown in Figure 7.9.

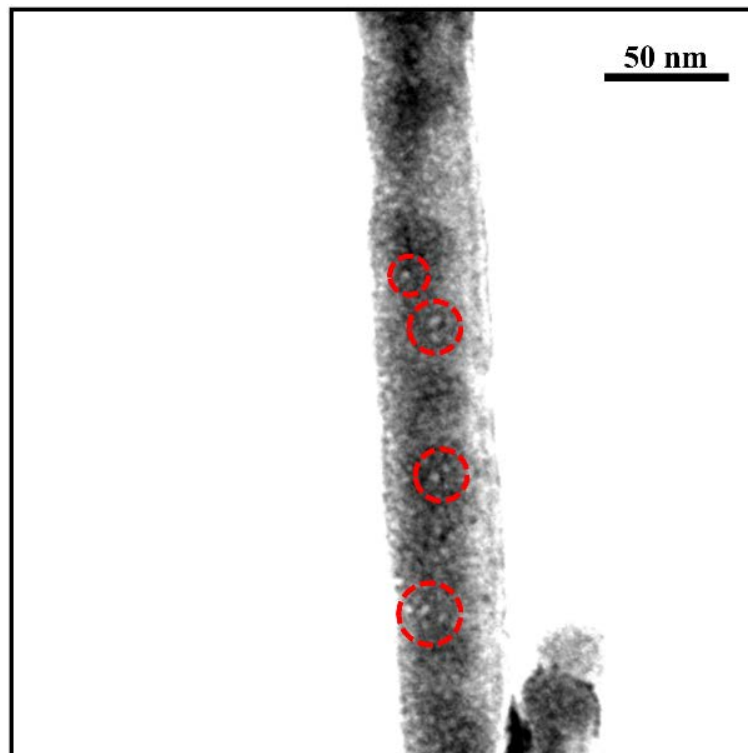


**Figure 7.9:** Micrograph showing a bright-field image of a Si NW demonstrating the formation of bubbles following irradiation with 7 keV  $\text{Xe}^+$  to a fluence of  $4.4 \times 10^{16}$  ions. $\text{cm}^{-2}$ . Greyscale levels have been enhanced to optimise the contrast of the bubbles.

## 7.4 Measurement of Damage Depth

A series of irradiation experiments were designed to measure the depth of the damage caused by the 7 keV  $\text{Xe}^+$  ions. Silicon NWs with both ends attached to the grid such that the middle section was in free space were selected for these experiments. The ion and electron beam geometry in the MIAMI facility along with appropriate sample tilts were utilised to create and then observe the damage depth. The maximum damage depth in the irradiated NWs was measured when the electron beam was normal to the direction in which the ion irradiation had been performed. To facilitate this measurement, both bright-field and dark-field TEM imaging were utilised.

In order to be able to observe and irradiate in directions normal to each other, it was necessary to devise a combination of tilts and rotations which would allow this within the geometry of the MIAMI facility and TEM sample holder. This was achieved by construction of 3D computer model containing the ion beam, electron beam and sample. It was determined that a rotation of  $25^\circ$  and a x-tilt of  $65.0^\circ$  would achieve the desired orientations. A schematic of the tilt procedure utilised in these experiments for the irradiations and observations is shown in Figure 7.10.

Firstly, a selected Si NW was aligned along the x-axis of the TEM sample rod (i.e. the *zero-rotation zero-tilt* position) and x-tilted *plus-32.5°* by ACW rotation of the goniometer. The BF and DF images of the NWs were then captured at the *zero-rotation plus-32.5°-tilt* position before the irradiation. In this position, the electron beam was normal to the direction the ion beam would be in subsequently as illustrated in Figure 7.10. The angle of  $32.5^\circ$  was determined as the correct

Secondly, the NW was x-tilted back to  $0^\circ$  and rotated  $25^\circ$  about the z-axis in the xy-plane of the TEM such that the ion beam direction was at normal incidence to the axis of the NW. The NW was then tilted *minus-32.5°* by clockwise rotation of the goniometer and irradiated at this position (*25°-rotation minus-32.5°-tilt*).

Thirdly, observations were made after the irradiation by bringing the NW back to the *zero-rotation zero-tilt* position and then x-tilted *plus-32.5°* (i.e. the *zero-rotation plus-32.5°-tilt* position). The tilt image series of the NWs were performed after the

irradiations from *plus*-32.5° to *minus*-32.5° with an increment of 3° during which BF images and SAED patterns of the NW were captured. The expected depth of the damage calculated using SRIM was compared with the experimental results.

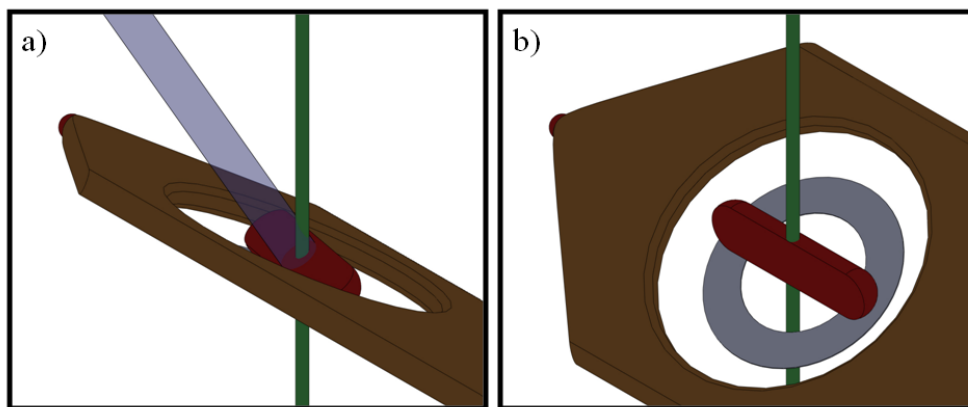


**Figure 7.10:** Schematic of the procedure to observe a Si NW normal to the ion irradiation direction in the MIAMI facility geometry using a tilt-rotate TEM sample holder: (a) the sample is irradiated at an *x*-tilt of minus-32.5° and a rotation of 25° from the *x*-axis; and (b) the NW is tilted to plus-32.5° and rotated back to the *x*-axis for analysis. The NW is shown in red with a faceted surface representing the direction in which it was ion irradiated. The electron beam is shown in green and the ion beam in translucent blue.

The Si NW shown in Figure 7.12 was irradiated to a fluence of  $1.7 \times 10^{16}$  ions.cm<sup>-2</sup>. The  $R_p$  for 7 keV Xe<sup>+</sup> ions into 50 nm Si obtained through SRIM and was found to be 10.5 nm while the maximum range of the ions was found to be ~21 nm. A 2D surface plot obtained using the multislice calculations is shown in Figure 7.11 illustrating the atomic displacements in the NW. Thinning of the NWs was detected by comparison of the BF images captured before and after irradiation demonstrating the effect of sputtering at this relatively-high fluence as shown in Figure 7.13.

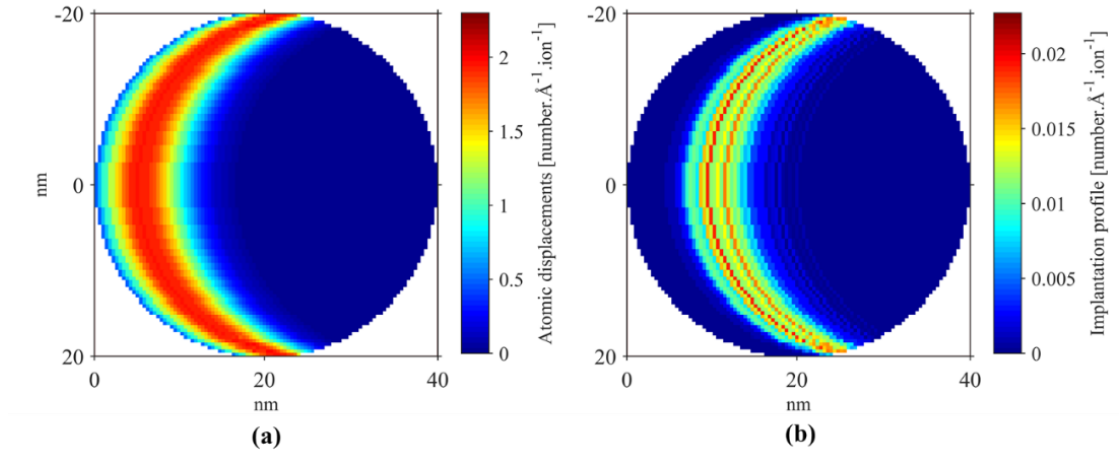


**Figure 7.11:** Two-dimensional plots showing the (a) atomic displacements and (b) ion implantation in a 40 nm diameter Si NW obtained using the multislice SRIM method.

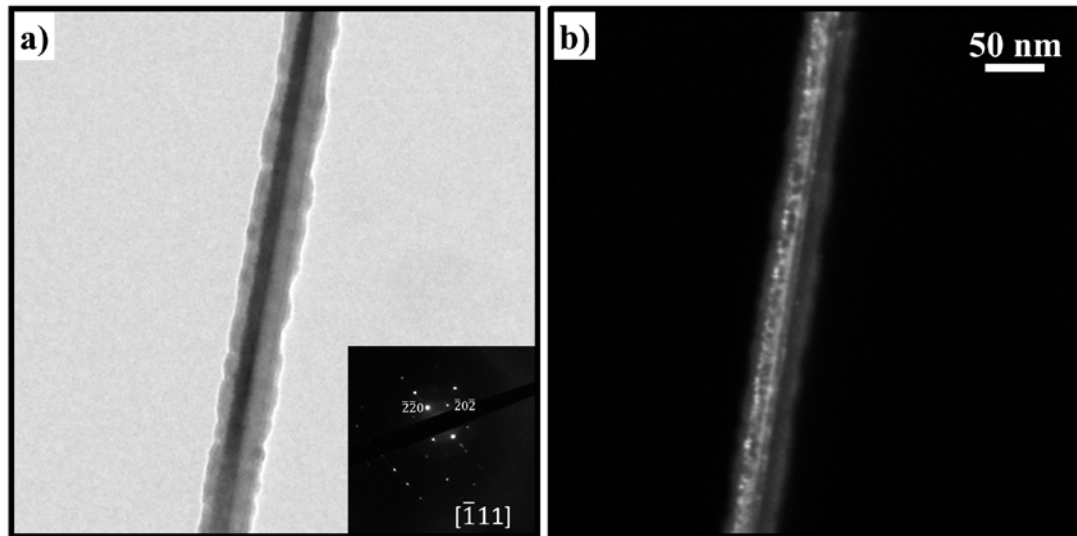


**Figure 7.12:** Micrographs showing (a) bright-field and (b) dark-field images of a Si NW before irradiation captured at zero-rotation plus-32.5°-tilt, Inset is showing the corresponding diffraction pattern The scale bar in (b) applies to both images.



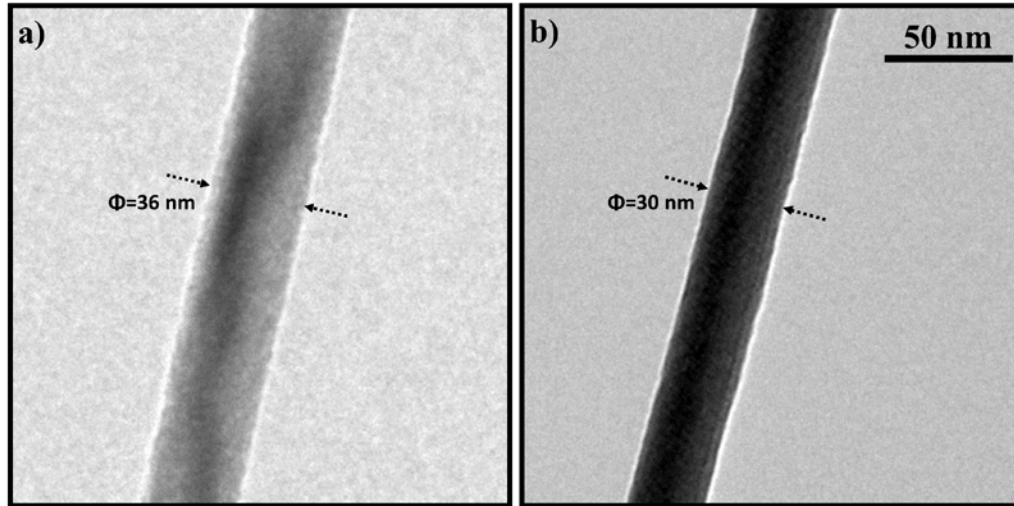


**Figure 7.13:** Micrographs showing bright-field images of a Si NWs demonstrating the effect of sputtering: (a) before and (b) after irradiation with 7 keV Xe<sup>+</sup> ions to a fluence of  $8.1 \times 10^{16}$  ions.cm<sup>-2</sup>. The scale bar in (b) applies to both images.

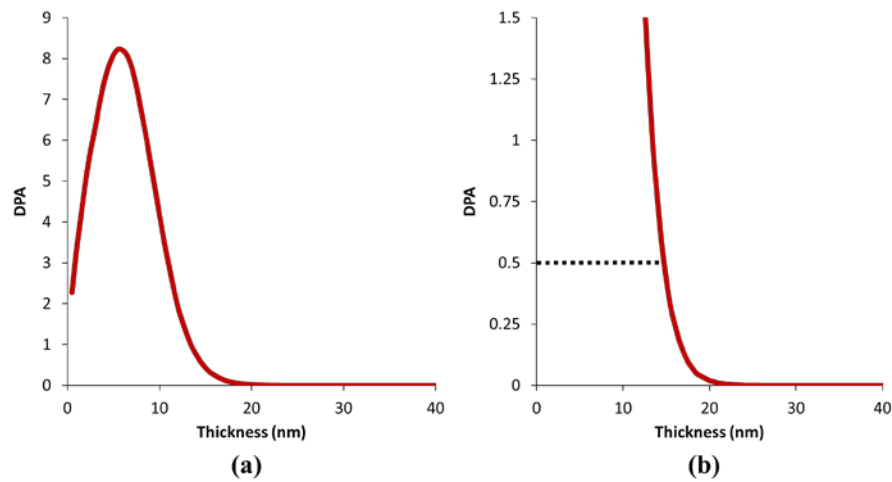


**Figure 7.14:** Graphs showing: (a) DPA calculated from SRIM for 7 keV Xe<sup>+</sup> ion irradiation of Si to a fluence of  $1.7 \times 10^{16}$  ions.cm<sup>-2</sup>; and (b) a closer view of the tail of the damage profile with the dotted line indicating the required DPA to amorphise Si with Xe<sup>+</sup> ions at room temperature.

The DPA value for amorphisation of Si with  $\text{Xe}^+$  ions was found to be 0.5 DPA in a recent study carried out by Edmondson *et al.* [340]. The DPA for Si at a 7 keV  $\text{Xe}^+$  fluence of  $10^{16} \text{ ions.cm}^{-2}$  is shown in Figure 7.14 as a function of depth and it can be seen that the damage was greater than 0.5 DPA to a depth of about 15 nm. The depth of the damage caused by the irradiation in Si NWs was measured from the DF TEM images captured at *zero-rotation plus-32.5°-tilt*. A c-a interface was observed in the DF images and is indicated with a dashed line in Figure 7.15b. The experimentally measured damage depth was found to be ~21 nm (Figure 7.15b) which is about 40% higher than the predicted maximum range of SRIM.

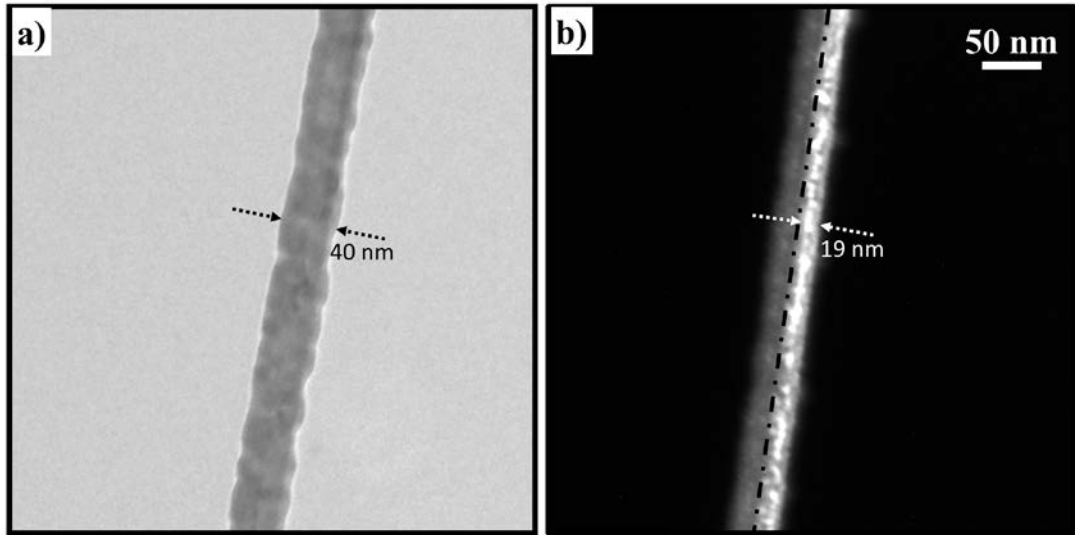


**Figure 7.15:** Micrographs showing (a) bright-field and (b) dark-field images of a Si NW at *zero-rotation plus-30°-tilt* after irradiation to measure the depth of the damage caused by 7 keV  $\text{Xe}^+$  ions to a fluence of  $1.7 \times 10^{16} \text{ ions.cm}^{-2}$ . The scale bar in (b) applies to both images.

Since SRIM does not consider the ordered arrangement of atoms in crystalline materials, the ions are being channelled through open positions and travel deep in the material thereby increasing the maximum range of ions. The [111] crystallographic orientation of the irradiated NW was determined from DP and has been shown in Figure 7.12 confirming the channelling effects were likely to be present during

irradiation which potentially increases the range of the ions and allowed the damage to penetrate deeper into the NWs than predicted by SRIM.

## **7.5 Summary**

The 7 keV Xe<sup>+</sup> ion irradiation modification of Si NWs was studied using *in-situ* ion irradiation with TEM to simulate plasma bombardment in a PLAD system as used in the semiconductor industry. During the irradiation experiments, bending, damage accumulation and amorphisation, bubble formation and surface modifications in the form of sputtering and cracking were observed. The total depth of the damage caused by the 7 keV Xe<sup>+</sup> ions was measured normal to the ion beam direction by utilising the MIAMI geometry and appropriate tilt-rotation procedures. The measured depth of damage was then compared to the calculated data from SRIM and a difference of 40% was found between experimentally measured depth of damage and predicted value of SRIM.

## 8 Finite Element Modelling of Si Nanowires

### 8.1 Introduction

The objective of the work presented in this chapter was to determine the actual temperature of the NWs. The Si NWs were deposited onto Mo grids and were typically of  $\sim 50$  nm in diameter and greater than  $2\text{ }\mu\text{m}$  in length. The NWs selected for experiments were attached at one end to the grid and held in place by VDW forces (discussed in detail in Chapter 2). The samples were loaded into a Gatan heating holder model 652 for *in-situ* experiments above room temperature. In the heating holder, a thermocouple is attached to the heating stage and thus measures that temperature and not of the NWs directly. As it would be extremely difficult to measure the temperature on the nanoscale, a more practical approach is to calculate the temperature along the NWs using finite element (FE) modelling. In order to realistically set up the model, a number of inputs are needed including the bulk and nanoscale properties of the materials involved and the characterisation of the contacting surfaces. A schematic representation of a NW on Mo grid is shown in Figure 8.1.

### 8.2 Setting up of the Problem for Modelling

In order to calculate the temperature along the NWs, the relevant parameters have been found from the literature which will be used to set up the FE modelling. These include the correct Hamaker's constant for the VDW forces as well as the Young's modulus, thermal conductivity and specific heat capacity of Si NWs and the ultra-thin oxide layer on their surface.

It has been found from the literature that the Young's modulus of Si NWs is thickness dependent [59], [63], [65], [219]. Young's modulus for thin Si NWs

decreases with decreasing the diameter below 20 nm but above that thickness it tends to the value for bulk Si (154–168 GPa [228]). In the experiments reported here, no NWs were found to be less than ~24 nm in diameter. Therefore, it is reasonable to estimate the value for Young's modulus of the NWs to the same as for bulk Si.

The values for the thermal conductivity of Si NWs have been reported in the literature and depend on the surface morphologies. The thermal conductivity of nanostructured bulk Si is  $6.3 \text{ W.m}^{-1}.\text{K}^{-1}$  [252] at room temperature. For 48 nm and 52 nm in diameter rough-surfaced Si NWs it has been reported to be 1.6 [233] and  $1.2 \text{ W.m}^{-1}.\text{K}^{-1}$  [256], respectively. The Si NWs used for the experiments reported here were surrounded by a self-passivating thin  $\text{SiO}_2$  layer of about 2–4 nm [341]. The thermal conductivity of  $\text{SiO}_2$  on the nanoscale tends to decrease with film thickness below 250 nm [8]. For 50, 8.5 and 2 nm  $\text{SiO}_2$  films it was found from the literature to be 0.5, 0.4 and  $0.2 \text{ W.m}^{-1}.\text{K}^{-1}$ , respectively [9,10].

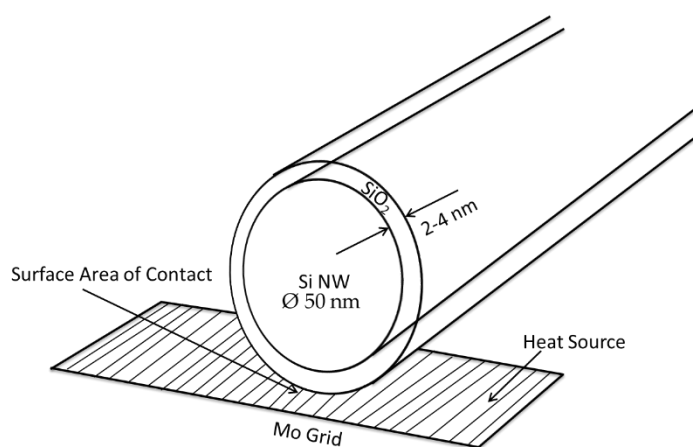


**Figure 8.1:** Schematic of a Si NW on a Mo grid.

The specific heat capacity at constant pressure for bulk crystal of Si has been reported to be  $20.24 \text{ J.mol}^{-1}.\text{K}^{-1}$  [244]. The specific heat capacity at constant volume for Si NWs calculated from first principal has been found to be  $\approx 16 \text{ J.mol}^{-1}.\text{K}^{-1}$  which is lower than the nanostructure bulk Si ( $22.5 \text{ J.mol}^{-1}.\text{K}^{-1}$ ) [342].

As well as the physical properties of the materials in the system, the contact area is determined by the surface morphology and the VDW forces acting between the Si NWs and the Mo grid. Therefore, these are of vital importance in order to understand the effective thermal contact. Studies on the relaxation and deformation of NWs on a surface and evaluation of the resulting contact area have not been reported in the literature. Therefore, prior to the FE thermal calculations it will be necessary to determine the effective thermal contact under these conditions.

As discussed in chapter 2, the VDW forces which adhere the NWs to the grid can be calculated using the appropriate Hamaker constant which describes the interaction of two materials separated by a third medium (air, vacuum or water etc.). A wide range of values for the Hamaker constant for various combinations of materials have been found in the literature ranging from  $3.8 \times 10^{-20}$  J for insulators (PTFE-vacuum-PTFE) to  $5.0 \times 10^{-19}$  J [343] for metals (metal-vacuum-metal). In this study, the VDW interaction is between the SiO<sub>2</sub> and the Mo grid. The Hamaker constant values in vacuum for PTFE-SiO<sub>2</sub> (insulator-vacuum-oxide) and W-SiO<sub>2</sub> (metal-vacuum-oxide) have been reported to be  $4.8 \times 10^{-20}$  [191] and  $(13 \pm 2) \times 10^{-20}$  J [344], respectively. Unfortunately, a value for Mo-vacuum-SiO<sub>2</sub> could not be found in the literature. The closest comparable system for which a value could be found in the literature is W-vacuum-SiO<sub>2</sub>. Therefore, this value of  $1.3 \times 10^{-19}$  J [344] is the most appropriate value available to calculate the strength of the VDW force as an input into the FE modelling.

Using a value of  $1.3 \times 10^{-19}$  J for the Hamaker constant and a typical minimum separation of 0.35 nm [193], [196], [345], a maximum value for the VDW forces per unit area calculated using Equation 2.12 for two parallel planes and was found to be  $1.61 \times 10^8$  N.m<sup>-2</sup> for the W-vacuum-SiO<sub>2</sub> system. This approach can be applied across the area of interaction in the FE model using the separation at each node to calculate the VDW forces at that node.

**Table 8.1:** Values of physical properties obtained from the literature.

Parameters	Si NW	SiO <sub>2</sub>	Mo grid
Young's modulus	154–168 GPa [228]	75 GPa, Bulk [346]	317 GPa
Thermal conductivity	1.4–1.68 W.m <sup>-1</sup> .K <sup>-1</sup> [233]	0.2 W.m <sup>-1</sup> .K <sup>-1</sup> [242]	138 W.m <sup>-1</sup> .K <sup>-1</sup> [347], [348]
Specific heat	16 J.mole <sup>-1</sup> .K <sup>-1</sup> [349]		23.9 mole <sup>-1</sup> .K <sup>-1</sup> [350]
Density	2330 kg.m <sup>-3</sup> [351]	2140 kg.m <sup>-3</sup> [247]	10220 kg.m <sup>-3</sup> [347]

### 8.3 Surface Morphology of Silicon Nanowires

The surface investigations of Si NWs and Mo grids were carried using AFM. Surface profiles obtained from AFM can then be imported into FE modelling software to investigate the deformation of these surface under the VDW forces using the physical properties given in table 8.1. This will then allow calculation of the effective thermal contact between the grid and the NW. The data obtained from the literature given in Table 8.1 and the effective thermal contact will serve as an input for a second FE model to determine the temperature along a NW when a thermal load is applied to the grid.

#### 8.3.1 AFM Sample Preparation and Si NW Selection

Silicon NWs were dispersed onto optically-flat undoped Si wafers and mounted on a SEM specimen stub using carbon adhesive tape. The sample was mounted on the

AFM stage and the NWs were located using a large scan width of a few  $\mu\text{m}$  followed by zooming in to an individual Si NW with a scan size of a few hundred.

### 8.3.2 Roughness Measurements

The surface roughness of Si NWs and of Mo grids were examined using a Bruker OTespa probe with a tetrahedral geometry in a Bruker Dimension Edge AFM. The probe had an average radius of curvature less than 10 nm and was made of 10  $\Omega\text{-cm}$  Si back-coated with  $50\pm 10$  nm Aluminium (Al). The AFM was operated in the tapping and “ScanAsyst in Air” modes in which the cantilever oscillates at frequencies well below its resonant frequency. ScanAsyst in Air mode additionally uses an image-correlation algorithm developed by Bruker providing real-time feedback by continuously monitoring the image quality and automatically making appropriate adjustments to gain, scan rate and cantilever height [265]. This allowed images of the surfaces to be obtained with sub-nanometer resolution.

### 8.3.3 Roughness Analysis

Eight NWs were analysed with post-processing of five or six different regions from each carried out with the Nanoscope image processing software [40]. The surface roughness was evaluated according to the ISO specification standards 21588 (ISO 25178 standards, 2005 [361] and an area of  $50\times 50\text{ nm}^2$  per region was selected for the analysis. Prior to the roughness analysis, the AFM raw image data was filtered to remove low frequency noise, bow and tilt using the Zero order flatten command in the software. In second step, third order plane fitting was performed on the selected AFM image to remove distortions. The resulting AFM image was then reflecting a flat and planar profile.

Three different roughness measure were acquired through the software:  $R_a$ ,  $R_q$ ,  $R_z$ .  $R_a$  is the most commonly used parameter for roughness and according to ISO specification standard 4288 (ISO 4288 standards, 1996 [362]) is defined as the arithmetic average height of surface irregularities from the mean line – i.e. the



average of the heights between the peaks and the valleys from the average surface height.  $R_a$  is defined in Equation 8.1:

$$R_a = \frac{1}{N} \sum_{j=1}^N |Z_j| \quad \text{Equation 8.1}$$

where  $N$  is the number of points and  $Z_j$  is the height of point  $j$ .

$R_q$  is the root-mean-square roughness defined as the average of the measured height deviations from the mean line and is defined in Equation 8.2:

$$R_q = \sqrt{\frac{1}{N} \sum_{j=1}^N |Z_j|^2} \quad \text{Equation 8.2}$$

$R_z$  is the ten-point mean roughness and is an absolute roughness measurement of five highest peaks and five deepest valleys.

The measured values for  $R_a$  in the current work have a wide range from 0.05–1.9 nm for the Si NWs and 0.09–0.24 nm for the Mo grids. The distributions of values are shown in the histograms in Figure 8.2 and Figure 8.3, respectively.

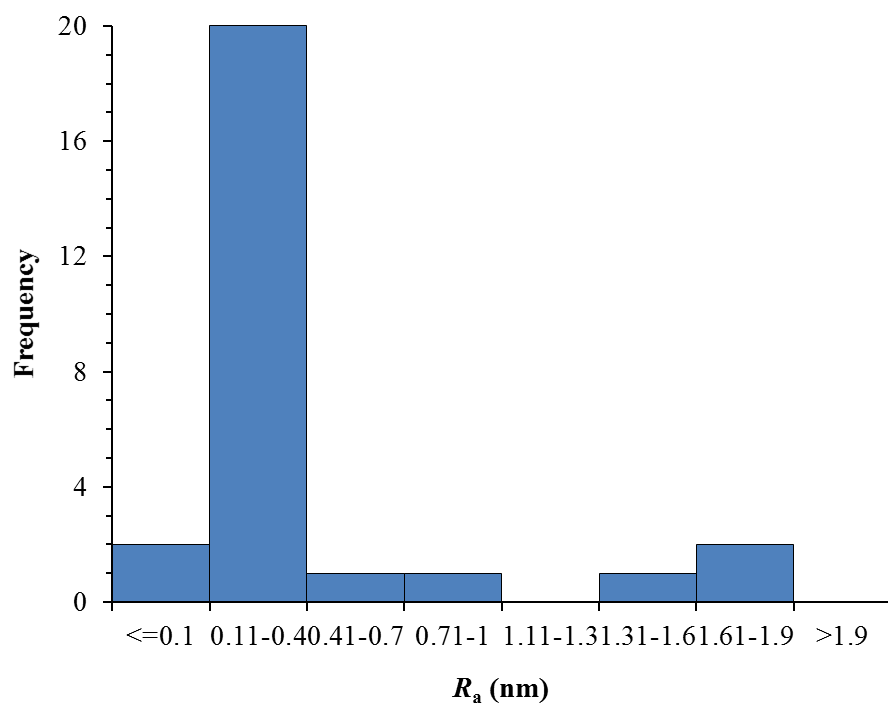


**Figure 8.2:** Histogram of  $R_a$  surface roughness measurements of the Si NWs.

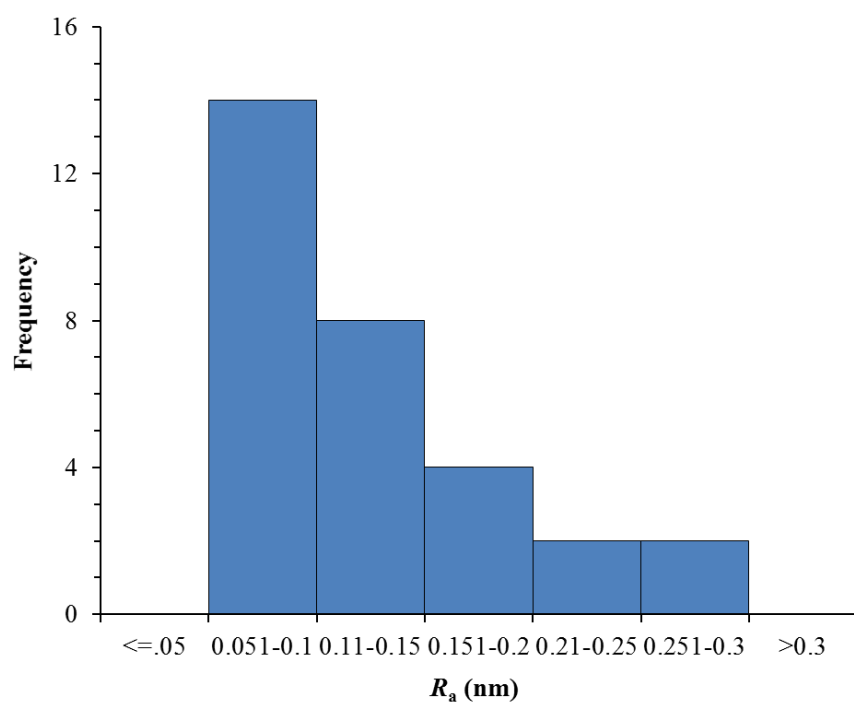


**Figure 8.3:** Histogram of  $R_a$  surface roughness measurements of the molybdenum TEM grids.

The median surface roughness measurements of 27 different regions of eight Si NWs and 32 different regions of six different Mo grids are given in Table 8.2. This experimental data was collected to determine the roughness of Si NWs and Mo grids and the value closest to the median value of roughness will be imported into FE modelling.

**Table 8.3:** *Surface roughness measurements of Si NWs and the Mo grid.*

<b>Parameter</b>	<b><math>R_a</math> (nm)</b>	<b><math>R_q</math> (nm)</b>	<b><math>R_z</math> (nm)</b>
Median of Si NW roughness	0.147	0.892	0.301
Experimental example closest to median value	0.153	0.185	0.265
Median of Mo grid roughness	0.10	0.134	0.362
Experimental example closest to median value	0.121	0.158	0.386

The surface roughness of a typical Si NW and Mo grid are shown in Figure 8.4 and Figure 8.5:

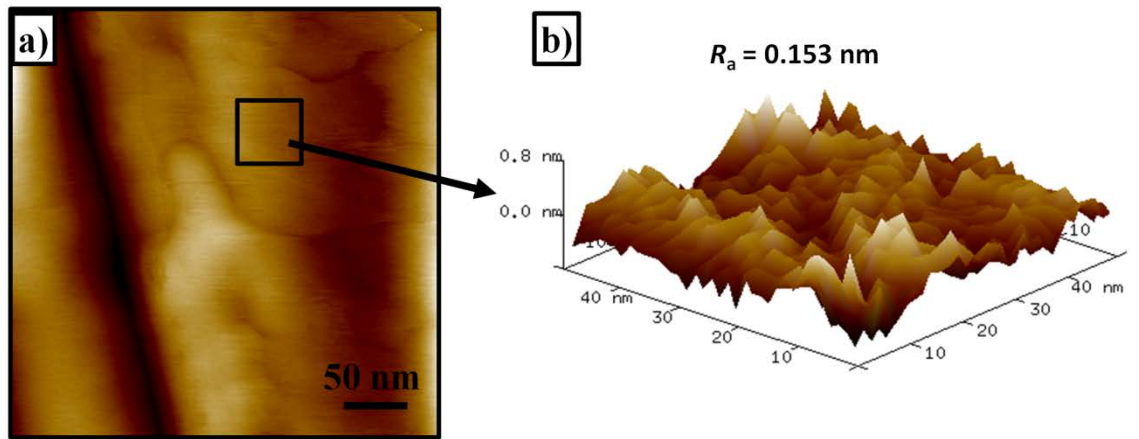


**Figure 8.4:** AFM scanned image showing the (a) topography of a Si NW and (b) 3D view of the roughness of a typical Si NW.

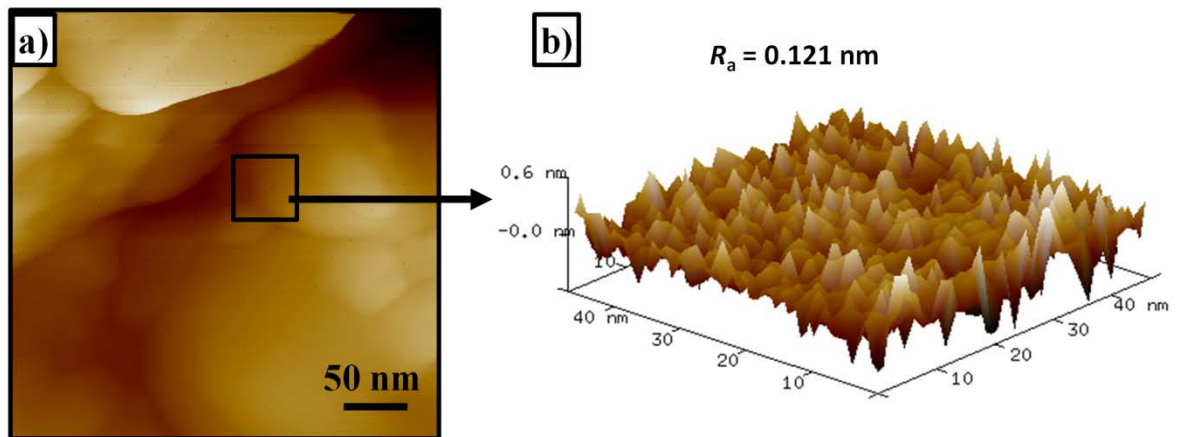


**Figure 8.5:** AFM scanned image showing the (a) topography of a Mo grid and (b) 3D view of the roughness of a typical Mo grid.

#### 8.4 Summary

Experimental measurements of the surfaces of Si NW and Mo grids were carried out using AFM and physical properties for the bulk and nanomaterials present were

found from the literature. Using this information, Equation 2.12 can be applied in an FE model to calculate the VDW forces at each point across the area of interaction between the rough surfaces of a typical Si NW and Mo grid. In the FE model to calculate the effective thermal contact, the two surfaces will need to be brought together under this force which will need to be recalculated as the separation distances change. The surfaces will be allowed to deform and then reach equilibrium at the point where the elastic force due their deformation equals the VDW forces. This will then allow the effective thermal contact to be calculated. The effective thermal contact will then be fed into a larger FE model of an entire Si NW suspended in free-space on a Mo grid with a thermal load applied. This model will then be used to calculate the temperature profile along the Si NW.

## 9 Discussion

### 9.1 Introduction

Ion-beam-induced bending, morphological and structural changes of Si NWs have been observed in the irradiation experiments discussed in chapters 5, 6 and 7. Ion-beam-induced bending of NWs has been extensively studied by different authors and various mechanisms have been reported in the literature [55], [178]–[183]. However, the mechanisms of NW bending have not yet been fully understood and has so has been explored through the *in-situ* irradiation experiments reported here.

In the current work, ion-irradiation-induced bending of Si NWs was explored using different combinations of ion species and energy to understand the underlying mechanisms of the bending. It has been observed during the irradiation experiments that Si NWs bend towards the ion beam when irradiated with 6 keV Ne<sup>+</sup> ions and also with 7 or 9.5 keV Xe<sup>+</sup> ions as shown in Figure 5.9, Figure 7.5 and Figure 6.5, respectively. In these experiments, the bending direction of the Si NWs was observed to be contrary to the GaAs NWs results reported by Borschel *et al.* [181], [318] prompting the experiments reported in chapter 6. From the results of *in-situ* ion irradiation experiments it has been found that bending towards the ion beam does not necessitate a 50% implantation threshold as proposed by Borschel *et al.* Therefore a tipping point for NWs bending has been identified and is classified into shallow and deep implantation.

Other irradiation experiments performed as part of this work, resulted in bending away from the ion beam. A tipping point for the reversal of bending direction of 50 nm Si NWs irradiated with Xe<sup>+</sup> ions at normal incidence was found to lie between 5 and 7 keV.

The ion-beam-induced damage and implantation profiles were calculated using the SRIM Monte Carlo computer code. The results of the SRIM calculations were

combined into a multislice model developed for non-planar surfaces and is discussed in chapter 4.

Damage and implantation profiles were calculated for all the various combinations of NW material and irradiation conditions reported here and in the literature as shown in table 9.1. This allows all of these different experimental results to be compared against each in a systematic analysis in order for trends to be identified in the complex data set.

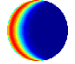
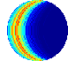
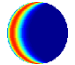
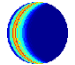
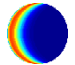
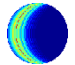
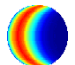
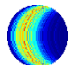
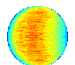
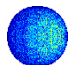
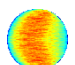
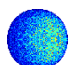
In order to compare the 2D displacement and implant profiles it is useful to define parameters to quantify the depth within the circular cross-sectional geometry. The average depth of the atomic displacements,  $\bar{x}_{\text{disp}}$ , and implanted ions,  $\bar{x}_{\text{ion}}$ , were determined using Equation 9.1:

$$\bar{x} = \frac{\sum_{n=1}^{100} \left( \frac{\sum_{m=1}^{100} (N_{m,n} \times x_{m,n})}{\sum_{m=1}^{100} N_{m,n}} \right)}{100} \quad \text{Equation 9.1}$$

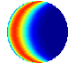
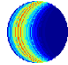
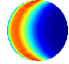
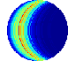
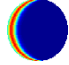
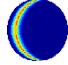
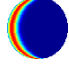
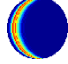
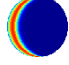
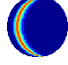
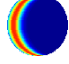
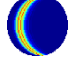
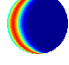
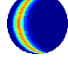
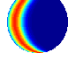
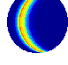
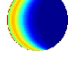
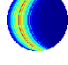
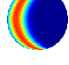
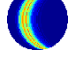
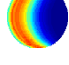
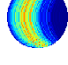
where:  $\bar{x}$  is  $\bar{x}_{\text{disp}}$  (or  $\bar{x}_{\text{ion}}$ );  $N_{m,n}$  is the number of atomic displacements (or implanted ions) calculated by SRIM in slice  $n$  at depth  $x_m$  in the multislice model.

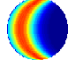
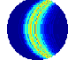
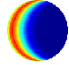
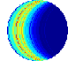
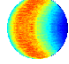
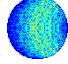
The average displacement and implantation depths normalised to NW diameter are therefore  $\frac{\bar{x}_{\text{disp}}}{\varnothing}$  and  $\frac{\bar{x}_{\text{ion}}}{\varnothing}$ , respectively. The values of  $\bar{x}_{\text{disp}}$ ,  $\bar{x}_{\text{ion}}$ ,  $\frac{\bar{x}_{\text{disp}}}{\varnothing}$  and  $\frac{\bar{x}_{\text{ion}}}{\varnothing}$  are given in table 9.1 alongside the 2D damage and implantation profiles. The table is demonstrating the semiconductor NWs under different irradiation conditions when arranged by average displacement depth relative to the NW diameter. Table 9.1 has revealed a trend that NWs bend away from the ion beam for shallow implantation but the situation is reversed for deep implantation. However it does not require a condition that only those NWs bend towards the ion beam for which range of ions is greater than 50% of NW thickness as proposed by Borschel *et al.* [318].

**Table 9.1:** Summary of experiments on the ion-irradiation-induced bending of semiconductor NWs reported in the literature and combined with those presented in this thesis. For each experiment, the damage and implantation profiles are shown as calculated using the multislice SRIM method described in chapter 4. Experiments are grouped by NW material and ordered by the average displacement depth ( $\bar{x}_{disp}$ ) relative to the nanowire diameter ( $\emptyset$ ).

Reference	Nanowire		Irradiation Conditions			Multislice SRIM Calculations				Bending [b]
	Material	$\emptyset$ (nm)	Ion	$E$ (keV)	$\theta$ [a]	$\frac{\bar{x}_{disp}}{\emptyset}$	Damage	Implant	$\frac{\bar{x}_{ion}}{\emptyset}$	
[318]	GaAs	150	Ar	35	35°	0.2284			0.2743	Away
[318]	GaAs	150	Xe	80	35°	0.2285			0.2562	Away
[318]	GaAs	150	S	30	35°	0.2300			0.2773	Away
[318]	GaAs	150	Xe	210	35°	0.3422			0.4174	Away
[318]	GaAs	150	S	180	35°	0.4965			0.5381	Towards
[318]	GaAs	150	Ar	210	35°	0.5010			0.5462	Towards



This work	Ge	46	Xe	30	45°	0.2886			0.3251	Away
[188]	Ge	50	Ga	30	45°	0.3225			0.3753	Towards
This work	Si	50	Xe	5	35°	0.1883			0.2503	Away
[179]	Si	210 [c]	Ga	30	0°	0.2029			0.2435	Away
This work	Si	50	Xe	5	0°	0.2052			0.2647	Away
This work	Si	50	Xe	7	0°	0.2267			0.3165	Away
This work	Si	50	Xe	9.5	35°	0.2275			0.3061	Towards
This work	Si	50	Xe	9.5	0°	0.2519			0.3501	Towards
[189]	Si [e]	50	Ga	16	54°	0.2661			0.3206	Towards
This work	Si	36	Xe	7	0°	0.2727			0.3948	Towards
This work	Si	50	Ne	6	0°	0.3281			0.3998	Towards

This work	Si	24	Xe	7	0°	0.3506			0.5250	Towards
[181]	ZnO	60	Ar	20	38° [d]	0.2657			0.3063	Away
[181]	ZnO	90	Ar	90	38° [d]	0.4402			0.5329	Towards

[a] Defined as the angle from the normal to the NW axis

[b] Relative to the direction of the incident ion beam

[c] Based on figure 5 and text in JVSTB 27 (2009) p3043

[d] Based on figures 1, 2 and 6 in Nanotechnol 22 (2011) p185307

[e] Polycrystalline silicon

The mechanisms of ion-irradiation-induced bending previously proposed in the literature have been explored in the context of the current experimental findings. These include the ion-irradiation-induced effects of density change, the spatial distribution of ion beam damage and viscoelastic flow and thermal spike models as discussed below.

## 9.2 Semiconductor Nanowire Bending Mechanisms

### 9.2.1 Volume Change due to Damage Accumulation

Density change due to ion-beam-induced damage accumulation has been suggested as a driving mechanism for NW bending in the literature by Romano *et al.* [188] and Borschel *et al.* [318]. For the purposes of testing this proposed mechanism, a model with some maximising assumptions is considered in which an expansion due to damage accumulation in one half of the NW leads to a bending moment. The first maximising assumption is that the damage accumulation leads to amorphisation and is confined to one side of the NW. The NW is modelled with the boundary between the two halves running along the arc of the induced curvature as shown in the Figure 9.1. The second maximising assumption is that there is no residual stress – i.e. all induced stress is able to relax through the bending of the NW and thus drive the bending to its maximum extent.

Consider a bent section of a NW of diameter,  $2r$ , and radius of curvature,  $R$ . This can be modelled as being composed of two volumes sharing an interface running along the axis of the NW and normal to the radius of curvature as shown in Figure 9.1. The ratio,  $\sigma$ , between the volume on the outside of the radius of curvature,  $V_{>R}$ , and the volume on the inside,  $V_{<R}$ , can be calculated using Equation 9.2. (see Appendix B for derivation):

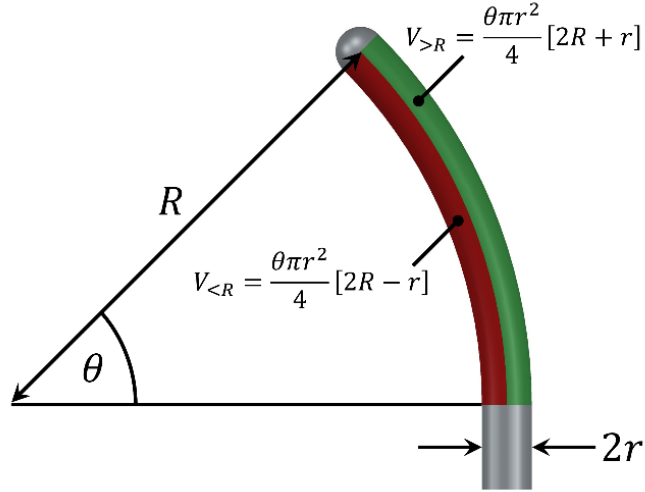


**Figure 9.1:** Schematic of a NW of diameter,  $2r$ , illustrating a bent section with a radius of curvature,  $R$ , and arc length,  $\theta R$ . The volumes of the bent section on the outside,  $V_{>R}$ , and inside,  $V_{<R}$ , of  $R$  can be calculated using the expressions shown.

The ratio of the volume on the outside of  $R$ ,  $V_{>R}$ , and inside of  $R$ ,  $V_{<R}$ , can be calculated using equation 9.2:

$$\sigma = \frac{V_{>R}}{V_{<R}} = \frac{2R + r}{2R - r} \quad \text{Equation 9.2}$$

In order to test whether a damage accumulation mechanism could potentially explain the ion-irradiation-induced bending observed in the experiments on Si NWs reported here, consider the typical experimental result of a NW as shown in Figure 9.2 of diameter  $2r = 50$  nm which has undergone a transition from being straight to having a radius of curvature  $R = 700$  nm at a 6 keV  $\text{Ne}^+$  ion fluence of  $1.16 \times 10^{16}$  ions. $\text{cm}^{-2}$ . In order for damage accumulation to be responsible for this bending then amorphisation would have to account for the volume change in  $V_{>R}$  relative to  $V_{<R}$ . For the NW under consideration,  $\sigma = 1.036$  indicating that  $V_{>R}$  had a 3.6% greater volume relative to  $V_{<R}$ .

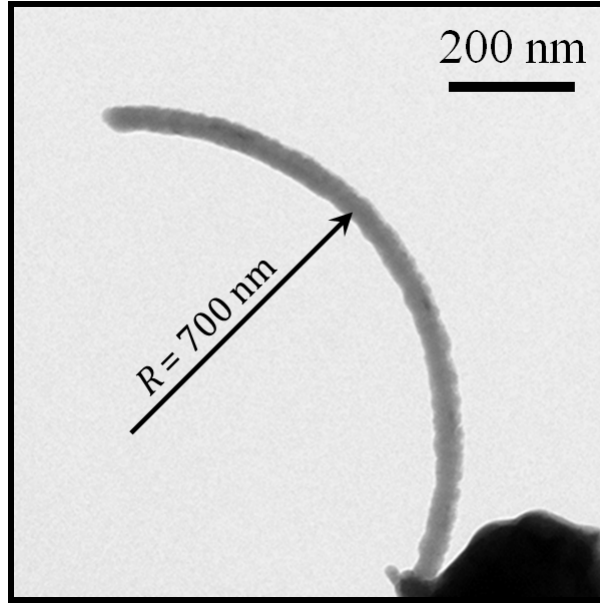


**Figure 9.2:** A typical Si NW bending irradiated with 6 keV  $\text{Ne}^+$  ions to a fluence of  $1.16 \times 10^{16} \text{ ions.cm}^{-2}$ .

Due to the open structure of Si, the volume increase due to an interstitial is expected to be small ( $0.90 \Omega_{\text{atomic}}$  [93], where  $\Omega_{\text{atomic}}$  is the atomic volume) and the decrease for a vacancy is small ( $0.5 \Omega_{\text{atomic}}$  [363]). Although there are a range of values in the literature for volume change due to point defects, the cumulative effect of the introduction of these defects manifests itself in the difference between the densities of crystalline and amorphous silicon. Amorphous Si is known to be 1.8% less dense than c-Si [353]. Therefore, even under the maximising assumption that the NW remains in the densest crystalline form on one side and is saturated with damage on the other side, simple volume expansion due to the ion-beam-induced damage accumulation appears unable to solely account for the degree of bending observed.

### 9.2.2 Amorphisation Facilitated Mechanisms

It was observed during the *in-situ* irradiation experiments reported here that Si NWs start bending immediately upon exposure to the ion beam. This is consistent with the work of Borschel *et al.* on GaAs NWs [318] and ZnO NWs [181] but is notably in

contradiction to the work on Si NWs by Pecora *et al.* [180], [185]. Although the immediate response observed rules out complete amorphisation as a requirement for ion-beam-induced bending, it is known that amorphous pockets can be induced at the centre of dense atomic-collision cascades [354]. In such a scenario, the amorphous core is surrounded by damaged crystalline region and as irradiation continues the loss of crystallinity progresses by a combination of heterogeneous and homogeneous amorphisation. As stated above by considering the maximised case where one half of NW remained crystalline and other turned fully amorphous, simple volume change due to amorphisation does not account the observed bending.

### 9.2.3 Spatial Distributions of Vacancy and Interstitials

Ion-irradiation-induced collision cascades (discussed in detail in chapter 4) have directionality determined by the trajectory of the instigating particle. The point defects (i.e. vacancies and interstitials) produced within a collision cascade can be calculated using SRIM. The distribution of interstitials is always slightly deeper than that of the vacancies; the interstitials are by definition displaced from the vacancies and those displacements are, on average, further along that trajectory. This spatial separation of the two point defect populations has been proposed as a possible mechanism as it could cause a contraction in the vacancy-rich shallower region and an expansion in the deeper interstitial-rich region [71], [181], [318]. Based on multislice SRIM calculations, the two point defect distributions have a considerable degree of overlap and the difference between them is small as shown in Figure 9.3 for 9.5 keV  $\text{Xe}^+$  ions irradiation of a Si NW. Furthermore, as discussed above, arguments based on the volume change associated with point defects in Si suggests that even the total effect due to the point defects cannot account for the observed bending and so the second-order effects of the separation of the vacancies and interstitials is certainly a minor contributor at best.

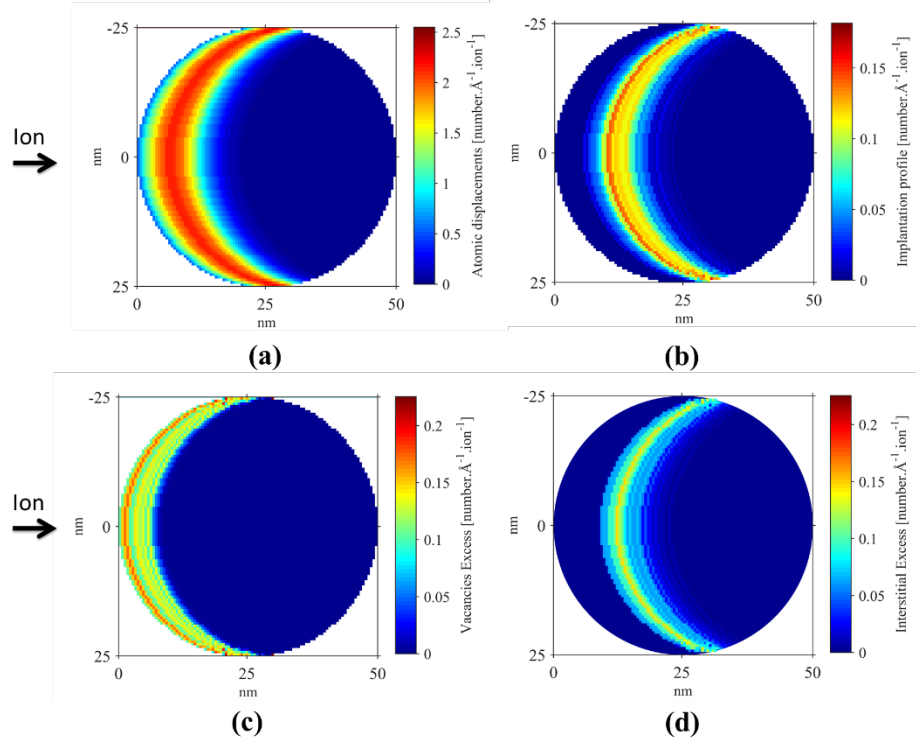


**Figure 9.3:** Example of a SRIM multislice calculation for 9.5 keV  $\text{Xe}^+$  ion irradiation of a Si NW showing the distributions of: (a) vacancies; (b) interstitials; and (c) surpluses of vacancies and (d) interstitials.

#### 9.2.4 Viscoelastic Thermal Spike Models

Ion irradiation induced NW bending has been attributed to viscoelastic flow processes which have been proposed as a possible driving mechanism for bending [188]. The viscoelastic thermal spike model is valid only for amorphous materials and has not been observed in crystalline materials [355]. The Si NWs were irradiated with  $\text{Ne}^+$  and  $\text{Xe}^+$  ions in these experiments.  $\text{Xe}^+$  ions could induce amorphous pockets in the NWs in a single collision cascade due to its high mass [354] compared to  $\text{Ne}^+$  ions in Si under same irradiation conditions and could rendered the crystal amorphous.

Under conditions in which amorphisation has already been induced, subsequent ions thus may experience amorphous material which could facilitate viscoelastic flow in a thermal spike model in which contraction occurs along the ion trajectory and expansion normal to it. The net effect of this phenomenon is the expansion

perpendicular to the ion beam direction and contraction in the parallel direction. Since the Si NWs we observed to start bending immediately when irradiated with either  $\text{Ne}^+$  or  $\text{Xe}^+$  ions, the possibility of NWs bending due to viscoelastic thermal spike model as a major driving force can be ruled out as the amorphous material would not have had a chance to accumulate to a significant degree. However, the effect of viscoelastic flow in a thermal spike model at higher fluences may be a supporting factor especially for heavier ions such as  $\text{Xe}^+$ .

### 9.3 Damage and Its Distance from NW Surface

Ion irradiation induces more damage to the surface of NWs compared to that of the bulk with enhancement up to a factor of three for 3 nm diameter Si NWs at 1 keV  $\text{Ar}^+$  ions by virtue of their high surface-to-volume ratio [356]. However, the defect production at the surface decreases significantly with ion energy and increasing NW diameter.

Hoilijoki *et al.* [356] suggested using MD simulations that the damage distribution at the surface compared to inside a NW is also different from bulk Si. Their simulation results showed that ion-beam-induced damage was largely created on surface of the NWs and population of vacancies at the surface of the NW was higher than interstitials due to the fact that each sputtered atom leaves a vacancy but the defect creation was same in the middle of the NW [356]. Since the displacement energy for sputtering,  $E_s$ , is less than  $E_d$  by a factor of two to three [357] thereby increasing the damage at surface.

Sputtering has been observed in the irradiation experiments reported here and at high fluences this can cause a significant reduction in the diameter of the NWs (see Figure 7.13). The displacement of atoms from the surface due to sputtering and the subsequent surface reconstruction through rearrangements of broken bonds to heal the vacancy sites creates compressive stresses. This shrinkage of the irradiated surface causes a bending momentum and favours NW bending towards the ion beam.

Tensile stresses on the irradiated side of the NWs have been attributed as driving mechanism for NWs bending away from the ion beam direction by some authors in



the literature [188], [318]. Others proposed ion-beam-induced damage and build-up of compressive stresses due to sputtering [181], [189], [358] as a major driving mechanism for NWs bending towards the ion beam. It has been corroborated from the qualitative results of *in-situ* ion irradiation experiments reported in this work that either ion-beam-induced amorphisation along with implantation or sputtering along with surface reconstruction effects could be the major driving mechanisms for NWs bending.

For shallow implantations conducted as part of the current work, where the average depth of the atomic displacements,  $\frac{\bar{x}_{disp}}{\varnothing}$ , is  $\leq 20\%$  of the NW thickness, the Si NWs have been observed to bend away from the ion beam. Ion-beam-induced damage in the irradiated side of the NW can increase the volume up to a maximum of 1.8%. Furthermore, the implanted ions may also lead to an swelling in the irradiated side of the NW. This volume expansion in the irradiated side will produce tensile stresses relative to the unirradiated side of the NW causing it to bend away from the ion beam. Such bending due to volume change in the irradiated side of the NW due to ion-beam-induced damage has concluded by Borschel *et al* [318] and additionally to the extent of amorphisation by Romano *et al* [188].

However, for deep implantation where the average depth of the displacements,  $\frac{\bar{x}_{disp}}{\varnothing}$  is  $\geq 22.6\%$  of the NW thickness, the Si NWs tend to bend towards the ion beam. As discussed above, the loss of atoms due to sputtering and surface reconstruction induces compressive stresses in the irradiated surface of the NW. It has already been reported in the literature that ion-irradiation-induced defect formation and annihilation could produce significant amount of stresses of the order of GPa at the surface [189], [359], [360]. The relaxation of these compressive stresses will cause the NW to bend towards the ion beam. Similar mechanism for Si NWs bending towards the ion beam has been suggested by Rajput *et al.* [189], [358] in the literature.

## 9.4 Recrystallisation of Si NWs

According to Pecorae *et al.* [185], [339], thermal annealing causes straightening of bent NWs via a SPEG process in those NWs which have a c–a interface present. The only NWs which remain bent after thermal annealing are those in which the crystalline strip (i.e. crystallinity in backside of the NW) does not drive epitaxial regrowth and the NW remains partially amorphous. Small pockets of crystalline order in otherwise amorphous NWs can act as nucleation centres for recrystallisation [185]. In such NWs, recrystallisation occurred through a RNG process.

In the current experimental findings, the Si NWs were not observed to straighten after thermal annealing when SPEG, RNG or mixed regrowth (SPEG and RNG) occurred. This is again contrary to the results described previously in the literature [185] that the bent NWs straighten upon thermal annealing. Recrystallisation in Si NWs has been observed in the current work to start above  $\sim 450^{\circ}\text{C}$  for SPEG and above  $\sim 550^{\circ}\text{C}$  for RNG recovery.

A typical example of mixed SPEG and RNG recovery can be seen from the DP shown in Figure 5.14 showing intense bright spots indicating SPEG and polycrystalline rings denoting RNG. It is therefore suggested that the activation energy for these processes in Si NWs is different from the bulk ( $\sim 2.7$  eV for SPEG and  $\sim 4$  eV for RNG [164]) with the RNG in Si NWs starting at a much lower temperature of  $\sim 550^{\circ}\text{C}$  compared to  $\sim 750^{\circ}\text{C}$  in the bulk. It is further hypothesised that around the temperature of  $550^{\circ}\text{C}$ , there is a competition between SPEG and RNG recovery in amorphous NWs leading to the potential for mixed growth as has been observed. More experiments with detailed analysis of these recovery processes are required to further understand the recrystallisation kinetics of Si in nanostructures.

## 9.5 Summary and Conclusion

Based on the experimental results presented in this work and previously in the literature, the ion-irradiation-induced bending direction of NW and the underlying

mechanisms have been explored. A tipping point of the average displacement depth has been identified for NWs to bend towards or away from the ion beam incident direction. This trend has been shown to be common to all reports of semiconductor NW bending in Si, GaAs, ZnO and Ge. For shallow implantations, it has been suggested that ion-beam-induced amorphisation along with ion implantation can cause a volume expansion in the irradiated side relative to the unirradiated side leading to a bending momentum of the NW away from the ion beam. On the other hand, for deeper implantations the ion-beam-induced sputtering and alleviating surface reconstruction effects cause the NWs to bend towards the ion beam.

## 10 Summary and Conclusion

Ion-irradiation-induced modification of 24–50 nm diameter Si NWs were investigated *in-situ* with TEM in the experiments reported in this thesis. Calculations to design the ion irradiation conditions were performed using a custom implementation of the SRIM Monte Carlo computer code using a multislice method to model the circular cross-sectional geometry of a NW.

Irradiation experiments were carefully designed utilising appropriate tilt and rotation procedures in the MIAMI facility to observe the Si NW structural and morphological modification. Ion-beam-induced bending of Si NWs was explored and the dominant mechanisms were identified for two situations of bending towards and away from the ion beam. It has been corroborated from the results of the *in-situ* ion irradiation experiments that for shallow implantation (where the average normalised depth of displacements is less than ~20.0% of the thickness of NW) that the bending is away from the ion beam while for deep implantations (where the average normalised depth of displacements is more than ~22.6% of the thickness of NW) the NWs bend towards the ion beam. For shallow implantation, the volume change in the irradiated side due to the ion-beam-induced damage accumulation and implanted ions relative to the unirradiated side produce tensile stresses causing the NW to bend away from the ion beam. For deep implantations, ion-beam-induced compressive stresses due to sputtering cause shrinkage of the NW surface and relaxation of these stresses through surface reconstruction produces a bending momentum towards the ion beam.

Chapter 7 has been dedicated to the study of ion-beam-induced effects under semiconductor processing conditions relevant to industry. For this purpose, the effect of 7 keV Xe<sup>+</sup> ions into Si NWs was investigated for their potential applications in the Si NWs finFET technology. Structural and morphological changes of Si NWs have been observed when irradiated with 7 keV Xe<sup>+</sup> ions. These include NWs bending, cracking and bubble formation. Depth of damage for 7 keV Xe<sup>+</sup> ions in Si NWs was also measured experimentally and the results were compared with the calculated depth of damage using SRIM.

In chapter 8, the necessary input parameters for FE modelling of Si NWs to calculate the temperature along a NW whilst being heated in a TEM holder have been presented. Surface roughness measurements to determine the effective thermal contact between the NW and Mo grid have been made via AFM. Additionally, appropriate physical properties for this nanoscale system have been researched in the literature. This work will underpin future investigations into the actual temperature of nanostructure investigated using *in-situ* TEM techniques.

## **10.1 Future Work**

Different kinetics for the recrystallization of Si NWs compared to the bulk observed in the current experiments will be explored in more detail to measure the activation temperature of SPEG and RNG of Si NWs. In support of this, FE modelling of Si NWs will be completed based on the results of chapter 8 to calculate the temperature difference between the thermocouple on a TEM holder and the Si NWs themselves.

The Matlab code developed using multislice SRIM method will be further improved and will be extended to other non-planar geometries to better understand the damage and ion implantation in nanostructures. The results of the calculated damage will then be compared with the experiments.

Ion-beam-induced defects in thin Si NWs (less than 20 nm diameter) will be further investigated for their potential use in the next generation of novel electronic devices under industry-relevant irradiation conditions using more-advanced imaging conditions such as weak-beam dark-field, analytical techniques such as electron energy loss spectroscopy and tomographic reconstructions. These investigations could be extended to III-nitride NWs for potential use in photovoltaics and high temperature electronics.

## References

- [1] W. Shockley, “The Theory of p-n Junctions in Semiconductors and p-n Junction Transistors,” *Bell Syst. Tech. J.*, vol. 28, no. 3, pp. 435–489, Jul. 1949.
- [2] J. Bardeen and W. H. Brattain, “Physical Principles Involved in Transistor Action,” *Phys. Rev.*, vol. 75, no. 8, pp. 1208–1225, Apr. 1949.
- [3] “History of The Transistor (the ‘Crystal Triode’).” [Online]. Available: [http://www.beatriceco.com/bti/porticus/bell/belllabs\\_transistor.html](http://www.beatriceco.com/bti/porticus/bell/belllabs_transistor.html). [Accessed: 01-Sep-2016].
- [4] R. W. Keyes, “Physical limits of silicon transistors and circuits,” *Reports Prog. Phys.*, vol. 68, no. 12, pp. 2701–2746, 2005.
- [5] G. E. Moore, “Cramming more components onto integrated circuits, Reprinted from Electronics, volume 38, number 8, April 19, 1965, pp.114 ff.,” *IEEE Solid-State Circuits Newsl.*, vol. 20, no. 3, pp. 33–35, Sep. 2006.
- [6] T. Ihn, *Semiconductor Nanostructures: Quantum States and Electronic Transport*. 2010.
- [7] P. Valizadeh, *Field Effect Transistors, A Comprehensive Overview: From Basic Concepts to Novel Technologies*, Illustrate. John Wiley & Sons, 2016.
- [8] M. Hopkinson, “With silicon pushed to its limits, what will power the next electronics revolution?,” 2015. [Online]. Available: <http://phys.org/news/2015-08-silicon-limits-power-electronics-revolution.html>. [Accessed: 21-Aug-2016].
- [9] “Microprocessor Quick Reference Guide.” [Online]. Available: <http://www.intel.com/pressroom/kits/quickreffam.htm>.
- [10] D. J. Frank, R. H. Dennard, E. Nowak, P. M. Solomon, Y. Taur, and H. P. Wong, “Device Scaling Limits of Si MOSFETs and Their Application Dependencies,” *Proc. IEEE*, vol. 89, no. 3, 2001.

- [11] N. Z. Haron and S. Hamdioui, “Why is CMOS scaling coming to an END?,” *Proc. - 2008 3rd Int. Des. Test Work. IDT 2008*, pp. 98–103, 2008.
- [12] T. Simonite, “Moore’s Law Is Dead. Now What?” [Online]. Available: <https://www.technologyreview.com/s/601441/moores-law-is-dead-now-what/>. [Accessed: 02-Sep-2016].
- [13] Y. C. and T. A. F. T. Ytterdal, *Device Modeling for Analog and RF CMOS Circuit Design*. John Wiley & Sons, 2003.
- [14] F. Hussain, S. S. Hayat, M. Imran, S. a. Ahmad, and F. Bouafia, “Sintering and deposition of nanoparticles on surface of metals: A molecular dynamics approach,” *Comput. Mater. Sci.*, vol. 65, pp. 264–268, Dec. 2012.
- [15] H. Search, C. Journals, A. Contact, M. Iopscience, and I. P. Address, “Nanostructured materials,” *Rep. Prog. Phys.*, vol. 64, pp. 297–381, 2001.
- [16] J.-P. Salvetat, G. Briggs, J.-M. Bonard, R. Bacsá, A. Kulik, T. Stöckli, N. Burnham, and L. Forró, “Elastic and Shear Moduli of Single-Walled Carbon Nanotube Ropes,” *Phys. Rev. Lett.*, vol. 82, no. 5, pp. 944–947, Feb. 1999.
- [17] K. Lee, B. Lukić, A. Magrez, J. W. Seo, G. A. D. Briggs, A. J. Kulik, and L. Forró, “Diameter-dependent elastic modulus supports the metastable-catalyst growth of carbon nanotubes,” *Nano Lett.*, vol. 7, no. 6, pp. 1598–602, Jun. 2007.
- [18] S. Iijima, “Helical microtubules of graphitic carbon,” *Nature*, vol. 354, no. 6348, pp. 56–58, Nov. 1991.
- [19] B. Seijo, E. Fattal, L. Roblot-Treupel, and P. Couvreur, “Design of nanoparticles of less than 50 nm diameter: preparation, characterization and drug loading,” *International Journal of Pharmaceutics*, vol. 62, no. 1, pp. 1–7, 1990.
- [20] C. T. Campbell, “The energetics of supported metal nanoparticles: relationships to sintering rates and catalytic activity,” *Acc. Chem. Res.*, vol. 46, no. 8, pp. 1712–9, Aug. 2013.

- [21] H. Pinto-Alphandary, A. Andremont, and P. Couvreur, "Targeted delivery of antibiotics using liposomes and nanoparticles: Research and applications," *Int. J. Antimicrob. Agents*, vol. 13, no. 3, pp. 155–168, 2000.
- [22] S. K. Bux, J.-P. Fleurial, and R. B. Kaner, "Nanostructured materials for thermoelectric applications," *Chem. Commun. (Camb)*, vol. 46, no. 44, pp. 8311–24, Nov. 2010.
- [23] B. W. Ashutosh Tiwari, Rui Wang, *Advanced Surface Engineering Materials*. John Wiley & Sons, 2016.
- [24] X. Yu, J. Rong, Z. Zhan, Z. Liu, and J. Liu, "Effects of grain size and thermodynamic energy on the lattice parameters of metallic nanomaterials," *Mater. Des.*, vol. 83, pp. 159–163, 2015.
- [25] Y. W. Guozhong Cao, *Nanostructures and Nanomaterials: Synthesis, Properties, and Applications*, Illustrate. World Scientific, 2011.
- [26] Y. Ma, L. Qi, J. Ma, and H. Cheng, "Micelle-Mediated Synthesis of Single-Crystalline Selenium Nanotubes," *Adv. Mater.*, vol. 16, no. 12, pp. 1023–1026, Jun. 2004.
- [27] C. J. Shadi A. Dayeh, Anna Fontcuberta i Morral, *Semiconductor Nanowires II: Properties and Applications*. Academic Press, 2016.
- [28] Y. Cui, Y. Cui, Z. Zhong, Z. Zhong, D. Wang, D. Wang, W. U. Wang, W. U. Wang, C. M. Lieber, and C. M. Lieber, "High Performance Silicon Nanowire Field Effect Transistors," *Nano Lett.*, vol. 3, no. 2, pp. 149–152, 2003.
- [29] J. Xiang, W. Lu, Y. Hu, Y. Wu, H. Yan, and C. M. Lieber, "Ge/Si nanowire heterostructures as high-performance field-effect transistors," *Nature*, vol. 441, no. 7092, pp. 489–493, 2006.
- [30] Sung Dae Suk, Sung-Young Lee, Sung-Min Kim, Eun-Jung Yoon, Min-Sang Kim, Ming Li, Chang Woo Oh, Kyoung Hwan Yeo, Sung Hwan Kim, Dong-Suk Shin, Kwan-Heum Lee, Heung Sik Park, Jeong Nam Han, C. J. Park, Jong-Bong Park, Dong-Won Kim, Donggun Park, and Byung-Il Ryu, "High



- performance 5nm radius twin silicon nanowire MOSFET (TSNWFET) : fabrication on bulk si wafer, characteristics, and reliability,” in *IEEE International Electron Devices Meeting, 2005. IEDM Technical Digest.*, 2005, vol. 0, no. c, pp. 717–720.
- [31] G. Rosaz, B. Salem, N. Pauc, P. Gentile, a Potié, a Solanki, and T. Baron, “High-performance silicon nanowire field-effect transistor with silicided contacts,” *Semicond. Sci. Technol.*, vol. 26, no. 8, p. 85020, 2011.
  - [32] H. Iwai, K. Natori, K. Kakushima, P. Ahmet, K. Shiraishi, J. Iwata, a Oshiyama, K. Yamada, and K. Ohmori, “Si nanowire device and its modeling,” in *2010 International Conference on Simulation of Semiconductor Processes and Devices*, 2010, pp. 63–66.
  - [33] Z. L. Wang and J. Song, “Piezoelectric nanogenerators based on zinc oxide nanowire arrays,” *Science*, vol. 312, no. 5771, pp. 242–246, 2006.
  - [34] C. Zheng, C. M. Lieber, M. Biology, and A. M. Edt, “Nanoproteomics,” vol. 790, 2011.
  - [35] B. J. Ohlsson, T. Sass, A. I. Persson, C. Thelander, M. H. Magnusson, K. Deppert, L. R. Wallenberg, and L. Samuelson, “One-dimensional Steeplechase for Electrons Realized,” pp. 1–3, 2002.
  - [36] L. Mu, Y. Chang, S. D. Sawtelle, M. Wipf, X. Duan, and M. A. Reed, “Silicon Nanowire Field-Effect Transistors—A Versatile Class of Potentiometric Nanobiosensors,” *IEEE Access*, vol. 3, pp. 287–302, 2015.
  - [37] Sung Dae Suk, Sung-Young Lee, Sung-Min Kim, Eun-Jung Yoon, Min-Sang Kim, Ming Li, Chang Woo Oh, Kyoung Hwan Yeo, Sung Hwan Kim, Dong-Suk Shin, Kwan-Heum Lee, Heung Sik Park, Jeong Nam Han, C. J. Park, Jong-Bong Park, Dong-Won Kim, Donggun Park, and Byung-Il Ryu, “High performance 5nm radius Twin Silicon Nanowire MOSFET (TSNWFET) : fabrication on bulk si wafer, characteristics, and reliability,” in *IEEE International Electron Devices Meeting, 2005. IEDM Technical Digest.*, 2005, no. c, pp. 717–720.

- [38] A. Cao, E. J. R. Sudhölter, and L. C. P. M. de Smet, “Silicon nanowire-based devices for gas-phase sensing,” *Sensors (Basel)*, vol. 14, no. 1, pp. 245–271, 2013.
- [39] J. Wan, S.-R. Deng, R. Yang, Z. Shu, B.-R. Lu, S.-Q. Xie, Y. Chen, E. Huq, R. Liu, and X.-P. Qu, “Silicon nanowire sensor for gas detection fabricated by nanoimprint on SU8/SiO<sub>2</sub>/PMMA trilayer,” *Microelectron. Eng.*, vol. 86, no. 4–6, pp. 1238–1242, Apr. 2009.
- [40] K. Skucha, Z. Fan, K. Jeon, A. Javey, and B. Boser, “Palladium/silicon nanowire Schottky barrier-based hydrogen sensors,” *Sensors Actuators, B Chem.*, vol. 145, no. 1, pp. 232–238, 2010.
- [41] C. K. Chan, H. Peng, G. Liu, K. McIlwrath, X. F. Zhang, R. A. Huggins, and Y. Cui, “High-performance lithium battery anodes using silicon nanowires,” *Nat. Nanotechnol.*, vol. 3, no. 1, pp. 31–35, Jan. 2008.
- [42] B. Laik, L. Eude, J. P. Pereira-ramos, C. Sorin, B. Laik, L. Eude, J. P. Pereira-ramos, C. S. Cojocar, D. Pribat, and B. La, “Silicon nanowires as negative electrode for lithium-ion microbatteries” To cite this version : Electrochimica Acta Silicon nanowires as negative electrode for lithium-ion microbatteries,” 2013.
- [43] A. I. Boukai, Y. Bunimovich, J. Tahir-Kheli, J.-K. Yu, W. a Goddard, and J. R. Heath, “Silicon nanowires as efficient thermoelectric materials,” *Nature*, vol. 451, no. 7175, pp. 168–71, Jan. 2008.
- [44] G. Zheng, X. P. A. Gao, and C. M. Lieber, “Frequency Domain Detection of Biomolecules Using Silicon Nanowire Biosensors,” *Nano Lett.*, vol. 10, no. 8, pp. 3179–3183, Aug. 2010.
- [45] N. Shehada, G. Brönstrup, K. Funke, S. Christiansen, M. Leja, and H. Haick, “Ultrasensitive silicon nanowire for real-world gas sensing: Noninvasive diagnosis of cancer from breath volatolome,” *Nano Lett.*, vol. 15, no. 2, pp. 1288–1295, 2015.
- [46] G.-J. Zhang, G. Zhang, J. H. Chua, R.-E. Chee, E. H. Wong, A. Agarwal, K.

- D. Buddharaju, N. Singh, Z. Gao, and N. Balasubramanian, "DNA Sensing by Silicon Nanowire: Charge Layer Distance Dependence," *Nano Lett.*, vol. 8, no. 4, pp. 1066–1070, Apr. 2008.
- [47] D. W. Pashley and A. E. B. Presland, "Ion damage to metal films inside an electron microscope," *Philos. Mag.*, vol. 6, no. 68, pp. 1003–1012, Aug. 1961.
- [48] L. M. Howe, R. W. Gilbert, and G. R. Piercy, "Direct observation of radiation damage produced in copper below 30K during ion bombardment in the electron microscope," *Appl. Phys. Lett.*, vol. 3, no. 8, p. 125, 1963.
- [49] L. M. Howe and J. F. McGurn, "Direct observation of disappearance and collapse of stacking-fault tetrahedra in gold foils during ion bombardment in the electron microscope," *Appl. Phys. Lett.*, vol. 4, no. 6, p. 99, 1964.
- [50] J. R. Parsons and L. M. Howe, "Measurement of the ion flux emanating from oxide coated emission filaments in a Siemens electron microscope," *J. Sci. Instrum.*, vol. 41, no. 12, pp. 773–775, 1964.
- [51] D. S. Whitmell, W. A. D. Kennedy, D. J. Mazey, and R. S. Nelson, "A heavy-ion accelerator-electron microscope link for the direct observation of ion irradiation effects," *Radiat. Eff.*, vol. 22, no. 3, pp. 163–168, Jan. 1974.
- [52] F. R. Brotzen, P. J. Loos, and D. P. Brady, "Thermal conductivity of thin SiO<sub>2</sub> films," *Thin Solid Films*, vol. 207, no. 1–2, pp. 197–201, Jan. 1992.
- [53] J.-F. Mercure, R. Karmouch, Y. Anahory, S. Roorda, and F. Schiettekatte, "Dependence of the structural relaxation of amorphous silicon on implantation temperature," *Phys. Rev. B*, vol. 71, no. 13, p. 134205, Apr. 2005.
- [54] K. T. Regner, D. P. Sellan, Z. Su, C. H. Amon, A. J. H. McGaughey, and J. a Malen, "Broadband phonon mean free path contributions to thermal conductivity measured using frequency domain thermoreflectance.," *Nat. Commun.*, vol. 4, p. 1640, Jan. 2013.
- [55] C. Borschel, R. Niepelt, S. Geburt, C. Gutsche, I. Regolin, W. Prost, F.-J. Tegude, D. Stichtenoth, D. Schwen, and C. Ronning, "Alignment of

- semiconductor nanowires using ion beams.,” *Small*, vol. 5, no. 22, pp. 2576–80, Nov. 2009.
- [56] A. Chemseddine, “Fibrous and oriented quantum dots. Synthesis and characterization,” *Chem. Phys. Lett.*, vol. 216, no. 3–6, pp. 265–269, Dec. 1993.
- [57] J. Lian and B. Baudelet, “A modified Hall-Petch relationship for nanocrystalline materials,” *Nanostructured Mater.*, vol. 2, no. 4, pp. 415–419, Jul. 1993.
- [58] M. Knobel, D. R. Santos, I. L. Torriani, and R. S. Turtelli, “Structural evolution of nanocrystalline Fe<sub>73.5</sub>Cu<sub>1</sub>Nb<sub>3</sub>Si<sub>13.5</sub>B<sub>9</sub>,” *Nanostructured Mater.*, vol. 2, no. 4, pp. 399–405, Jul. 1993.
- [59] X.-F. Li, H. Zhang, and K. Y. Lee, “Dependence of Young’s modulus of nanowires on surface effect,” *Int. J. Mech. Sci.*, vol. 81, pp. 120–125, Apr. 2014.
- [60] Y. W. Guozhong Cao, *Nanostructures and Nanomaterials: Synthesis, Properties, and Applications*, Illustrate. World Scientific, 2011.
- [61] C. M. Lieber, “Nanoscale Science and Technology: Building a Big Future from Small Things,” *MRS Bull.*, vol. 28, no. 7, pp. 486–491, 2003.
- .
- [62] H. Park and P. Klein, “Surface Cauchy-Born analysis of surface stress effects on metallic nanowires,” *Phys. Rev. B*, vol. 75, no. 8, p. 85408, Feb. 2007.
- [63] B. Lee and R. E. Rudd, “First-principles calculation of mechanical properties of Si{001} nanowires and comparison to nanomechanical theory,” *Phys. Rev. B*, vol. 75, no. 19, p. 195328, May 2007.
- [64] M. Law, J. Goldberger, and P. Yang, “Semiconductor Nanowires and Nanotubes,” *Annu. Rev. Mater. Res.*, vol. 34, no. 1, pp. 83–122, Aug. 2004.
- [65] C.-Y. Nam, P. Jaroenapibal, D. Tham, D. E. Luzzi, S. Evoy, and J. E. Fischer, “Diameter-dependent electromechanical properties of GaN nanowires.,” *Nano*

*Lett.*, vol. 6, no. 2, pp. 153–8, Feb. 2006.

- [66] R. Chen, A. I. Hochbaum, P. Murphy, J. Moore, P. Yang, and A. Majumdar, “Thermal Conductance of Thin Silicon Nanowires,” *Phys. Rev. Lett.*, vol. 101, no. 10, pp. 1–4, 2008.
- [67] W. L. Ng, M. a Lourenço, R. M. Gwilliam, S. Ledain, G. Shao, and K. P. Homewood, “An efficient room-temperature silicon-based light-emitting diode,” *Nature*, vol. 410, no. 6825, pp. 192–4, Mar. 2001.
- [68] C. F. Dee, I. Ahmad, L. Yan, X. Zhou, and B. Y. Majlis, “Amorphization of zno nanowires by proton beam irradiation,” *Nano*, vol. 6, no. 3, pp. 259–263, Jun. 2011.
- [69] A. Colli, A. Fasoli, C. Ronning, S. Pisana, S. Piscanec, and A. C. Ferrari, “Ion beam doping of silicon nanowires,” *Nano Lett.*, vol. 8, pp. 2188–2193, 2008.
- [70] E. W. Werner Wesch, *Ion Beam Modification of Solids: Ion-Solid Interaction and Radiation Damage*, Illustrate. Springer.
- [71] C. Ronning, C. Borschel, S. Geburt, and R. Niepelt, “Ion beam doping of semiconductor nanowires,” *Mater. Sci. Eng. R Reports*, vol. 70, no. 3–6, pp. 30–43, Nov. 2010.
- [72] A. M. & F. W. Zhipei Sun, “Optical modulators with 2D layered materials,” *Nat. Photonics*, vol. 10, no. 4, pp. 201–201, Mar. 2016.
- [73] K. D. Sattler, *Handbook of Nanophysics: Functional Nanomaterials*, Illustrate. CRC Press, 2010.
- [74] E. C. Garnett and P. Yang, “Silicon nanowire radial p-n junction solar cells,” *J. Am. Chem. Soc.*, vol. 130, no. 29, pp. 9224–9225, 2008.
- [75] J. Wan, S. R. Deng, R. Yang, Z. Shu, B. R. Lu, S. Q. Xie, Y. Chen, E. Huq, R. Liu, and X. P. Qu, “Silicon nanowire sensor for gas detection fabricated by nanoimprint on SU8/SiO<sub>2</sub>/PMMA trilayer,” *Microelectron. Eng.*, vol. 86, no. 4–6, pp. 1238–1242, 2009.

- [76] D.-M. Tang, C.-L. Ren, M.-S. Wang, X. Wei, N. Kawamoto, C. Liu, Y. Bando, M. Mitome, N. Fukata, and D. Golberg, "Mechanical properties of Si nanowires as revealed by in situ transmission electron microscopy and molecular dynamics simulations.," *Nano Lett.*, vol. 12, no. 4, pp. 1898–904, Apr. 2012.
- [77] M. D. Kelzenberg, S. W. Boettcher, J. A. Petykiewicz, D. B. Turner-Evans, M. C. Putnam, E. L. Warren, J. M. Spurgeon, R. M. Briggs, N. S. Lewis, and H. A. Atwater, "Enhanced absorption and carrier collection in Si wire arrays for photovoltaic applications," *Nat. Mater.*, vol. 9, no. 3, pp. 239–244, 2010.
- [78] J. I. Abdul Rashid, J. Abdullah, N. A. Yusof, R. Hajian, J. I. Abdul Rashid, J. Abdullah, N. A. Yusof, and R. Hajian, "The Development of Silicon Nanowire as Sensing Material and Its Applications," *J. Nanomater.*, vol. 2013, pp. 1–16, 2013.
- [79] J.-P. Colinge, C.-W. Lee, A. Afzalian, N. D. Akhavan, R. Yan, I. Ferain, P. Razavi, B. O'Neill, A. Blake, M. White, A.-M. Kelleher, B. McCarthy, and R. Murphy, "Nanowire transistors without junctions," *Nat. Nanotechnol.*, vol. 5, no. 3, pp. 225–229, Mar. 2010.
- [80] D. L. N. Singh, K.D. Buddharaju, A. Agarwal, S.C. Rustagi, C.Q. Lo, N. Balasubramanian and Kwong, "Fully gate-all-around silicon nanowire CMOS devices," *Solid State Tech.*, vol. 51, p. 34, 2008.
- [81] T. Mikolajick, A. Heinzig, J. Trommer, S. Pregl, M. Grube, G. Cuniberti, and W. M. Weber, "Silicon nanowires - a versatile technology platform," *Phys. status solidi - Rapid Res. Lett.*, vol. 7, no. 10, pp. 793–799, Oct. 2013.
- [82] R. G. Elliman and J. S. Williams, "Advances in ion beam modification of semiconductors ," *Curr. Opin. Solid State Mater. Sci.* , vol. 19, no. 1, pp. 49–67, 2015.
- [83] Christopher Hammond, *The Basics of Crystallography and Diffraction*, illustrated edition. Oxford University Press, 2001.
- [84] K. M. K. Anthony A. Kelly, *Crystallography and Crystal Defects*, Illustrate.

John Wiley & Sons, 2012.

- [85] C. Kittel, *Introduction to Solid State Physics*, 8, illustred edition. Wiley, 2004.
- [86] “<http://chemistrytextbookcrawl.blogspot.co.uk/2012/08/chapter-3.html>.”  
[Online]. Available:  
<http://chemistrytextbookcrawl.blogspot.co.uk/2012/08/chapter-3.html>.  
[Accessed: 03-Jan-2016].
- [87] A. Bravais, “Ueber den Refractions- und Dispersionsindex des Eises,” *Ann. der Phys. und Chemie*, vol. 149, no. S4, pp. 576–578, 1848.
- [88] T. C. Ozawa and S. J. Kang, “Balls & Sticks: easy-to-use structure visualization and animation program,” *J. Appl. Crystallogr.*, vol. 37, no. 4, pp. 679–679, Aug. 2004.
- [89] R. J. D. Tilley, *Understanding Solids: The Science of Materials*. John Wiley & Sons, 2005.
- [90] W. W. Donald Askeland, *Essentials of Materials Science & Engineering*, SI Edition. Cengage Learning, 2013.
- [91] P. F. Donald Askeland, *The Science & Engineering of Materials*. Cengage Learning, 2005.
- [92] N. W. Egon Wiberg, *Inorganic Chemistry*. Academic Press, 2001.
- [93] M. Tang, L. Colombo, J. Zhu, and T. D. La Rubia, “Intrinsic point defects in crystalline silicon: Tight-binding molecular dynamics studies of self-diffusion, interstitial-vacancy recombination, and formation volumes,” *Phys. Rev. B*, vol. 55, no. 21, pp. 279–289, 1997.
- [94] P. Schmuki, *Pits and Pores II: Formation, Properties, and Significance for Advanced Materials: Proceedings of the International Symposium*. New Jersey, USA: The Electrochemical Society, Inc, 2001.
- [95] M. J. Caturla, T. Diaz de la Rubia, and G. H. Gilmer, “Recrystallization of a planar amorphous ~~-crystalline interface~~ in silicon by

- molecular dynamics study,” *J. Appl. Phys.*, vol. 77, no. 7, pp. 3121–3125, Apr. 1995.
- [96] L. Pelaz, L. a. Marqués, and J. Barbolla, “Ion-beam-induced amorphization and recrystallization in silicon,” *J. Appl. Phys.*, vol. 96, no. 11, p. 5947, 2004.
- [97] W. K. Jean P Mercier, Gerald Zambelli, *Introduction To Materials Science*. Elsevier, 2012.
- [98] Selladurai, *Engineering Physics Part - I*. PHI Learning Pvt. Ltd., 2010.
- [99] I. Lazanu and S. Lazanu, “The role of primary point defects in the degradation of silicon detectors due to hadron and lepton irradiation,” *Phys. Scr.*, vol. 74, no. 2, pp. 201–207, 2006.
- [100] G. D. Watkins, “Intrinsic defects in silicon,” *Mater. Sci. Semicond. Process.*, vol. 3, pp. 227–235, 2000.
- [101] R. Hull, *Properties of Crystalline Silicon*, Illustrate. IET, 1999.
- [102] C. P. S. Bhargava A. K., *Mechanical Behaviour and Testing of Materials*. PHI Learning Pvt. Ltd, 2011.
- [103] T. A. Pagava, N. T. Bzhalava, N. I. Maisuradze, D. Z. Khocholava, and L. S. Chkhartishvili, “Two mechanisms of annealing of divacancies in irradiated n - si crystals,” *Ukrayins' kij Fyizichnij Zhurnal (Kyiv)*, 55(11), 1195-1200. .
- [104] Frank Honniger, “Radiation Damage in Silicon - Defect analysis and Detector Properties,” p. 196, 2007.
- [105] J. F. Gibbons, “Ion Implantation in Semiconductors-Part Production and Annealing II : Damage,” *Proc. IEEE, VOL. 60, NO. 9, Sept. 1972*, vol. 6, no. 9, pp. 1062–1096, 1972.
- [106] L. Pelaz, L. A. Marqués, M. Aboy, J. Barbolla, G. H. Gilmer, and G. H. Gilmer, “Atomistic modeling of amorphization and recrystallization in silicon Atomistic modeling of amorphization and recrystallization in silicon,” *Appl. Phys. Lett.*, vol. 2038, pp. 1–4, 2003.



- [107] S. Coffa, F. Priolo, and A. Battaglia, “Defect production and annealing in ion-implanted amorphous silicon,” *Phys. Rev. Lett.*, vol. 70, no. 24, pp. 3756–3759, Jun. 1993.
- [108] S. Pantelides, “Defects in Amorphous Silicon: A New Perspective,” *Phys. Rev. Lett.*, vol. 57, no. 23, pp. 2979–2982, Dec. 1986.
- [109] W. G. Spitzer, G. K. Hubler, and T. A. Kennedy, “Properties of amorphous silicon produced by ion implantation: Thermal annealing,” *Nucl. Instruments Methods Phys. Res.*, vol. 209–210, pp. 309–312, May 1983.
- [110] S. Roorda, W. Sinke, J. Poate, D. Jacobson, S. Dierker, B. Dennis, D. Eaglesham, F. Spaepen, and P. Fuoss, “Structural relaxation and defect annihilation in pure amorphous silicon,” *Phys. Rev. B*, vol. 44, no. 8, pp. 3702–3725, Aug. 1991.
- [111] S. Roorda, S. Doorn, W. Sinke, P. Scholte, and E. van Loenen, “Calorimetric evidence for structural relaxation in amorphous silicon,” *Phys. Rev. Lett.*, vol. 62, no. 16, pp. 1880–1883, Apr. 1989.
- [112] E. P. Donovan, G. K. Hubler, and C. N. Waddell, “Correlation of optical changes in amorphous Ge with enthalpy of relaxation,” *Nucl. Instruments Methods Phys. Res. Sect. B Beam Interact. with Mater. Atoms*, vol. 19–20, pp. 590–594, Jan. 1987.
- [113] E. P. Donovan, F. Spaepen, J. M. Poate, and D. C. Jacobson, “Homogeneous and interfacial heat releases in amorphous silicon,” *Appl. Phys. Lett.*, vol. 55, no. 15, p. 1516, 1989.
- [114] J. E. Fredrickson, “Effects of thermal annealing on the refractive index of amorphous silicon produced by ion implantation,” *Appl. Phys. Lett.*, vol. 40, no. 2, p. 172, 1982.
- [115] R. Tsu, J. Gonzalez-Hernandez, and F. H. Pollak, “Determination of the energy barrier for structural relaxation in amorphous Si and Ge by Raman scattering,” *Solid State Commun.*, vol. 54, no. 5, pp. 447–450, May 1985.

- [116] A. Battaglia and S. U. Campisano, “Mechanisms of amorphization in crystalline silicon,” *J. Appl. Phys.*, vol. 74, no. 10, p. 6058, 1993.
- [117] P. Thomas, M. Brodsky, D. Kaplan, and D. Lepine, “Electron spin resonance of ultrahigh vacuum evaporated amorphous silicon: In situ and ex situ studies,” *Phys. Rev. B*, vol. 18, no. 7, pp. 3059–3073, Oct. 1978.
- [118] G. Bai and M. A. Nicolet, “Defects production and annealing in self-implanted Si,” *J. Appl. Phys.*, vol. 70, no. 2, pp. 649–655, 1991.
- [119] C. J. Lucia Romano, Vittorio Privitera, *Defects in Semiconductors Volume 91 of Semiconductors and Semimetals*. Academic Press, 2015.
- [120] P. G. Coleman, “Activation energies for vacancy migration, clustering and annealing in silicon,” *J. Phys. Conf. Ser.*, vol. 265, p. 12001, Jan. 2011.
- [121] R. Poirier, V. Avalos, S. Dannefaer, F. Schiettekatte, and S. Roorda, “Annealing mechanisms of divacancies in silicon,” *Phys. B Condens. Matter*, vol. 340–342, pp. 609–612, 2003.
- [122] J. W. Corbett and G. D. Watkins, “Production of divacancies and vacancies by electron irradiation of silicon,” *Phys. Rev.*, vol. 138, no. 2A, 1965.
- [123] Y. Zhong, C. Bailat, R. S. Averback, S. K. Ghose, and I. K. Robinson, “Damage accumulation in Si during high-dose self-ion implantation,” *J. Appl. Phys.*, vol. 96, no. 3, pp. 1328–1335, 2004.
- [124] Y. A. Du, R. G. Hennig, T. J. Lenosky, and J. W. Wilkins, “From compact point defects to extended structures in silicon,” *Eur. Phys. J. B*, vol. 57, no. 3, pp. 229–234, 2007.
- [125] J. Kim, F. Kirchhoff, W. G. Aulbur, J. W. Wilkins, F. S. Khan, and G. Kresse, “Thermally Activated Reorientation of Di-interstitial Defects in Silicon,” *Phys. Rev. Lett.*, vol. 83, no. 10, pp. 1990–1993, Sep. 1999.
- [126] L. Pelaz, L. a. Marqués, and J. Barbolla, “Ion-beam-induced amorphization and recrystallization in silicon,” *J. Appl. Phys.*, vol. 96, no. 11, p. 5947, 2004.

- [127] M. Posselt, F. Gao, and D. Zwicker, “Migration of di- and tri-interstitials in silicon,” *Nucl. Instruments Methods Phys. Res. Sect. B Beam Interact. with Mater. Atoms*, vol. 228, no. 1–4 SPEC. ISS., pp. 212–217, 2005.
- [128] S. K. Estreicher, M. Gharaibeh, P. A. Fedders, and P. Ordejón, “Unexpected Dynamics for Self-Interstitial Clusters in Silicon,” *Phys. Rev. Lett.*, vol. 86, no. 7, pp. 1247–1250, Feb. 2001.
- [129] P. D. Edmondson, D. J. Riley, R. C. Birtcher, and S. E. Donnelly, “Amorphization of crystalline Si due to heavy and light ion irradiation,” *J. Appl. Phys.*, vol. 106, no. 4, p. 43505, 2009.
- [130] W. J. Weber, “Models and mechanisms of irradiation-induced amorphization in ceramics,” *Nucl. Instruments Methods Phys. Res. Sect. B Beam Interact. with Mater. Atoms*, vol. 166, pp. 98–106, 2000.
- [131] J. A. Hinks and P. D. Edmondson, “Transmission electron microscopy of the amorphization of copper indium diselenide by in situ ion irradiation,” *J. Appl. Phys.*, vol. 111, no. 5, p. 53510, 2012.
- [132] L. Pelaz, L. a. Marqués, and J. Barbolla, “Ion-beam-induced amorphization and recrystallization in silicon,” *J. Appl. Phys.*, vol. 96, no. 11, pp. 5947–5976, 2004.
- [133] J. R. Dennis and E. B. Hale, “Crystalline to amorphous transformation in ion-implanted silicon: a composite model,” *J. Appl. Phys.*, vol. 49, no. 3, p. 1119, 1978.
- [134] O. W. Holland, S. J. Pennycook, and G. L. Albert, “New model for damage accumulation in Si during self-ion irradiation,” *Appl. Phys. Lett.*, vol. 55, no. 24, p. 2503, 1989.
- [135] E. C. Baranova, V. M. Gusev, Y. V. Martynenko, and I. B. Haibullin, “Effect of irradiation temperature on Si amorphization process,” *Radiat. Eff.*, vol. 25, no. 3, pp. 157–162, Jan. 1975.
- [136] M.-J. Caturla, T. Díaz de la Rubia, L. Marqués, and G. Gilmer, “Ion-beam

- processing of silicon at keV energies: A molecular-dynamics study,” *Phys. Rev. B*, vol. 54, no. 23, pp. 16683–16695, 1996.
- [137] J. R. Dennis and E. B. Hale, “Model correction for the formation of amorphous silicon by ion implantation,” *Radiat. Eff.*, vol. 19, no. 1, pp. 67–68, Jan. 1973.
- [138] B. L. C. Morehead, F. F., “Formation of Amorphous Silicon by Ion Bombardment as a Function of Ion, Temperature, and Dose,” *J. Appl. Phys.*, vol. 43, no. 3, p. 1112, 1972.
- [139] D. A. Thompson, “High density cascade effects,” *Radiat. Eff.*, vol. 56, no. 3–4, pp. 105–150, Jan. 1981.
- [140] J. Narayan, O. S. Oen, D. Fathy, and O. W. Holland, “Atomic structure of collision cascades in ion-implanted silicon and channeling effects,” *Mater. Lett.*, vol. 3, no. 3, pp. 67–72, Jan. 1985.
- [141] F. F. Morehead and B. L. Crowder, “A model for the formation of amorphous Si by ion bombardment,” *Radiat. Eff.*, vol. 6, no. 1, pp. 27–32, Jan. 1970.
- [142] R. A. B. and C. J. J.S. Williamsa, H.H. Tana1, R.D. Goldberga, “Dynamic Annealing and Amorphous Phase Formation in Si, GaAs and AlGaAs Under Ion Irradiation,” *MRS Proc.*, vol. 316, no. 15, 1993.
- [143] W. L. B. Harry A. Atwater, “Grain boundary mediated amorphization in silicon during ion irradiation,” *Appl. Phys. Lett.*, vol. 56, no. 1, p. 30, 1990.
- [144] K. S. Jones, K. Moller, J. Chen, M. Puga-Lambers, B. Freer, J. Berstein, and L. Rubin, “Effect of implant temperature on transient enhanced diffusion of boron in regrown silicon after amorphization by Si<sup>+</sup> or Ge<sup>+</sup> implantation,” *J. Appl. Phys.*, vol. 81, no. 9, p. 6051, 1997.
- [145] A. Battaglia, S. U. Campisano, K. S. Jones, K. Moller, J. Chen, M. Puga-Lambers, B. Freer, J. Berstein, and L. Rubin, “Mechanisms of amorphization in crystalline silicon,” *J. Appl. Phys.*, vol. 81, no. 9, p. 6051, 1993.
- [146] R. Karmouch, Y. Anahory, J.-F. Mercure, D. Bouilly, M. Chicoine, G.

- Bentoumi, R. Leonelli, Y. Wang, and F. Schiettekatte, “Damage evolution in low-energy ion implanted silicon,” *Phys. Rev. B*, vol. 75, no. 7, p. 75304, Feb. 2007.
- [147] O. W. Holland, C. W. White, M. K. El-Ghor, and J. D. Budai, “MeV, self-ion implantation in Si at liquid nitrogen temperature; a study of damage morphology and its anomalous annealing behavior,” *J. Appl. Phys.*, vol. 68, no. 5, p. 2081, 1990.
- [148] K. Minowa and K. Sumino, “Stress-induced amorphization of silicon crystal by mechanical scratching,” *Phys. Rev. Lett.*, vol. 69, no. 2, pp. 320–322, Jul. 1992.
- [149] D. Clarke, M. Kroll, P. Kirchner, R. Cook, and B. Hockey, “Amorphization and Conductivity of Silicon and Germanium Induced by Indentation,” *Phys. Rev. Lett.*, vol. 60, no. 21, pp. 2156–2159, May 1988.
- [150] J. A. Davies, G. C. Ball, F. Brown, and B. Domeij, “Range of energetic Xe<sup>125</sup> ions in monocrystalline silicon,” *Can. J. Phys.*, vol. 42, no. 6, pp. 1070–1080, Jun. 1964.
- [151] K.-W. Wang, W. G. Spitzer, G. K. Hubler, and D. K. Sadana, “Ion implantation of Si by <sup>12</sup>C, <sup>29</sup>Si, and <sup>120</sup>Sn: Amorphization and annealing effects,” *J. Appl. Phys.*, vol. 58, no. 12, p. 4553, 1985.
- [152] T. Motooka, “Model for amorphization processes in ion-implanted Si,” *Phys. Rev. B*, vol. 49, no. 23, pp. 16367–16371, Jun. 1994.
- [153] J. Linnros, R. G. Elliman, and W. L. Brown, “Divacancy control of the balance between ion-beam-induced epitaxial crystallization and amorphization in silicon,” *Journal of Materials Research*, vol. 3, no. 6, pp. 1208–1211, 1988.
- [154] G. Etherington, A. C. Wright, J. T. Wenzel, J. C. Dore, J. H. Clarke, and R. N. Sinclair, “A neutron diffraction study of the structure of evaporated amorphous germanium,” *Journal of Non-Crystalline Solids*, vol. 48, no. 2–3, pp. 265–289, 1982.

- [155] S. Kugler, G. Molnár, G. Petö, E. Zsoldos, L. Rosta, A. Menelle, and R. Bellissent, “Neutron-diffraction study of the structure of evaporated pure amorphous silicon,” *Phys. Rev. B*, vol. 40, no. 11, pp. 8030–8032, Oct. 1989.
- [156] W. Kamitakahara, H. Shanks, J. McClelland, U. Buchenau, F. Gompf, and L. Pintschovius, “Measurement of Phonon Densities of States for Pure and Hydrogenated Amorphous Silicon,” *Phys. Rev. Lett.*, vol. 52, no. 8, pp. 644–647, Feb. 1984.
- [157] J. A. Van Vechten, “Abstract: H4.00013 : What happens to the energy of recrystallization of amorphous Si?,” *Bull. Am. Phys. Soc. 13th Annu. Meet. Northwest Sect. APS*, vol. 56, no. 10, 2011.
- [158] D. Stock, B. Weber, and K. Gärtner, “Role of the bond defect for structural transformations between crystalline and amorphous silicon: A molecular-dynamics study,” *Phys. Rev. B*, vol. 61, no. 12, pp. 8150–8154, Mar. 2000.
- [159] D. M. Stock, G. H. Gilmer, M. Jaraíz, and T. Diaz de la Rubia, “Point defect accumulation in silicon irradiated by energetic particles: A molecular dynamics simulation,” *Nucl. Instruments Methods Phys. Res. Sect. B Beam Interact. with Mater. Atoms*, vol. 102, no. 1–4, pp. 207–210, Aug. 1995.
- [160] S. Franssila, *Introduction to Microfabrication*, 2nd ed. John Wiley & Sons, 2010.
- [161] S. Vepřek, Z. Iqbal, and F.-A. Sarott, “A thermodynamic criterion of the crystalline-to-amorphous transition in silicon,” *Philos. Mag. Part B*, vol. 45, no. 1, pp. 137–145, Jan. 1982.
- [162] H. S. Wolfgang Skorupa, *Subsecond Annealing of Advanced Materials: Annealing by Lasers, Flash Lamps and Swift Heavy Ions*. Springer Science & Business Media, 2013.
- [163] J. A. D. J. W. Mayer, L. Eriksson, S. T. Picraux, “Ion implantation of silicon and germanium at room temperature. Analysis by means of 1.0-MeV helium ion scattering,” *Can. J. Phys.*, vol. 46, no. 6, pp. 68–82, 1968.

- [164] G. L. Olson and J. A. Roth, “Kinetics of solid phase crystallization in amorphous silicon,” *Mater. Sci. Reports*, vol. 3, no. 1, pp. 1–77, Jan. 1988.
- [165] G. L. Olson and J. A. Roth, “Kinetics of solid phase crystallization in amorphous silicon,” *Mater. Sci. Reports*, vol. 3, no. 1, pp. 1–77, Jan. 1988.
- [166] L. Csepregi, E. F. Kennedy, J. W. Mayer, and T. W. Sigmon, “Substrate-orientation dependence of the epitaxial regrowth rate from Si-implanted amorphous Si,” *J. Appl. Phys.*, vol. 49, no. 7, p. 3906, 1978.
- [167] F. Spaepen, “A structural model for the interface between amorphous and crystalline Si or Ge,” *Acta Metall.*, vol. 26, no. 7, pp. 1167–1177, 1978.
- [168] M. Caturla, Díaz de la Rubia T, L. Marqués, and G. Gilmer, “Ion-beam processing of silicon at keV energies: A molecular-dynamics study.,” *Phys. Rev. B. Condens. Matter*, vol. 54, no. 23, pp. 16683–16695, Dec. 1996.
- [169] G.-Q. Lu, E. Nygren, and M. J. Aziz, “Pressure-enhanced crystallization kinetics of amorphous Si and Ge: Implications for point-defect mechanisms,” *J. Appl. Phys.*, vol. 70, no. 10, p. 5323, 1991.
- [170] E. Rimini, *Ion Implantation: Basics to Device Fabrication*. Boston: Kluwer Academic Publishers, 1995.
- [171] R. G. Elliman, J. S. Williams, W. L. Brown, A. Leiberich, D. M. Maher, and R. V. Knoell, “Ion-beam-induced crystallization and amorphization of silicon,” *Nucl. Instruments Methods Phys. Res. Sect. B Beam Interact. with Mater. Atoms*, vol. 19–20, no. Part2, pp. 435–442, Jan. 1987.
- [172] F. Priolo, A. Battaglia, R. Nicotra, and E. Rimini, “Low-temperature reordering in partially amorphized Si crystals,” *Appl. Phys. Lett.*, vol. 57, no. 8, p. 768, 1990.
- [173] L. A. and L. C. Rossano Lang, Alan de Menezes, Adenilson dos Santos, Shay Reboh, Eliermes Meneses, “Lang, R., de Menezes, A., dos Santos, A., Reboh, S., Meneses, E., Amaral, L., & Cardoso, L. (2012). Ion-beam-induced epitaxial recrystallization method and its recent applications.

in *recrystallization*. InTech.

- [174] G. L. Olson and J. A. Roth, “Kinetics of solid phase crystallization in amorphous silicon,” *Mater. Sci. Reports*, vol. 3, no. 1, pp. 1–77, Jan. 1988.
- [175] J. Narayan, O. S. Oen, D. Fathy, and O. W. Holland, “Atomic structure of collision cascades in ion-implanted silicon and channeling effects,” *Mater. Lett.*, vol. 3, no. 3, pp. 67–72, Jan. 1985.
- [176] D. Stock, B. Weber, and K. Gärtner, “Role of the bond defect for structural transformations between crystalline and amorphous silicon: A molecular-dynamics study,” *Phys. Rev. B*, vol. 61, no. 12, pp. 8150–8154, Mar. 2000.
- [177] L. A. Marqués, L. Pelaz, I. Santos, P. López, and R. Duffy, “Molecular dynamics simulation of the regrowth of nanometric multigate Si devices,” *J. Appl. Phys.*, vol. 111, no. 3, p. 34302, Feb. 2012.
- [178] F. Cargnoni, C. Gatti, and L. Colombo, “Formation and annihilation of a bond defect in silicon: An ab initio quantum-mechanical characterization,” *Phys. Rev. B*, vol. 57, no. 1, pp. 170–177, Jan. 1998.
- [179] K. Jun, J. Joo, and J. M. Jacobson, “Focused ion beam-assisted bending of silicon nanowires for complex three dimensional structures,” *J. Vac. Sci. Technol. B Microelectron. Nanom. Struct.*, vol. 27, no. 6, p. 3043, 2009.
- [180] K. Jun, J. Joo, and J. M. Jacobson, “Focused ion beam-assisted bending of silicon nanowires for complex three dimensional structures,” *J. Vac. Sci. Technol. B Microelectron. Nanom. Struct.*, vol. 27, no. 6, p. 3043, 2009.
- [181] E. F. Pecora, A. Irrera, and F. Priolo, “Ion beam-induced bending of silicon nanowires,” *Phys. E Low-dimensional Syst. Nanostructures*, vol. 44, no. 6, pp. 1074–1077, Mar. 2012.
- [182] C. Borschel, S. Spindler, D. Lerose, A. Bochmann, S. H. Christiansen, S. Nietzsche, M. Oertel, and C. Ronning, “Permanent bending and alignment of ZnO nanowires,” *Nanotechnology*, vol. 22, no. 18, p. 185307, 2011.
- [183] G. Yun and H. Park, “Surface stress effects on the bending properties of fcc



- metal nanowires,” *Phys. Rev. B*, vol. 79, no. 19, p. 195421, May 2009.
- [184] J. He and C. M. Lilley, “Surface effect on the elastic behavior of static bending nanowires,” *Nano Lett.*, vol. 8, no. 7, pp. 1798–802, Jul. 2008.
- [185] C. Borschel and C. Ronning, “Ion beam irradiation of nanostructures - A 3D Monte Carlo simulation code,” *Nucl. Instruments Methods Phys. Res. Sect. B Beam Interact. with Mater. Atoms*, vol. 269, no. 19, pp. 2133–2138, 2011.
- [186] E. F. Pecora, A. Irrera, S. Boninelli, L. Romano, C. Spinella, and F. Priolo, “Nanoscale amorphization, bending and recrystallization in silicon nanowires,” *Appl. Phys. A*, vol. 102, no. 1, pp. 13–19, Sep. 2011.
- [187] A. Cui, J. C. Fenton, W. Li, T. H. Shen, Z. Liu, Q. Luo, and C. Gu, “Ion-beam-induced bending of freestanding amorphous nanowires: The importance of the substrate material and charging,” *Appl. Phys. Lett.*, vol. 102, no. 21, p. 213112, 2013.
- [188] T. Van Dillen, M. J. A. De Dood, J. J. Penninkhof, A. Polman, S. Roorda, and A. M. Vredenberg, “Ion beam-induced anisotropic plastic deformation of silicon microstructures,” *Appl. Phys. Lett.*, vol. 84, no. 18, pp. 3591–3593, 2004.
- [189] L. Romano, N. G. Rudawski, M. R. Holzworth, K. S. Jones, S. G. Choi, and S. T. Picraux, “Nanoscale manipulation of Ge nanowires by ion irradiation,” *J. Appl. Phys.*, vol. 106, no. 11, p. 114316, 2009.
- [190] N. S. Rajput, Z. Tong, and X. Luo, “Investigation of ion induced bending mechanism for nanostructures,” *Mater. Res. Express*, vol. 2, no. 1, p. 15002, 2014.
- [191] W. J. W. Donald R. Askeland, *The Science and Engineering of Materials*, 7th ed. 2015.
- [192] F. L. Leite, C. C. Bueno, A. L. Da Róz, E. C. Ziemath, and O. N. Oliveira, *Theoretical models for surface forces and adhesion and their measurement using atomic force microscopy*, vol. 13, no. 10. 2012.

- [193] D. Maugis, “Adhesion of spheres: The JKR-DMT transition using a dugdale model,” *J. Colloid Interface Sci.*, vol. 150, no. 1, pp. 243–269, Apr. 1992.
- [194] S. Alvo, U. Pierre, C. Paris, and U. M. R. Cnrs, “A van der Waals Force-Based Adhesion Model for Micromanipulation,” *J. Adhes. Sci. Technol.*, vol. 16, pp. 15–16, 2010.
- [195] B. Derjaguin, “Untersuchungen über die Reibung und Adhäsion, IV,” *Kolloid-Zeitschrift*, vol. 69, no. 2, pp. 155–164, Nov. 1934.
- [196] H. C. Hamaker, “The London—van der Waals attraction between spherical particles,” *Physica*, vol. 4, no. 10, pp. 1058–1072, 1937.
- [197] B. Cappella and G. Dietler, “Force-distance curves by atomic force microscopy,” *Surf. Sci. Rep.*, vol. 34, no. 1–3, pp. 1–104, 1999.
- [198] E. M. Lifshitz, “the Theory of Molecular Attractive Forces Between Solids,” *Sov. Phys. JETP*, vol. Vol: 2, no. 1, 1956.
- [199] I. E. Dzyaloshinskii, E. M. Lifshitz, and L. P. Pitaevskii, “General theory of van der waals’ forces,” *Sov. Phys. Uspekhi*, vol. 4, no. 2, pp. 153–176, Feb. 1961.
- [200] U. Hartmann, “Manifestation of zero-point quantum fluctuations in atomic force microscopy,” *Phys. Rev. B*, vol. 42, no. 3, pp. 1541–1546, Jul. 1990.
- [201] P. Tabeling, *Introduction to Microfluidics*. New York: Oxford University Press, 2011.
- [202] F. L. Leite, C. C. Bueno, A. L. Da Róz, E. C. Ziemath, and O. N. Oliveira, *Theoretical Models for Surface Forces and Adhesion and Their Measurement Using Atomic Force Microscopy*, vol. 13, no. 12. 2012.
- [203] el Gauthier, E. Alvo, O. Dejeu, B. Tamadazte, and P. Rougeot, “Analysis and Specificities of Adhesive Forces Between Microscale and Nanoscale,” *IEEE Trans. Autom. Sci. Eng.*, vol. 10, no. 3, pp. 562–570, Jul. 2013.
- [204] M. Marz, K. Sagisaka, and D. Fujita, “Ni nanocrystals on hopg(0001): A

- scanning tunnelling microscope study,” *Beilstein J. Nanotechnol.*, vol. 4, no. 1, pp. 406–417, 2013.
- [205] B. Bhushan, *Handbook of Micro/Nano Tribology*, Second. CRC Press, 1998.
- [206] G. Binnig, C. F. Quate, and C. Gerber, “Atomic Force Microscope,” *Phys. Rev. Lett.*, vol. 56, no. 9, pp. 930–933, Mar. 1986.
- [207] N. H. W. Richard Bowen, *Atomic Force Microscopy in Process Engineering: An Introduction to AFM for Improved Processes and Products*, Illustrate. Butterworth-Heinemann, 2009.
- [208] J. N. Israelachvili and D. Tabor, “The Measurement of Van Der Waals Dispersion Forces in the Range 1.5 to 130 nm,” *Proc. R. Soc. A Math. Phys. Eng. Sci.*, vol. 331, no. 1584, pp. 19–38, Nov. 1972.
- [209] R. R. Laszlo Solymar, Donald Walsh, *Electrical Properties of Materials*. New York: Oxford University Press, 2014.
- [210]   
“<http://www.olympusmicro.com/primer/java/nearfield/vanderwaal/index.html> .” [Online]. Available: <http://www.olympusmicro.com/primer/java/nearfield/vanderwaal/index.html>. [Accessed: 15-Aug-2015].
- [211] A. L. Weisenhorn, P. K. Hansma, T. R. Albrecht, and C. F. Quate, “Forces in atomic force microscopy in air and water,” *Appl. Phys. Lett.*, vol. 54, no. 26, p. 2651, 1989.
- [212] N. a. Burnham, “Measuring the nanomechanical properties and surface forces of materials using an atomic force microscope,” *J. Vac. Sci. Technol. A*, vol. 7, no. 4, p. 2906, 1989.
- [213] N. A. Burnham, D. D. Dominguez, R. L. Mowery, and R. J. Colton, “Probing the surface forces of monolayer films with an atomic-force microscope,” *Phys. Rev. Lett.*, vol. 64, no. 16, pp. 1931–1934, Apr. 1990.
- [214] F. O. Goodman and N. Garcia, “Roles of the attractive and repulsive forces in

- atomic-force microscopy,” *Phys. Rev. B*, vol. 43, no. 6, pp. 4728–4731, 1991.
- [215] R. Alley, K. Komvopoulos, and R. Howe, “Self-assembled monolayer film for enhanced imaging of rough surfaces with atomic force microscopy,” *J. Appl. Phys.*, vol. 76, no. 10, pp. 5731–5737, 1994.
- [216] T. Stifter, O. Marti, and B. Bhushan, “Theoretical investigation of the distance dependence of capillary and van der Waals forces in scanning force microscopy,” *Phys. Rev. B*, vol. 62, no. 20, pp. 13667–13673, 2000.
- [217] J. Diao, K. Gall, and M. L. Dunn, “Surface-stress-induced phase transformation in metal nanowires,” *Nat. Mater.*, vol. 2, no. 10, pp. 656–60, Oct. 2003.
- [218] H. a. Wu, “Molecular dynamics study on mechanics of metal nanowire,” *Mechanics Research Communications*, vol. 33, no. 1, pp. 9–16, Jan. 2006.
- [219] G. S. D Fiorani, *Fundamental Properties of Nanostructured Materials*. World Scientific, 1994.
- [220] B. Wu, A. Heidelberg, and J. J. Boland, “Mechanical properties of ultrahigh-strength gold nanowires,” *Nat. Mater.*, vol. 4, no. 7, pp. 525–9, Jul. 2005.
- [221] H. Liang, M. Upmanyu, and H. Huang, “Size-dependent elasticity of nanowires: Nonlinear effects,” *Phys. Rev. B*, vol. 71, no. 24, p. 241403, Jun. 2005.
- [222] F. Ma and K. Xu, “Size-dependent multilayer relaxation of nanowires and additional effect of surface stresses,” *Solid State Commun.*, vol. 141, no. 5, pp. 273–278, Feb. 2007.
- [223] P. Sharma, S. Ganti, and N. Bhate, “Effect of surfaces on the size-dependent elastic state of nano-inhomogeneities,” *Appl. Phys. Lett.*, vol. 82, no. 4, p. 535, 2003.
- [224] M. T. McDowell, A. M. Leach, and K. Gall, “On the elastic modulus of metallic nanowires,” *Nano Lett.*, vol. 8, no. 11, pp. 3613–8, Nov. 2008.

- [225] L. Philippe, Z. Wang, I. Peyrot, a. W. Hassel, and J. Michler, “Nanomechanics of rhenium wires: Elastic modulus, yield strength and strain hardening,” *Acta Mater.*, vol. 57, no. 14, pp. 4032–4035, Aug. 2009.
- [226] E. G. Karpov, H. Yu, H. S. Park, W. K. Liu, Q. J. Wang, and D. Qian, “Multiscale boundary conditions in crystalline solids: Theory and application to nanoindentation,” *Int. J. Solids Struct.*, vol. 43, no. 21, pp. 6359–6379, Oct. 2006.
- [227] G. Jing, H. Duan, X. Sun, Z. Zhang, J. Xu, Y. Li, J. Wang, and D. Yu, “Surface effects on elastic properties of silver nanowires: Contact atomic-force microscopy,” *Phys. Rev. B*, vol. 73, no. 23, p. 235409, Jun. 2006.
- [228] S. Cuenot, C. Frétiigny, S. Demoustier-Champagne, and B. Nysten, “Surface tension effect on the mechanical properties of nanomaterials measured by atomic force microscopy,” *Phys. Rev. B*, vol. 69, no. 16, p. 165410, Apr. 2004.
- [229] K. Kang and W. Cai, “Size and temperature effects on the fracture mechanisms of silicon nanowires: Molecular dynamics simulations,” *Int. J. Plast.*, vol. 26, no. 9, pp. 1387–1401, Sep. 2010.
- [230] G. . Srivastava, *The Physics of Phonons*, Illustrate. CRC Press, 1990.
- [231] J. H. Lienhard, *A Heat Transfer Textbook: Fourth Edition*. Courier Corporation, 2013.
- [232] G. A. Slack, “The Thermal Conductivity of Nonmetallic Crystals,” *Solid State Phys. - Adv. Res. Appl.*, vol. 34, no. C, pp. 1–71, 1979.
- [233] S. Callard, “Thermal conductivity of SiO<sub>2</sub> flms by scanning thermal microscopy,” vol. 245, pp. 203–209, 1999.
- [234] T. Zhang, S. Wu, R. Zheng, and G. Cheng, “Significant reduction of thermal conductivity in silicon nanowire arrays,” *Nanotechnology*, vol. 24, no. 50, p. 505718, Dec. 2013.
- [235] H. Shanks, P. Maycock, P. Sidles, and G. Danielson, “Thermal Conductivity of Silicon from 300 to 1400°K,” *Phys. Rev.*, vol. 130, no. 5, pp. 1743–1748,

Jun. 1963.

- [236] G. A. Slack, “Thermal Conductivity of Pure and Impure Silicon, Silicon Carbide, and Diamond,” *J. Appl. Phys.*, vol. 35, no. 12, p. 3460, 1964.
- [237] A. I. Hochbaum, R. Chen, R. D. Delgado, W. Liang, E. C. Garnett, M. Najarian, A. Majumdar, and P. Yang, “Enhanced thermoelectric performance of rough silicon nanowires,” *Nature*, vol. 451, no. 7175, pp. 163–7, Jan. 2008.
- [238] S. K. Bux, R. G. Blair, P. K. Gogna, H. Lee, G. Chen, M. S. Dresselhaus, R. B. Kaner, and J.-P. Fleurial, “Nanostructured Bulk Silicon as an Effective Thermoelectric Material,” *Adv. Funct. Mater.*, vol. 19, no. 15, pp. 2445–2452, Aug. 2009.
- [239] J. Tang, H.-T. Wang, D. H. Lee, M. Fardy, Z. Huo, T. P. Russell, and P. Yang, “Holey silicon as an efficient thermoelectric material,” *Nano Lett.*, vol. 10, no. 10, pp. 4279–83, Oct. 2010.
- [240] P. Martin, Z. Aksamija, E. Pop, and U. Ravaioli, “Impact of phonon-surface roughness scattering on thermal conductivity of thin Si nanowires,” *Phys. Rev. Lett.*, vol. 102, no. 12, pp. 1–12, 2009.
- [241] C. T. Bui, R. Xie, M. Zheng, Q. Zhang, C. H. Sow, B. Li, and J. T. L. Thong, “Diameter-dependent thermal transport in individual ZnO nanowires and its correlation with surface coating and defects,” *Small*, vol. 8, no. 5, pp. 738–45, Mar. 2012.
- [242] R. Costescu, M. Wall, and D. Cahill, “Thermal conductance of epitaxial interfaces,” *Phys. Rev. B*, vol. 67, no. 5, pp. 1–5, 2003.
- [243] M. Hinz, O. Marti, B. Gotsmann, M. a. Lantz, and U. Dürig, “High resolution vacuum scanning thermal microscopy of HFO<sub>2</sub> AND SiO<sub>2</sub>,” *Appl. Phys. Lett.*, vol. 92, no. 4, p. 43122, 2008.
- [244] S. Gomès, P. Newby, B. Canut, K. Termentzidis, O. Marty, L. Fréchette, P. Chantrenne, V. Aimez, J.-M. Bluet, and V. Lysenko, “Characterization of the thermal conductivity of insulating thin films by scanning thermal

- microscopy,” *Microelectronics J.*, vol. 44, no. 11, pp. 1029–1034, Nov. 2013.
- [245] M. Hinz, O. Marti, B. Gotsmann, M. A. Lantz, and U. Dürig, “High resolution vacuum scanning thermal microscopy of HfO<sub>2</sub> and SiO<sub>2</sub>,” *Appl. Phys. Lett.*, vol. 92, no. 4, p. 43122, 2008.
- [246] D. G. Cahill, K. Goodson, and A. Majumdar, “Thermometry and Thermal Transport in Micro/Nanoscale Solid-State Devices and Structures,” *J. Heat Transfer*, vol. 124, no. 2, p. 223, 2002.
- [247] E. P. Donovan, F. Spaepen, D. Turnbull, J. M. Poate, and D. C. Jacobson, “Calorimetric studies of crystallization and relaxation of amorphous Si and Ge prepared by ion implantation,” *J. Appl. Phys.*, vol. 57, no. 6, p. 1795, 1985.
- [248] T. Yamane, N. Nagai, S. Katayama, and M. Todoki, “Measurement of thermal conductivity of silicon dioxide thin films using a 3 $\omega$  method,” *J. Appl. Phys.*, vol. 91, no. 12, p. 9772, 2002.
- [249] J. Alvarez-Quintana and J. Rodríguez-Viejo, “Extension of the 3 $\omega$  method to measure the thermal conductivity of thin films without a reference sample,” *Sensors Actuators, A Phys.*, vol. 142, no. 1, pp. 232–236, 2008.
- [250] W. J. Parker, R. J. Jenkins, C. P. Butler, and G. L. Abbott, “Flash Method of Determining Thermal Diffusivity, Heat Capacity, and Thermal Conductivity,” *J. Appl. Phys.*, vol. 32, no. 9, pp. 1679–1684, Sep. 1961.
- [251] M. J. O’Neill, “Measurement of Specific Heat Functions by Differential Scanning Calorimetry,” *Anal. Chem.*, vol. 38, no. 10, pp. 1331–1336, Sep. 1966.
- [252] S.-M. Lee and D. G. Cahill, “Heat transport in thin dielectric films,” *J. Appl. Phys.*, vol. 81, no. 6, p. 2590, 1997.
- [253] S. K. Bux, R. G. Blair, P. K. Gogna, H. Lee, G. Chen, M. S. Dresselhaus, R. B. Kaner, and J.-P. Fleurial, “Nanostructured Bulk Silicon as an Effective Thermoelectric Material,” *Adv. Funct. Mater.*, vol. 19, no. 15, pp. 2445–2452, Aug. 2009.

- [254] A. I. Boukai, Y. Bunimovich, J. Tahir-Kheli, J.-K. Yu, W. A. Goddard, and J. R. Heath, "Silicon nanowires as efficient thermoelectric materials.," *Nature*, vol. 451, no. 7175, pp. 168–71, Jan. 2008.
- [255] M. Itsumi, *SiO2 in Si Microdevices*, Illustrate. Springer, 2002.
- [256] T. Yamane, N. Nagai, S. Katayama, and M. Todoki, "Measurement of thermal conductivity of silicon dioxide thin films using a 3 omega method," *J. Appl. Phys.*, vol. 91, no. 12, pp. 9772–9776, 2002.
- [257] A. I. Hochbaum, R. Chen, R. D. Delgado, W. Liang, E. C. Garnett, M. Najarian, A. Majumdar, and P. Yang, "Enhanced thermoelectric performance of rough silicon nanowires.," *Nature*, vol. 451, no. 7175, pp. 163–7, Jan. 2008.
- [258] K. Biswas, C. W. Myles, M. Sanati, and G. S. Nolas, "Thermal properties of guest-free Si136 and Ge136 clathrates: A first-principles study," *J. Appl. Phys.*, vol. 104, no. 3, p. 33535, 2008.
- [259] E. R. M. Knoll, "Das Elektronenmikroskop.," *Zeitschrift für Phys.*, vol. 318, pp. 318–339, 1932.
- [260] D. Williams and C. Carter, *The Transmission Electron Microscope*, illustrated edition. Springer Science & Business Media, 1996.
- [261] A. Fleming, "On the history and development of the thermionic valve," *J. Sci. Instrum.*, vol. 11, no. 2, pp. 44–49, Feb. 1934.
- [262] "Tecnai on-line help manual-Alignments." [Online]. Available: [http://www.bio.brandeis.edu/KeckWeb/emdoc/en\\_US.ISO8859-1/align\\_F2030.pdf](http://www.bio.brandeis.edu/KeckWeb/emdoc/en_US.ISO8859-1/align_F2030.pdf). [Accessed: 01-Jan-2016].
- [263] J. Hinks, "Radiation damage in Indium Copper Diselenide," University of Salford, 2007.
- [264] J. a. Hinks, J. a. van den Berg, and S. E. Donnelly, "MIAMI: Microscope and ion accelerator for materials investigations," *J. Vac. Sci. Technol. A*, vol. 29, no. 2, p. 21003, 2011.



- [265] “Beam Imaging Solutions.” [Online]. Available: <http://www.beamimaging.com/IGUN.html>. [Accessed: 01-Jun-2016].
- [266] S. B. Kaemmar, “Introduction to Bruker’s ScanAsyst and PeakForce Tapping AFM Technology,” 2011. [Online]. Available: [https://www.bruker.com/fileadmin/user\\_upload/8-PDF-Docs/SurfaceAnalysis/AFM/ApplicationNotes/Introduction\\_to\\_Brukers\\_ScanAsyst\\_and\\_PeakForce\\_Tapping\\_Atomic\\_Force\\_Microscopy\\_Technology\\_AFM\\_AN133.pdf](https://www.bruker.com/fileadmin/user_upload/8-PDF-Docs/SurfaceAnalysis/AFM/ApplicationNotes/Introduction_to_Brukers_ScanAsyst_and_PeakForce_Tapping_Atomic_Force_Microscopy_Technology_AFM_AN133.pdf). [Accessed: 16-Jun-2015].
- [267] “AFM: Beginner’s Guide.” [Online]. Available: [http://afmhelp.com/index.php?option=com\\_content&view=article&id=51&Itemid=57](http://afmhelp.com/index.php?option=com_content&view=article&id=51&Itemid=57). [Accessed: 02-Feb-2016].
- [268] B. Bhushan, *Scanning Probe Microscopy in Nanoscience and Nanotechnology* 2, Illustrate. Springer Science & Business Media, 2010.
- [269] G. Haugstad, *Atomic Force Microscopy: Understanding Basic Modes and Advanced Applications*. John Wiley & Sons, 2012.
- [270] F. J. Giessibl, “Advances in atomic force microscopy,” *Rev. Mod. Phys.*, vol. 75, pp. 949–983, 2003.
- [271] P. Avouris, T. Hertel, and R. Martel, “Atomic force microscope tip-induced local oxidation of silicon: kinetics, mechanism, and nanofabrication,” *Appl. Phys. Lett.*, vol. 71, no. 2, p. 285, 1997.
- [272] T. Effects and C. Condensation, “Atomic-Scale Friction : Thermal Effects and Capillary Condensation,” University of Leyden, 2006.
- [273] N. Starostina and P. West, “Part II: Sample Preparation for AFM Particle Characterization,” *Probe Microscopy*, 2006. [Online]. Available: <http://nanoparticles.org/pdf/Starostina-West.pdf>. [Accessed: 27-Sep-2015].
- [274] Y. Chen, J. Cai, M. Liu, G. Zeng, Q. Feng, and Z. Chen, “Research on double-probe, double- and triple-tip effects during atomic force microscopy scanning,” *Scanning*, vol. 26, no. 4, pp. 155–161, Dec. 2006.

- [275] P. Grütter, W. Zimmermann-Edling, and D. Brodbeck, “Tip artifacts of microfabricated force sensors for atomic force microscopy,” *Appl. Phys. Lett.*, vol. 60, no. 22, p. 2741, 1992.
- [276] U. D. Schwarz, H. Haefke, P. Reimann, and H. J. Güntherodt, “Tip artefacts in scanning force microscopy,” *Journal of Microscopy.*, vol. 173, no. 3, pp. 183–197, Mar. 1994.
- [277] P. M. Williams, K. M. Shakesheff, M. C. Davies, D. E. Jackson, C. J. Roberts, and S. J. B. Tendler, “Toward True Surface Recovery: Studying Distortions in Scanning Probe Microscopy Image Data,” *Langmuir*, vol. 12, no. 14, pp. 3468–3471, 1996.
- [278] K. L. Westra, A. W. Mitchell, and D. J. Thomson, “Tip artifacts in atomic force microscope imaging of thin film surfaces,” *J. Appl. Phys.*, vol. 74, no. 5, p. 3608, 1993.
- [279] J. E. Griffith and D. A. Grigg, “Dimensional metrology with scanning probe microscopes,” *J. Appl. Phys.*, vol. 74, no. 9, p. R83, 1993.
- [280] R. V Gainutdinov and P. a Arutyunov, “Artifacts in Atomic Force Microscopy,” vol. 30, no. 4, pp. 219–224, 2001.
- [281] S. B. Velegol, S. Pardi, X. Li, D. Velegol, and B. E. Logan, “AFM imaging artifacts due to bacterial cell height and AFM tip geometry,” *Langmuir*, vol. 19, no. 3, pp. 851–857, 2003.
- [282] a. P. Gunning, a. R. Mackie, P. J. Wilde, and V. J. Morris, “Atomic Force Microscopy of Emulsion Droplets: Probing Droplet-Droplet Interactions,” *Langmuir*, vol. 20, no. 1, pp. 116–122, 2004.
- [283] F. Golek, P. Mazur, Z. Ryszka, and S. Zuber, “AFM image artifacts,” *Appl. Surf. Sci.*, vol. 304, pp. 11–19, Jun. 2014.
- [284] D. Ricci and P. C. Braga, “Recognizing and avoiding artifacts in AFM imaging,” in *Atomic Force Microscopy*, vol. 242, Humana Press, 2004, pp. 25–37.

- [285] P. West and N. Starostina, “A Guide to AFM Image Artifacts,” 2002. .
- [286] H. Vancso, G. Julius, Schönherr, “Atomic Force Microscopy in Practice,” in *Scanning Force Microscopy of Polymers*, 1st ed., Springer-Verlag Berlin Heidelberg, 2010, p. XIV, 248.
- [287] Y. Liu and P. Grütter, “Magnetic dissipation force microscopy studies of magnetic materials,” *J. Appl. Phys.*, vol. 83, no. 11, pp. 7333–7338, Jun. 1998.
- [288] M. Raposo, Q. Ferreira, and P. a Ribeiro, “A Guide for Atomic Force Microscopy Analysis of Soft- Condensed Matter,” *Mod. Res. Educ. Top. Microsc.*, pp. 758–769, 2007.
- [289] J. F. Ziegler, M. D. Ziegler, and J. P. Biersack, “SRIM – The stopping and range of ions in matter (2010),” *Nucl. Instruments Methods Phys. Res. Sect. B Beam Interact. with Mater. Atoms*, vol. 268, no. 11–12, pp. 1818–1823, Jun. 2010.
- [290] M. D. Z. James F. Ziegler, J. P. Biersack, *SRIM, the Stopping and Range of Ions in Matter*, Illustrate. SRIM Company, 2008.
- [291] G. Was, *Fundamentals of Radiation Materials Science*. Berlin, Heidelberg: Springer Berlin Heidelberg, 2007.
- [292] G. H. K. and R. S. Pease, “The Displacement of Atoms in Solids by Radiation,” *Reports Prog. Phys.*, vol. 18, p. 1, 1955.
- [293] G. Carter and W. A. Grant, *Ion Implantation of Semiconductors*. Edward Arlond, 1976.
- [294] J. A. Brinkman, “Production of Atomic Displacements by High-Energy Particles,” *Am. J. Phys.*, vol. 24, no. 4, p. 246, 1956.
- [295] J. W. M. and J. K. H. M Nastasi, *Ion-Solid Interactions: Fundamentals and Applications*. Cambridge: Cambridge University Press, 1996.
- [296] J. A. Brinkman, “Production of Atomic Displacements by High-Energy Particles,” *Am. J. Phys.*, vol. 24, no. 4, p. 246, 1956.

- [297] A. E. Stuchbery and E. Bezakova, “Thermal-Spike Lifetime from Picosecond-Duration Preequilibrium Effects in Hyperfine Magnetic Fields Following Ion Implantation,” *Phys. Rev. Lett.*, vol. 82, no. 18, pp. 3637–3640, May 1999.
- [298] M. W. Thompson and R. S. Nelson, “Evidence for heated spikes in bombarded gold from the energy spectrum of atoms ejected by 43 keV  $\alpha$  and Xe<sup>+</sup> ions,” *Philos. Mag.*, vol. 7, no. 84, pp. 2015–2026, Dec. 1962.
- [299] K. Nordlund, “Energy loss of energetic ions,” 1996. [Online]. Available: <http://beam.helsinki.fi/~knordlun/mdh/rangetext.html>. [Accessed: 06-Mar-2016].
- [300] J. W. M. Michael Nastasi, *Ion Implantation and Synthesis of Materials*, Illustrate. Springer Science & Business Media, 2007.
- [301] G. H. Kinchin and R. S. Pease, “The Displacement of atoms in solids by radiation,” *Reports Prog. Phys.*, vol. 18, no. 1, p. 301, Jan. 1955.
- [302] J. C. Bourgoin, P. Ludeau, and B. Massarani, “Threshold energy determination in thick semiconductor samples,” *Rev. Phys. Appliquée*, vol. 11, no. 2, pp. 279–284, 1976.
- [303] P. L. F. Hemment, “Study of the Anisotropy of Radiation Damage Rates in n-Type Silicon,” *J. Appl. Phys.*, vol. 40, no. 12, p. 4893, 1969.
- [304] J. D. Cheryl, G. P. Summers, and E. A. Wolicki, “High energy electron induced displacement damage in silicon - Nuclear Science, IEEE Transactions on.pdf,” vol. 35, no. 6, pp. 1208–1214, 1988.
- [305] Y. Zhang and W. J. Weber, “Role of energy partitioning on electron-hole recombination, trapping, and detection in silicon detectors,” *Phys. Rev. B - Condens. Matter Mater. Phys.*, vol. 82, no. 7, pp. 1–6, 2010.
- [306] E. Holmström, K. Nordlund, and A. Kuronen, “Threshold defect production in germanium determined by density functional theory molecular dynamics simulations,” *Phys. Scr.*, vol. 81, no. 3, p. 35601, 2010.
- [307] J. C. Barbour, D. Dimos, and T. R. Guilinger, “Control of photoluminescence

from,” *Sci. York*, vol. 3, pp. 202–204, 1992.

- [308] M. Mazzarolo, L. Colombo, G. Lulli, and E. Albertazzi, “Low-energy recoils in crystalline silicon: Quantum simulations,” *Physical Review B*, vol. 63, no. 19. 2001.
- [309] E. Holmström, a. Kuronen, and K. Nordlund, “Threshold defect production in silicon determined by density functional theory molecular dynamics simulations,” *Phys. Rev. B - Condens. Matter Mater. Phys.*, vol. 78, no. 4, pp. 1–6, 2008.
- [310] R. E. Stoller, M. B. Toloczko, G. S. Was, A. G. Certain, S. Dwaraknath, and F. A. Garner, “On the use of SRIM for computing radiation damage exposure,” *Nucl. Instruments Methods Phys. Res. Sect. B Beam Interact. with Mater. Atoms*, vol. 310, pp. 75–80, 2013.
- [311] G. Yu, X. Li, M. Lieber, and A. Cao, “Nanomaterial-incorporated blown bubble films for large-area , aligned nanostructures,” *J. Mater. Chem.*, vol. 18, pp. 728–734, 2008.
- [312] P. A. Smith, C. D. Nordquist, T. N. Jackson, T. S. Mayer, B. R. Martin, J. Mbindyo, and T. E. Mallouk, “Electric-field assisted assembly and alignment of metallic nanowires,” *Appl. Phys. Lett.*, vol. 77, no. 9, pp. 1399–1401, 2000.
- [313] T. Motooka and O. W. Holland, “Amorphization processes in ion implanted Si: Ion species effects,” *Appl. Phys. Lett.*, vol. 61, no. 25, p. 3005, 1992.
- [314] J. S. Custer, “Evidence for vacancies in amorphous Silicon,” *Phys. Rev. Lett.*, vol. 68, no. 25, pp. 3714–3717, 1992.
- [315] D. Stichtenoth, K. Wegener, C. Gutsche, I. Regolin, F. J. Tegude, W. Prost, M. Seibt, and C. Ronning, “P -type doping of GaAs nanowires,” *Appl. Phys. Lett.*, vol. 92, no. 16, pp. 148–151, 2008.
- [316] I. Jenčič, M. W. Bench, I. M. Robertson, and M. A. Kirk, “Electron-beam-induced crystallization of isolated amorphous regions in Si, Ge, GaP, and GaAs,” *J. Appl. Phys.*, vol. 78, no. 2, p. 974, 1995.

- [317] E. Oliviero, S. Peripolli, L. Amaral, P. F. P. Fichtner, M. F. Beaufort, J. F. Barbot, and S. E. Donnelly, "Damage accumulation in neon implanted silicon," *J. Appl. Phys.*, vol. 100, no. 4, p. 43505, 2006.
- [318] C. Borschel, R. Niepelt, S. Geburt, C. Gutsche, I. Regolin, W. Prost, F.-J. Tegude, D. Stichtenoth, D. Schwen, and C. Ronning, "Alignment of semiconductor nanowires using ion beams.," *Small*, vol. 5, no. 22, pp. 2576–80, Nov. 2009.
- [319] A. Cui, J. C. Fenton, W. Li, T. H. Shen, Z. Liu, Q. Luo, and C. Gu, "Ion-beam-induced bending of freestanding amorphous nanowires: The importance of the substrate material and charging," *Appl. Phys. Lett.*, vol. 102, no. 21, p. 213112, 2013.
- [320] C. Ronning, C. Borschel, S. Geburt, and R. Niepelt, "Ion beam doping of semiconductor nanowires," *Mater. Sci. Eng. R Reports*, vol. 70, no. 3–6, pp. 30–43, 2010.
- [321] J. A. Grimshaw and P. C. Banbury, "The displacement energy in GaAs," *Proc. Phys. Soc.*, vol. 84, no. 1, p. 151, 1964.
- [322] D. Pons, "Anisotropic defect introduction in n and p-GaAs by electron irradiation," *Phys. B+C*, vol. 116, no. 1–3, pp. 388–393, Feb. 1983.
- [323] D. Pons, P. M. Mooney, and J. C. Bourgoin, "Energy dependence of deep level introduction in electron irradiated GaAs," *J. Appl. Phys.*, vol. 51, no. 4, p. 2038, 1980.
- [324] B. Lehmann and D. Bräunig, "A deep-level transient spectroscopy variation for the determination of displacement threshold energies in GaAs," *J. Appl. Phys.*, vol. 73, no. 6, p. 2781, 1993.
- [325] S. M. Folies, "Comparison of Binary Collision Approximation and Molecular Dynamics for Displacement Cascades in GaAs." [Online]. Available: <http://prod.sandia.gov/techlib/access-control.cgi/2011/118082.pdf>. [Accessed: 20-Jan-2016].

- [326] “ITRS Reports.” [Online]. Available: <http://www.itrs2.net/itrs-reports.html>. [Accessed: 10-Oct-2016].
- [327] N. A. Sherwani, *Algorithms for VLSI Physical Design Automation*, Illustrate. Springer Science & Business Media, 2013.
- [328] M. C. Petty, *Molecular Electronics: From Principles to Practice*. John Wiley & Sons, 2008.
- [329] M. Amato, M. Palummo, R. Rurali, and S. Ossicini, “Silicon-germanium nanowires: Chemistry and physics in play, from basic principles to advanced applications,” *Chem. Rev.*, vol. 114, no. 2, pp. 1371–1412, 2014.
- [330] Y. Cui, Z. Zhong, D. Wang, W. U. Wang, and C. M. Lieber, “High performance silicon nanowire field effect transistors,” *Nano Lett.*, vol. 3, no. 2, pp. 149–152, 2003.
- [331] X. Jiang, Q. Xiong, S. Nam, F. Qian, and Y. Li, “InAs/InP radial nanowire heterostructures as high electron mobility devices,” *Nano Lett.*, vol. 7, no. 10, pp. 3214–3218, 2007.
- [332] Y. Li, J. Xiang, F. Qian, S. Gradečak, Y. Wu, H. Yan, D. A. Blom, and C. M. Lieber, “Dopant-free GaN/AlN/AlGaIn radial nanowire heterostructures as high electron mobility transistors,” *Nano Lett.*, vol. 6, no. 7, pp. 1468–1473, 2006.
- [333] F. Qian, Y. Li, S. Gradečak, and C. M. Lieber, “nitride-based nanowire radial heterostructures for nanophotonics,” *Nano Lett.*, vol. 4, no. 10, pp. 1975–1979, 2004.
- [334] J. Goldberger, A. I. Hochbaum, R. Fan, and P. Yang, “Silicon Vertically Integrated Nanowire Field Effect Transistors,” *Nano Lett.*, vol. 6, no. 5, pp. 973–977, 2006.
- [335] R. Beckman, “Bridging dimensions: demultiplexing ultrahigh-density nanowire circuits,” *Science*, vol. 310, no. 5747, pp. 465–468, Oct. 2005.
- [336] B. El-Kareh, *Fundamentals of Semiconductor Processing Technology*,

Illustrate. Springer Science & Business Media, 2012.

- [337] R. D. Yoshio Nishi, *Handbook of Semiconductor Manufacturing Technology*, Second Edi. CRC Press, 2007.
- [338] J. E. Stephen Donnelly, Graeme Greaves, “Private communication.” 2015.
- [339] E. F. Pecora, A. Irrera, and F. Priolo, “Ion beam-induced bending of silicon nanowires,” *Phys. E Low-Dimensional Syst. Nanostructures*, vol. 44, no. 6, pp. 1074–1077, 2012.
- [340] P. D. Edmondson, K. J. Abrams, J. A. Hinks, G. Greaves, C. J. Pawley, I. Hanif, and S. E. Donnelly, “An in situ transmission electron microscopy study of the ion irradiation induced amorphisation of silicon by He and Xe,” *Scr. Mater.*, vol. 113, pp. 190–193, 2016.
- [341] N. E. Grant and K. R. McIntosh, “Surface Passivation Attained by Silicon Dioxide Grown at Low Temperature in Nitric Acid,” *24th Eur. Photovolt. Sol. Energy Conf.*, vol. 30, no. 9, pp. 1676–1679, 2009.
- [342] J. C. Li, C. L. Wang, H. Peng, M. X. Wang, R. Z. Zhang, H. C. Wang, J. Liu, M. L. Zhao, and L. M. Mei, “Vibrational and thermal properties of small diameter silicon nanowires,” *J. Appl. Phys.*, vol. 108, no. 6, p. 63702, 2010.
- [343] A. K. and N. B. D. Rajiv Asthana, *Materials Processing and Manufacturing Science*. Elsevier Academic Press, 2006.
- [344] S. Sounilhac, E. Barthel, and F. Creuzet, “The electrostatic contribution to the long-range interactions between tungsten and oxide surfaces under ultrahigh vacuum,” *Appl. Surf. Sci.*, vol. 140, no. 3–4, pp. 411–414, 1999.
- [345] M. Gauthier, S. Alvo, J. Dejeu, B. Tamadazte, P. Rougeot, and S. Régnier, “Analysis and specificities of adhesive forces between microscale and nanoscale,” *IEEE Trans. Autom. Sci. Eng.*, vol. 10, no. 3, pp. 562–570, 2013.
- [346] B. Halg, “On a nonvolatile memory cell based on micro-electro-mechanics,” in *IEEE Proceedings on Micro Electro Mechanical Systems, An Investigation of Micro Structures, Sensors, Actuators, Machines and Robots.*, pp. 172–176.



- [347] C. K. Gupta, *Extractive Metallurgy of Molybdenum*. CRC Press, 1992.
- [348] “Molybdenum - Mechanical Properties And Material Application.” [Online]. Available: <http://www.azom.com/article.aspx?ArticleID=7637>. [Accessed: 28-Aug-2016].
- [349] Y. Zhang, J. X. Cao, Y. Xiao, and X. H. Yan, “Phonon spectrum and specific heat of silicon nanowires,” *J. Appl. Phys.*, vol. 102, no. 10, pp. 1–4, 2007.
- [350] P. . D. Desai, “Thermodynamic Properties of Manganese and Molybdenum,” *Journal of Physical Chemistry Reference Data*, vol. 16, no. 1. pp. 91–108, 1987.
- [351] S. Aldrich, “Polydispersed silicon nanowires.” [Online]. Available: <http://www.sigmaaldrich.com/catalog/product/aldrich/731498?lang=en&region=GB>. [Accessed: 20-Jan-2014].
- [352] M. Tang, L. Colombo, J. Zhu, and T. Diaz de la Rubia, “Intrinsic point defects in crystalline silicon: Tight-binding molecular dynamics studies of self-diffusion, interstitial-vacancy recombination, and formation volumes,” *Phys. Rev. B*, vol. 55, no. 21, pp. 14279–14289, 1997.
- [353] J. S. Custer, M. O. Thompson, D. C. Jacobson, J. M. Poate, S. Roorda, W. C. Sinke, and F. Spaepen, “Density of amorphous Si,” *Appl. Phys. Lett.*, vol. 64, no. 4, p. 437, 1994.
- [354] S. E. Donnelly, R. C. Birtcher, V. M. Vishnyakov, P. D. Edmondson, and G. Carter, “Anomalous annealing behavior of isolated amorphous zones in silicon,” *Nucl. Instruments Methods Phys. Res. Sect. B Beam Interact. with Mater. Atoms*, vol. 242, no. 1–2, pp. 595–597, Jan. 2006.
- [355] A. Meftah, F. Brisard, J. M. Costantini, E. Dooryhee, M. Hage-Ali, M. Hervieu, J. P. Stoquert, F. Studer, and M. Toulemonde, “Track formation in SiO<sub>2</sub> quartz and the thermal-spike mechanism,” *Phys. Rev. B*, vol. 49, no. 18, pp. 12457–12463, May 1994.
- [356] S. Hoilijoki, E. Holmström, and K. Nordlund, “Enhancement of irradiation-

- induced defect production in Si nanowires,” *J. Appl. Phys.*, vol. 110, no. 4, 2011.
- [357] E. Holmström, L. Toikka, A. V. Krasheninnikov, and K. Nordlund, “Response of mechanically strained nanomaterials to irradiation: Insight from atomistic simulations,” *Phys. Rev. B - Condens. Matter Mater. Phys.*, vol. 82, no. 4, pp. 1–5, 2010.
- [358] N. S. Rajput, X. Luo, H. C. Verma, and Z. Tong, “Ion-beam-assisted fabrication and manipulation of metallic nanowires,” *Micro & Nano Lett.*, vol. 10, no. 7, pp. 334–338, 2015.
- [359] Y. Ishii, C. S. Madi, M. J. Aziz, and E. Chason, “Stress evolution in Si during low-energy ion bombardment,” *J. Mater. Res.*, vol. 29, no. 24, pp. 2942–2948, 2014.
- [360] J. Tersoff, “New empirical approach for the structure and energy of covalent systems,” *Phys. Rev. B*, vol. 37, no. 12, pp. 6991–7000, Apr. 1988.
- [361] *ISO 25178:2005 Geometrical Product Specifications (GPS). Surface Texture: Areal—Part 2. Terms, definitions and surface texture parameters*; ISO: Genève, Switzerland, 2005.
- [362] *ISO 4288:1996 Geometrical Product Specifications (gps). Surface Texture: Profile Method. Rules and Procedures for the Assessment of Surface Texture*; ISO: Genève, Switzerland, 1996.
- [363] L. Fedina, O. I. Lebedev, G. Van Tendeloo, J. Van Landuyt, O. A. Mironov, and E. H. C. Parker, “In situ HREM irradiation study of point-defect clustering in MBE-grown strained  $\text{Si}_{1-x}\text{Ge}_x/(001)\text{Si}$  structures,” vol. 61, no. 15, pp. 336–345, 2000.

## Appendix A

A multislice SRIM Computer code to produce two-dimensional plots of ion irradiation induced damage and ion implantation:

```
% Variables %

% Nanowire diameter
prompt = 'What is the nanowire diameter? [nm]\n';
Diameter = input(prompt);
Diameter = 10*Diameter;
% Nanowire density
prompt = 'What is the nanowire density? [g/cc]\n';
density = input(prompt);
% Nanowire diameter
prompt = 'How many slices in a half circle do you want? \n';
slices = input(prompt);

% while nn == 0
%     if rem(slices,2) == 0
%         prompt = 'How many slices in a half circle do you want?
(enter a odd number slices) \n';
%         slices = input(prompt);
%     else
%         prompt = 'OKOK! \n';
%         nn=1;
%     end
% end

width(1)=Diameter;
D1=1;
D2=2;
for n=2:slices
```

```

        width(n)          =          2*sqrt(((Diameter/2)^2)-((Diameter*(n-
1)/(2*slices))^2));

        D1 = (Diameter*(n-1)/(2*slices));

        D2 = (Diameter/2);

        if D1 > D2

            prompt = 'Warning: the number of slices chosen exceeds the
real condition in the root \n';

            n = slices+100;

        end
end

% create the folders and copy the file TRIM.IN
for k=1:slices

    f = 'trim';

    folder = strcat(f,num2str(k));

    mkdir(folder);

    copyfile('TRIM.IN',[ 'trim',num2str(k),'/TRIM.IN'],'f');

end

%read the number of lines
for ii=1:slices

    ff = 'trim';

    ff2 = '/TRIM.IN';

    folder = strcat(ff,num2str(ii),ff2);

    fid = fopen(folder,'rt');

    i = 1;

    tline = fgetl(fid);

    A{i} = tline;

    while ischar(tline)

        i = i+1;

        tline = fgetl(fid);

        A{i} = tline;

    end

    fclose(fid);

```

```

    thickness = width(ii);
    % calculate dummy gas thickness
    DummyThick(ii) = Diameter - width(ii);
    % Change line 11 17 18
    A{11} = sprintf('          5                                0
%d',Diameter);
    A{17} = sprintf(' 1          "Nanowire"                %.2f  %.2f          1
0',thickness,density);
    A{18} = sprintf(' 2          "Dummy Gas"                %.2f  .0001
1          0',DummyThick(ii));

    % Write cell A into txtA
    folder = strcat(ff,num2str(ii),ff2);
    fid = fopen(folder,'wt+');
    for i = 1:numel(A)
        if A{i+1} == -1
            fprintf(fid,'%s\n', A{i});
            break
        else
            fprintf(fid,'%s\n', A{i});
        end
    end
    fclose(fid);

end

%phase 02 copying srим to all folders and run!
for k=1:slices
    f = 'trim';
    folder = strcat(f,num2str(k));
    copyfile('TRIM.exe',[f,num2str(k),'/TRIM.exe'],'f');
    copyfile('TRIMAUTO',[f,num2str(k),'/TRIMAUTO'],'f');
    copyfile('Data/*',[f,num2str(k),'/Data'],'f');
    copyfile('SRIM Restore/*',[f,num2str(k),'/SRIM
Restore'],'f');
    copyfile('SRIM Outputs/*',[f,num2str(k),'/SRIM
Outputs'],'f');
end

```

```

%phase 02 running srim...
for k=1:slices
    f = 'trim';
    folder = strcat(f,num2str(k));
    cd(folder);
    fname = 'TRIM.IN';
    prompt = '\n Running slice number ';
    k

    system(['TRIM.exe < ' fname]); %run executable with content of
    fname as inputs
    cd ..
end

%importing_vacancies_data_from_files.txt VACANCY.TXT
for k=1:slices
    f = 'trim';
    folder = strcat(f,num2str(k));
    cd(folder);
    ss(k) = importdata('VACANCY.txt');
    sss(k) = importdata('NOVAC.txt');
    ssss(k) = importdata('RANGE.txt');
    cd ..
end

%build the vector with vacancies + knock-on produced by ions
% full damage
% simulation
for k=1:slices
    zz(:,k)=ss(k).data(:,3)+sss(k).data(:,2); %total
    damage/displacement
    zzz(:,k)=(ssss(k).data(:,3)/(1e8))-sss(k).data(:,2);%build the
    vector with interstitials
    zzzz(:,k)=ss(k).data(:,3); %build the vector with vacancies
    zzzzz(:,k)=(ssss(k).data(:,2)/(1e7)); %build the vector of
    implantation

```

```

end

%build first slice without change it for total damage (displacement)
%build remaining slice without change it for total damage
(displacement)

for k=1:100
    zz1(k,slices) = zz(k,1);
end

ratio = Diameter/length(zz);
[M,I]=max(zz(:));
M = M*1.15;
for j=2:slices
    position = round(DummyThick(j)/2);
    position = round(position/ratio)
    for i=1:100
        if position+i < 101
            zz1(position+i,slices+j-1) = zz(i,j);
            zz1(position+i,slices-j+1) = zz(i,j);
        end
    end

    for l = 1:position
        zz1(l,slices+j-1) = M;
        zz1(l,slices-j+1) = M;
        zz1(100 + 1 - l,slices+j-1) = M;
        zz1(100 + 1 - l,slices-j+1) = M;
    end
end

zz2 = zz1';

%build first slice without change it for interstitials
(displacement)
%build remaining slices without change it for interstitials
(displacement)

```

```

for k=1:100
    zzz1(k,slices) = zzz(k,1);
end

ratio = Diameter/length(zzz);
[M,I]=max(zzz(:));
M = M*1.15;
for j=2:slices
    position = round(DummyThick(j)/2);
    position = round(position/ratio)
    for i=1:100
        if position+i < 101
            zzz1(position+i,slices+j-1) = zzz(i,j);
            zzz1(position+i,slices-j+1) = zzz(i,j);
        end
    end
end

for l = 1:position
    zzz1(l,slices+j-1) = M;
    zzz1(l,slices-j+1) = M;
    zzz1(100 + 1 - l,slices+j-1) = M;
    zzz1(100 + 1 - l,slices-j+1) = M;
end
end

%build first slice without change it for vacancies
%build remaining slices without change it for vacancies

for k=1:100
    zzzz1(k,slices) = zzzz(k,1);
end

ratio = Diameter/length(zzzz);
[M,I]=max(zzzz(:));

```



```

M = M*1.15;
for j=2:slices
    position = round(DummyThick(j)/2);
    position = round(position/ratio)
    for i=1:100
        if position+i < 101
            zzzz1(position+i,slices+j-1) = zzzz(i,j);
            zzzz1(position+i,slices-j+1) = zzzz(i,j);
        end
    end

    for l = 1:position
        zzzz1(l,slices+j-1) = M;
        zzzz1(l,slices-j+1) = M;
        zzzz1(100 + 1 - l,slices+j-1) = M;
        zzzz1(100 + 1 - l,slices-j+1) = M;
    end
end

%build first slice without change it for implantation
%build remaining slices without change it for implantation

for k=1:100
    zzzzz1(k,slices) = zzzzz(k,1);
end

ratio = Diameter/length(zzzzz);
[M,I]=max(zzzzz(:));
M = M*1.15;
for j=2:slices
    position = round(DummyThick(j)/2);
    position = round(position/ratio)
    for i=1:100
        if position+i < 101
            zzzzz1(position+i,slices+j-1) = zzzzz(i,j);
            zzzzz1(position+i,slices-j+1) = zzzzz(i,j);

```

```

        end
    end

    for l = 1:position
        zzzzz1(l,slices+j-1) = M;
        zzzzz1(l,slices-j+1) = M;
        zzzzz1(100 + 1 - l,slices+j-1) = M;
        zzzzz1(100 + 1 - l,slices-j+1) = M;
    end
end

% generate plots

zz2 = zz1';
zzz2 = zzz1';
zzzz2 = zzzz1';
zzzzz2 = zzzzz1';

createfigure2(zz2,Diameter,slices) %total damage
createfigure3(zzz2,Diameter,slices) %interstitials
createfigure4(zzzz2,Diameter,slices) %vacancies
createfigure5(zzz2-zzzz2,Diameter,slices) %interstitials-vacancies
createfigure6(zzzzz2,Diameter,slices) %implantation

toc

```

## Appendix B

Volume change calculation for toroid:

Let:  $R$  be the radius from the centre of a torus to the centre of its tube; and  
 $r$  be the radius of the tube.

Ratio of area of a circle of diameter  $2r$  to area of a square with sides  $2r$ :

$$\frac{\pi r^2}{4r^2} = \frac{\pi}{4}$$

Volume of a ring,  $V_{\text{ring}}$ , with a square cross-section with sides  $2r$ :

$$\begin{aligned} V_{\text{ring}} &= 2r[\pi(R+r)^2 - \pi(R-r)^2] = 2\pi r[(R^2 + r^2 + 2Rr) - (R^2 + r^2 - 2Rr)] \\ &= 2\pi r[R^2 + r^2 + 2Rr - R^2 - r^2 + 2Rr] = 8\pi Rr^2 \end{aligned}$$

Therefore, the volume of a torus is given by:

$$V_{\text{torus}} = \frac{\pi}{4} V_{\text{ring}} = \frac{\pi}{4} 8\pi Rr^2 = 2\pi^2 Rr^2$$

Now calculate the volume of a torus outside the radius,  $R$ :

$$V_{>R} = \frac{\pi}{4} 2r[\pi(R+r)^2 - \pi R^2] = \frac{\pi^2 r}{2} [R^2 + r^2 + 2Rr - R^2] = \frac{\pi^2 r^2}{2} [2R + r]$$

Similarly, calculate the volume of a torus inside the radius,  $R$ :

$$V_{<R} = \frac{\pi}{4} 2r[\pi R^2 - \pi(R-r)^2] = \frac{\pi^2 r}{2} [R^2 - R^2 - r^2 + 2Rr] = \frac{\pi^2 r^2}{2} [2R - r]$$

Check that  $V_{>R} + V_{<R} = V_{\text{torus}}$ :

$$V_{>R} + V_{<R} = \frac{\pi^2 r^2}{2} [2R + r] + \frac{\pi^2 r^2}{2} [2R - r] = \frac{\pi^2 r^2}{2} [4R] = 2\pi^2 Rr^2 = V_{\text{torus}}$$

The difference,  $\Delta V$ , between  $V_{>R}$  and  $V_{<R}$  is given by:

$$\begin{aligned}\Delta V &= \frac{\pi^2 r^2}{2} [2R + r] - \frac{\pi^2 r^2}{2} [2R - r] = \frac{\pi^2 r^2}{2} [2R + r - 2R + r] = \frac{\pi^2 r^2}{2} [2r] \\ &= 2\pi^2 r^3\end{aligned}$$

Which surprisingly is independent of  $R$ .

The ratio,  $\sigma$ , of  $V_{>R}$  to  $V_{<R}$  is given by:

$$\sigma = \frac{V_{>R}}{V_{<R}} = \frac{\frac{\pi^2 r^2}{2} [2R + r]}{\frac{\pi^2 r^2}{2} [2R - r]} = \frac{2R + r}{2R - r}$$